SAPIENZA
UNIVERSITÀ DI ROMA

Sapienza University of Rome

Department of Physics
PhD in Physics

Thesis For The Degree Of Doctor Of Philosophy

Diverse Applications of the Quantum Walk model in Quantum Information: a theoretical and experimental analysis in the optical framework

Thesis Advisor
Prof. Paolo Mataloni

Candidate
Alessandro Laneve
ID 1653564

Academic Year MMXXI-MMXXII (XXXV cycle)

Thesis defended on 30th January 2023
in front of a Board of Examiners composed by:
Prof. Paolo Postorino (chairman)
Prof. Fabrice Laussy
Prof. Emanuele Pelucchi
Referees: Prof Fabrice Laussy, Prof. Fabrizio Illuminati.

Diverse Applications of the Quantum Walk model in Quantum Information: a theoretical and experimental analysis in the optical framework
Ph.D. Thesis, Sapienza - University of Rome

This thesis has been typeset by LATEX and the Overleaf Template "Sapienza PhD Thesis".
Author's email: alessandro.laneve@uniroma1.it

For the wanderers in joyful pursuit,
treading through the night and sorrow,
there's a warmth along the route
holding off them looking backward.

A colourful quilt and patchy,
made of voices and cherished eyes,
To release the heart from aching
and to comfort 'til sunrise.

Without mine, where would be I?
Without mine, would any of this
make sense? Would it exist?
Mere reflection of their light.

Contents

Foreword

I loafe and invite my soul,
I lean and loafe at my ease observing a spear of summer grass.
..
Creeds and schools in abeyance,
Retiring back a while sufficed at what they are, but never forgotten,
I harbor for good or bad, I permit to speak at every hazard,
Nature without check with original energy.

Leaves of Grass, Walt Whitman

In the last thirty years, after their first definition and rigorous formulation, Quantum Walks have been adopted as a general model for coherent propagation phenomena, featuring a plethora of fruitful applications. This very simple and general theoretical platform has been found suitable for many tasks, such as the simulation of quantum and coherent systems, even biological ones, or the development of quantum algorithms; moreover, they are generally useful for quantum information protocols. The great success of the Quantum Walk model as a tool for the analysis of physical systems or for the design of efficient protocols resides in the general underlying idea that a *dynamical* study of a system can deliver more information about it than a static measurement of its features, an idea that has been spreading through all fields of research, inside and outside of physics.
The present thesis revolves around this main idea: we can use dynamical methods both to study and control quantum systems, and some instances of this framework are exhibited, with a particular focus on optical experimental implementations. In Fig. 1, an outlook of the topics discussed in this manuscript is reported.

In Chapter 1, I provide a general introduction to the concepts and frameworks that are addressed throughout the rest of the thesis. In particular, I review some of the fundamental ideas underlying quantum information and some selected topics in quantum optics, in order to provide a clear context for the following theoretical and experimental discussion. In addition to that, I also illustrate the problem of Quantum State Discrimination in a general fashion, concluding with a thorough overview of studies regarding ordered and disordered Quantum Walks. The latter represent the core of Chapter 2: I present the p-diluted model, a very general disorder model for Quantum Walks, and an experimental platform capable of reproducing such inhomogeneous evolution. I report on two works I participated in with theoretical contributions, that fully display the ductility of Quantum Walk model: in the first one, a disordered Quantum Walk is employed as a simulator for subdiffusive propagation regimes and experimentally realized in an optical framework. In the second, we show that disordered Quantum Walks are a useful model to describe how collection of information regarding the parameters of a network is influenced by the presence of fluctuations.
A natural evolution of this approach is an investigation on how genuine quantum traits, such as quantum correlations, behave when they evolve in a disordered medium. In Chapter 3, this problem is addressed, reporting on an experiment dealing with the behavior of indistinguishable photons subject to an inhomogeneous Quantum Walk evolution. This experiment was realized by means of the platform discussed in Chapter 2 and it revealed that there exist some inhomogeneity patterns that enhance, on a local and global scale, quantum correlations emerging at the output of the evolution.

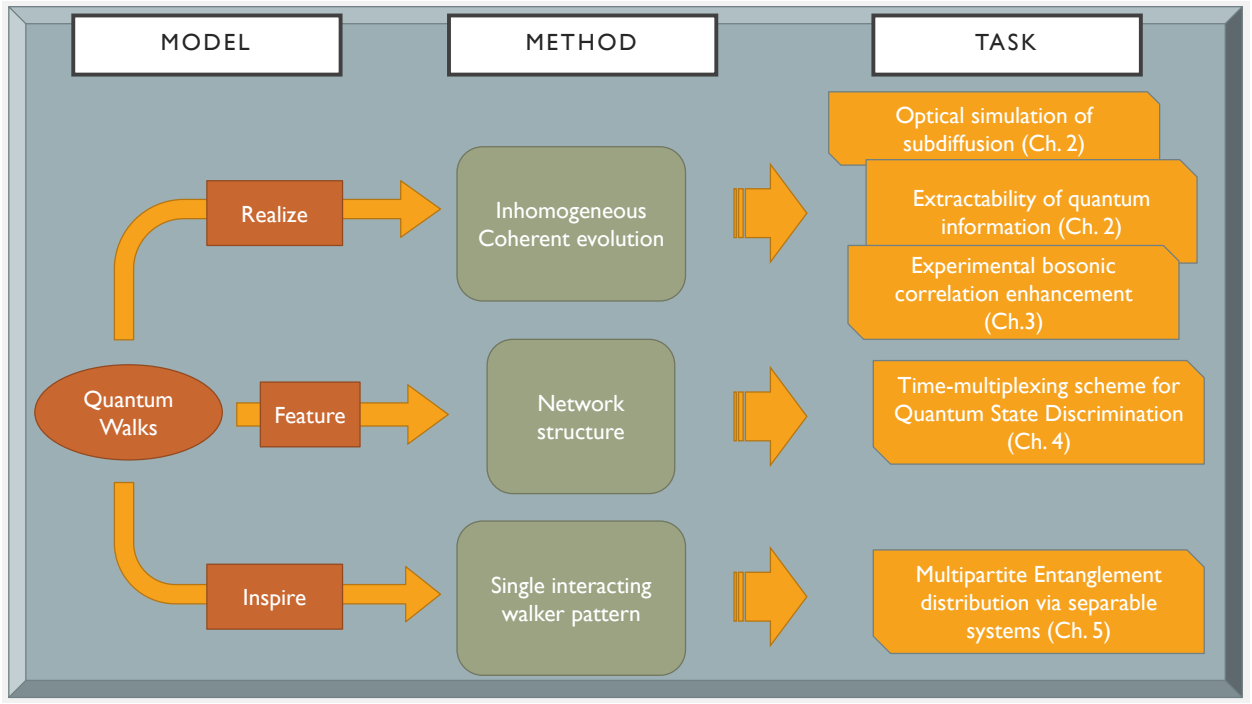

Figure 1: Outlook of the thesis. *The Quantum Walk model has directly represented a pivotal concept for almost half of my PhD course. Indeed, the general idea of coherent propagation permeates the entirety of the three years work we report in this manuscript, as a practical approach to quantum information tasks as well as a conceptual framework.*

These works dealt with the simulation and analysis of dynamical phenomena through disordered Quantum Walks. However, as mentioned above, there are also contexts in which Quantum Walks, or rather dynamical approaches, are useful for the implementation of quantum information tasks. Indeed, I show how the employment of a coherent dynamic can be useful for Quantum State Discrimination in Chapter 4: specifically, a protocol is discussed that exploits a network-like quantum receiver to process a quantum system and discriminate among its possible states, by mapping them into the amount of time the system travels back and forth through the network before being detected. This approach is very general, so that, after being experimentally implemented for a two-dimensional system (photonic polarization), it is extended to a four dimensional quantum system, represented by polarization and energy of single photons. In continuity with earlier attempts, that employed coherent states in order to apply dynamical Quantum State Discrimination methods relying on sequential measurements and machine learning, we demonstrate that harnessing dynamical processing of information allows to achieve optimal performances while crucially simplifying practical implementation. The last chapter of this thesis, Chapter 5, is devolved to the description of an attempt to apply a dynamical approach to the problem of Entanglement Distribution: the design of efficient and noise-robust ways to distribute entanglement among remote nodes is one of the most important issues towards the practical employment of quantum technologies. I report on the generalization of a protocol I devised for Entanglement Distribution via Separable Systems that relies on the interaction of the nodes of a network with an always separable carrier system. This carrier consists of a walker travelling from place to place, interacting and tying quantum correlations among the remote nodes, weaving over the network the entanglement pattern we require. And, at the end of the process, we can always measure out this "quantum spool", and eventually obtain an entangled network, similarly to the way you are left with information after measuring out a walker, as in the previous Chapters.
In conclusion, this thesis deals with a multiplicity of diverse topics, spanning from quantum simulation to quantum entanglement distribution, from the study of the behavior of stirred quantum

systems to the attempt to drive and control them.
In order to help recognizing my own contribution to the projects reported in this manuscript, a brief "personal acknowledgements" paragraph concludes the discussion of each different one.
This is necessary because many of the different works that are reported here were the result of a synergy with different scientific groups, each of them with its own approaches and its own ansatz regarding the issues we faced. Indeed, quantum mechanics can feature a variety of interpretations even when dealing with applications. I try to pull a thread out of this apparently inhomogeneous bundle, recognizing the presence of a common denominator, being the ubiquitous quest for dynamical theoretical and experimental approaches, and showcasing the capabilities of optics as a flexible and powerful experimental framework for fundamental investigation as well as for technological applications.

Chapter 1

Introduction

In order to allow clear access to the contents of this thesis, we can not avoid providing a general introduction to the concepts and tools at the foundation of the findings we deliver in the following. This Chapter is devolved to a general review of selected topics in quantum mechanics, quantum information and quantum optics, as well as an introduction to the problem of Quantum State Discrimination and the Quantum Walk model.

1.1 Quantum Mechanics for Quantum Information

Quantum Information theory and applications intrinsically rely on the basic features of quantum description of reality. Indeed, genuine quantum features, that distinguish systems that need a quantum mechanical description from classical ones, represent the reason behind the enormous amount of effort and resources that have been funneled in Quantum Technologies as of recent years. Exotic quantum phenomena, such as quantum superposition, quantum entanglement and general quantum correlation, have been found amenable for technological exploitation, way before they were fully understood. In this section, we succinctly review some of these concepts, in order to establish the preliminary ideas that yield the following theoretical and experimental results we report.

1.1.1 State of a quantum system

Pure states

The first postulate of Quantum Mechanics states that any isolated physical system is represented and completely described by a unitary vector living in a Hilbert space [1]. In general, any physical object can be treated as a quantum system, even if there are systems that can not be effectively described in a classical way, because that would not frame all of their features. In an optical framework, single photons represent such type of object, in contrast with coherent states of light, that we will describe in the next section. The standard approach to quantum mechanics describes a quantum system in a pure state by a *wave function*, that can be addressed as a complex unit vector $|\psi\rangle$, in the Dirac's bra-ket notation, living in a Hilbert space $\mathcal{H}$ of some dimension. If we consider the system to be closed, its state in time $|\psi(t)\rangle$ evolves according to Schrödinger's equation:

$$i\hbar \frac{d\,|\psi(t)\rangle}{dt} = H\,|\psi(t)\rangle \tag{1.1}$$

where $\hbar$ is the reduced Planck's constant and H is an Hermitian operator that acts as the generator of time evolution, i.e. the Hamiltonian of the system. If we consider the initial state of the system at t_0 to be $|\psi(t_0)\rangle$, we can solve the equation above and write down the evolution of $|\psi(t)\rangle$ as:

$$|\psi(t)\rangle = U(t, t_0)\,|\psi(t_0)\rangle \tag{1.2}$$

where, considering a time independent H, $U(t, t_0) = e^{-\frac{i}{\hbar}H(t-t_0)}$.

The second postulate of quantum theory states that any physical observable can be described in terms of a self-adjoint operator O of rank D acting on the Hilbert space $\mathcal{H}_D$ of the same dimension. According to the third postulate, a measurement of this observable will yield one of the eigenvalues of the associated operator as an outcome. We have $\{|k\rangle\}_{k=0}^{D-1}$ the set of eigenstates of O, and $\{o_k\}$ the corresponding eigenvalues, so that $O\,|k\rangle = o_k\,|k\rangle$. We can expand any state vector in $\mathcal{H}_D$ over such basis: $|\psi(t)\rangle = \sum_k c_k(t)\,|k\rangle$ with $\sum_k |c_k(t)|^2 = 1$, since the state must be correctly normalized at any evolution time t. The probability of obtaining o_k as outcome of a measurement of the observable O at time t, is given by the Born rule:

$$p_k(t) = |\,\langle k|\psi(t)\rangle\,|^2 = |c_k(t)|^2 \tag{1.3}$$

with normalization condition $\sum_k p_k(t) = 1$. This last equation exemplifies the probabilistic nature of quantum theory.

Mixed states

In the previous section, we have described systems in a *pure state*, namely systems for which complete knowledge on the state is available and is encoded in the corresponding wave function vector. Nonetheless, in all practical situations and experiments, information about the system under observation is not complete and the state is not perfectly determined. In general, our knowledge of the state of the system is limited to a set of possible states, taken from a statistical ensemble :

$$\{|\psi_1\rangle\,, |\psi_2\rangle\,, ..., |\psi_N\rangle\} \in \mathcal{H} \text{ with } \{p_1, p_2, ..., p_N\} \tag{1.4}$$

where $\sum_k p_k = 1$ and $\{|\psi\rangle_k\}$ are pure states. This ensemble describes uncertainties in the preparation process of the state, which is always not under perfect control. In this case, the probabilities p_k associated to each of the states of the statistical ensemble represent the classical "epistemic" ignorance and lack of information about the state of the system, rather than the intrinsic probabilistic nature of quantum theory. A state featured by such uncertainty is called a *mixed state*. The most suitable way to describe such state of a system is employing the *density operator (matrix)* formalism. The wavefunction description is generalized to account for classical ignorance by means of the density operator:

$$\rho = \sum_{i=1}^{N} p_i\,|\psi_i\rangle\,\langle\psi_i| \tag{1.5}$$

that for a pure state $|\psi\rangle$ reduces to $\rho = |\psi\rangle\,\langle\psi|$, which is the projector on the $|\psi\rangle$ vector, $\rho^2 = \rho$. The density operator ρ, or density matrix, features the following properties:

- ρ is Hermitian $\rho = \rho^+$

- ρ has unit trace $Tr(\rho) = 1$
- ρ is a positive operator $\langle\psi|\,\rho\,|\psi\rangle \geq 0$, $\forall\,|\psi\rangle \in \mathcal{H}$

It is possible to determine if a state is pure by computing its *purity* $Tr(\rho^2)$: if $Tr(\rho^2) = 1$ the state is pure, while if $Tr(\rho^2) < 1$ the state is mixed. The diagonal elements of the density matrix, with respect to a given basis $\{|k\rangle\}$, $\rho_{kk} = \langle k|\,\rho\,|k\rangle$, are called *populations* of the basis states, while the off-diagonals terms $\rho_{kl} = \langle k|\,\rho\,|l\rangle$ represent the interference terms between the states $|k\rangle$ and $|l\rangle$, and we will refer to them as *coherences*. We can now define the dynamics of a quantum system in terms of the density matrix. The Schrödinger equation reads:

$$i\hbar\frac{d\rho(t)}{dt} = [H, \rho(t)] \tag{1.6}$$

and the solution, given $\rho(t_0)$, is:

$$\rho(t) = U(t, t_0)\rho(t_0)U(t, t_0)^{+}. \tag{1.7}$$

After this general definition of the state of a system, we can proceed with a generalized definition of the measurement process for quantum systems.

1.1.2 General measurement theory

In case we are performing the act of measuring a property represented by an observable O, the probability of having the outcome o_k, where o_k is an eigenvalue of O, is given by:

$$p(o_k) = \mathrm{Tr}(P_k\rho) \tag{1.8}$$

where $P_k = |k\rangle\langle k|$ is the projection operator on the subspace spanned by the eigenvector $|k\rangle$ with eigenvalue o_k. After we perform such a measurement, the state of the system has changed:

$$\rho' = \frac{P_k\rho P_k}{\mathrm{Tr}(P_k\rho)}. \tag{1.9}$$

Using again the spectral decomposition of A:

$$O = \sum_k o_k P_k. \tag{1.10}$$

we can write the average value (the *expectation value*) of the measurement of O in terms of the density matrix:

$$\langle O\rangle = \mathrm{Tr}(O\rho) \tag{1.11}$$

The system experiences a completely different dynamic if it is measured, featuring an irreversible jump towards the state ρ', in contrast to the unitary and reversible evolution driven by U. Such class of measurements is known as a *Von Neumann measurement* or *projective measurement*. In general, a measurement is described by a set of N operators $\{M_k\}_{k=1}^{N}$ acting on the state ρ with some outcomes $m_{k=1}^{N} \in \mathbb{R}$ and corresponding probabilities $p_k = Tr(\rho M_k M_k^{+})$. These operators must obey completeness relation $\sum_k M_k M_k^{+} = 1$ and produce a state after measurement $\rho' = \frac{M_k\rho M_k^{+}}{\mathrm{Tr}\left(\rho M_k M_K^{+}\right)}$

We can also devise more general measurement schemes, called *Positive Operator-Valued Measures* (**POVM**s), which are often used to describe situations where we are not interested in the state of the system after the measurement. A POVM measurement is described by a set of positive definite operators E_i, $i = 1, \ldots, n$ such that

$$\sum_i^n E_i = 1 \tag{1.12}$$

featuring corresponding outcomes e_i, $i = 1, \ldots, n$. The probability of having a given e_j as the result of the test is

$$p_j = \mathrm{Tr}(E_j \rho) \tag{1.13}$$

It can be shown that a POVM can be reproduced by a unitary transformation (possibly in an extended Hilbert space) followed by a projective measurement [1].

1.1.3 Two level system: the quantum bit

The simplest quantum system we can think of is one that can be represented by a two-dimensional state space $\mathcal{H}$. This kind of system represents the most basic unit in quantum information, the fundamental building block for more complex systems, and it is called quantum bit or *qubit*, in analogy with the computational unit in classical information theory, namely the *bit*. We choose a basis $\{|0\rangle, |1\rangle\}$ in the Hilbert space $\mathcal{H}$, known as the *computational basis*, in analogy with the two possibile values 0 and 1 of a classical bit. On the other hand, in contrast with the classical bit, a qubit can occupy a much wider variety of states. The general pure state of a qubit can be represented by the vector

$$|\psi\rangle = \alpha\,|0\rangle + \beta\,|1\rangle \;\text{ where }\quad |\alpha|^2 + |\beta|^2 = 1. \tag{1.14}$$

Observables measured on this kind of systems can be expressed using the Pauli matrices:

$$\sigma_x = \begin{pmatrix} 0 & 1 \\ 1 & 0 \end{pmatrix}, \quad \sigma_y = \begin{pmatrix} 0 & -i \\ i & 0 \end{pmatrix}, \quad \sigma_z = \begin{pmatrix} 1 & 0 \\ 0 & -1 \end{pmatrix} \tag{1.15}$$

which together with the two dimensional identity matrix $\mathbb{I}$ form a complete basis of Hermitian operators over $\mathcal{H}$. The orthonormal states of the computational basis $\{|0\rangle, |1\rangle\}$ are chosen as the eigenvectors of the σ_z matrix, $|0\rangle = (1, 0)$ and $|1\rangle = (0, 1)$, while a specific notation is used for the eigenstates of the other Pauli matrices:

- The diagonal basis, eigenvectors of σ_x: $|+\rangle = \frac{|0\rangle+|1\rangle}{\sqrt{2}}$ and $|-\rangle = \frac{|0\rangle-|1\rangle}{\sqrt{2}}$,
- The circular basis (right and left states), eigenvectors of σ_y: $|R\rangle = \frac{|0\rangle-i|1\rangle}{\sqrt{2}}$ and $|L\rangle = \frac{|0\rangle+i|1\rangle}{\sqrt{2}}$.

These three bases together form what is called *mutually unbiased bases* (MUB), from the fact that if the state of the qubit corresponds to one of the vectors belonging to one of these bases, then we have no knowledge about the outcome of a measurement performed considering one of the other two bases. Since $\mathbb{I}, \sigma_x, \sigma_y, \sigma_z$ can be regarded as a basis for the qubit operators, we can also represent any qubit density matrix as

$$\rho = \frac{1}{2}\left(\mathbb{I} + \vec{r}\cdot\vec{\sigma}\right) = \frac{\mathbb{I}}{2} + r_x\sigma_x + r_y\sigma_y + r_z\sigma_z \tag{1.16}$$

with $|\vec{r}| \leq 1$ and where $\vec{\sigma} = (\sigma_x, \sigma_y, \sigma_z)$ is the vector with components given by the Pauli matrices. These states can be identified, using the vector $\vec{r}$, by points inside the Bloch sphere, depicted in Fig. 1.1. In this way the distance from the surface indicates the degree of purity of the state, the center of the sphere being the completely mixed state.

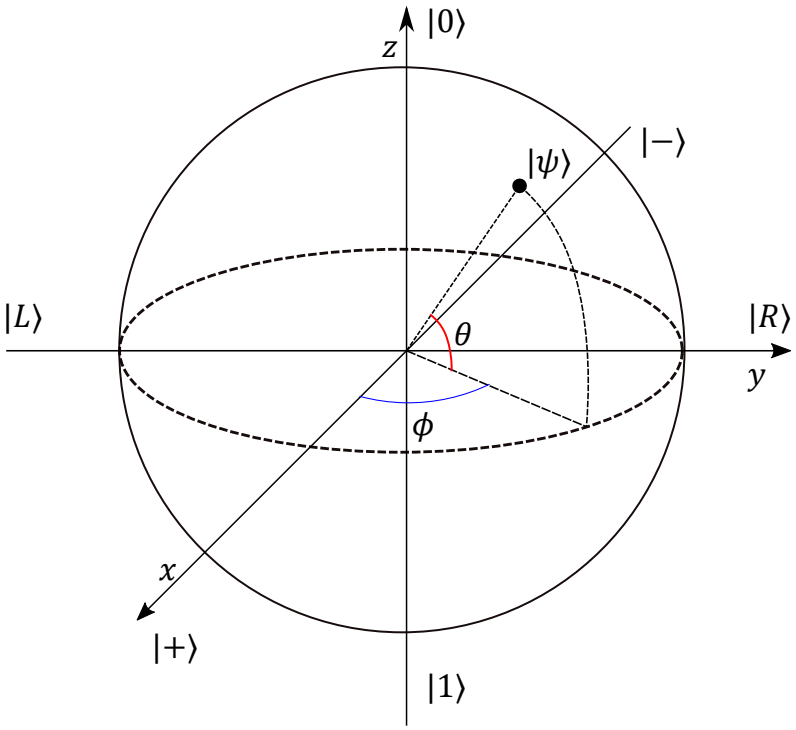

Figure 1.1: Bloch sphere representation of a qubit state. *The MUB define the three axes of a sphere with radius $R = 1$, corresponding to the purity of the basis states. The general state $|\psi\rangle$ of a qubit can be described as a point on the surface of the sphere, if it is a pure state, or in its inside, if it is a mixed state ρ. The corresponding $\vec{r}$ can be identified in terms of the two angles $\{\theta, \phi\}$: $\vec{r} = \{r\cos\phi\cos\theta, r\sin\phi\cos\theta, r\sin\theta\}$.*

1.1.4 Entanglement

If we leave single qubits in favour of composite systems, some of the most striking quantum features arise, such as quantum *entanglement*. Introduced by Einstein, Podolsky and Rosen in the EPR paper [2], nonlocal entanglement is now regarded as a fundamental concept of quantum theory and a fundamental resource for quantum protocols: from dense coding [3], to quantum cryptography [4] and quantum teleportation [5]. In the following, we present a brief description of entanglement and its properties.

Separable and entangled systems

The state of a system composed of N subsystems can be described as a vector in a total Hilbert space $\mathcal{H}$ defined as the tensor product of the Hilbert spaces $\mathcal{H}_1, \ldots, \mathcal{H}_N$ corresponding to each subsystem, $\mathcal{H} = \otimes_{i=1}^{N} \mathcal{H}_i$. We consider a composite system of N qubits, thus each $\mathcal{H}_i$ has dimension 2 and features an orthogonal basis $\{|e\rangle_i\}_{e=0}^{1}$. We can define an orthogonal basis for the total $\mathcal{H}$ so that we can express any vector in $\mathcal{H}$ using the tensor product basis given by the vectors

$|i_1, j_2, \ldots, k_N\rangle = |i\rangle_1 \otimes |j\rangle_2 \otimes \cdots \otimes |k\rangle_n$:

$$|\psi\rangle = \sum_{i,j,\ldots,k} \alpha_{i,j,\ldots,k} |i_1, i_2, \ldots, i_n\rangle \quad \text{where} \quad \sum_{i,j,\ldots,k} |\alpha_{i,j,\ldots,k}|^2 = 1. \tag{1.17}$$

where all the indices can have values in $\{0, 1\}$. We can also express any density operator ρ using the same basis.

The definition of entanglement can be given by defining which states are not entangled, the so-called *separable states*. We call a state $\rho \in \mathcal{H}_1 \otimes \ldots \otimes \mathcal{H}_N$ *separable* if it can be expressed as a convex combination of tensor product states, i.e.

$$\rho = \sum_i p_i \rho_1^i \otimes \rho_2^i \otimes \ldots \otimes \rho_N^i \tag{1.18}$$

for a set of states $\{\rho_1^i, \ldots, \rho_N^i\}_i$ and corresponding probabilities $\{p_i\}$, satisfying $\sum_i p_i = 1$. Every state which is not *separable* is *entangled*.

Partial trace

It is possible to get a description of the individual subsystems of a multipartite system by performing an operation called *partial trace*, which is defined on the density operator representing the state of the whole system. If we consider a composite system described by the state ρ, the partial trace on the i-th subsystem is defined as:

$$\rho' = \mathrm{Tr}_i(\rho) = \sum_k \langle k|_i \, \rho \, |k\rangle_i \tag{1.19}$$

In this way, we are discarding information regarding the i-th subsystem, and we get the reduced state ρ' that describes the physical properties of the remaining ones, as an observer who has no knowledge about the state of subsystem i would see it.

This destructive operation generally maps pure quantum states into mixed ones, unless the original state was separable. The operation of partial tracing is particularly disruptive for entangled states: for some states the resulting reduced density matrix is the completely mixed one. These states are called *maximally entangled*, and play a fundamental role in quantum information and communication.

Bell states

In the simple case of a bipartite system, we can describe its state in terms of a vector in $\mathcal{H}_1 \otimes \mathcal{H}_2$, where subspaces are two dimensional. Any pure state of the system can be written as: $|\psi\rangle = \sum_{i,j=0}^{1} \alpha_{i,j} |ij\rangle$ with $\sum_{i,j} \left|\alpha_{i,j=0}^1\right|^2 = 1$.

Maximally entangled bipartite states, are called *Bell* or *EPR* states, and are defined as

$$\begin{aligned} \left|\phi^{\pm}\right\rangle &= \frac{1}{\sqrt{2}}(|00\rangle \pm |11\rangle) \\ \left|\psi^{\pm}\right\rangle &= \frac{1}{\sqrt{2}}(|01\rangle \pm |10\rangle). \end{aligned} \tag{1.20}$$

These states are an orthonormal basis for the global space $\mathcal{H}_1 \otimes \mathcal{H}_2$.

Entanglement characterization

We give some preliminary definitions that are required for a consistent description of entanglement characterization. In the case of a multipartite system shared by multiple parties, a quantum information protocol based on local operations of remote parties, the outcome of which can be only transmitted between the parties through a classical channel is said to rely on **Local Operations and Classical Communication (LOCC)**. We refer to Ref. [6] for a detailed definition of LOCC. Given a multipartite system described by the density matrix ρ, we define the **partial transpose** with respect to a given bipartition of the system as:

$$\rho^{T_{P_1|P_2}} := (\mathbb{I}_{P_1} \otimes T_{P_2})\rho = \sum_{i,j,k,l} p_{i,j}^{k,l} \left|i\right\rangle_{P_1} \left\langle j\right| \otimes (\left|k\right\rangle_{P_2} \left\langle l\right|)^T = \sum_{i,j,k,l} p_{i,j}^{k,l} \left|i\right\rangle_{P_1} \left\langle j\right| \otimes \left|l\right\rangle_{P_2} \left\langle k\right|. \tag{1.21}$$

The detection and quantification of entanglement in a multipartite system is in general a difficult task. Several different entanglement characterization methods exist [7, 8] in order to witness and quantify entanglement. In general, entanglement measures rely on a function $E(\rho)$ called *entanglement monotone* [9]. We define an *entanglement monotone* as a quantity $E(\rho)$ computed on the state ρ that satisfies the following properties:

- Convexity, i.e. $E(\sum_i p_i \rho_i) \leq \sum_i p_i E(\rho_i)$.
- $E(\rho) = 0$ when ρ is a separable state.
- $E(\rho)$ is invariant under local unitaries.
- $E(\rho)$ is non-increasing under LOCC.

Among the various entanglement monotones we consider the *negativity* of entanglement $\mathcal{N}$, as defined in [10], that we will extensively use in Chapter 5. This quantity is based on the trace norm of the partial transpose $\rho^{T_{A|B}}$ of a mixed state, with respect to a bipartition A-B of the system, whose evaluation is completely straightforward using standard linear algebra. Negativity essentially measures the degree to which $\rho^{T_{A|B}}$ fails to be positive, and therefore it can be regarded as a quantitative version of Peres' criterion for separability [11]. Given the trace norm of ρ^{T_A} : $||\rho^{T_{A|B}}|| = Tr(\rho^{T_{A|B}})$, we define the negativity with respect to a bipartition A|B as:

$$\mathcal{N}_{A|B}(\rho) = \frac{||\rho^{T_{A|B}}|| - 1}{2} \tag{1.22}$$

which corresponds to the absolute value of the sum of negative eigenvalues of $\rho^{T_{A|B}}$. In [10], it is demonstrated that negativity is an entanglement monotone, hence it is suitable for quantifying entanglement.

1.2 Quantum Optics

In this section, we review some of the main concepts in quantum optics that are useful for access to the content of this thesis. We provide a special focus on the quantum description of optical elements and different sources of quantum light, such as non-linear crystals and Quantum Dots.

1.2.1 Photonic states

It is worth reporting the description of quantum states of photons, since we are often going to need a particle description of light in the following, as opposed to coherent states, which also have a wide applicability in quantum information.

Second quantization formalism A suitable formalism for the description of quantum photonic states is the second quantization, that we briefly review here. The second quantization formalism is based on the Heisenberg picture of the dynamics, hence we describe the system evolution in terms of operators rather than states. We define annihilation and creation operators, indicated by $a_{\vec{k}}$ and $a^\dagger_{\vec{k}}$, respectively, in order to describe the dynamics of a photon state corresponding to a light oscillation in the mode $\vec{k}$, that represents all the photonic degrees of freedom [12]. These operators correspond to photons featuring energy $\omega_{\vec{k}}$ and follow the commutation rules:

$$[a_{\vec{k_i}}, a_{\vec{k_j}}] = [a^\dagger_{\vec{k_i}}, a^\dagger_{\vec{k_j}}] = 0 \qquad\qquad [a_{\vec{k_i}}, a^\dagger_{\vec{k_j}}] = \delta_{ij} \tag{1.23}$$

where $\vec{k_i}$ and $\vec{k_j}$ are two modes of the field, that are deemed as independent for $i \neq j$. The Hamiltonian of a free electromagnetic field has the form of a quantum harmonic oscillator:

$$H = \sum_{\vec{k}} \omega_{\vec{k}} (a^\dagger_{\vec{k}} a_{\vec{k}} + \frac{1}{2}). \tag{1.24}$$

and can be written as: $H = \sum_{\vec{k}} \omega_{\vec{k}} (n_{\vec{k}} + \frac{1}{2})$, where the *number operator* $n_{\vec{k}}$ along the mode $\vec{k}$ is defined by:

$$n_{\vec{k}} = a^\dagger_{\vec{k}} a_{\vec{k}} \tag{1.25}$$

and represents the observable measuring the number of photons occupying the mode it refers to. The eigenstates of this operator, i.e. the discrete states with fixed number of photons are called the *Fock states*.

Annihilation and creation operators act on Fock states by respectively destroying and creating a photon along a given mode $\vec{k}$, according to the relations:

$$a_{\vec{k}} \left| N_{\vec{k}} \right\rangle = \sqrt{N_{\vec{k}}} \left| N_{\vec{k}} - 1 \right\rangle \qquad\qquad a^\dagger_{\vec{k}} \left| N_{\vec{k}} \right\rangle = \sqrt{N_{\vec{k}} + 1} \left| N_{\vec{k}} + 1 \right\rangle \tag{1.26}$$

These equalities describe the entire *Fock space* that can be built from the *vacuum* state $|0\rangle$ through the iterative application of the creation operators. Operators corresponding to different modes commute, so that the general Fock state featuring N_{k_i} photons along modes $k_1, \ldots, k_d$ can be written as

$$\left| N_{\vec{k_1}}, \ldots, N_{\vec{k_d}} \right\rangle = \prod_{i=1}^{d} a_{\vec{k_i}} \left| 0 \right\rangle . \tag{1.27}$$

This formalism frames collective photon states, highlighting the fundamental *indistinguishability* of photons occupying the same mode $\vec{k_i}$.

Coherent states

In real-world scenarios, it is very hard to produce light states with a fixed number of photons. In general, we globally have a superposition of states featuring different photon numbers. A very important class of this kind of states is *coherent states*: for instance, laser light can be generally described to be in a coherent state. These states are the eigenstates of the annihilation operator a in a given mode, and they can be written as:

$$|\alpha\rangle = e^{-\frac{|\alpha|^2}{2}} \sum_{N=0}^{\infty} \frac{\alpha^N}{\sqrt{N!}} |N\rangle \,, \tag{1.28}$$

where $|\alpha| \in \mathbb{R}$ is called *displacement*, and is tightly related to the expectation value of the photon number of the system:

$$\langle n \rangle = \langle \alpha | a^\dagger a | \alpha \rangle = |\alpha|^2 \tag{1.29}$$

The variance Δn^2 of this expected value is again $|\alpha|^2$; indeed, the underlying photon distribution is a Poissonian one, which represents a distinctive trait of a system in a coherent state. It can be explicitly shown that the probability of having a given photon number n is

$$P(n) = |\langle n|\alpha\rangle|^2 = e^{-\langle n \rangle} \frac{\langle n \rangle^n}{n!} \tag{1.30}$$

As we will systematically discuss in Subsec. 1.2.4, photon number statistics yield information regarding the nature of light under analysis. Genuine quantum light, lacking any classical description, features sub-Poissonian behavior of the photon number distribution. Indeed, for many quantum information tasks, such as secure Quantum Key Distribution, entangled quantum states are often required, featuring a fixed number of photons [4, 13, 14]. However, coherent states can be employed instead of actual single photons in protocols that do not necessarily require more than one particle (such as "prepare and measure" QKD schemes [15, 16]).

1.2.2 Quantum description of a Beam-Splitter

A Beam Splitter (BS) is an optical element that separates an incoming electromagnetic field into two output beams, by transmitting and reflecting two portions of the original light. In case quantum states of light are involved, such as for a single photon, a BS has the capability to convert the input state into a linear superposition of the output states. A BS generally features two input and two output ports. For a quantum treatment, we use the second quantization description. The reflection and transmission coefficients $R, T \in \mathbb{C}$ satisfy the classical relations:

$$|R|^2 + |T|^2 = 1, \; RT^* + TR^* = 0. \tag{1.31}$$

The operator corresponding to the action of a BS is given by (we consider the transmittance as the off-diagonal term):

$$\hat{BS} = \begin{bmatrix} R & T \\ T & R \end{bmatrix}. \tag{1.32}$$

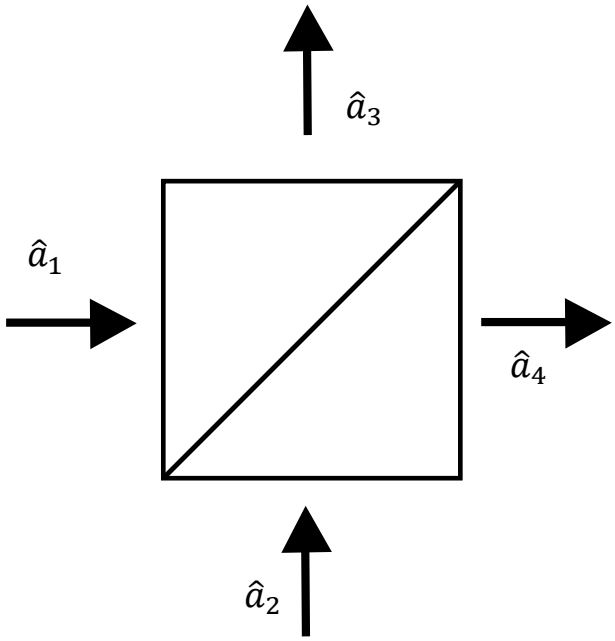

Figure 1.2: Representation of a lossless Beam Splitter. *The quantum scheme of a Beam Splitter, with destruction operators associated with input and output fields.*

The relations between the input and output destruction operators for a BS are:

$$\hat{a}_3 = R\hat{a}_1 + T\hat{a}_2, \tag{1.33}$$

$$\hat{a}_4 = T\hat{a}_1 + R\hat{a}_2. \tag{1.34}$$

On the other hand, the inverse relations stand:

$$\hat{a}_1 = R^*\hat{a}_3 + T^*\hat{a}_4, \tag{1.35}$$

$$\hat{a}_2 = T^*\hat{a}_3 + R^*\hat{a}_4. \tag{1.36}$$

Indeed, it can be readily verified that $\hat{BS}^{-1} = \begin{bmatrix} R^* & T^* \\ T^* & R^* \end{bmatrix}$. Equations for the adjoint operators follow straightforwardly. We assume that the input fields are independent, so that the creation and annihilation operators satisfy the bosonic commutation relations:

$$[\hat{a}_1, \hat{a}_1^\dagger] = [\hat{a}_2, \hat{a}_2^\dagger] = 1 \tag{1.37}$$

$$[\hat{a}_1, \hat{a}_2^\dagger] = [\hat{a}_2, \hat{a}_1^\dagger] = 0 \tag{1.38}$$

For the output fields we have the following commutation relations:

$$[\hat{a}_3, \hat{a}_3^\dagger] = [\hat{a}_4, \hat{a}_4^\dagger] = |R|^2 + |T|^2 = 1 \tag{1.39}$$

$$[\hat{a}_3, \hat{a}_4^\dagger] = [\hat{a}_4, \hat{a}_3^\dagger] = RT^* + TR^* = 0 \tag{1.40}$$

Applying to Eq. (1.33) the adjoint operator $\hat{a}_3^\dagger$ and doing the same for Eq. (1.34) we get:

$$\hat{a}_3^\dagger \hat{a}_3 = (R^* \hat{a}_1^\dagger + T^* \hat{a}_2^\dagger) R \hat{a}_1 + (R^* \hat{a}_1^\dagger + T^* \hat{a}_2^\dagger) T \hat{a}_2 \tag{1.41}$$

$$\hat{a}_4^\dagger \hat{a}_4 = (T^* \hat{a}_1^\dagger + R^* \hat{a}_2^\dagger) T \hat{a}_1 + (T^* \hat{a}_1^\dagger + R^* \hat{a}_2^\dagger) R \hat{a}_2 \tag{1.42}$$

Summing these two relations and using the commutation relations we get:

$$\hat{n}_3 + \hat{n}_4 = \hat{n}_1 + \hat{n}_2 \tag{1.43}$$

where the definition of number operator $\hat{n} = \hat{a}^\dagger \hat{a}$ has been used. This relation represents the conservation of the number of particles. We can also compute the photon number variances for the two output modes when one input only is illuminated, which is common in experimental situations. The output variances are:

$$(\Delta n_3)^2 = |R|^4 (\Delta n_1)^2 + |R|^2 |T|^2 \langle \hat{n}_1 \rangle \tag{1.44}$$

$$(\Delta n_4)^2 = |T|^4 (\Delta n_1)^2 + |T|^2 |R|^2 \langle \hat{n}_1 \rangle. \tag{1.45}$$

Each of the two outputs features one contribution from the input variance and another one, proportional to the mean photon number; the latter is generally regarded as due to a beating occurring between input field in input 1 and the vacuum state of input 2, or as a *partition noise*, produced by the random splitting of the photon stream. When a single photon impinges in input 1, while input 2 is in a vacuum state, the input state is denoted as:

$$|1\rangle_1 |0\rangle_2 = \hat{a}_1^\dagger |0\rangle \tag{1.46}$$

where $|0\rangle = |0\rangle_1 |0\rangle_2$ is the joint vacuum state of the two input arms. The corresponding output state can be derived by the adjoint of relation (1.35):

$$\hat{a}_1^\dagger |0\rangle = (R\hat{a}_3^\dagger + T\hat{a}_4^\dagger) |0\rangle = R |1\rangle_3 |0\rangle_4 + T |0\rangle_3 |1\rangle_4 \tag{1.47}$$

which is a superposition state of the two output modes. This superposition is the standard effect of a Beam Splitter in the quantum case. It is useful to write down the expression of the average

number of photons expected for the two output arms, given the input state of Eq. (1.46):

$$\langle \hat{n}_3 \rangle = \langle 0|_2 \langle 1|_1 \hat{n}_3 |1\rangle_1 |0\rangle_2 = \langle 0|_2 \langle 1|_1 (R^* \hat{a}_1^\dagger + T^* \hat{a}_2^\dagger)(R\hat{a}_1 + T\hat{a}_2)_3 |1\rangle_1 |0\rangle_2 = |R|^2 \tag{1.48}$$

and similarly:

$$\langle \hat{n}_4 \rangle = |T|^2. \tag{1.49}$$

This result recovers the classical case, because the number of photons is well known to be proportional to the beam intensity, so that the beam intensity (and then number of photons) is split in the two outputs according to transmissivity and reflectivity. Indeed, the particle nature of single-photons arises when evaluating the correlation between the two output modes:

$$\begin{aligned} \langle n_3 n_4 \rangle = \langle 0|_2 \langle 1|_1 \hat{n}_3 \hat{n}_4 |1\rangle_1 |0\rangle_2 = \\ = \langle 0|_2 \langle 1|_1 (R^* \hat{a}_1^\dagger + T^* \hat{a}_2^\dagger)(R\hat{a}_1 + T\hat{a}_2)(R^* \hat{a}_2^\dagger + T^* \hat{a}_1^\dagger)(R\hat{a}_2 + T\hat{a}_1) |1\rangle_1 |0\rangle_2 = \\ = R^* R T^* T \langle 1|_1 \hat{a}_1^\dagger \hat{a}_1 \hat{a}_1^\dagger \hat{a}_1 |1\rangle_1 + R^* T R^* T \langle 0|_2 (\hat{a}_2^\dagger \hat{a}_2 |0\rangle_2 \langle 1|_1 \hat{a}_1^\dagger \hat{a}_1) |1\rangle_1 = \\ = R^*(RT^* + T^* R)T = 0 \end{aligned} \tag{1.50}$$

The zero average is a direct consequence of the particle nature of the single photon: it is not possible to find it in both output modes. This effect can not be obtained by any classical input field.

Polarization of light

Polarization is the degree of freedom of light associated with the spin component of the angular momentum carried by the electromagnetic field [17]. From a classical point of view, polarization corresponds to the direction of oscillations of the electromagnetic wave. Thus, in free space, polarization can be represented as a vector lying in the transversal plane with respect to the propagation direction of light. Since this is clearly a two-dimensional space, the Hilbert space representing polarization can be deemed as a perfect candidate for the encoding of a qubit. We can identify the two vectors of the computational basis with the horizontal $|H\rangle$ and vertical $|V\rangle$ components of the polarization (identified with respect to a given reference frame), then the two other bases $\{|+\rangle, |-\rangle\}$ and $\{|R\rangle, |L\rangle\}$ will correspond to the *diagonal* and *circular* polarization respectively, that can be represented as vectors on the Bloch sphere, that in this case we can address as the Poincaré sphere (Fig. 1.3).

The most commonly employed optical devices for polarization manipulation are based on the properties of birifringent materials.

Waveplates The most common way of manipulating photon polarization is by means of thin slabs of birifringet material, called *retarders* or *waveplates*. These devices are cut so to have their optical axis parallel to the surface. In this way, it is possible to insert an arbitrary optical retardation between the two polarization states corresponding to the the *extraordinary* and *ordinary* axes of the material, without changing the propagation mode of the photon. The difference in the refraction indices n_e and n_o of the two axes generates a polarization-dependent phase shift ϕ that depends on

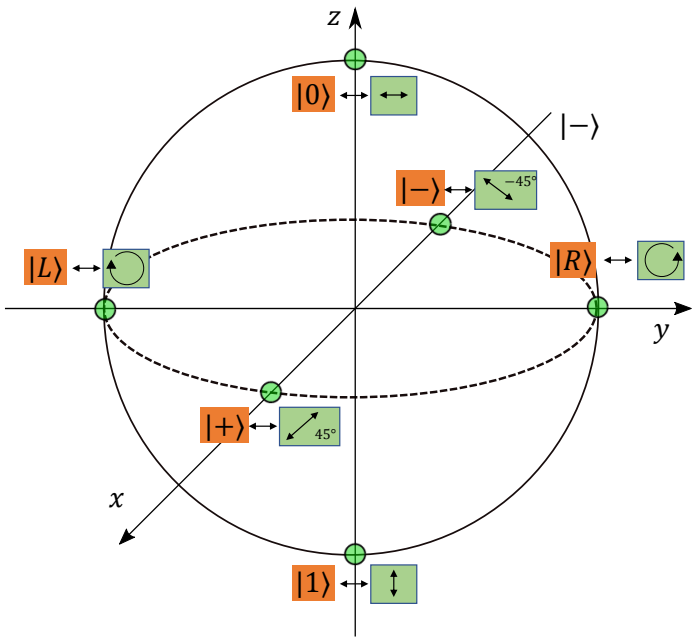

Figure 1.3: Bloch sphere for polarization qubit. *Standard identification of the polarization states in the Bloch sphere. The z axis corresponds to linearly polarized states with the horizontal and vertical polarizations while the x and y axes correspond to diagonal and circular polarizations respectively. When used for polarization states the polar representation of qubit states is also called a "Poincaré sphere".*

n_e, n_o and the thickness h of the material:

$$\phi = \frac{2\pi h(n_e - n_o)}{\lambda} \tag{1.51}$$

where λ is the wavelength of the incoming light. In the basis corresponding to the directions of the optical axes of the material, the transformation can be written as a matrix

$$U_{\mathrm{WP}}(\phi) = \begin{pmatrix} 1 & 0 \\ 0 & e^{i\phi} \end{pmatrix} \tag{1.52}$$

but, in general, if the optical axis is rotated by an angle θ with respect to the horizontal polarization state, we can write the action of a waveplate as a general unitary transformation in terms of the Pauli matrices:

$$U_{\mathrm{WP}}(\phi, \theta) = \cos\frac{\phi}{2} - \sigma_z i \sin\frac{\phi}{2}\cos 2\theta - \sigma_x i \sin\frac{\phi}{2}\sin 2\theta. \tag{1.53}$$

Typically, two kind of waveplate retarders are employed, featuring respectively a fixed retardation $\phi = \pi$ and $\phi = \pi/2$; they are known as *half waveplates* (HWP) and *quarter waveplates*. Their action, when they are rotated by an angle θ with respect to the horizontal polarization, can be written as the operators:

$$U_{\mathrm{HWP}}(\theta) = \sigma_z \cos 2\theta + \sigma_x \sin 2\theta \tag{1.54}$$

$$U_{\mathrm{QWP}}(\theta) = \frac{\mathbb{I}}{\sqrt{2}} - \frac{i}{\sqrt{2}}(\sigma_z \cos 2\theta + \sigma_x \sin 2\theta) \tag{1.55}$$

The operators defined by (1.53), (1.54) and (1.55) are also called *Jones matrices*. The great usefulness of these devices resides in the fact that a sequence of a QWP, a HWP and another QWP, is capable of implementing any unitary transformation on the polarization space, by setting the right combination of the three rotation angles [18].

1.2.3 Interferometers

We also need to introduce some more complex optical elements, that we employ extensively in the next Chapters, namely the so-called *interferometers*.

Mach-Zehnder Interferometer

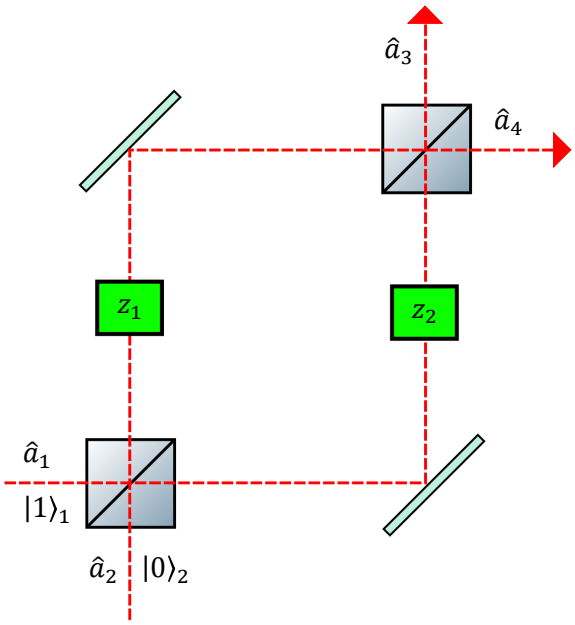

Figure 1.4: Representation of a Mach Zehnder interferometer. *Scheme of a Mach Zender Interferometer, according to the notation used by [12] for destruction operators associated with input and output fields; $z_{1,2}$ indicate the lengths of the different paths travelled by the interfering beams. The difference between them determines the interference outcome.*

A Mach-Zehnder inteferometer (MZI) consists of two BSs in sequence; the outputs of the first BS are sent to the inputs of the second one. We regard the two Beam Splitters as identical and symmetrical ($R = T = \frac{1}{\sqrt{2}}$); the full interferometer can be described as a composite total BS, where the output operators can be written as:

$$\hat{a}_3 = R_{MZ}\hat{a}_1 + T_{MZ}\hat{a}_2 \tag{1.56}$$

$$\hat{a}_4 = T_{MZ}\hat{a}_1 + R'_{MZ}\hat{a}_2 \tag{1.57}$$

and the composite coefficients satisfy the relations:

$$\begin{cases} R_{MZ} = R^2 \exp\{ikz_1\} + T^2 \exp\{ikz_2\} \\ R'_{MZ} = T^2 \exp\{ikz_1\} + R^2 \exp\{ikz_2\} \\ T_{MZ} = RT(\exp\{ikz_1\} + \exp\{ikz_2\}) \end{cases} \tag{1.58}$$

where $k = \frac{\omega}{c}$, with ω the frequency of the travelling light and c the speed of light, while z_1, z_2 represent the different lengths of the two possible internal paths of the MZ. It is straightforward to show that these coefficients satisfy the relations:

$$|R_{MZ}|^2 + |T_{MZ}|^2 = |T_{MZ}|^2 + \left|R'_{MZ}\right|^2 = 1, \qquad R'_{MZ}T^*_{MZ} + T_{MZ}R^*_{MZ} = 0. \tag{1.59}$$

We consider again the case of illuminating one input only, as for the BS, so that the input state is $|1\rangle_1 |0\rangle_1$, as depicted in Fig. 1.4. We can write the expected value of the output number of photons for the MZI using the composite coefficients. As a result of the computation, we obtain:

$$\langle \hat{n}_3 \rangle = |R_{MZ}|^2 = 4|T|^2|R|^2 \sin^2[\frac{k}{2}(z_1 - z_2)], \tag{1.60}$$

$$\langle \hat{n}_4 \rangle = |T_{MZ}|^2 = 4|T|^2|R|^2 \cos^2[\frac{k}{2}(z_1 - z_2)]. \tag{1.61}$$

Thus, according to the path difference which affects the beams, light (i.e. the photons) travelling through the interferometer is subject to constructive or destructive interference (or produces fringes). It is possible to tune this path difference, which consists of a phase shifting, by inserting suitable optical components along one of the paths. For instance, if we place a glass plate in one of the two MZI arms, the corresponding path becomes longer to the propagating light, because of the higher refractive index of glass with respect to free space (air).

Sagnac Interferometer

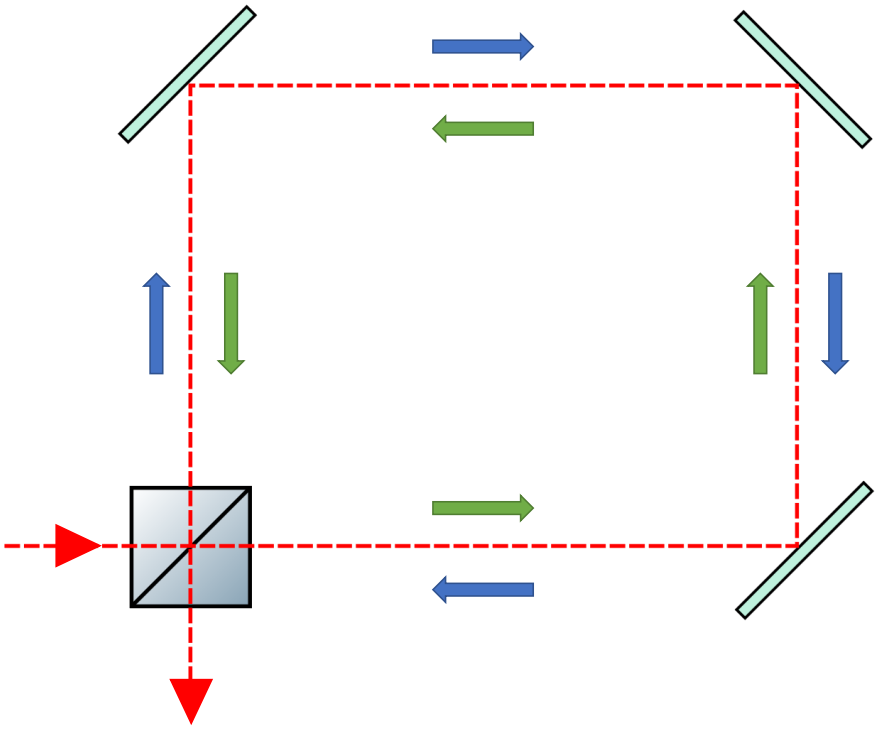

Figure 1.5: Representation of a Sagnac interferometer. *We depict the case of light entering from one input only of the Beam Splitter, the different colours indicate the two possible paths the light can travel, which are identical by construction.*

A Sagnac interferometer (SI) is an interferometric setup in which the two possible paths travelled by light are implemented by the same optical loop. This scheme, that is sketched in Fig. 1.5, corresponds to a "folded" MZI and features identical arms by construction, so that the output interference is in principle maximized. Since the two paths are practically the same, travelled in opposite directions, both paths have necessarily the same length. A crucial property deriving from this design consists of the fact that any accidental phase shift experienced by light travelling in one direction of the optical loop will be also experienced by light propagating in the opposite direction. Thus, this scheme provides an *a priori* phase stability, without any necessity to engineer the platform in order to achieve it. This feature is very convenient as we wish to investigate interferometric effects of specific phase shifts between different trajectories. Indeed, as we will show in the next Chapter, by means of some slight modifications to the scheme, it is possible to impose different phase shifts on the clockwise and the counterclockwise paths, while maintaining stability for accidental phases.

1.2.4 Photon statistics and light classification

We briefly report here on the classification of light by using statistics and intensity correlation measurements in order to contextualize our following references to quantum or classical states of light. For further details, we suggest suitable textbooks [12, 19]. Light can be categorized according to its photon number statistics [19]:

- **super-Poissonian**: $\Delta n > \sqrt{\langle n \rangle}$, typical of incoherent or partially coherent light,
- **Poissonian**: $\Delta n = \sqrt{\langle n \rangle}$, that is typical of coherent light,
- **sub-Poissonian**: $\Delta n < \sqrt{\langle n \rangle}$, that can not be achieved by any kind of classically described light.

It is worth noting that in an experimental framework, light statistics interplay with photodetection statistics, because the photodetector quantum efficiency η is lower than 1. We do not discuss this topic here, for a matter of conciseness, thus, from this point we suppose to work in the ideal case of photodetectors with quantum effciency $\eta = 1$. A very useful tool allowing classification of light is the second order correlation $g^{(2)}(\tau)$:

$$g^{(2)}(\tau) = \frac{\langle I(t) I(t+\tau) \rangle}{\langle I(t) \rangle \langle I(t+\tau) \rangle} \tag{1.62}$$

where $I(t)$ is the intensity of the light field we are analyzing and τ is a given time delay. This definition of $g^{(2)}(\tau)$ quantifies the coherence of light in time, hence its autocorrelation, as the result of a Hanbury Brown and Twiss (HBT)-like experiment [20].

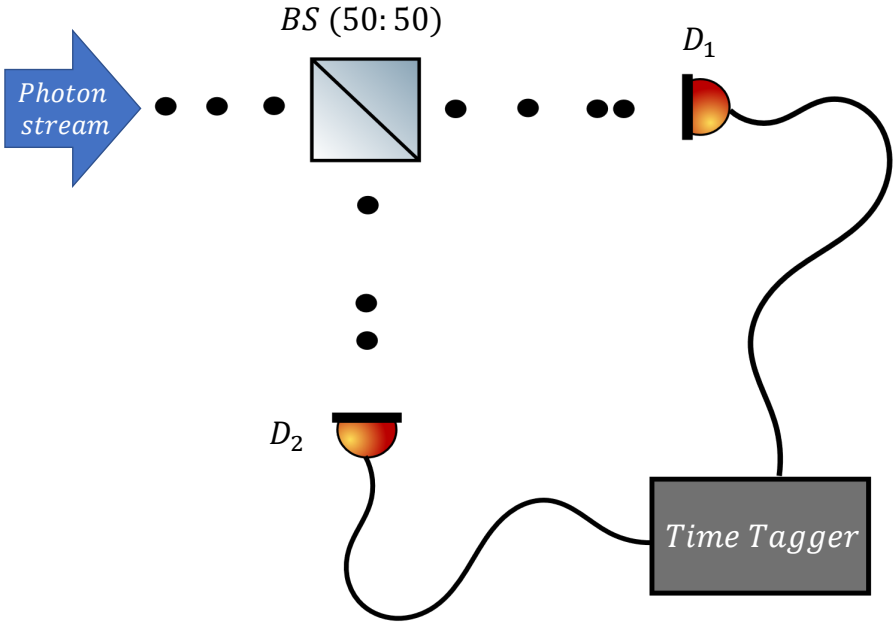

Figure 1.6: Scheme of a Hanbury Brown and Twiss experiment with photons: *A stream of photons impinge on a BS, and the coincidences between detectors D_1 and D_2 are computed by a time tagger, that can digitally apply a desired delay τ. Actual single photon sources will produce no coincidences between the two outputs for $\tau = 0$.*

The quantum formulation of the second order correlation, involving photons rather than electromagnetic waves, considers the case of light entering a BS and emerging from the two outputs:

$$g^{(2)}(\tau) = \frac{\langle n_1(t) n_2(t+\tau) \rangle}{\langle n_1(t) \rangle \langle n_2(t+\tau) \rangle} \tag{1.63}$$

where $n_i(t)$ is the number of photons counted at the BS output port i at time t (see Fig. 1.6). This definition leads to a second approach for light classification, depending on the value $g^{(2)}(0)$:

- bunched light: $g^{(2)}(0) \geq 1$, typical of incoherent or partially coherent light,
- coherent light: $g^{(2)}(0) = 1$,
- antibunched light: $g^{(2)}(0) \leq 1$.

Without lingering on details, antibunched light can be produced by **single photon sources**, namely sources emitting one photon as a consequence of a stimulation. In the present thesis, we deal with two different types of sources, that we describe in the following sections. The first one, based on the non-linear process of Spontaneous Parametric Down Conversion, represents the most widely spread source of single photons, yet the inherent probabilistic nature of its photon generation process imposes a post-selection procedure in order to retrieve photon antibunching. On the other hand, Quantum Dots represent a reliable source of fixed number photon states, as it can be understood by the example of experimental $g^{(2)}(\tau)$ shown in Fig. 1.7.

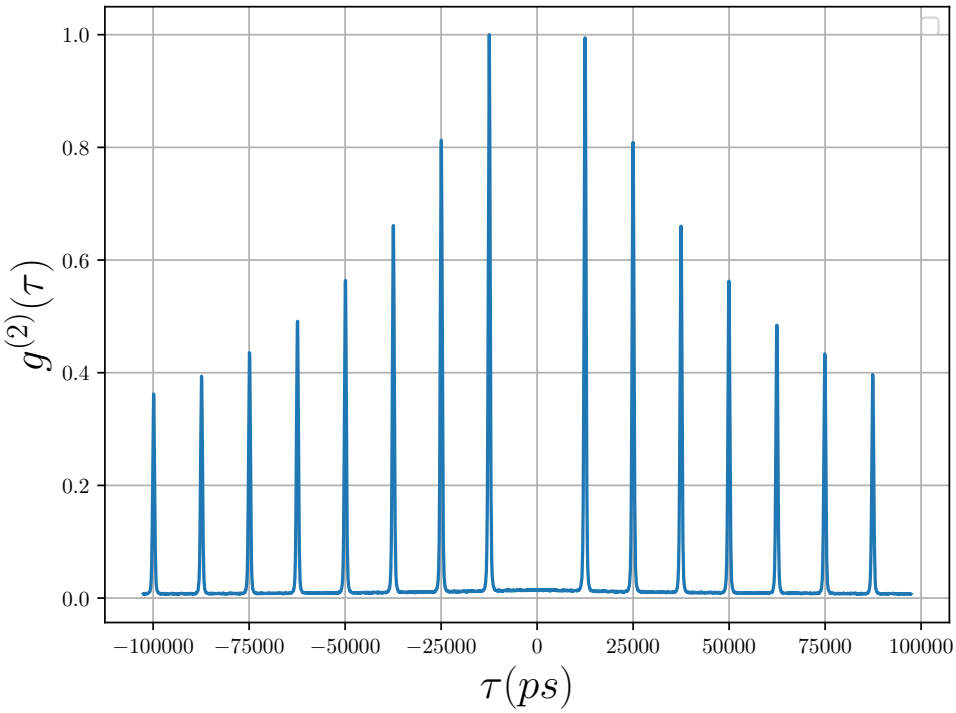

Figure 1.7: Normalized $g^{(2)}(\tau)$ of the biexciton photon stream of a Quantum Dot. *A Quantum Dot driven to Two Photon Excitation (see Subsec. 1.2.7) emits photon pairs that can be spatially separated according to their energy. The two paths, travelled by the so-called exciton and biexciton, represent very pure single photon streams, as it is highlighted by their extremely low value of $g^{(2)}(0)$. The delay τ is digitally tuned by a time tagger while the time separation among two different emissions $\sim 12.5ns$ is imposed by the repetition rate of the pumping laser. The correlation decreases for longer delays as an effect of emission efficiency drops of the quantum dot.*

1.2.5 Single Photons Source by Spontaneous parametric Down Conversion

The importance of employing actual quantum states in quantum information and communication protocols has required the technological development of reliable and bright sources of such genuine quantum states. In the specific field of photonics, the most successful platforms to generate single photons or photon pairs have been based on non-linear optical effects. In the following we will briefly review the working principles of a Spontaneous Parametric Down Conversion (SPDC) source, with a specific focus on Periodically Poled Potassium Tytanil Phosphate (PPKTP) as a non-linear medium.

Non-linear Optics

Nonlinear optics describe phenomena occurring when the optical properties of a material system are modified by the presence of light. Typically, only laser light is sufficiently intense to modify the optical properties of a material system [21]. We are interested in three-wave mixing, i.e. phenomena involving three radiation fields, considering both inputs and outputs. We have a general formulation for the polarization of a material travelled by an electric field:

$$P(t) = \chi^{(1)}E(t) + \chi^{(2)}E^2(t) + \chi^{(3)}E^3(t) + ... \tag{1.64}$$

where $\chi^{(i)}$ is the electrical susceptivity of order i and $E(t)$ is the field in the material. For example, for an input field:

$$E(t) = E_1 e^{-i\omega_1 t} + E_2 e^{-i\omega_2 t} + c.c \tag{1.65}$$

the second order of polarization is the sum of multiple terms:

$$\begin{aligned} P^{(2)}(t) = \chi^{(2)}E^2(t) = \chi^{(2)}(E_1^2 e^{-i2\omega_1 t} + E_2^2 e^{-i2\omega 21 t} + \\ +2E_1E_2e^{-i(\omega_1+\omega_2)t} + 2E_1E_2^* e^{-i(\omega_1-\omega_2)} + c.c) + 2\chi^{(2)}(E_1E_1^* + E_2E_2^*) \end{aligned} \tag{1.66}$$

where each term represents a different non linear effect:

$$\begin{cases} P^{(2)}(2\omega_{1,2}) = \chi^{(2)}E_{1,2}^2 & \text{Second Harmonic Generation (SHG)} \\ P^{(2)}(\omega_1+\omega_2) = \chi^{(2)}E_1E_2 & \text{Sum Frequency Generation (SFG)} \\ P^{(2)}(\omega_1-\omega_2) = \chi^{(2)}E_1E_2^* & \text{Difference Frequency Generation (DFG)} \\ P^{(2)}(0) = \chi^{(2)}E_{1,2}E_{1,2}^* & \text{Optical Rectification (OR)} \end{cases} \tag{1.67}$$

Thus, it is possible to generate an output field featuring any of these frequencies, through the interaction with a non-linear medium, namely a medium with particularly high susceptivity.

Non-linear wave equation We start by writing down the Maxwell equations in Gauss form:

$$\begin{cases} \vec{\nabla}\cdot\vec{D} = 4\pi\rho \\ \vec{\nabla}\cdot\vec{B} = 0 \\ \vec{\nabla}\times\vec{E} = -\frac{1}{c}\frac{\partial\vec{H}}{\partial t} \\ \vec{\nabla}\times\vec{H} = \frac{1}{c}\frac{\partial\vec{D}}{\partial t} + \frac{4\pi}{c}\vec{J} \end{cases} \tag{1.68}$$

with boundary conditions:

$$\begin{cases} \rho = 0 \\ \vec{J} = 0 \\ \vec{B} = \vec{H} & (\mu = 1) \\ \vec{D} = \vec{E} + 4\pi\vec{P} & (\epsilon = 1) \end{cases} \tag{1.69}$$

We can write down the wave equation:

$$\begin{aligned} \vec{\nabla} \times \vec{\nabla} \times \vec{E} + \frac{1}{c^2}\frac{\partial^2 \vec{D}}{\partial t^2} = 0 \\ \rightarrow \vec{\nabla} \times \vec{\nabla} \times \vec{E} + \frac{1}{c^2}\frac{\partial^2 \vec{E}}{\partial t^2} = -\frac{4\pi}{c^2}\frac{\partial^2 \vec{P}}{\partial t^2} \end{aligned} \tag{1.70}$$

and decompose $\vec{P}$ in its linear and non-linear parts:

$$\vec{D} = \vec{D}^{(1)} + \vec{P}_{NL} = \epsilon^{(1)}\vec{E} + \vec{P}_{NL} \tag{1.71}$$

Thus, considering the differential relation $\vec{\nabla} \times \vec{\nabla} \times \vec{E} = \vec{\nabla}(\vec{\nabla}\vec{E}) - \nabla^2\vec{E}$, we finally get the equation:

$$-\nabla^2\vec{E} + \frac{\epsilon^{(1)}}{c^2}\frac{\partial^2 \vec{E}}{\partial t^2} = -\frac{4\pi}{c^2}\frac{\partial^2 \vec{P}^{NL}}{\partial t^2} \tag{1.72}$$

The wave equation stands for each spectral component, since the material reaction depends on frequency:

$$-\nabla^2\vec{E_n} + \frac{\epsilon^{(1)}(\omega_n)}{c^2}\frac{\partial^2 \vec{E_n}}{\partial t^2} = -\frac{4\pi}{c^2}\frac{\partial^2 \vec{P}^{NL}}{\partial t^2} \tag{1.73}$$

We now apply this propagation equation to three-wave mixing phenomena. We consider propagation along z axis; the "product" field intensity can be written as:

$$E_3(z,t) = A_3 e^{i(k_3 z - \omega_3 t)} + c.c. \tag{1.74}$$

where:

$$\begin{cases} k_3 = n_3\omega_3 \\ n_3 = \sqrt{\epsilon^{(1)}(\omega_3)} \\ A_3 & \text{constant for plane wave} \end{cases} \tag{1.75}$$

The polarization features the same oscillation frequency:

$$P_3(z,t) = P_3 e^{-i\omega_3 t} \tag{1.76}$$

where P_3 depends on the input fields of the mixing:

$$P_3(z) = 4d^{(2)}E_1(z)E_2(z) \tag{1.77}$$

and $d^{(2)} = \frac{1}{2}\chi^{(2)}$. The final wave equation for the three wave mixing can be written as:

$$\begin{aligned} -\frac{\partial^2}{\partial z^2}(A_3 e^{i(k_3 z-\omega_3 t)}) + \frac{\epsilon^{(1)}(\omega_3)}{c^2}\frac{\partial^2}{\partial t^2}A_3 e^{i(k_3 z-\omega_3 t)} = \\ = -\frac{4\pi}{c^2}\frac{\partial^2}{\partial t^2}[4d^{(2)}A_1 A_2 e^{i(k_1+k_2)z-i\omega_3 t}] \end{aligned} \tag{1.78}$$

We calculate the derivatives and obtain:

$$[-\frac{\partial^2 A_3}{\partial z^2} - 2ik_3\frac{\partial A_3}{\partial z} + k_3^2 A_3 - \frac{\epsilon^{(1)}(\omega_3)}{c^2}\omega_3^2 A_3]e^{ik_3 z-i\omega_3 t} = [\frac{16\pi}{c^2}d\omega_3^2 A_1 A_2]e^{i(k_1+k_2)z-i\omega_3 t} \tag{1.79}$$

It is possible to elide the temporal dependence of the exponential and use the fact that $k_3^2 = \epsilon^{(1)}(\omega_3)\frac{\omega_3^2}{c^2}$ to get:

$$-\frac{d^2 A_3}{dz^2} - 2ik_3\frac{dA_3}{dz} = \frac{16\pi}{c^2}d\omega_3^2 A_1 A_2 e^{i(k_1+k_2-k_3)z} \tag{1.80}$$

(without time dependence, the only parameter left is z, thus the derivative is a total derivative). We now use the Slow Varying Envelope Approximation: we assume that the envelope of the wave changes slowly with respect to the wave spatial period:

$$\left|\frac{d^2 A_3}{dz^2}\right| \ll \left|k_3\frac{dA_3}{dz}\right| \tag{1.81}$$

So we get an approximated wave equation:

$$\frac{dA_3}{dz} = \frac{8\pi i\omega_3^2}{k_3 c^2}dA_1 A_2 e^{iz} \tag{1.82}$$

where $\Delta k = k_1 + k_2 - k_3$ is the momentum mismatch. This mismatch has to be 0 to get the most efficient production of the requested effect, by a procedure named phase matching. The wave equations for the other two fields are given by:

$$\frac{dA_{1,2}}{dz} = \frac{8\pi i\omega_{1,2}^2}{k_{1,2}c^2}d^{(2)}A_3 A_{1,2}^* e^{-iz} \tag{1.83}$$

We assumed the medium to be lossless and a complete permutation symmetry, taking $d^{(2)}$ equal for each field. The solution found in this way features an almost constant amplitude of the input fields; the event we are observing is rare, the non-linear effect not very efficient. Indeed, these kind of processes are realizable only by means of laser light inputs, which provide a high number of coherent input photons hence large input power. The process we actually need to describe is the opposite of the typical one depicted before: a material stimulated by a radiation pump of frequency ω_3, relaxes by emitting two photons with frequency such that $\omega_1 + \omega_2 = \omega_3$, for energy conservation; this phenomenon is called spontaneous parametric down conversion (SPDC) and it needs a quantum description to be properly explained.

Quantum description In order to quantize the electric field theory in a non-linear medium, we assume to have a finite volume $V = L^3$, such that the possible modes of the systems are:

$$\begin{cases} k_x = \frac{2\pi\nu_x}{L} \\ k_y = \frac{2\pi\nu_y}{L} \\ k_z = \frac{2\pi\nu_z}{L} \end{cases} \tag{1.84}$$

The vector potential is, in general, defined as:

$$\vec{A}(\vec{r},t) = \sum_{\vec{k}} \sum_{l=1,2} \hat{e}_{\vec{k},l} A_{\vec{k},l}(\vec{r},t) \tag{1.85}$$

where l stands for the polarization (1,2 are the two orthogonal directions of polarization chosen as a basis) and $\{\hat{e}_{\vec{k},l}\}$ are the orthogonal polarization vectors, satisfying Coulomb gauge $\hat{e}_{\vec{k},l}\vec{k} = 0$. The vector potential component is complex $A_{\vec{k},l}(\vec{r},t) = A_{\vec{k},l}(t)e^{i\vec{k}\vec{r}} + A^*_{\vec{k},l}(t)e^{-i\vec{k}\vec{r}}$. We define the creation and annihilation field operators, in analogy with the harmonic oscillator:

$$\begin{aligned} \hat{a}_{\vec{k},l} \left| n_{\vec{k},l} \right\rangle &= \sqrt{n_{\vec{k},l}} \left| n_{\vec{k},l} - 1 \right\rangle \\ \hat{a}^+_{\vec{k},l} \left| n_{\vec{k},l} \right\rangle &= \sqrt{n_{\vec{k},l} + 1} \left| n_{\vec{k},l} + 1 \right\rangle \end{aligned} \tag{1.86}$$

so that the energy contribution of each photon is $\hbar\omega_k$, since there is an oscillator for each mode $k = (\vec{k}, l)$. Following this analogy, the radiation Hamiltonian will have the form:

$$\hat{H}_R = \sum_{\vec{k},l} \frac{1}{2}\hbar\omega_k (\hat{a}_{\vec{k},l}\hat{a}^+_{\vec{k},l} + \hat{a}^+_{\vec{k},l}\hat{a}_{\vec{k},l}) \tag{1.87}$$

and the vector potential operator, for each mode, will be:

$$\hat{A}_{\vec{k},l} = \sqrt{\frac{\hbar}{2\epsilon V\omega_k}} [\hat{a}_{\vec{k},l} e^{-i\omega_k t + i\vec{k}\vec{r}} + \hat{a}^+_{\vec{k},l} e^{+i\omega_k t - i\vec{k}\vec{r}}] \tag{1.88}$$

. We define the phase term $\chi_k = \omega_k t - \vec{k}\vec{r} - \frac{\pi}{2}$ and the transverse electric field operator $\hat{E}_T(\vec{r},t) = \hat{E}^+_T(\vec{r},t) + \hat{E}^-_T(\vec{r},t)$. Since $\vec{E}_T = -\partial_t \vec{A}$ we have:

$$\begin{aligned} \hat{E}^+_T(\vec{r},t) &= \sum_{\vec{k}} \sum_{l} \hat{e}_{\vec{k},l} \sqrt{\frac{\hbar}{2\epsilon V\omega_k}} \hat{a}_{\vec{k},l} e^{-i\chi_k(\vec{r},t)} \\ \hat{E}^-_T(\vec{r},t) &= \sum_{\vec{k}} \sum_{l} \hat{e}_{\vec{k},l} \sqrt{\frac{\hbar}{2\epsilon V\omega_k}} \hat{a}^+_{\vec{k},l} e^{+i\chi_k(\vec{r},t)}. \end{aligned} \tag{1.89}$$

Finally, the quantum expression for the electric field operator of a single mode is:

$$\hat{E}_T(\chi) = \sqrt{\frac{\hbar}{2\epsilon V\omega}} (\hat{a}e^{-i\chi} + \hat{a}^+ e^{+i\chi}) \tag{1.90}$$

, which is the expression we need to describe the SPDC process.

Phase matching

The conservation of energy $\omega_3 = \omega_1 + \omega_2$ is not sufficient to generate photon pairs, since momentum conservation has to be satisfied by the wave vectors of the three waves, too:

$$\vec{k_3} = \vec{k_1} + \vec{k_2}, \tag{1.91}$$

where $k = \frac{n\omega}{c}$. If this condition is satisfied, a perfect *phase matching* condition is achieved. Therefore, given $\omega_3 = \omega_1 + \omega_2$, the phase matching condition can be written as:

$$\begin{aligned} n_1\omega_1 + n_2\omega_2 &= n_3\omega_3 \\ \rightarrow n_3 - n_1 &= (n_1 - n_2)\frac{\omega_1}{\omega_3}. \end{aligned} \tag{1.92}$$

In general, the two terms could present opposite signs; as a consequence, in order to satisfy the phase matching condition, it is necessary to use birefringent materials, where the refraction index is different depending on the polarization of radiation coming through; the two different indices, acting on orthogonal polarization directions, are defined as ordinary index n_0 and extraordinary index n_e. We discuss two types of phase matching, depending on the polarization state assumed by the output photons with respect to the pump radiation.

Phase matching type I The polarization of the products is homogeneous and it is orthogonal to the input radiation one. There are two cases, depending on the non-linear medium under observation:

- **Uniaxial positive crystal**: two photons, in input or output, show the same polarization, corresponding to the extraordinary index n_e.

$$\begin{cases} n_3^o\omega_3 = n_1^e\omega_1 + n_2^e\omega_2 \\ n_1^e\omega_1 + n_2^e\omega_2 = n_3^o\omega_3 \end{cases}. \tag{1.93}$$

- **Uniaxial negative crystal**: two photons, in input or output, show the same polarization, corresponding to the extraordinary index n_0.

$$\begin{cases} n_3^e\omega_3 = n_1^o\omega_1 + n_2^o\omega_2 \\ n_1^o\omega_1 + n_2^o\omega_2 = n_3^e\omega_3 \end{cases}. \tag{1.94}$$

Phase matching type II The polarization of the two output or input photons is orthogonal. There are two cases, depending on the non-linear medium under observation:

- **Uniaxial positive crystal**:

$$\begin{cases} n_3^o\omega_3 = n_1^o\omega_1 + n_2^e\omega_2 \\ n_1^o\omega_1 + n_2^e\omega_2 = n_3^o\omega_3 \end{cases}. \tag{1.95}$$

- **Uniaxial negative crystal**:

$$\begin{cases} n_3^e\omega_3 = n_1^e\omega_1 + n_2^o\omega_2 \\ n_1^e\omega_1 + n_2^o\omega_2 = n_3^e\omega_3 \end{cases} . \tag{1.96}$$

The choice of the type of phase matching to harness depends on the crystal that is employed. In order to understand how phase-matching condition is actually fulfilled, it is worth focusing on the realization of the first type of phase-matching: we take into account a uniaxial negative crystal (such that $n_0 > n_e$). The ordinary index does not depend on the crystal orientation, while the extraordinary one changes with respect to the angle between the radiation propagation direction and the optical axis (fig. 1.8. We consider the case of degenerate SPDC, which is characterized by the phase matching condition $n_e(\omega)\omega = 2n_o(\frac{\omega}{2})\frac{\omega}{2}$. Thus, we need to fulfill the following equality between the two indices:

$$n_e(2\omega) = n_o(\omega). \tag{1.97}$$

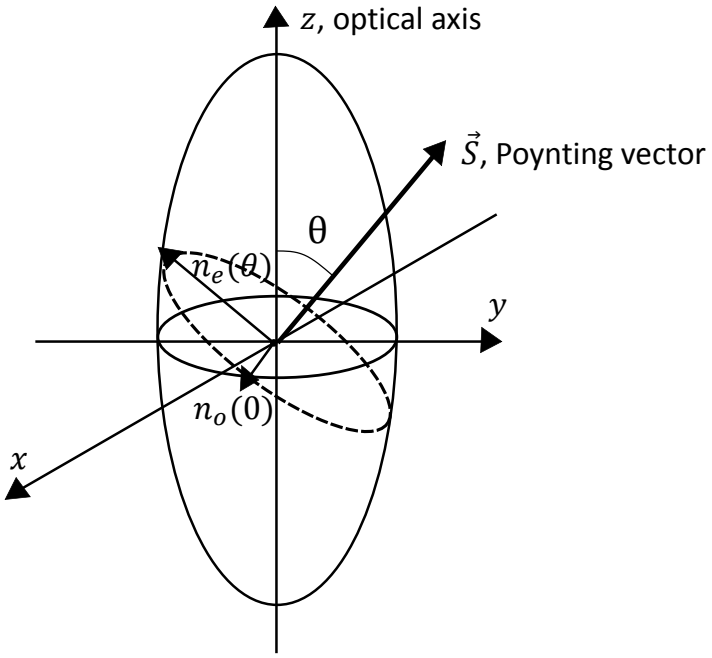

Figure 1.8: The index ellipsoid for a uniaxial negative crystal. *As the angle θ between the Poynting vector and the optical axis of the crystal grows, $n_e(\theta)$ grows as well. This effect corresponds to a translation of the dispersion curve of $n_e(\omega)$, in a homogeneous way with respect to frequency.*

In order to do this, we use the relation [22]:

$$\frac{1}{n_e(\theta)} = \frac{cos^2(\theta)}{n_0^2} + \frac{sin^2(\theta)}{\bar{n_e}^2}, \tag{1.98}$$

where $\bar{n_e}$ is the principal value of the extraordinary index, i.e. the value assumed by the index at $\theta = \frac{\pi}{2}$. In conclusion, we impose the phase matching condition and find an equation depending on

θ:

$$sin^2(\theta) = \frac{\frac{1}{n_0^2(\omega)} - \frac{1}{n_o^2(2\omega)}}{\frac{1}{\bar{n_e}^2(2\omega)} - \frac{1}{n_0^2(2\omega)}}, \tag{1.99}$$

which provides the angle of orientation needed to achieve the phase matching condition. The angle tuning procedure has the consistent drawback of yielding nonparallel Poynting vector $\vec{S}$ and propagation vector $\vec{k}$ for extraordinary rays. As a result, ordinary and extraordinary rays with parallel propagation vectors quickly diverge one from another as they propagate through the crystal. This effect limits the spatial overlap of the two waves and decreases the efficiency of any nonlinear mixing process involving them. For some crystals, the amount of birefringence is strongly temperature-dependent. As a result, it is possible to phase-match the mixing process by holding θ fixed at 90° while tuning the temperature of the crystal [23]. The maximum intensity of output field is achieved when Eq.(1.91) is satisfied; in that case the output wave has a constant phase relation with the non-linear polarization stimulated by the input fields and the generation is more effective [23].

Quasi-phase-matching There are cases in which phase-matching can not be practically fulfilled, such as for materials that have a normal dispersion for the frequencies under study. For such instances, there is a technique, known as *quasi-phase-matching* [24], which partially allows to achieve the same effect by means of a clever arrangement of the active medium. This scheme is known as *periodical poling*; the structure of a periodically poled material has been manufactured in such a way that the orientation of one of the two crystalline axes is periodically inverted as a function of position. As a consequence, the medium features a sequence of domains characterized by a nonlinear coupling coefficient $d^{(2)}$ with a sign that inverts each time the optical axis direction is overturned. This periodic succession of opposite signs of $d^{(2)}$ can compensate for a nonzero wavevector mismatch ΔK. This effect can be explained in terms of the interplay between the wavevector mismatch oscillations and the periodically poled structure of the material: the nonzero Δk produces periodical oscillations in the output wave amplitude, but the poled pattern of the medium is engineered so as to reverse the $d^{(2)}$ in a way that hinders the decrease of the amplitude, producing an overall monotonic growth of the output field as the distance travelled by the pump into the crystal increases. In Fig. 1.9, we report a comparison of output field amplitudes in different phase-matching situations.

PPKTP Crystal We consider a Periodically Poled crystal of Potassium Tytanil Phosphate (PPKTP) with a vertical ordinary polarization axis and horizontal extraordinary polarization axis as our reference non-linear medium; KTP is a ferroelectric crystal featuring wide transparency, large nonlinear coefficient, low refractive index change with temperature, large thermal phase-matching bandwidth, and high chemical and mechanical stability. Nevertheless, the probably most important property of KTP is its very low sensitivity (compared to other media) to photorefractive damage. In order to provide KTP with a better efficiency in the realization of non-linear emission of photons, we need to implement quasi-phase matching (QPM). Indeed, the most popular technique for generating quasi-phase-matched crystals is periodical poling of ferroelectric nonlinear crystal materials by *ferroelectric domain engineering*. Here, a strong electric field is applied to the crystal for a given

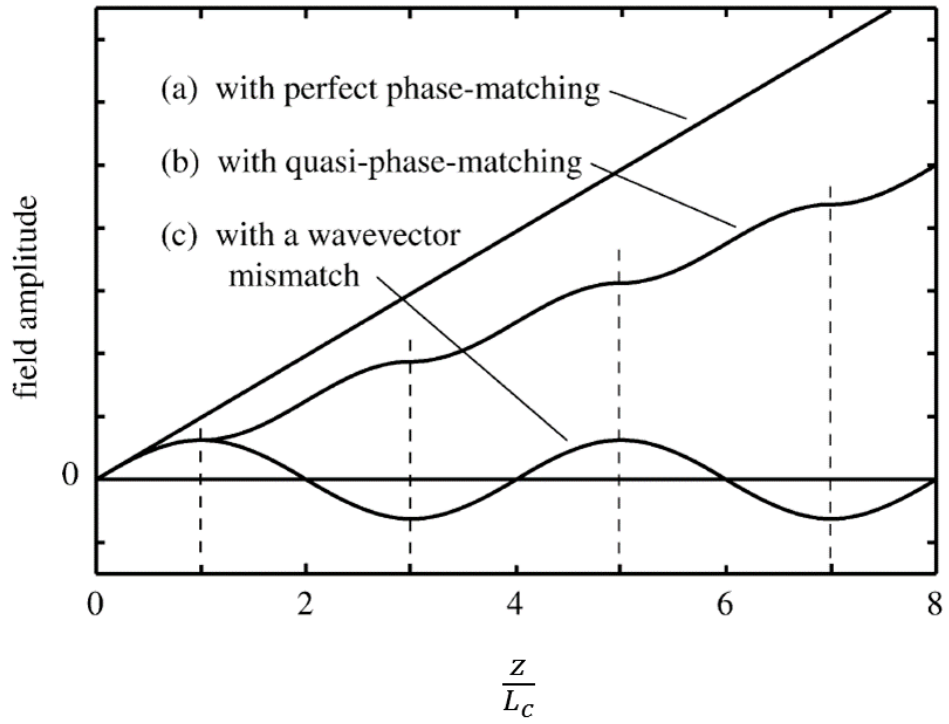

Figure 1.9: Field amplitude computed in function of the distance of interaction with the material. *Curve (a) shows that, in a perfectly phase matched interaction in an ordinary single-crystal nonlinear optical material, the field strength of the generated wave grows linearly with propagation distance. In the presence of a wavevector mismatch (curve c), the field amplitude of the generated wave oscillates with propagation distance. The behavior in the quasi-phase-matching condition is illustrated by curve (b). Here it is assumed that the period of the alternation of the crystalline axis has been set equal to twice the coherent buildup length L_c of the nonlinear interaction. Figure taken from [23].*

amount of time, using microstructured electrodes, so that the crystal orientation and thus the sign of the nonlinear coefficient is permanently reversed only below the electrode fingers. The poling period (the period of the electrodes pattern) determines the wavelengths for which certain non-linear processes can be quasi-phase-matched. In this case, the fulfillment of quasi-phase matching condition can be controlled by tuning the temperature of an oven enclosing the PPKTP crystal.

Parametric Down Conversion

The process consists of the annihilation of a photon of frequency ω_p from a single narrow-band incident pump beam and the generation of two photons of frequency ω and $\omega_p - \omega$. We review this phenomenon in the quantum framework, using the annihilation and creation operators of fields defined above. This kind of event is characterized by a low probability, such that the single event has not a negligible occurrence, while, on the other hand, a double event does. It is customary to address the generated photon with higher frequency as the *signal*, while the second one is called *idler*. Both the signal and idler modes are initially in their vacuum state, until the photons are generated by spontaneous emission. In particular, we are interested in *degenerate* Parametric Down Conversion, characterized by two emitted photons which are indistinguishable in frequency, as depicted in Fig. 1.10. The Hamiltonian of the process can be written as:

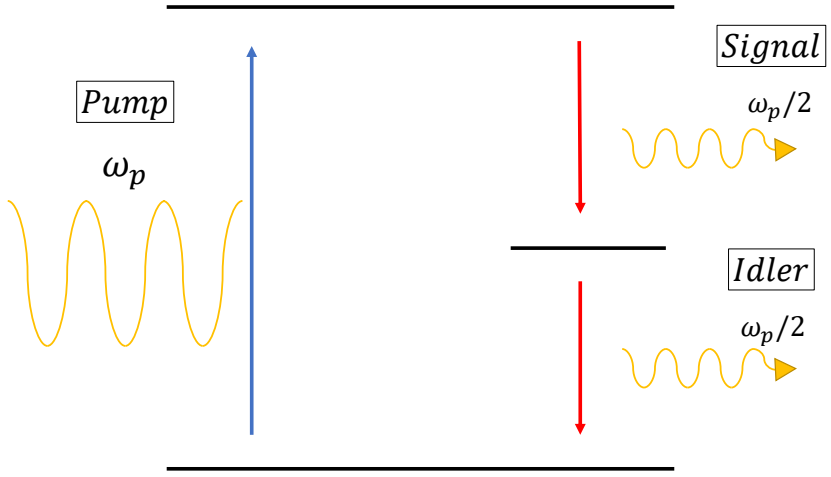

Figure 1.10: Sketch of degenerate SPDC. *An intense pump field stimulates the generation of a pair of photons, signal and idler, such that $\omega_s + \omega_i = \omega_p$ for energy conservation. In the degenerate case we are interested in $\omega_s = \omega_i = \frac{\omega}{2}$.*

$$H = \gamma(\hat{a}_s^+ \hat{a}_i^+ \hat{a}_p + \hat{a}_s \hat{a}_i \hat{a}_p^+) \tag{1.100}$$

where γ includes the pump amplitude, the non-linear coefficient, the crystal thickness and any other relevant parameter. The pump is assumed to be strong enough to not experience sensitive amplitude changes during the process, while the signal and idler do; it can be treated like a classical radiation,

in a plane wave fashion:

$$H = \gamma E_p(\hat{a}_s^+ \hat{a}_i^+ - \hat{a}_s \hat{a}_i) \tag{1.101}$$

the minus sign arising from the definition of the annihilation and creation operators in Eq. (1.90). We apply the temporal evolution operator to the initial state:

$$|0\rangle = |0\rangle_s |0\rangle_i \rightarrow |\Psi(t)\rangle = e^{-\frac{iHt}{\hbar}} |0\rangle \sim |0\rangle_s |0\rangle_i - \frac{iHt}{\hbar} |0\rangle_s |0\rangle_i - \frac{H^2 t^2}{2\hbar^2} |0\rangle_s |0\rangle_i + ... \tag{1.102}$$

We have expanded the exponential accounting for the fact that the probability of interaction (thus the strength of the interaction Hamiltonian) is low. In this framework, the production of a double photon pair can be neglected. In this process, post-selection is clearly necessary for a fruitful employment of the generated photons. In fact:

- the time of photon generation is unknown
- there are many losses
- dark counting of photodetectors may be significant, due to the generally low probability of the event

Therefore, even if only one of the two photons has to be exploited, the other one is still necessary in order to perform a coincidence measurement and assess the actual occurrence of a generation event.

1.2.6 Hong-Ou-Mandel effect

The Hong-Ou-Mandel (HOM) effect [25] is a unique quantum phenomenon, that can be observed when two indistinguishable bosonic wavefunctions overlap, as in the case of two indistinguishable photons that are injected at the same time in the two input modes of a BS. Two photons are indistinguishable if they are identical with respect to all of their degrees of freedom; the detector must have no clue about which photon of the pair it is counting (for example the signal or the idler generated by an SPDC process). Thus, the two photons must have same frequency (like the outcome of a degenerate SPDC), same polarization (a phase-matching type I would be needed), they must feature the same propagation mode $\vec{k}$, and they must arrive at the detectors at the same time, i.e. they have to travel equally long paths. Thus, we have the initial state of the two photons $\hat{a}_1 \hat{a}_2 |0\rangle_1 |0\rangle_2 = |1\rangle_1 |1\rangle_2$. The BS is again represented by the operator:

$$\hat{BS} = \begin{bmatrix} R & T \\ T & R \end{bmatrix}, \tag{1.103}$$

where $R = |R|e^{i\phi_R}$ and $T = |T|e^{i\phi_T}$. From the commutation relations, we have that $\phi_R - \phi_T = \frac{\pi}{2}$. Thus, we can write the BS operator as:

$$\hat{BS} = \begin{bmatrix} |R| & i|T| \\ i|T| & |R| \end{bmatrix}. \tag{1.104}$$

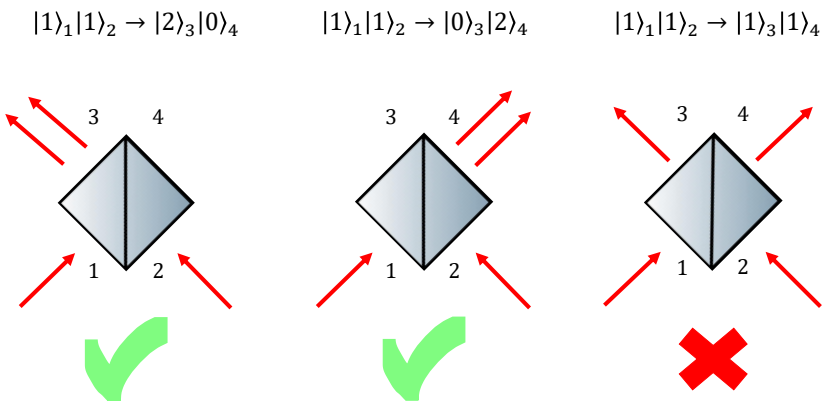

Figure 1.11: Sketch of the outcome of Hong-Ou-Mendel effect. Hong-Ou-mandel effect arises when two identical bosons, namely particles described by an identical symmetrical wavefunction, overlap their wavefunction completely. We consider the case of two photons impinging on a Beam Splitter (BS) from two opposite input ports. The system emerging from the BS can not be found in a configuration such that the two photons travel opposite paths, due to their indistinguishably and their bosonic nature.

We can now compute the output state:

$$\hat{BS}\,|1\rangle_1\,|1\rangle_2 = (|R|\hat{a}_3 + i|T|\hat{a}_4)(i|T|\hat{a}_3 + |R|\hat{a}_4)\,|0\rangle = |R|^2\,|1\rangle_3\,|1\rangle_4 - |T|^2\,|1\rangle_3\,|1\rangle_4 + \\ +i|R||T|\,|2\rangle_3\,|0\rangle_4 + i|R||T|\,|0\rangle_3\,|2\rangle_4 \tag{1.105}$$

The four terms represent the four possible occurrences:

1. first term: both the photons are reflected
2. second term: both the photons are transmitted
3. third and fourth term: one photon is transmitted and the other one is reflected

If the BS is symmetrical, namely $|R| = |T| = \frac{1}{\sqrt{2}}$, it is straightforward that the probability to find an output state with the photon travelling along different modes is 0. The photons are said to *bunch*; this effect, summarized in Fig. 1.11, is genuinely quantum and only occurs when the photons are completely indistinguishable. This phenomenon can be used as a tool to evaluate the indistinguishability of photons; collecting the number of coincidences occurring between the two output modes of the BS, we can assess the indistinguishability of the input photons. It is also worth noting that the output state of a photonic HOM effect is an entangled state of the two particles $\frac{1}{2}\big(\,|2\rangle_3\,|0\rangle_4 + |0\rangle_3\,|2\rangle_4\big)$, known as a **NOON** state with $N = 2$. This bosonic phenomenon, also known as *bosonic coalescence*, can also be applied to the study of fermionic interactions; in fact, in the case of two indistinguishable fermions, we would expect to find a peak of coincidences between two distinct outputs of the BS, namely an anti-bunching phenomenon, due to Pauli's principle. This situation could be simulated by means of an entangled pair of photons, if we generate an anti-symmetric state, for instance, in the polarization degree of freedom:

$$\frac{1}{\sqrt{2}}(|H\rangle\,|V\rangle - |V\rangle\,|H\rangle) \tag{1.106}$$

and we inject them in the two output ports of a BS. This strategy has been employed to study the behavior of particles featuring different statistics undergoing a coherent disordered evolution [26, 27].

1.2.7 Quantum Dots

SPDC has been considered for decades the most prominent and efficient way of producing single or pairs of photons, notwithstanding the intrinsic issues related to the non-linear nature of the underlying physical process. Indeed, the production of a high flux of photon pairs requires great input power stimulating down-conversion, leading in turn to an increase of undesired multi-photon emission, which is detrimental for the properties pursued in genuine photon pairs generation. Solid-state based quantum emitters, such as Quantum Dots (QDs), promise to bypass this issue, thanks to their near deterministical single-photon generation and their capability of producing entangled photon pairs without a significant corresponding amount of multi-photon emission [28]. In this section, we review general properties of this kind of emitters, with a particular focus on Gallium Arsenide (GaAs)-based Quantum Dots.

From semiconductors to Quantum Dots

Quantum Dots working principles rely on semiconductors' properties. A semiconductor is any crystal with Fermi energy sitting in an electronic band Energy gap E_g, whose optical and electronic properties can be modified by inserting a certain percentage of dopants in the crystal lattice [29]. A semiconductor material that does not need the addition of any dopants is called intrinsic and is characterized by having its Fermi level in the middle of the bandgap. At $0K$ all the available states in the valence band (VB) are occupied by the electrons. By pumping an electron with light featuring a frequency ν such that $\hbar\nu \geq E_g$, it is possible to make the electron jump from the VB to the next available band, the conduction band (CB). Regarding the momentum k, if an available state is present (at the bottom of the CB) directly above the current occupied state by the electron (top of the VB), it is possible to achieve a vertical transition by just pumping the right energy into the material: such crystals are known as direct bandgap materials. In the case of indirect bandgap, these two states are found with a $\Delta k \neq 0$ so that the promotion (or demotion) of an electron between these two states in the band structure requires a contribution in momentum from another excitation, such as a phonon. We are interested in particular in direct bandgap semiconductors, that are widely used for quantum information applications. After an electron is promoted from the VB to the CB, it leaves an empty state in the VB, a *hole* h, a collective excitation behaving as a positively charged quasi-particle. These excitation, before annihilation by either emission of a photon (a phenomenon known as **luminescence**) or through non-radiative alternative channels, endures in the crystal for a time ranging from nanoseconds to hundreds of picoseconds depending on the final recombination process. If the excitation of an electron from VB to CB is triggered by the absorption of light, the phenomenon is classified as **photoluminescence** (PL) [19]. The fundamental idea underlying the realization of a QD is reducing the spatial extension of a semiconductor down to the De Broglie length of electrons in the material: this represents the operative definition of a QD. In this framework, the system can be described by the model of an electron confined in a 3D well, hence featuring discretized energy levels rather than continuous energetic bands. In order to apply

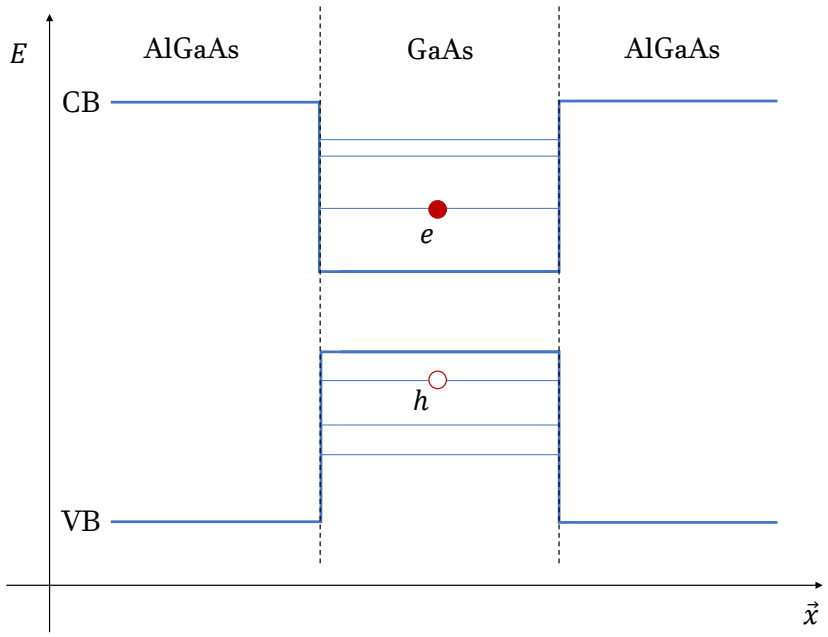

Figure 1.12: Qualitative sketch of hybrid energy diagram a QD with type I band alignment. *The energy bands are reported as a function of the spatial coordinates of the QD. As we scan along the heterojunction, energy bandgap changes since we are considering different materials, that in this case are AlGaAs and GaAs. The flat bands reflect the effective-mass approximation around the CB minimum and VB maximum.*

this model to the behavior of an electron/hole excitation in a semiconductor we have to add the 3D potential to the crystal Hamiltonian and look for a solution to the corresponding eigenfunction problem. In order to do this, we have to invoke the effective-mass approximation [30]. Specifically, from [31] we get that the energy dispersion of the CB at its bottom is approximately parabolic:

$$\epsilon_n(\mathbf{k}) \sim E_c + \frac{\hbar^2 k^2}{2m_0 m_e} \tag{1.107}$$

where E_c is the energy of the bottom of the conduction band and m_e is the effective mass of electrons. The corresponding Schrödinger equation is similar to the one for free electrons with an effective mass and energy measured from the bottom of the CB:

$$\left(-\frac{\hbar^2}{2m_0 m_e}\nabla^2 + V_{imp}(\mathbf{R}) \right)\chi(\mathbf{R}) = (E - E_c)\chi(\mathbf{R}) \tag{1.108}$$

where $\chi(\mathbf{R})$ is the envelope spatial part of the electron wave-function. This equation is useful to describe heterojunctions between different materials, where V_{imp} is represented by the offset between the two energy bands.

Indeed, a way to fabricate a QD is by enclosing a semiconductor material of size in the order of the nanometer inside another one with a wider bandgap, by choosing materials so as to obtain a band alignment of type I, i.e., the smaller bandgap material CB and VB are respectively lower and higher than the CB and VB of the larger bandgap material, such as in the diagram in Fig. 1.12. In this framework, the potential well is represented by the energy mismatch between the CB minimum and VB maximum at the boundary of the two materials. In a heterostructure, effective masses and Bloch

functions are in principle different between materials, but, under the approximation we mentioned above, electron and holes in a QD can be modeled as free particles with effective masses depending on the curvature of bands at the interface, enclosed in a potential well of the same magnitude of the CB and VB offsets respectively. In particular, we can consider such a system as a QD if the size of the small semiconductor is $L < \frac{\pi\hbar}{\sqrt{2mk_BT}}$.

Excitations

The presence of an electron-hole pair generates a further contribution to the system Hamiltonian, consisting of a Coulomb interaction potential. In particular, this effect results in the generation of an electron-hole bound state, that we refer to as *exciton*, or X for brevity. This system can be

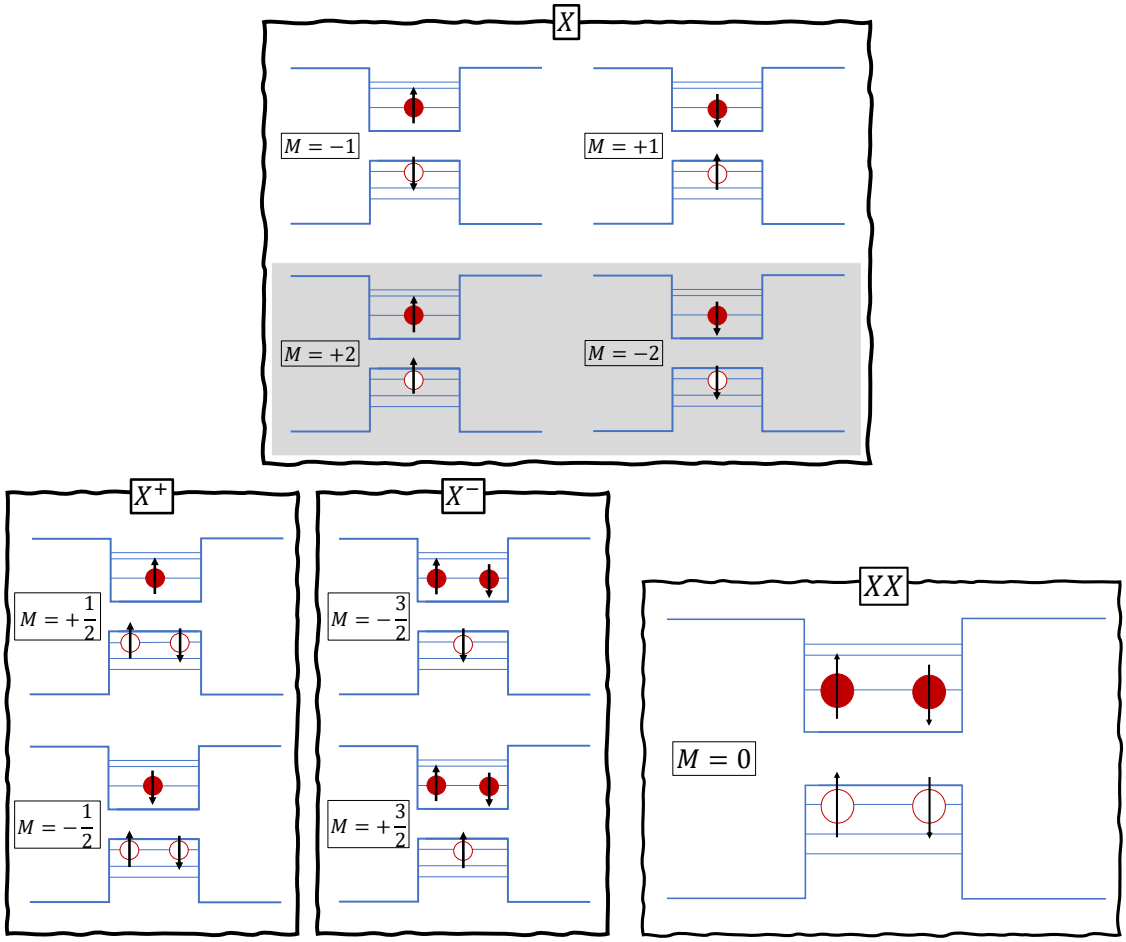

Figure 1.13: Electron and hole spins configurations for the *s*-shell of a quantum dot. *The absolute value of the total angular momentum M is given for every configuration. The exciton (X) state has four possible configurations that can be identified as "bright" states (top, white background) which can decay emitting a single photon and "dark" ones (bottom, gray background), which can not decay emitting a single photon. The two trion states (X^+ and X^-) feature two possible configurations each. The biexciton state (XX) represents the completely filled up shell and can occupy one feasible configuration.*

described as a hydrogen-like atom, thus X can in principle occupy various possible energetic shells, although in the following we will focus on the fundamental *s*-shell, corresponding to both electron and hole being in the ground state. In a QD at low temperature, because of quantum confinement, no free electron-hole pairs can exist and the fundamental excitation is the neutral X. Because of Pauli's exclusion principle, two electron-hole pairs at most with antiparallel spins can occupy the

same energy level. For the neutral X state, there are 4 possible states, as we show in Fig. 1.13. The two states with $|M| = 2$ can not decay to the ground state by the emission of a single photon and are called "dark" states. The remaining two, with anti-parallel spin projection configuration and $|M| = 1$ can emit a photon when decaying to the ground state and are known as "bright" states. An odd particle number excited state of the s-shell is known as a trion or charged exciton (X^+ with $|M| = \frac{1}{2}$ and X^- with $|M| = \frac{3}{2}$). When the whole s-shell is complete, two electron-hole pairs are present and we have a single possible configuration, known as biexciton (XX), featuring $|M| = 0$. Electrons are usually excited using photons with an energy above the bandgap of the barrier semiconductor. The generated electron-hole pairs are trapped in the QD and afterwards thermalize to the lowest available energy level, before recombination through the emission of a photon. Exciton recombination transition is customarily employed for efficient generation of single photons, but it is also possible to exploit the XX state to realize a cascade emission of two entangled photons, as sketched in Fig. 1.14. The XX state consists of two electron-hole pairs. As soon as one of the excitations recombines by the emission of a photon of energy equal to the difference of the XX energy and the X energy, the system is left in one of the two degenerate X bright state. Depending on the emission path followed by the biexciton state, the first emitted photon has right (R) or left (L) circular polarization. A second photon is then emitted after the recombination of the remaining X in the QD, with an energy corresponding to the X state energy and orthogonal circular polarization with respect to the previously emitted XX photon. If the X state is truly degenerate, i.e., the energy difference between the two exciton states, commonly known as fine structure splitting (FSS), is much smaller then the homogeneous linewidth of the photons, the two-photons cascade delivers as an outcome the entangled state of two photons $|\phi_+\rangle = \frac{1}{\sqrt{2}}(|R_{XX}\rangle |L_X\rangle + |L_{XX}\rangle |R_X\rangle)$. It is worth pointing out that the energy levels corresponding to a biexciton and an exciton does not follow the relation $E_{XX} = 2E_X$, so that the photons resulting from the cascade emission feature different frequencies $\omega_{XX} \neq \omega_X$. In conclusion, Quantum Dots are near-deterministic source of single photons, that have fostered new and favourable perspectives for the further development of quantum technologies. Their high brightness and their negligible generation of multiphoton states make them great candidates for future implementation of Quantum Communication protocols [32–35].

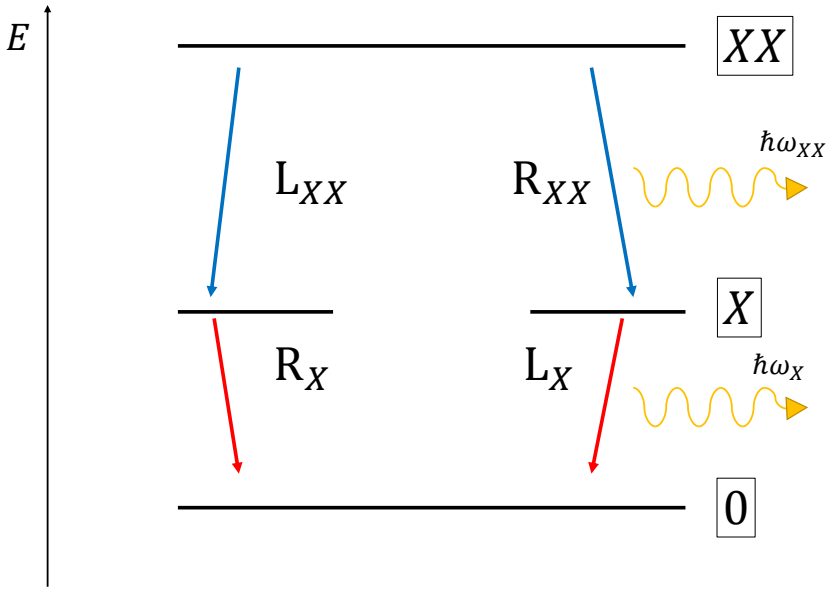

Figure 1.14: The two-photon cascade from the XX state in a QD. *The two radiative decay paths toward the ground state pass through the degenerate X state emitting two photons with orthogonal polarization configurations. If the degeneracy is not broken, the two paths are indistinguishable and the emitted photon pair is entangled in polarization.*

1.3 Quantum State Discrimination

As we discussed in Sec. 1.1, the state of a quantum system is not an observable itself, thus it can not be measured. Nevertheless, there are some choices of observables that can help gaining information about it. We can look at this task as a game between two parties, Alice and Bob (see Fig. 1.15).

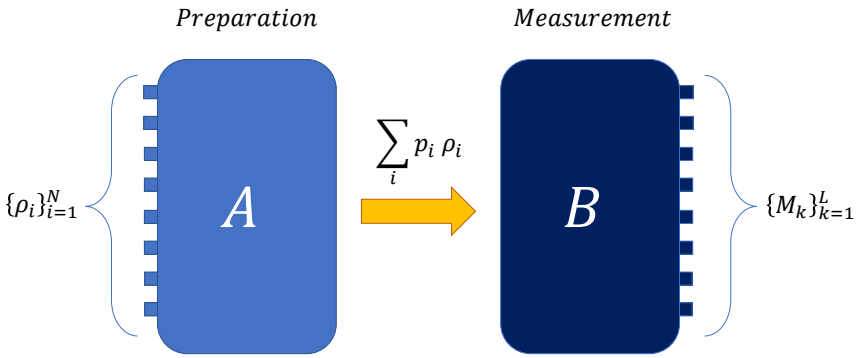

Figure 1.15: Basic setting for Quantum State Discrimination. *Alice (A) prepares a system in one of N possible states $\{\rho_i\}$, her alphabet. Bob (B) does not know the state chosen by Alice, thus he receives the system in a statistical mixture and tries to learn something about its state by performing one of a set of L measurements $\{M_k\}_{k=1}^L$.*

Alice prepares a quantum state and sends it to Bob, who performs a suitable measurement. We assume that the two parties have agreed on a limited "alphabet" of quantum states that Alice can prepare. Knowledge about the set of possible quantum states and their probability of preparation provides Bob with a priori information, that allows him to optimize the choice of the measurement he applies. It is not trivial to understand how much information Bob can extract about the quantum state by a single measurement. Indeed, a measurement on a quantum system does not provide full information about its state (since it is not an observable) and an arbitrary set of quantum states is not generally orthogonal so that they are generally not distinguishable one from each other by a single shot measurement. We remark that this indistinguishability is not due to lack of knowledge, but rather to the way quantum states are described. In classical systems, indistinguishability of states come from uncertainty in the preparation stage, hence is due to overlapping probability distributions. This is not true for quantum states, as we mentioned in Sec.1.1, and as it was demonstrated in [36]. Thus, quantum states can not in general be discriminated perfectly, by direct measurement. This apparently annoying feature bears various benefits for applications. Bennett and Brassard demonstrated that this impossibility in precisely measuring the state of a quantum state allows the existence of fundamentally secure protocols for secret communication. Unlike classical cryptographic protocols, relying on the complexity of the key (such as RSA) or a secure private channel, the quantum ones rely on physical laws [15]. The discrimination between quantum states is also related to other matters, such as the issue of cloning quantum states, and the manipulation of non-local correlations between quantum systems [37]. Thus, we need to discriminate quantum states, but an alternative strategy to straightforward measurement is required: a figure of merit is adopted, the discrimination scheme is developed and the measurement set to apply to the states is

optimized accordingly. In particular, this procedure corresponds to designing a *quantum receiver*, a device aimed at discriminating quantum states given some boundaries. It is possible to choose among many different figures of merit, depending on the requirements we wish to impose, that are usually derived from the application we are considering. This results in a variety of theoretical and experimental approaches to the method: it is possible to apply measurement in a single-shot fashion, which is suitable for actual quantum platform (once measured, the state collapses), or measurements can be repeated, with the chance of developing adaptive protocols, applicable to coherent light experimental implementations. In the following, we review the two main approaches for Quantum State Discrimination together with various examples of theoretical and experimental strategies.

1.3.1 Quantum Hypothesis Testing or Minimum Error Discrimination

The aim of Quantum Hypothesis Testing (QHT) [37] or Minimum Error Discrimination (MED) [38] is the minimization of the average error occurring in the discrimination procedure (or the maximization of success probability for the guess). The outcome of the measurement performed by the receiver Bob gives him information about the state sent to him by Alice. Schematically, if a detection event occurs at the kth output port, Bob concludes that Alice has prepared state ρ_k. Such a deduction cannot be certain unless states $\{\rho_i\}_{i=1}^N$ are all pairwise orthogonal. Otherwise, the process is inevitably prone to errors. Quantum measurements are described by POVMs, so an optimization procedure that yields measurement devices featuring minimum error is a quest for optimal and experimentally viable POVMs. We seek for a set of POVMs $\{M_k\}_{k=1}^N$ such that outcome k reveals state ρ_k with the minimum average error probability. We address the device implementing these measurements as the quantum receiver; when the state ρ_i is sent to the receiver, the probability of the POVM M_i producing a detection event is $p(i|i) = Tr[M_i\rho_i]$. The average probability of correct guess is given by taking into account the *a priori* probability q_i of each possible input state ρ_i, so that the maximum probability of correct guess is:

$$P_{guess}^{max} = \max_M \sum_{i=1}^N q_i p(i|i) = \max_M \sum_{i=1}^N q_i Tr[M_i\rho_i] \\ \text{subject to} \sum_i M_i = I,\ \forall M_i \geq 0 \tag{1.109}$$

where $M = \{M_i\}_{i=1}^N$. The minimum failure probability is readily obtained: $P_{err}^{min} = 1 - P_{guess}^{max}$.
In general, it is not straightforward to find the measurement realizing the optimal P_{guess}, even if the latter has been calculated. The aim of MED consists both of finding the maximum achievable P_{guess} and determining the POVMs that fulfill it. The optimal measurement for a set of quantum states $\{q_i, \rho_i\}_{i=1}^N$ is not unique and there is not a general method for the identification of such measurements, but for the case of some specific applications. Numerical methods are usually employed, such as semidefinite programming [39].

Two State Discrimination

We discuss the basic case of minimum error discrimination of two quantum states: we have two states $\{q_i, \rho_i\}_{i=1}^2$ and two output ports corresponding to the POVMs $\{M_1, M_2\}$. The maximum

probability of correct guess is easily computed:

$$P_{guess}^{max} = \max_{\{M_1,M_2\}} (q_1 Tr[M_1\rho_1] + q_2 Tr[M_2\rho_2]) = \max_{\{M_1,M_2\}} Tr[K] \tag{1.110}$$

where $K = q_1 M_1\rho_1 + q_2 M_2\rho_2$ is an operator determined by the optimization of the measurement. Since $M_1 + M_2 = I$:

$$K = \begin{cases} q_2\rho_2 + M_1 X \\ q_1\rho_1 - M_2 X \end{cases} \quad \text{where } X = q_1\rho_1 - q_2\rho_2 \tag{1.111}$$

and by symmetrization:

$$K = \frac{1}{2}(q_1\rho_1 + q_2\rho_2) + \frac{1}{2}(M_1 - M_2)X \tag{1.112}$$

If we define $M = M_1 - M_2$, the maximization procedure turns into a simpler one-parameter optimization in function of $-I \leq M \leq I$:

$$P_{guess}^{max} = \max_M Tr[K] = \frac{1}{2}\big(1 + \max_M Tr[MX]\big) \tag{1.113}$$

We can find the optimal M by spectral decomposition of operator X: for the case of two states $\{q_i, \rho_i\}_{i=1}^2$, we can write X as $X = \lambda_+ X_+ - \lambda_- X_-$ with positive (negative) projector X_+ (X_-) and λ_+ (λ_-) a positive (negative) eigenvalue. The optimal choice of M is $M = X_+ - X_-$, resulting in $P_{guess}^{max} = \frac{1}{2}(1 + \lambda_+ + \lambda_-)$. We can also rewrite the maximum guessing probability:

$$P_{guess}^{max} = \frac{1}{2}\big(1 + ||q_1\rho_1 - q_2\rho_2||\big) \tag{1.114}$$

that is known as the Helstrom bound [40]. In conclusion, $M_1 = X_+$ and $M_2 = X_-$ which together form a quantum measurement. This method is valid for any given pair of quantum states, while multiple states discrimination problems are seldom prone to general strategies.

Multiple state discrimination: the case of geometrically uniform states

For more than two states, optimal state discrimination can be only achieved in some limited cases where the given states possess certain symmetries or the dimension of the Hilbert space of the quantum states is small. For instance, optimal discrimination of multiple states is known for arbitrary qubit states that are given equal *a priori* probabilities, or for *geometrically uniform* states. A set of quantum states $\{\rho_i\}_{i=1}^N$, where $\rho_i \in S(\mathcal{H}_d)$, is said to be geometrically uniform [41] if there exists a symmetry represented by a unitary transformation U such that each state ρ_i is transformed cyclically into ρ_{i+1} by application of the unitary transformation for all $i = 1, \ldots, N$; in other words, they form a finite Abelian commutative group jointly with U [42]. So, we have that $\rho_{i+1} = U\rho_i U^\dagger$ $\forall i = 1, ..., N$ where $U^N = I$ and we define $\rho_{N+1} = \rho_1$. It is possible to exploit this symmetry for quantum state discrimination: we consider d non-orthogonal states in a d-dimensional Hilbert space $\mathcal{H}_d$ assuming equal *a priori* probability $q = 1/d$ for each state. We consider the states:

$$|\psi_\alpha\rangle = \sum_{n=0}^{d-1} c_n \exp\left(\frac{2\pi i}{d} n\alpha\right) |x_n\rangle \;\text{ for } \alpha = 0, ..., d-1 \tag{1.115}$$

where $\{|x_n\rangle\}_{n=0}^{d-1}$ form an orthonormal basis for the space $\mathcal{H}_d$. The symmetry is here related to the unitary operator:

$$U = \sum_{m=0}^{d-1} \exp\left(\frac{2\pi i}{d} m\right) |x_n\rangle \langle x_n| \text{ such that } U|\psi_\alpha\rangle = |\psi_{\alpha+1}\rangle \, \forall \alpha \tag{1.116}$$

For these states, it is possible to find an orthogonal basis that spans explicitly their support:

$$|x_n\rangle = \frac{1}{dc_n} \sum_{\alpha} \exp\left(-\frac{2\pi i}{d} n\alpha\right) |\psi_\alpha\rangle \tag{1.117}$$

such that the mixed state sent to the receiver, with equally likely terms, will result in:

$$\rho = \frac{1}{d} \sum_{\alpha} |\psi_\alpha\rangle \langle\psi_\alpha| = \sum_{n} c_n^2 |x_n\rangle \langle x_n| \,. \tag{1.118}$$

We can use the spectral decomposition in terms of the basis $\{|x_n\rangle\}$ to compute the probability of correct guess. From the eigenvalues

$$\lambda_n = c_n^2 = \frac{1}{d^2} \sum_{\alpha,\beta} \exp\left(\frac{2\pi i}{d} n(\beta - \alpha)\right) \langle\psi_\beta|\psi_\alpha\rangle \tag{1.119}$$

we can find a spectral decomposition for the basis corresponding to the optimal measurement, following the method depicted in [41]. The optimal POVMs are the set $\{M_j = |m_j\rangle \langle m_j|\}_{j=0}^{d-1}$ where:

$$|m_j\rangle = \frac{1}{\sqrt{d}} \sum_{k} \exp\left(\frac{2\pi i}{d} jk\right) |x_k\rangle \tag{1.120}$$

where the equivalence $\langle\psi_\beta|\psi_\alpha\rangle = \langle\psi_{\beta-\alpha}|\psi_0\rangle$ has been implemented. This measurement is known as a square root measurement, and it is considered as a "pretty good" measurement in the general case, while optimal for specific scenarios such as the one we are considering [43]. In conclusion, the maximum probability of correct guess can be expressed as:

$$P_{guess}^{max} = \sum_{j} q_j \langle m_j|\psi_j\rangle = \frac{1}{d^2} \left| \sum_{\eta} \Big(\sum_{m} \exp\left(\frac{2\pi i}{d} \eta m\right) \langle\psi_m|\psi_0\rangle \Big)^{\frac{1}{2}} \right|^2 \tag{1.121}$$

since $q_j = 1/d$ for all js. It is interesting to understand how this maximum achievable probability of correct guess changes as we increase the number of states we wish to encode in the d-dimensional system. In [44], it is proved that in a Quantum Hypothesis Testing problem (i.e. MED problem) where the states are equally likely and pure, the error probability is bound from below:

$$P_{err} \geq 1 - \frac{d}{N} \tag{1.122}$$

where d is the dimension of the Hilbert space $\mathcal{H}_d$ in which the states are defined and N is the number of states we are trying to discriminate among. As a consequence, the general equality stands $P_{guess}^{max} = 1 - \frac{d}{N}$, which is only fulfilled under some conditions. We give here a heuristic demonstration of the above inequality and we explicitly state these conditions, relying on the discussion reported in [44]. The problem of MED of N states $\rho_{i_1}^N$, with corresponding preparation probabilities can be

summarized as choosing the set of projectors $\{\pi_j\}_{j=1}^N$ that minimize the cost function:

$$P_{err} = \sum_i \sum_{j \neq i} p_i Tr(\pi_i \rho_j) \tag{1.123}$$

which represents the average probability of applying one of the "wrong" projectors π_j when the state is ρ_i. We consider the case of equally likely states $p_i = 1/N \ \forall i$ and pure states, i.e. states for which the density matrix is a projector on a corresponding vector $l_i \in \mathcal{H}_d$: $\rho_i = P_{l_i}$. As a consequence $\rho_i^2 = \rho_i$. In this framework, if it is possible to find N real numbers $\{\alpha_j\}_{j=1}^N$ such that $\sum_i \alpha_i \rho_i = I_d$, the N optimal projectors are represented by $\pi_j = \alpha_j \rho_j$ for $j = 1, \ldots, N$. Indeed, these projectors fulfill all the optimality conditions that are discussed in [44]. In this case, we can compute the minimized error probability:

$$\begin{aligned} P_{err} = \frac{1}{N} \sum_i \sum_{j \neq i} Tr(\pi_i \rho_j) = \frac{1}{N} (\sum_i \sum_j Tr(\alpha_i \rho_i \rho_j) - \sum_i Tr(\alpha_i \rho_i \rho_i)) = \\ = \frac{1}{N} (\sum_j Tr(I_d \rho_j) - Tr(I_d)) = \frac{1}{N}(1-d) = 1 - \frac{d}{N} \end{aligned} \tag{1.124}$$

If the condition on the α_j is not fulfilled, we have that:

$$\begin{aligned} P_{err} = \frac{1}{N} \sum_i \sum_{j \neq i} Tr(\pi_i \rho_j) = \frac{1}{N} (\sum_i \sum_j Tr(\pi_i \rho_j) - \sum_i Tr(\pi_i \rho_i)) = \\ = \frac{1}{N} (\sum_j Tr(I_d \rho_j) - \sum_i Tr(\pi_i \rho_i)) \geq \frac{1}{N}(1 - \sum_i Tr(\pi_i)) = 1 - \frac{d}{N} \end{aligned} \tag{1.125}$$

given that $I_d > P_{l_j}$ and, as we assumed, $\rho_j = P_{l_j}$ then $\sum_i Tr(\pi_i \rho_i) \leq \sum_i Tr(\pi_i) = d$. The equality is only achieved in the optimal case, when the π_is are proportional to the ρ_is. Geometrically uniform states satisfy these conditions thanks to their symmetry properties, thus it is possible to achieve the general maximum guess probability for them.

1.3.2 Quantum State Estimation or Unambiguous State Discrimination

We briefly review also the other main approach in Quantum State Discrimination problems. In this case, we want to address an error-free case: we wish to have a discrimination strategy that always yields correct results, with no uncertainty. This is possible, but at some cost: we have to allow for inconclusive measurements, i.e. measurements from the outcome of which we can not get any information about the state we have received [37, 45]. For a given ensemble of quantum states $\{q_i, \rho_i\}_{i=1}^N$, it is indeed possible to find a set of $N+1$ measurements $\{M_i\}_{i=1}^{N+1}$ such that:

$$p(i|j) = Tr[M_i \rho_j] = 0 \text{ for } i, j = 1, ..., N \tag{1.126}$$

A detection event on projector M_k unambiguously corresponds to the revelation of state ρ_k. In the case of pure states, the N POVMs associated to the N states can be found by considering the N orthogonal spaces to the N possible subsets of $N-1$ states, leaving one of the N states out of the grouping each time. Thus, if we wish to find the M_j corresponding to state $|\psi_j\rangle$, we have to

consider the subset $\{|\psi_i\rangle\}_{i\neq j}$ and then the projector on the orthogonal space to this subset will be M_j. Therefore, we can find $M_j = |\phi_j\rangle\langle\phi_j|$ such that:

$$\langle\phi_j|\psi_i\rangle = 0 \ \forall i \neq j \tag{1.127}$$

In general, the completeness relation is not satisfied by the N projectors $\sum_{i=1}^{N} M_i \neq I$ and it is possible to find a M_{N+1} measurement such that $\sum_{i=1}^{N+1} M_i = I$. This additional projector collects the probability that the state $|\psi_k\rangle$ is not detected by M_k, since $\langle\phi_k|\psi_k\rangle \neq 1$ unless the states are orthogonal. Therefore, it is possible to detect any of the N on M_{N+1} and the unavoidable detection events occurring in this measurement have to be discarded. It has been demonstrated that Unambiguous State Discrimination is only possible for linearly independent states [45]. It is worth noting that, as a consequence, it is not possible to discriminate among $N > D$ states, where D is the dimension of their encoding space. In general, it is necessary to minimize $Tr[M_{N+1}\rho]$ where $\rho = \sum_i q_i\rho_i$, to get the optimal strategy for the considered states set. General analytical approaches have been developed for linearly independent pure states [46], while for general purposes a numerical approach is necessary, like semidefinite programming [47].

1.3.3 Overview of experimental Quantum State Discrimination protocols

There are some theoretical bounds for the achievable performances in Quantum State Discrimination protocols, that vary depending on the number of states, the number of available copies and any boundary condition [40, 44, 48, 49]. These works yielded analytical results regarding two-state discrimination, while there aren't many general analytical results for multi-state discrimination, as mentioned above. Therefore, the quest for better achievements is quite platform-oriented and many experimental attempts have been produced in the last twenty years, aiming at developing effective protocols and correspondingly feasible experimental implementations. The first realization of USD [50] and of a multi-state MED [51] are very straightforward: they used a bulk-optics implementation where detection in a photodetector would signal the presence of a specific input state, with a maximum probability. In other terms, they unravel the differences among the target quantum states, encoded in photon polarization, turning them in a classical probability distribution in space, since each detector is placed at a different output port of their quantum receiver made of Polarizing Beam Splitters and Waveplates. This is the general procedure in Quantum State Discrimination protocols when the number of projectors that have to be applied is greater than the dimension of the system: some kind of multiplexing strategy, mapping in another degree of freedom, is necessary to distinguish among the quantum states. Another option is performing a set of measurements on the same system, which is only possible if multiple copies are available or we are working with coherent states, either as a simulation of quantum light (weak laser pulses) or in a continuous variable framework (as opposed to the discrete variable framework of photonic number states [52]). The latter case has been extensively investigated in the last years, with excellent results. In particular, many attempts have been produced employing the procedure of Quaternary Shift Phase Keying (QSPK) to encode four non-orthogonal states in a 2D coherent light system [53]. Many of them exploit the advantage of working with substantially classical light to implement adaptive protocols [54–60], which allow for a substantial enhancement of performances with respect to one-shot strategies. Although they generally demonstrate the effectiveness of their schemes for

a very low average photon number, this approach does not grant the fundamental security that single photons, hence actual quantum states, can guarantee. Following the success of adaptive protocols, neural networks [61, 62] and Machine Learning (ML) methods [63] have been applied to QSD problems from a theoretical point of view. In Chapter 3, we discuss our specific theoretical and experimental contribution to this approach.

1.3.4 Applications of Quantum State Discrimination strategies

Strategies developed in the framework of Quantum State Discrimination have wide applications. We briefly review some of them, with a specific attention for MED related issues.

Quantification of quantum state preparation For many Quantum Information and Communication tasks, the preparation of the quantum system in a precise state is rather important. In general, two states, although different, may not produce different outcomes, thus discrimination among two states can be applied to the problem of veryifing and quantifying how similar the actual and the ideal states are, by the guessing probability:

$$P_{guess} = \frac{1}{2}(1 + \frac{1}{2}||\rho_{actual} - \rho_{ideal}||). \tag{1.128}$$

It is possible to use this quantification via two-state distinguishability in many quantum information applications involving accurate state preparation [38].

Distinguishing measurements We have seen that in two-states Minimum Error Discrimination, the maximum probability of correct guess depends on the measurement M:

$$P_{guess} = \frac{1}{2} + \max_{-I \leq M \leq I} Tr[MX] \text{ where } X = q_1\rho_1 - q_2\rho_2 \tag{1.129}$$

If the two states and their preparation probabilities are fixed, there are different ways of choosing the measurement, each one producing different upper bounds for the guessing probability. Measurement classification is related to this issue, especially in the case of multipartite systems. We can have non-local, separable, and local measurements, or local operations and classical communication (LOCC). It is possible to demonstrate that the set of separable measurements is strictly larger than LOCC measurements, using quantum state discrimination. Indeed, there is a set of quantum states that can be perfectly distinguished by separable operations but not by LOCC protocols [6].

The Pusey–Barrett–Rudolph (PBR) theorem Notwithstanding the detailed formulation of Quantum Mechanics and its great effectiveness in describing the microscopic world, the interpretation of quantum mechanical states and concepts is still an issue. In this sense, many attempts have been devoted to establish ways to determine whether quantum states are mere states of knowledge (epistemic) or real physical entities (objective). In this sense, a *no-go theorem* was formulated by Pusey, Barrett, and Rudolph [64], asserting that *if a quantum state merely represents information about the real physical state of a system, then experimental predictions that contradict those of quantum theory can be constructed.* This theorem is valid under the assumption that two quantum systems at different locations can be prepared independently and its proof relies on a specific Quantum State Discrimination method, known as Quantum State Exclusion [65, 66].

Discrimination of unitary transformations A very interesting case is the one where we have a channel applying with a certain probability a unitary U_1 or U_2. We wish to discriminate which of the two unitaries was applied to the system travelling through the channel. It would be possible to straightforwardly choose a suitable state $|\psi\rangle$ and to perform Quantum State Discrimination among the states $U_1|\psi\rangle$ and $U_2|\psi\rangle$, but the problem can be addressed in a different and more effective way. Since we aim at discerning one of the two unitary transformations rather than discriminating among two states, it is possible to exploit ancillary systems, that is, discriminating between $I \otimes U_1$ and $I \otimes U_2$. The addition of ancillary systems can make two unitaries, even if they don't commute, completely distinguishable, though they were not without the ancillas [38, 67].

1.4 Quantum Walks

A Quantum Walk (QW) is ideally the quantum counterpart of a Classical Random Walk (CRW); first introduced by Aharonov et al. in 1993 [68], the Quantum Walk is a model for the coherent evolution of quantum particles. Its more distinctive feature is the possibility for the walker to occupy superposition states during the propagation, hence the occurrence of interference effects, that determine a stark dissimilarity with the classical model. Because of this fundamental difference, the way a Quantum Walk distribution spreads, quantifiable by the variance evolution, is quadratic in time and the spreading behaviour is said to be *ballistic*, in contrast with the linear, diffusive one of a CRW. In this section we will briefly review the Classical and Quantum RW models and discuss some of the main properties of ordered and disordered Quantum Walks, with a specific focus on the aspects that are more inherent to the object of our investigation. In addition to the applications we will discuss in this thesis, Quantum Walks have been found useful in a wide variety of frameworks, for instance as a tool for universal quantum computing [69–71], state engineering and transfer [72, 73], and modeling of biological processes [74].

1.4.1 Classical Random Walk

A classical discrete random walk on a line is a particular kind of stochastic process. The simplest classical random walk on a line consists of a particle ("the walker") jumping to either left or right depending on the outcomes of a probability system ("the coin") with (at least) two mutually exclusive results, i.e. the particle moves according to a probability distribution. The generalization to discrete random walks on spaces of higher dimensions (graphs) is straightforward. Classical random walks on graphs can be seen as Markov chains. Let Z_n be a stochastic process which consists of the path of a particle which moves along an axis with steps of one unit at time intervals also of one unit; each Z_n is the position of the particle at time n [75]. At any step, the particle has a probability p of going to the right and probability $q = 1 - p$ of going to the left. We define the random variables X_i, corresponding to the direction taken by the particle at a certain step i, which are independent and identically distributed; they take the value 1 or -1 according to the outcome of the try described above. Chosen as initial position $Z_0 = 0$, the position at a certain step n is given by:

$$Z_n = X_1 + X_2 + ... + X_n \tag{1.130}$$

We now define the random variable Y_i:

$$Y_i = \begin{cases} 1, X_i = 1 \\ 0, X_i = -1 \end{cases} \tag{1.131}$$

We can write $Y_i = \frac{1}{2}(X_i + 1)$ and, because of the fact that Y_i is a Bernoulli variable, we can define the random variable $T_n = \sum_{k=1}^{n} Y_i = \frac{1}{2}(Z_n + n)$, which is distributed according to the binomial distribution $\mathrm{Bin}(n, p)$. Therefore we can calculate the probability of finding the particle in position

k after n steps:

$$P(X_n = k|X_0 = 0) = P(T_n = \frac{1}{2}(Z_n + n) = \frac{1}{2}(k+n)) = \\ = \begin{cases} \frac{1}{2} \begin{bmatrix} n \\ \frac{1}{2}(k+n) \end{bmatrix} p^{\frac{1}{2}(k+n)} q^{\frac{1}{2}(n-k)}, \frac{1}{2}(k+n) \in \mathbb{N} \\ 0, \text{otherwise} \end{cases} \tag{1.132}$$

Since T_n follows $\text{Bin}(n, p)$, the expected value is $E[T_n] = np$ and the variance is $V[T_n] = npq$; thus, $V[Z_n] = 4npq$, hence $V[Z_n] = O(n)$. Therefore, the standard deviation of a classical random walk scales as $O(\sqrt{n})$ with the number of steps n.

1.4.2 Quantum Random Walk

It was demonstrated by Meyer in [76] that a quantum process consisting only of a quantum particle (the walker) which, at each time step, moves in superposition both to left and right with equal amplitudes, is physically impossible in general, except for the trivial case of motion in a single direction. Working on Quantum Cellular Automata (QCAs), Meyer formulated the following No-Go Lemma:

Theorem 1.1 *In one dimension there exists no nontrivial, homogeneous, local, scalar QCA. More explicitly, every band r-diagonal unitary matrix U which commutes with the one-step translation matrix T is also a translation matrix T^k for some $k \in \mathbb{Z}$, times a phase.*

We do not linger on the mathematical details of the matter, and we refer to [76] for the demonstration and further insights. We only report here the meaningful consequence of this theorem for Quantum Walks: a homogeneous, local process acting on a 1D system , hence represented by a band diagonal unitary commuting with the translation operator, must be a trivial translation itself. Thus, not a proper Quantum Random Walk, as required. In order to realize an actual Quantum Walk, it was suggested to incorporate a second auxiliary system in the Quantum Walk model, a *coin* system, as reported in [68] as well as in [77]. Thus, we should in principle speak of Coined Quantum Walks, but in the following we are going to simply address them as Quantum Walks (QWs). In particular, we are interested in a QW model with a very general applicability and a great flexibility, joint with a comparative simplicity: the Discrete Quantum Walk on a Line (DQWL). This model describes the coherent and time-discrete evolution of a quantum particle (walker) through a 1D lattice, mediated by an auxiliary coin system. The mathematical description of a DQWL was provided by [77] and [78] and we review it in the following.

Model of single coined DQWL

The main components of a coined DQWL are a walker, a coin, evolution operators for both walker and coin, and a set of observables.

Walker and Coin The walker is a quantum system described by a Hilbert space of infinite but countable dimension $\mathcal{H}_p$. It is customary to use vectors from the canonical (computational) basis of $\mathcal{H}_p$ as "position sites" for the walker. So, we denote the walker as $|position\rangle \in \mathcal{H}_p$ and

assume that the canonical basis states $|i\rangle_p$ that span $\mathcal{H}_p$, as well as any superposition of the form $\sum_i \alpha_i |i\rangle_p$, bound by $\sum_i |\alpha_i|^2$, are valid states to represent the walker's positions. The walker is usually initialized to the "origin" state, i.e. $|position\rangle_{initial} = |0\rangle_p$. The coin is a quantum system living in a 2-dimensional Hilbert space $\mathcal{H}_c$. The coin may take the canonical basis states $|0\rangle$ and $|1\rangle$ as well as any superposition of these basis states. Therefore $|coin\rangle \in \mathcal{H}_c$ and a general normalized state of the coin may be written as $|coin\rangle = a|0\rangle + b|1\rangle$, where $|a|^2 + |b|^2 = 1$. The total state of the quantum walk resides in $\mathcal{H}_T = \mathcal{H}_p \otimes \mathcal{H}_c$. It is customary to use product states of $\mathcal{H}_T$ as initial states $|initial\rangle = |position\rangle_{initial} |coin\rangle_{initial}$.

Evolution Operators The evolution of a QW is divided into two parts that closely resemble the behaviour of a CRW. In the classical case, chance plays a key role in the evolution of the system. In the quantum case, the equivalent of the previous process is to apply an evolution operator to the coin state followed by the application a *conditional shift operator* to the total quantum system. The purpose of the *coin operator* is to turn the coin state in a superposition, introducing randomness in the evolution in a quantum fashion. The most commonly employed coin operator (usually denoted as $\hat{C}$) is the Hadamard operator:

$$\hat{H} = \frac{1}{\sqrt{2}}(|0\rangle_c \langle 0| + |1\rangle_c \langle 0| + |0\rangle_c \langle 1| - |1\rangle_c \langle 1|) = \frac{1}{\sqrt{2}} \begin{bmatrix} 1 & 1 \\ 1 & -1 \end{bmatrix} \tag{1.133}$$

The conditional shift operator is a unitary operator, chosen so as to allow the walker to go one step forward if the joint coin system occupies one of the two basis states (e.g. $|0\rangle$), or one step backward if the coin state is in the other one (e.g. $|1\rangle$), in a coherent way. A suitable conditional shift operator has the form:

$$\hat{S} = |0\rangle_c \langle 0| \otimes \sum_i |i+1\rangle_p \langle i| + |1\rangle_c \langle 1| \otimes \sum_i |i-1\rangle_p \langle i| . \tag{1.134}$$

Thus, the unitary operator representing a single step of a DQWL is $\hat{U} = \hat{S}(\hat{C} \otimes \mathbb{I}_p)$, and the evolution of a DQWL for t steps can be written $|\psi(t)\rangle = (\hat{U})^t |\psi(0)\rangle$.

Observables Several potential application advantages of quantum walks over classical random walks are a consequence of interference effects appearing after several applications of $\hat{U}$ (other advantages come from quantum entanglement between walker(s) and coin(s) as well as partial measurement and/or interaction of coins and walkers with the environment). However, we must perform a measurement at some point in order to gather knowledge about our walker. To do so, we define a set of observables according to the basis states that have been used to define coin and walker. There are several ways to extract information from the composite quantum system. For example, we may first perform a measurement on the coin using the observable

$$\hat{M}_c = \alpha_0 |0\rangle_c \langle 0| + \alpha_1 |1\rangle_c \langle 1| . \tag{1.135}$$

A measurement must then be performed on the position states of the walker by using the operator

$$\hat{M}_p = \sum_i \alpha_i |i\rangle_p \langle i|_p . \tag{1.136}$$

In particular, we are interested in the average behavior of the Quantum Walk; we wish to compare the spreading behavior of a DQWL with its classical counterpart, through the analysis of the variance of operator M_p as a function of time, or rather the mean square displacement of the particle position $\sigma_p^2(t)$.

Properties of a DQWL A thorough mathematical analysis of the DQWL was carried by Nayak and Ambainis [77, 78], specifically oriented to establish the asymptotical behaviour of the Hadamard walk, i.e. the DQWL featuring a Hadamard coin operator. By means of a "Schrödinger approach", based on the Discrete Time Fourier Transform, they demonstrated that the Hadamard Walk has an asymptotic quadratic spreading of the position variance as the evolution proceeds, in contrast with the linear diffusion of CRWs. Therefore, Quantum Walks feature a pronounced superdiffusive spreading behavior, which is said to be *ballistic*. A stark difference in the spatial distribution of the walker arises with this behavior, as depicted in Fig. 1.16. It is worth observing the asymptotic ($t \to \infty$) output probability distribution for the particle to occupy a certain site i of the lattice at step t, after position measurement:

$$P(i,t) = p_0(i,t) + p_1(i,t) \tag{1.137}$$

where each term represents the probability of being in the site i with 0 or 1 coin state. We have a theorem about Hadamard Walks [77, 78]:

Theorem 1.2 *Let $\epsilon > 0$ be any constant and $\alpha \in [\frac{-1}{\sqrt{2}} + \epsilon, \frac{1}{\sqrt{2}} - \epsilon]$. For $t \to \infty$, we have, uniformly in n:*

$$\begin{aligned} p_0(i,t) &\sim \frac{2(1+\alpha)}{\pi(1-\alpha)\sqrt{1-2\alpha^2 t}} cos^2(-\omega t + \frac{\pi}{4}) \\ p_1(i,t) &\sim \frac{2}{\pi\sqrt{1-2\alpha^2 t}} cos^2(-\omega t + \frac{\pi}{4} - \rho) \end{aligned} \tag{1.138}$$

where $\omega = \alpha\rho + \theta$, $\rho = \arg(-B + \sqrt{\Delta})$, $\theta = arg(B + 2 + \sqrt{\nabla})$,$B = \frac{2\alpha}{1-\alpha}$ and $\Delta = B^2 - 4(B+1)$.

This result shows that the output probability distribution of the walker's position is almost uniformly spread in the region $\alpha \in [\frac{-1}{\sqrt{2}} + \epsilon, \frac{1}{\sqrt{2}} - \epsilon]$ and it decays very fast outside this area. By integrating the two probability distributions in Eq. 1.138, it is possible to see that the probability is mainly concentrated in the region $[(\frac{-1}{\sqrt{2}} + \epsilon)t, (\frac{1}{\sqrt{2}} - \epsilon)t]$, which provides an evidence of the fact that the width of the probability distribution grows linearly with time t, thus the distribution variance grows quadratically. The variance of the Hadamard Walk has been also computed by Konno [79] and by Kendon and Tregenna [80], confirming that the standard deviation of a Quantum Walk scales linear with time. Explicitly:

$$\frac{\sigma(X)}{t} \to \sqrt{\frac{\sqrt{2}-1}{2}} \text{ as } t \to \infty \tag{1.139}$$

it is in contrast with the behaviour of standard deviation for a Classical Random Walk, which scales as $O(\sqrt{t})$. We wish to stress out that any result standing for the Hadamard Walk is also valid for any other kind of coined DQWL, as demonstrated in [78]. There have been many efforts aiming at implementing more and more complex Quantum Walks, in particular on photonic platforms.

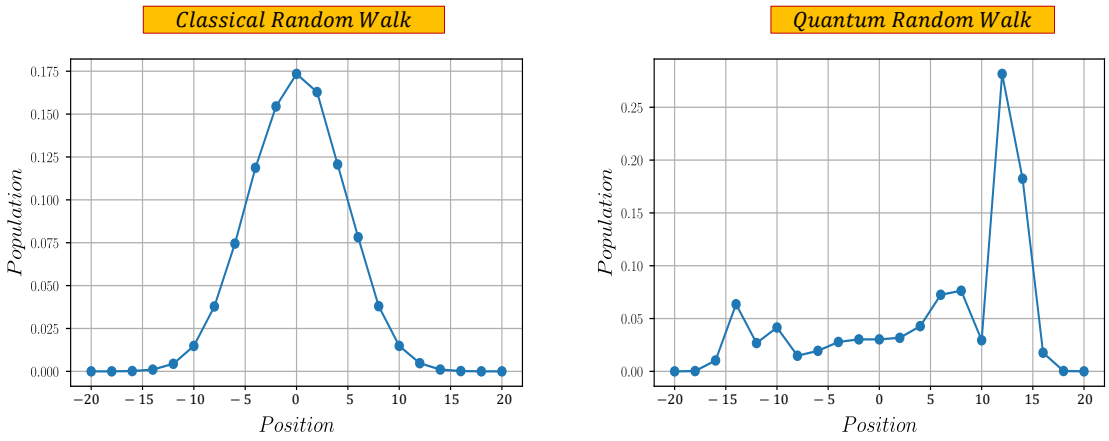

Figure 1.16: Comparison between spatial distribution of Quantum Walk (QW) and Classical Random Walk (CRW). *In the left, we report the spatial distribution of a classical random walker after 20 evolution steps: the probability of finding the walker is localized around the initial position ($x = 0$) and features the characteristic Gaussian shape. On the right, we see the completely different case of a quantum walker, which started its evolution at position 0, but with a specific initial coin state: as a consequence, the probability focus on a position far from the center, depending on the starting coin state. Thus, a QW process involve memory effects, in contrast with the CRW. Moreover, the rest of the population is distributed almost constantly around a very wide range of positions. This particular feature has been deemed useful in the development of quantum search algorithms [86].*

As of late, integrated optics have become the preeminent platform for QWs implementation [71, 81], and even more so since a way to fabricate tunable optical chips was designed [82]. Bulk optics remain important for high-dimensional QWs implementations, featuring the manipulation of alternative degrees of freedom to path and polarization [83–85]. In this section we focus on models and experimental implementations of QWs featuring disorder, in order to establish the framework for the next two Chapters.

1.4.3 Disordered Quantum Walks

Quantum Walks have been a powerful tool to analyze dynamical properties of a wide variety of systems and also a platform to investigate general quantum phenomena. For instance, there has been consistent interest towards the study of localization effects in Quantum Walks. The Anderson localization effect [87] implies that an excitation propagating through a lattice tends to localize, i.e. stops propagating, if inhomogeneities are inserted in the medium. This effect applies in principle to Quantum Walks, and it can and has been investigated through the years by means of QW platforms. The abundance of studies, that we will review in the following, highlighted how the insertion of disorder may in general produce a transition from a quantum regime (ballistic propagation) to a classical one (diffusive propagation). Disorder can be introduced in the QW evolution by means of *decoherence*, that is a physical phenomenon typically arising from the interaction between quantum systems and their environment, hence explicitly disrupting the coherence (and quantumness) of the system. Anyway, there are cases in which decoherence may result a useful noise, such as in application to quantum algorithms development [80]. Decoherence via measurement or free interaction with a classical environment is a typical framework for studying transitions of quantum walks into classical random walks [83, 88]. Nevertheless, disorder can be also imposed coherently on

the QW evolution, as we will explicitly show in the next Chapter. In the following, we will discuss different disorder regimes, each providing a different outcome in terms of spreading behaviour and we will focus on the corresponding experimental efforts, which mainly developed in an optical framework.

Static Disorder Regime

In 1958, P.W. Anderson [87] predicted that the wavefunction of a quantum particle shall localize under an inhomogeneous static potential. As a consequence, it is expected that particle and energy transport through a disordered medium should be strongly suppressed and that an initially localized wave packet should not spread out with time. Anderson analysed this problem for the case of an electron in a periodic crystal, in the quantum regime, leading to the conclusion that conductive materials can actually become insulators under a broad range of conditions. The localization phenomenon derives from path interference due to multiple scattering of the electron by lattice defects and relies on two hypotheses: the inhomogeneous potential is time-invariant and particles must be non-interacting. These conditions are hardly satisfied in solid state systems: the presence of temporal fluctuations (such as phonons) reduces the coherence of the scattering process and electrons are fermions, fundamentally interacting particles. As a consequence, the experimental demonstration of Anderson localization in crystals was very hard to perform. On the other hand, such conditions are readily achieved in photonic systems. Since localization is essentially a wave-mechanics related phenomenon, it can be naturally extended to any wave-like system, such as light [89–91]. Indeed, photonics are the ideal framework to study localization: coherence is easily preserved and photons are non-interacting bosons. Localization effect can be straightforwardly formulated for optical systems by a "transverse localization scheme" [91–93]. Anderson localization of light was observed in a 2D photonic lattice [94], highlighting three different disorder regimes as a function of disorder intensity:

- without any disorder, the light beam diffracts in the periodic medium, exhibiting ballistic transport
- introducing weak disorder, lattice symmetry is lost and light tunnels randomly among sites, in a diffusive transport regime
- with a high disorder level, the light intensity distribution narrows and the beam localizes (after a short diffusive propagation)

A similar experiment was carried out by Lahini et al. [95], showing that in a 1D photonic lattice, transport changes from ballistic to localized without any intermediate diffusive regime for low disorder levels. By definition, a photon undergoing a QW evolution is a particle propagating through a lattice. Hence, Quantum Walks are an advisable theoretical platform for investigating localization-related phenomena in optical system, because of many properties. They are unitary (unless decoherence is introduced), they provide a very general model, useful for photonic simulation of other systems [96]; inhomogeneities can be introduced easily in the evolution and the system can be measured after each evolution step (depending on the experimental implementation). In [83], thanks to a clever time-multiplexing platform that we will discuss in the next Chapter, it was possible to implement different disorder regimes in the Quantum Walk evolution of a laser pulse by

means of an Electro-Optical Modulator (EOM), observing a wide variety of spreading behaviors, such as localization.

Co-localization In the previous discussion, we have mentioned an experimental examples that employ laser light as a quantum walker, i.e. coherent states [83]. As we discussed in Sec. 1.2, coherent states can be described as classical objects, but they can simulate the behaviour of single photons in a QW. Indeed, the issue resides in the nature of single particle QW: they can effectively be described in terms of classical waves [97]. This is somewhat controversial, although the disagreement about the actual quantumness of single particle QWs revolves around the way light has to be considered, since light waves and particles feature very peculiar properties with respect to any other physical objects. This dispute does not extend to the case of multi-particle QWs: no classical system could simulate or reproduce the genuine quantum effects on the evolution of two or more indistinguishable/quantum correlated particles, such as the HOM effect reviewed in Subsec. 1.2.6. This motivated a large number of studies regarding the behaviour of indistinguishable and entangled particles undergoing a QW evolution. How correlations of two indistinguishable particles evolve under evolution through a periodic lattice was described in [98], inspiring further theoretical and experimental works, employing actual photon pairs [99–101]. In particular, it was demonstrated that the results were different for bosons and fermions, which could be simulated by suitably engineered two-photon states [26]. In the disordered case, theoretical studies [102, 103] implied that contemporary localization of two particles would be affected by correlation, different in case of bosonic or fermonic systems. This result was experimentally demonstrated by the groundbreaking experiment reported in [27], through an integrated photonic Quantum Walk platform, featuring static phase inhomogeneities.

Dynamical Disorder regime

In case we relax the hypothesis of stationary potential in time, localization breaks down, but other effects emerge. Specifically, transport resumes. There are many different ways of introducing dynamical disorder in a QW evolution, yielding different outcomes. We can have pure dynamical disorder, namely homogeneity in space but not in time, such as in the case of a medium with homogeneous refractive index but varying in time; in this situation, QWs feature classical-like diffusive spreading [104]. In [83], this regime was investigated by introducing decoherence through the imposition of random phases (space-wise uniformly) at each evolution step, leading to the expected diffusive propagation pattern. On the other hand, a spatially random potential which also fluctuates in time can produce hyper-transport, namely a super-ballistic behaviour [94]. Some earlier theoretical works [105–108] suggested hyper-transport was possible in presence of such a potential and the first experimental demonstration was provided by Levi et al. [109].
In the following Chapter, we present another disorder model for QWs and its application. This model, namely the p-diluted model, preserves the unitarity of the evolution and is characterized by spatial and temporal inhomogeneity; we will show how, thanks to its very general features, it is a particularly suitable model for investigating transitive regimes or for the manipulation of propagating quantum objects.

Chapter 2

Disordered Quantum Walks as a theoretical and experimental platform for the investigation of coherent propagation phenomena

In the introduction, I have illustrated different models of disordered Quantum Walks, providing a wide overview of the many possibilities offered by this theoretical platform. In the present Chapter, we start discussing the main contents of this thesis, presenting some of the works I contributed to. In particular, we introduce a theoretical and experimental framework that will be the basis for the next Chapter too: the p-diluted disorder model and its experimental implementation, that led to the first observation of superdiffusive behavior in a QW [110]. The idea of p-diluted served as a foundation for further works, that we report in this Chapter. This model was employed to observe subdiffusion in a QW [111], through an experiment based on my preliminary numerical analysis. My expertise in the field of disordered QWs also benefit a study regarding the relationship between extractable information and disorder in a QW-like network [112], establishing a first QW-based approach to quantum metrology problems.

2.1 The p-diluted model

In order to introduce the main subject of the thesis, we present another disorder model for Discrete Time Quantum Walks (DTQWs) which was explicitly developed in order to observe a transition from the ballistic to the diffusive behavior corresponding to the ordered and time-wise disordered case. In particular, the model is similar to the ones reported in the last subsection of Section 1.4, but for the important difference that the so-called p-diluted model introduces completely coherent disorder in the Quantum Walk evolution. In the p-diluted model, first introduced and employed in [110], we consider the case of a quantum particle propagating as a one dimensional (1D) DTQW that undergoes a sequence of phase shifts, each of which depends on the particular site and coin state where it is imposed, as well as on the step number. Therefore, the resulting disorder configuration will be inhomogeneous in the time, position and coin degrees of freedom. For sake of simplicity, we refer to the joint states of position and coin state as the *modes* $\{|k\rangle\}$ of the QW. We can always write

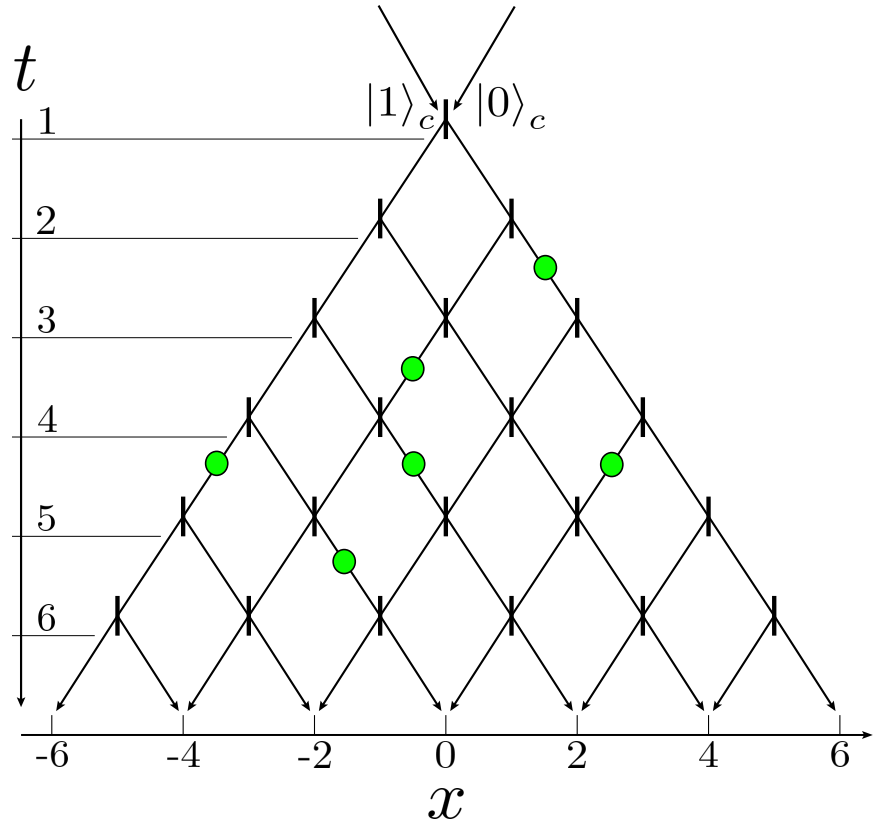

Figure 2.1: Example of a network representation of a p-diluted disordered QW. *The green circles represent π phases randomly added on the edges corresponding to QW modes, according to the p-diluted generated phase map. Coin and shift operations are here represented by black bars, that in a photonic framework can be straightforwardly implemented by Beam Splitters (BSs). The $|0\rangle_c$ and $|1\rangle_c$ coin basis states are reported.*

the state of the system as a superposition of these modes $|\Psi(t)\rangle = \sum_k \alpha_k(t)\,|k\rangle$. The probability amplitudes depend on the past evolution of the walker (a QW is a non-Markovian process) and we can write the single step evolution of the system as:

$$|\Psi(t+1)\rangle = \sum_k e^{i\phi_k(t)}\hat{U}_k\alpha_k(t)\,|k\rangle \tag{2.1}$$

where $\phi_k(t)$ is the phase shift that is imposed on the system at mode k and time step t, and $\hat{U}_k$ is the one-step evolution operator acting on the mode k. The phase shifts $\phi_k(t)$ are randomly chosen according to a sequence of independent Bernoulli processes characterized by the same real coefficient $p \in [0,1]$: for each possible joint pair of time steps and QW modes $\{t,k\}$, a random Bernoulli "coin toss" determines if $\phi_k(t) = 0$ with probability $1-p$ or $\phi_k(t) = \pi$ (a "flipped" phase) with probability p. All of these phase shifts form a so-called *phase map* [110]. A phase map generated with coefficient p is a set of matrices $\{\Phi_p(t)\}_{t=0,\dots t_{max}}$ describing the phase shifts that are imposed on the walker during the QW evolution. there are many different realizations, hence phase maps, that can be produced by the random generation protocol described above for a fixed p. Nevertheless, since we are considering a sequence of Bernoulli processes, i.e. binomial processes, we will have that, for a given probability p of "flipping" the individual phase, the average percentage of flipped phases

in a phase map will be equal to p [110]. For this reason, the model is referred to as p-diluted, in analogy to the model of diluted lattices in statistical mechanics [113]. In principle, the value p can be chosen in the range $[0, 1]$, but it is worth mentioning that half of this interval is enough for most applications: indeed, if we consider $p = \frac{1}{2}$, we will have, on average, half of the phase set to 0 and the other half set to 1, which we can consider as a completely disordered configuration. If we choose $p > \frac{1}{2}$, we will have an unbalanced ratio between 0 and π phase, with an exceeding amount of flipped phases, therefore we will face a situation of greater order than in the $p = \frac{1}{2}$ case. Thus, increasing the p above the $\frac{1}{2}$ value leads to a "return to order", symmetrical to the transition from $p = 0$ to $p = \frac{1}{2}$ and culminating in the completely ordered configuration consisting of all phases flipped. As we have shown in Section 1.4, inhomogeneities are usually inserted in Quantum Walks with the aim of investigating different disorder regimes: in this case, the possible disorder regimes are fully covered by p values in $[0, 0.5]$. In the applications of the model, the parameter p is redefined in order to run over the interval $[0, 1]$, while the actual "disorder level" corresponds to $\frac{p}{2}$. Thus, in the following, whenever we refer to the case of $p = 1$, or a transition up to $p = 1$, we are considering the situation of complete disorder, namely a disorder level of $\frac{1}{2}$. As a final remark, we stress the fact that the inhomogeneity model we described does not impose any decoherence effect on the system, mantaining the purity of the initial state throughout the whole evolution. This kind of disordered Quantum Walk has been realized for the first time via an optical implementation in [110], with the aim of demonstrating a continuous superdiffusive transition between ballistic and diffusive behaviour in Quantum Walks. This work was the starting point for further investigations on anomalous diffusion phenomena in Quantum Walks and their applications, that we discuss in this Chapter. In the next section, we describe an improved setup with respect to the one employed in [110], which made possible further studies and achievements.

2.2 A bulk-optics setup to implement disordered Quantum Walks in the time and space domains

As we mentioned in Sec 1.4, Quantum Walks have been mostly analyzed from an experimental point of view through photonic implementations. Both bulk and integrated setups have served as important platforms for the investigation of Quantum Walks behavior, especially in the case of disordered evolution. Integrated systems have a clear advantage in terms of compactness, hence technological applications, and losses reduction [114]. On the other hand, until recently, they lacked in flexibility: the ability to tune the parameters of a photon evolution imposed by an optical chip has been developed as of late only [82, 115, 116]. Moreover, it is not possible, in general, to measure each step of the Quantum Walk evolution in integrated implementations. In order to reproduce a Quantum Walk evolution featured by the p-diluted disorder model described above, the ability to address phase shifts both in the time and space degrees of freedom is necessary. Specifically, we wish to reproduce a Galton board made of BSs, reproducing the network structure of Fig. 2.1, that corresponds to a network of Mach-Zehnder Interferometers (MZIs), in which some edges of the network may feature a π phase shift. These phase shifts combine to determine the global phase shift of each MZI, corresponding to each mesh of the network. A setup for this task was realized, implementing both single photon and photon pair p-diluted disordered Quantum Walk evolution. Earlier application of the same experimental method can be found in [117], while the

complete setup is described in detail in [110, 118]. In this section, we describe the improved version of the experimental platform, that I implemented during my PhD and that was employed for the experimental investigation of enhancement in nonclassical correlation of a biphoton due to coherent disorder configurations [119], which will be discussed in the next Chapter.

2.2.1 Experimental scheme

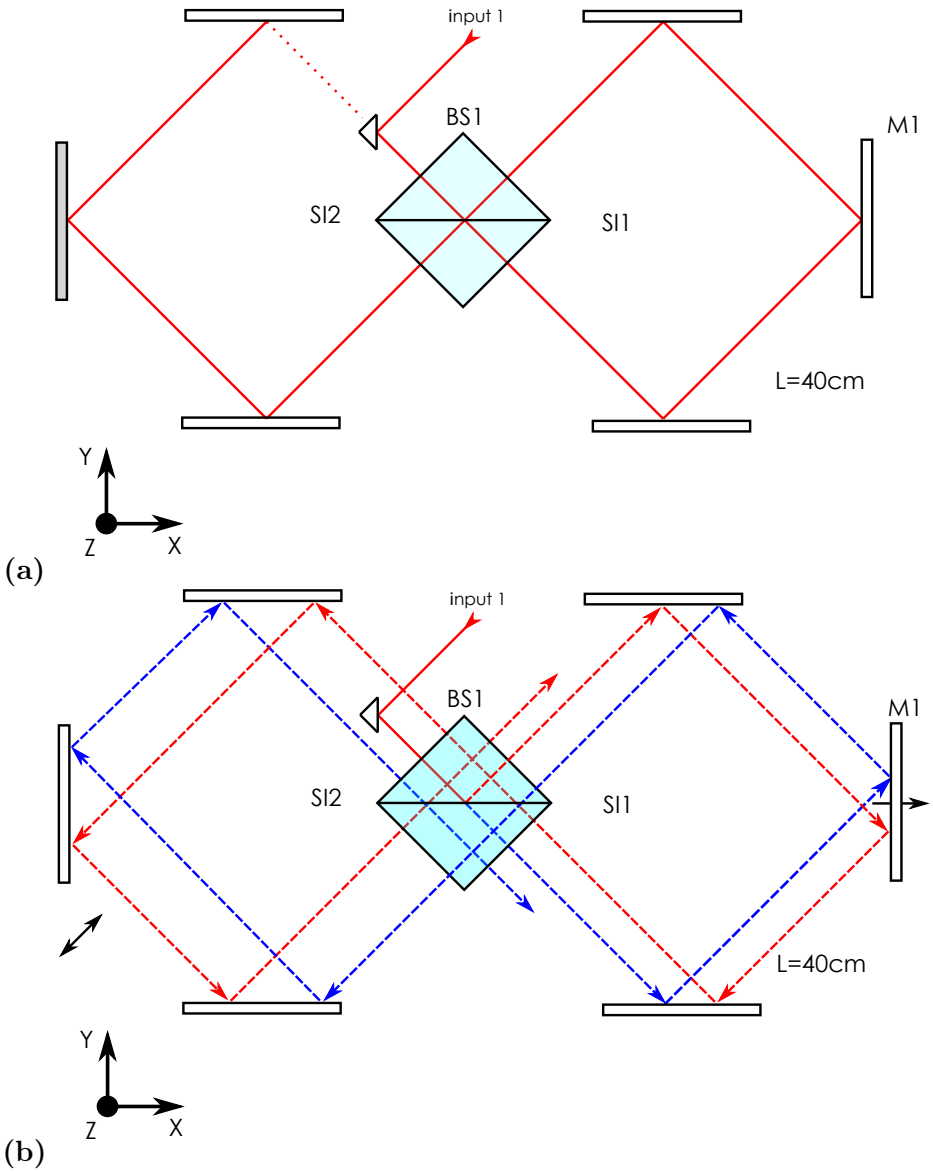

Figure 2.2: Building an all optical QW platform. (a) *Double Sagnac Interferometer (SI1 and SI2), for intrinsic phase stability;* **(b)** *displacing one mirror M1 generates different possible paths, which recombine on the central Beam Splitter (BS1) in different position as light propagates through the setup. This procedure effectively reproduces a chain of Mach-Zender interferometers, where it is possible, in principle, to individually address each phase shifting.*

The experimental setup consists of two displaced multi-pass Sagnac Interferometers (SIs), that are connected through a common BS. Figure 2.2 shows the first step for the realization of such a setup: at first, the two SIs are identical, so that light entering the system would just travel the same path over and over (Fig. 2.2 a)). By shifting the angular mirror of one of the two SIs, namely SI1, it

is possible to produce a horizontal displacement of photon trajectories as light passes through SI1. Eventually, a sequence of displaced loops lying in the X-Y plane is obtained (Fig. 2.2 b)). This is equivalent to a chain of Mach-Zehnder interferometers (MZIs), as the one reproduced in [117], where the length of the chain is determined by the amount of times light passes through the BS. These interferometers have intrinsical phase stability, because of the Sagnac geometry.
Using the propagation plane of light, it is possible to reproduce the evolution in time of the system, but we still lack the spatial propagation we require to reproduce a MZIs network as in Fig. 2.1. To this aim, the transversal direction to the propagation plane was exploited as well, thanks to the employment of suitably designed Beam Displacers (BDs). The BD consists of a thick tilted glass prism. Fig. 2.3 sketches its working principle: light passing through the BD is up-shifted by an amount which is determined by inclination, thickness and refraction index of the BD. Photons travelling multiple times through a BD will change their propagation height of a discrete amount, resulting in a discrete evolution in the transversal direction to the propagation plane. Two BDs were positioned so as to intercept clockwise light trajectories in SI1 and counter-clockwise ones in SI2. The QW sites are encoded in the transversal axis: the BS applies the coin operator, and, depending on the output port photons emerge, the path of light will either be lifted or not, representing the action of the shift operator and yielding as a result the QW one-dimensional propagation we wish to reproduce. In conclusion, we are able to reproduce the network structure of Fig. 2.1 by the setup

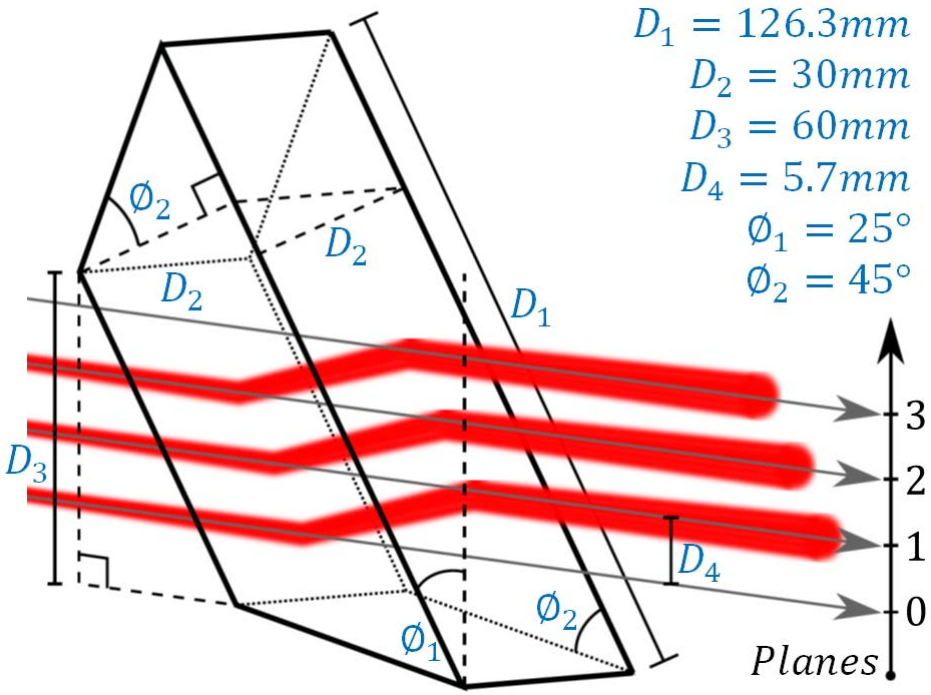

Figure 2.3: Sketch of the functioning of the Beam Displacer. *A beam travelling through the Beam Displacer (BD) is lifted off a set height, which is chosen aiming at keeping planes corresponding to different QW position well distinguishable one from another. Values of implemented geometrical parameters are reported. In order to get the optimal height step (around 6 mm) and to limit further effects on the beam, such as the unavoidable angular spreading, the parallelism between the BD's faces has to be accurate below* $1\mu rad$. *Figure from the Supplemental material to [110].*

sketched in Fig. 2.4: the multiple BSs are replaced by multiple passages in the central Beam Splitter, corresponding to different points on the planes parallel to the BS faces. Each of these points

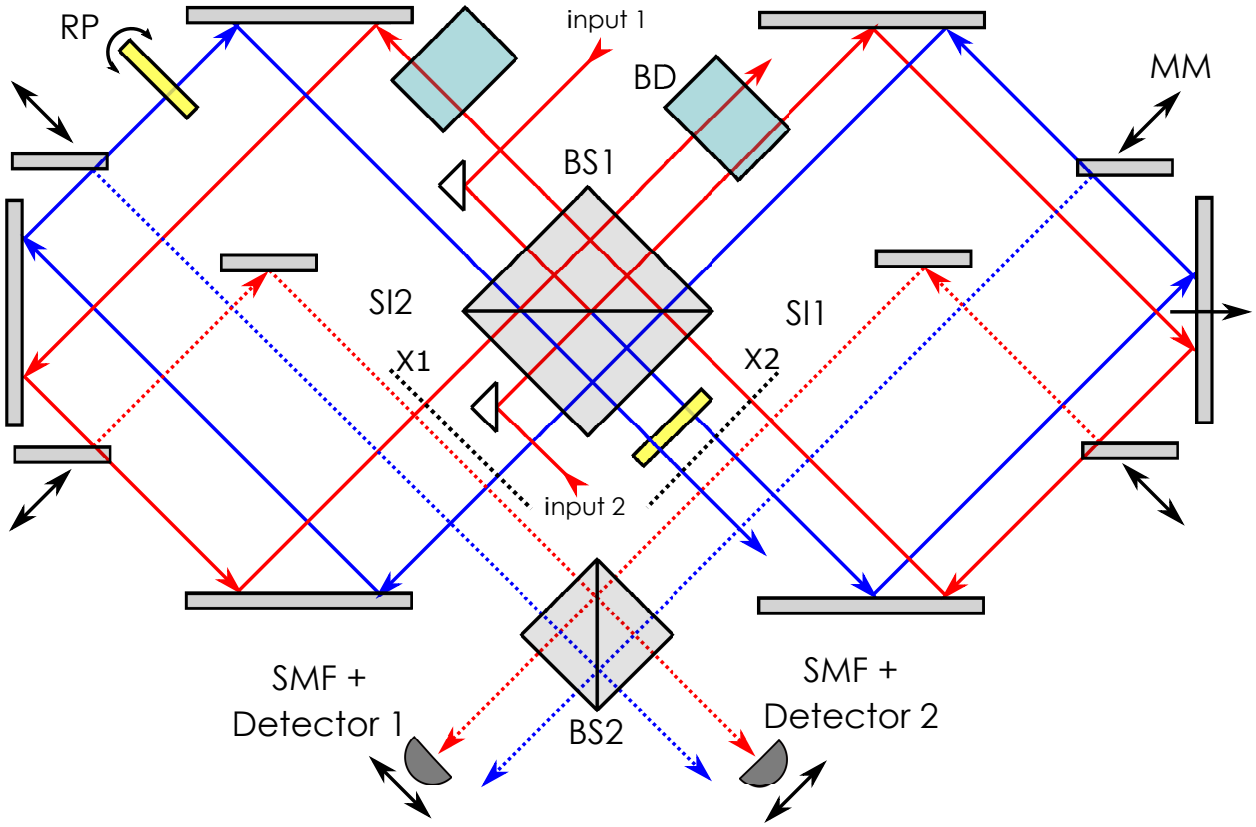

Figure 2.4: 2D sketch of the experimental setup. *Optical elements are refferred to as BS: beam splitter, BD: beam displacer, RP: rotating glass plates, MM: moving mirror, SI1: Sagnac Interferometer 1, SI2: Sagnac Interferometer 2. Blue and red beams circulate in opposite directions and impinge on the BS*1 *in the same horizontal point but at different heights along the z direction, due to the effect of BDs. BS2 allows the detection of two photon coincidences collected from the same output mode.*

corresponds to a different site, coin state and evolution step, so that it is possible, through some Moving Mirrors (MM) to collect signal at any evolution step and reconstruct the output probability distribution of the QW throughout the whole evolution. This peculiar spatial structure is clarified in Fig. 2.5.

Indeed, as we show in Fig. 2.4, it is possible to have two photons travelling the QW at the same time, by suitably engineering a second input path. As a consequence, this platform also allows us to study the behavior of two photons sharing quantum correlations (such as indistinguishability or entanglement) as they face a disordered QW evolution.

In fact, our very flexible setup grants the possibility of individually addressing the phase shift for each mesh of the network in Fig. 2.1, in order to implement p-diluted disordered configurations. This can be done by positioning some thin glass plates along the photon paths, one for each possible transversal propagation mode. By suitably tilting these Rotating Plates (RPs), it is possible to change the total phase shift corresponding to one of the BS network meshes from 0 to π at will. We provide a more detailed discussion of the phase tuning procedure in the following.

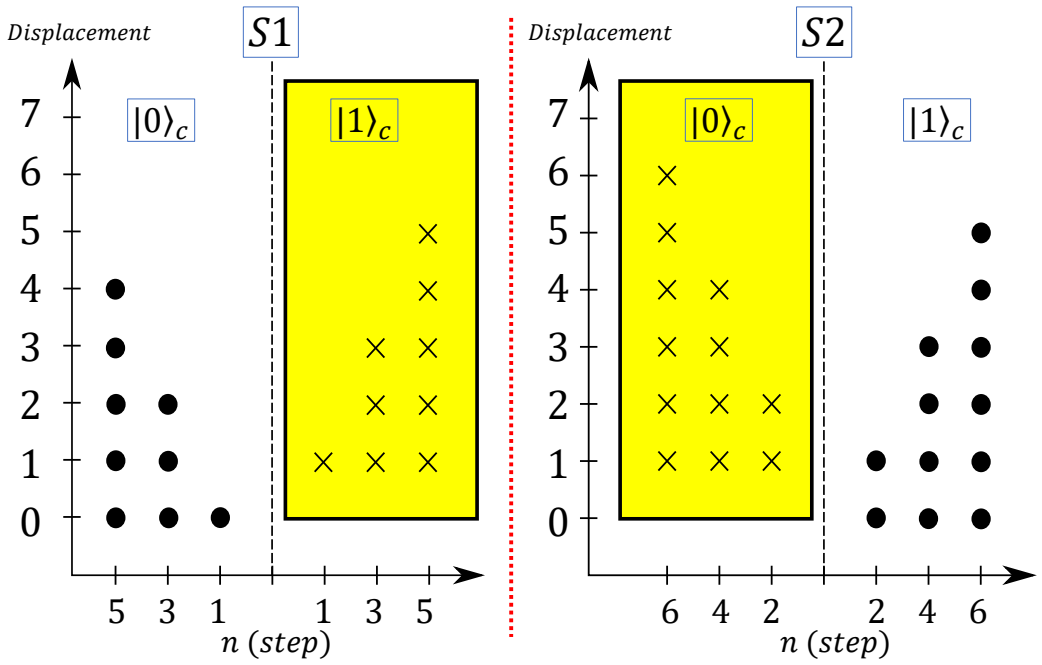

Figure 2.5: Transverse spatial distribution of light beam trajectories. *(**S1**) Looking at the BS from the plane X1 to light propagation in SI1. (**S2**) Looking at the BS from the plane X2 of SI2, defined as the orthogonal planes to light propagation direction. For each cut, the number of steps increases along the horizontal axis of the pattern, going from inside to outside with respect to the central dashed line. Indeed, paths exiting from the BS at step k are external with respect to the paths of the step $k-2$ (note that odd steps belong to SI1, while even steps belong to SI2). Columns with the same index k show the modes of the k^{th} step. Each step is represented twice because of the two possible states of the coin ($|0\rangle_c$, $|1\rangle_c$). Different planes of a column represent different sites, and the number associated with the site increases going from the bottom to the top. In this way, the same plane represents different sites for different steps. For example, in the S_1 cut, the zero-plane represents the site -1, but for step $k=3$, the same plane represents the site -3. Point-marked trajectories ($|0\rangle_c$) proceed towards the viewer, while cross-marked ones ($|1\rangle_c$) travel in the opposite direction. The yellow regions correspond to the effective transverse BD areas. Figure from [119].*

Phase tuning

As mentioned in Sec. 2.1, the disorder is inserted in the system by imposing a random phase, chosen in $\{0, \pi\}$ with probabilities $P_0 = 1-p$ and $P_\pi = p$, on each mode, at each step. A graphical example of phase map is depicted in Fig. 2.7: our Quantum Walk acts as a Mach-Zehnder interferometers network, so that the only meaningful quantities are the phase differences between the two branches of each MZ. Therefore, the operation of phase tuning consists in rotating the RP while observing the outputs of the selected MZ (this is possible by using the MMs) until the requested interference condition is satisfied. In order to do this, we need to individually address the phase shift of each MZI, hence use a different RP for each and every one. The RPs are designed to only intercept light corresponding to one QW mode at a given step, as we show in Fig. 2.6.
We consider the case of Fig. 2.7, where yellow circles indicate the actual presence of a RP intercepting light propagating along the corresponding edge of the BS network. By means of the Moving Mirrors we can collect the output of any mode we wish at any step. In order to correctly set the phase shift of a specific MZI, we need to observe in the output the interference effect corresponding to the desired MZI only. We can do this through a set of Path Selectors (PS), that can mechanically block single edges of the network, i.e. specific photon trajectories at any step, allowing the photon to propagate

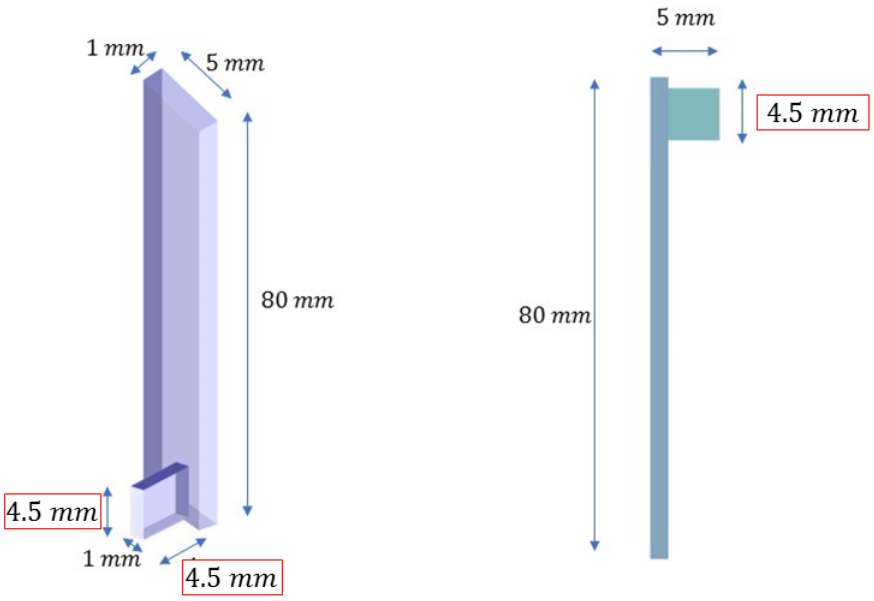

Figure 2.6: Sketch of the rotating glass plates used in the actual setup. *The glass plates naturally add a phase shift to travelling light, with respect to a path through air, due to the difference in refractive index. By mounting these plates on suitable rotating supports, it is possible to increase the distance travelled by light through glass, hence tuning the phase shifting. In order to realize this effect individually on each different mode, in a space and time wise fashion, the size of the device has to be accurately tailored. Values of relevant geometrical parameters are reported.*

only through the MZ under tuning. In this way, it is possible to observe the interference effect at the output of each MZ in Fig. 2.7, setting the $\{0, \pi\}$ phases according to the disorder configuration. It is worth noting that, as visible in Fig. 2.7, the phases of adjacent MZs are correlated, thus the phases have to be set step-wisely, considering earlier MZIs first.
The operation of positioning of the RPs and that of phase tuning are performed by means of a laser with the same wavelenght of the single photons exploited for the measurements; in fact the phase imposed on the radiation by the plates only depends on its wavelenght and we may expect the effect to be the same on single photons. The same procedure can be employed also in the preparation stage of two photon experiments.

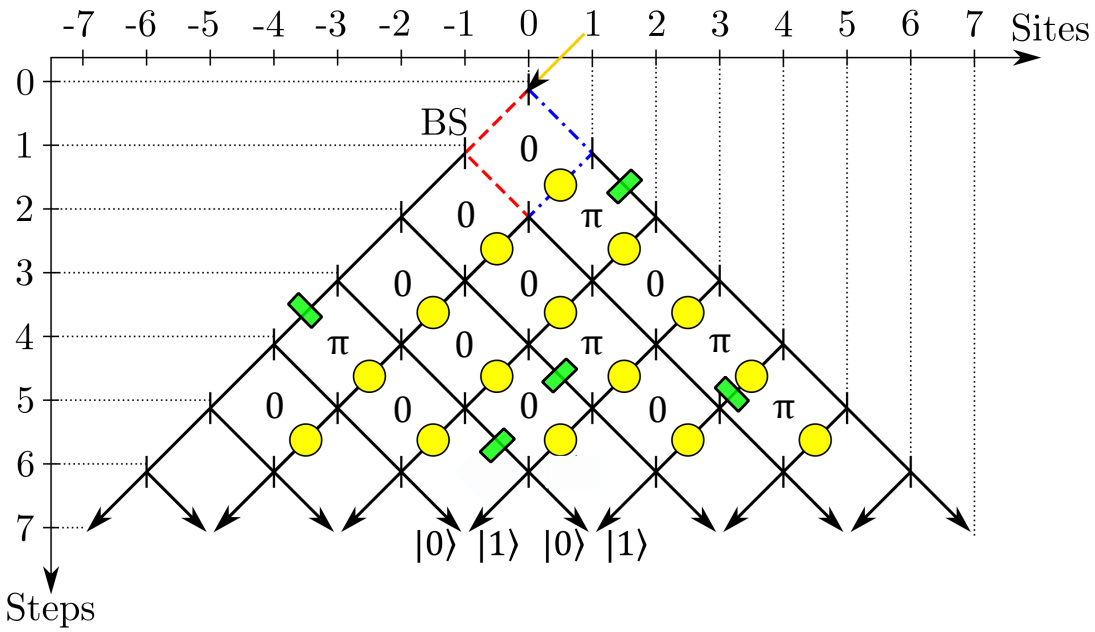

Figure 2.7: An example of phase map on the one-dimensional quantum walk (QW) realized by the setup. *Yellow circles represent the presence of a rotating glass plate, one for each individual MZI of the network. Green boxes highlight the modes where a π phase has been randomly extracted. The phase differences of each Mach-Zehnder, corresponding to the given phase map, are explicitly shown and actually implemented by the glass plates. It is worth noting that an even number of π phases within a Mach-Zehnder gives raise to a total phase difference* 0.

2.3 Experimental investigation of subdiffusive propagation regime in quantum walks

In [110], the experimental setup described above was used to demonstrate the transition from a ballistic to a diffusive propagation behavior in a single and two-particle one-dimensional discrete Quantum Walk, driven by the insertion of p-diluted disorder in the system. In particular, a phenomenon analogous to a phase transition as a function of the parameter p was observed. These results inspired further analysis and investigation: indeed, as we reported in Sec. 1.4, Quantum Walks are susceptible to a localization phenomenon similar to the so-called Anderson localization [87] even in their photonic implementations [91]. We have already mentioned the plethora of experimental demonstrations following this discovery in the corresponding Subsection. Nonetheless, as well as an experimental demonstration of an intermediate regime between ballistic and normal diffusion was missing, an exploration of the propagation behavior comprised between normal diffusion and localization had never been tackled, nor its very existence and actual feasibility had ever been demonstrated.

In this section, we report on our collaboration with the University of Paderborn that led to the experimental demonstration of the conceptual idea that p-diluted disorder can generate a subdiffusive spreading regime in a QW, at least for the accessible number of evolution steps [111]. In this case, the experimental setup is a highly flexible time-multiplexing platform [83, 120, 121] that acts like a simulator of subdiffusive processes. The results we review in the following demonstrate the possibility to realize any transient sublinear propagation regime ranging from statically disordered QWs, to completely disordered ones, by controlling disorder in the spatial degree of freedom (that

here is represented by time bins) and in time (that is the number of evolution steps).

2.3.1 Theoretical model

We use a very general model for transport processes to formalize our framework. Such broadly applicable model can be formulated in terms of the partial differential equation

$$0 = \partial_t P(x,t) + \mathcal{L}P(x,t), \tag{2.2}$$

where $P(x,t)$ represents a space-time dependent probability distribution and $\mathcal{L}$ is a potentially time-dependent differential operator in the spatial degree of freedom x. For a large family of randomized media, the asymptotic solution for large times t reads

$$P(x,t) \propto \exp\left(-\left|\frac{ax}{\sigma(t)}\right|^b\right), \tag{2.3}$$

where b describes the type of the exponential decay and a is a scaling factor. Furthermore, $\sigma(t)$ is the standard deviation with the characteristic power law behavior,

$$\sigma(t) = ct^d, \tag{2.4}$$

where $2d$ determines the spread of the variance over time and c is another scaling factor; see Ref. [122] for a thorough derivation of this model. We apply this model here as an heuristic approach to interpret the experimental data. For example, for $b = 2$ and $2d = 1$, we get from the rigorous model a Gaussian distribution in space with a linear increase of the variance, while the parameters $b = 1$ and $2d = 0$ result in Anderson-like localization as a consequence of the static disorder. Here, we aim at exploring the theoretically predicted intermediate regime, $1 < b < 2$, with a subdiffusive behavior, $0 < d < 1/2$.

We have mentioned how discrete QWs can simulate certain diffusion regimes, such as superdiffusive power laws [110]. We wish to study general anomalous diffusion in QWs, so we model different anomalous diffusion regimes with a corresponding mixture of static and dynamic disorder in the choice of a space-time dependent coin. In particular, the degree of dynamic disorder will be mapped into a parameter p, according to the p-diluted model of Sec. 2.1. First of all, we consider a coin operator which is inhomogeneuous in space, but static in time, $\hat{C}(x,t) = \hat{C}(x)$, leading to Anderson-like localization ($b = 1$), which is a static effect ($2d = 0$). Now, this static disorder can be perturbed by the p-diluted model to approximate the differential operators $\mathcal{L}$ in Eq. (2.2) for different physical scenarios. This perturbation consists of the independent and random choice of time-dependent coin configurations according to the percentage of dynamic disorder p,

$$\hat{C}(x,t) = \begin{cases} \hat{C}(x,t) & \text{with probability } p, \\ \hat{C}(x) & \text{with probability } 1-p, \end{cases} \tag{2.5}$$

so that an inhomogeneity in time is introduced, too. Specifically, $p = 0$ yields Anderson-like localization ($b = 1$ and $2d = 0$), and $p = 1$ results in a completely disordered QW ($b = 2$ and $2d = 1$). Most importantly, the region $0 < p < 1$ should theoretically enable us to control our QW in such a way that it explores the full intermediate range of exponential spatial decays, $1 < b < 2$ in

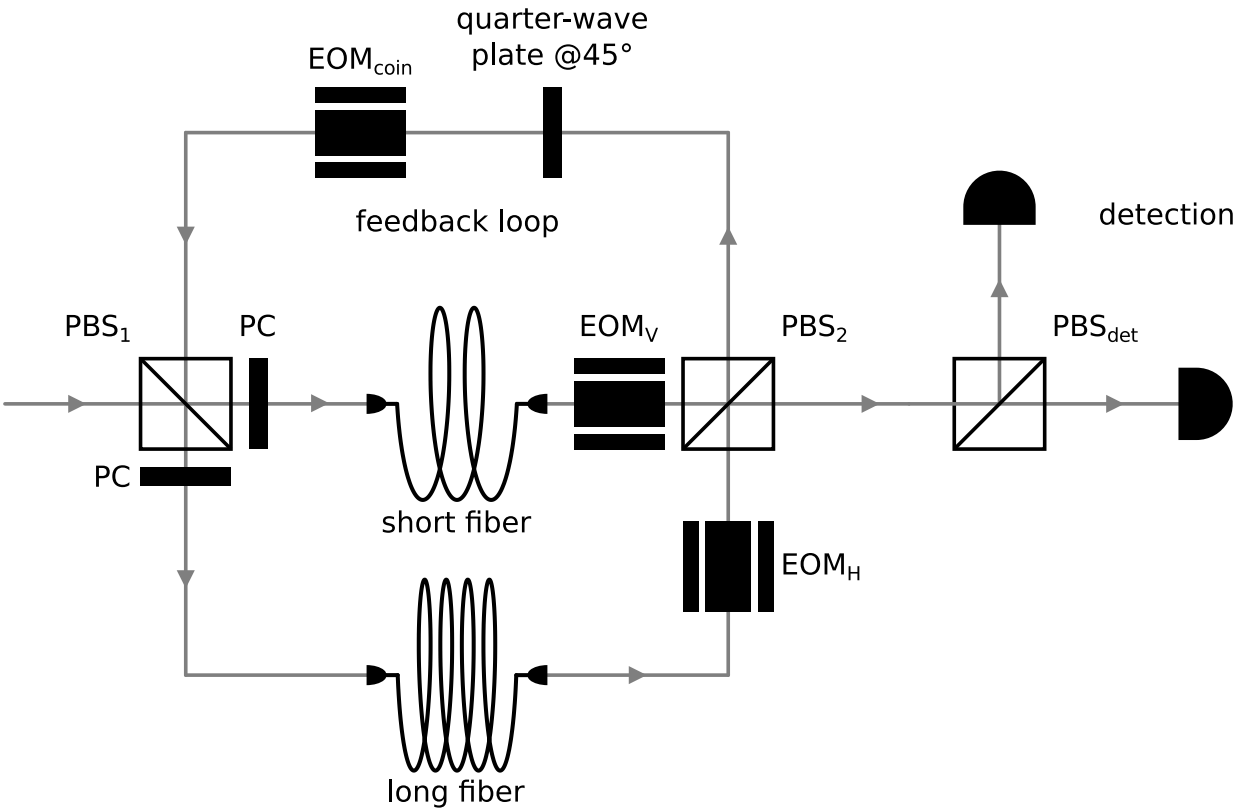

Figure 2.8: Sketch of the experimental setup. *The optical components depicted are polarization controllers (PCs), polarizing beam splitters (PBSs), and electro-optical modulators (EOMs). The PC allows to precisely compensate the polarization rotation caused by propagation through the fibers, while the required polarization-resolving detection is achieved by splitting the output of the loop with PBS_{det} followed by one detector for each polarization. Figure taken from [111].*

Eq. (2.3), with sublinear temporal spreads, $0 < 2d < 1$ in Eq. (2.4). It is important to mention that such p-diluted strategy applies to the transient regime of a limited step number in experiments and it is not confirmed for the rigorous asymptotic behavior, which may tend to saturate in a diffusive long-term propagation.

2.3.2 Experimental implementation

In order to implement this transient subdiffusion regime in a Quantum Walk, a well-established time-multiplexing scheme was employed, based on an unbalanced Mach-Zehnder interferometer with a feedback loop [83, 120, 121]; see Fig. 2.8. This platform, realized at the University of Paderborn, provides high resource efficiency, long-lasting stability, and homogeneity, which we exploit for the realization of QWs over a sufficiently large number of steps that is mandatory to clearly distinguishing signatures of subdiffusive behavior. In particular, the setup described in Sec. 2.2 couldn't have been employed for this study, because the finite size of the optical elements and the unavoidable losses crucially limit the number of evolution steps that can be achieved by a QW implemented via that platform.

In the scheme in Fig. 2.8, the QW sites are encoded in different time bins occupied by a weak coherent laser pulse at the single-photon level (central wavelength 1 550 nm, pulse width 1 ps, and repetition rate 4 kHz). This pulse acts as the walker while the coin information is embedded in its

polarization, $|H\rangle = |0\rangle$ or $|V\rangle = |1\rangle$. The QW evolution starts when the pulse impinges on the top port of PBS_1 for the first time. The initial position of the quantum walker is $x = 0$ with horizontal polarization, so that the initial state is globally $|\psi(0)\rangle = |0\rangle \otimes |0\rangle$.

The setup realizes an unbalanced interferometers with a well-defined time delay between the polarizations ($105ns$), realizing the shift operation $\hat{S}$ in the temporal degree of freedom. This includes polarization dependent splitting at PBS_1, propagation of horizontal and vertical polarization through long (~ 473 m) and short (~ 453 m) fibers, respectively, and the coherent recombination of the two paths at PBS_2 to introduce the delay between the two polarizations. The interferometer is closed with a free-space feedback loop that redirects the light back to PBS_1 for the next evolution step, corresponding to another trip through the MZI.

We harnessed a position- and step-dependent coin operation in order to apply p-diluted disorder to the evolution and realize subdiffusive dynamics. To this aim, a fast-switching Electro Optical Modulator (EOM) was employed in the feedback loop for a dynamical coin control via polarization rotations without introducing further significant losses. The two fast-switching EOMs, EOM_H and EOM_V, enable redirection of the pulses either back to the feedback loop or to detection, granting the ability to measure the output probability of the QW at any evolution step. This active polarization control makes deterministic in- and out-coupling easier to achieve, so that it is possible to effectively realize large evolution steps for a single particle QW. The detection unit allows for polarization-resolved photon counting at individual time bins, using PBS_{det} and high-efficiency ($> 90\%$) superconducting nanowire single-photon detectors with a dead time of ~ 100 ns, from which we can extract the output QW probability distributions.

The setup described above is designed to have a step separation of ~ 2.3 μs and site (time bin) separation of ~ 105 ns and, in principle, can be employed for the implementation of single particle QWs up to 36 steps by allowing time-bin interlacing for successive steps [121]. In the experiment reported in this section, we limited the investigation to 20 steps, which is enough to unambiguously discern transient subdiffusive dynamics, while minimizing the uncertainties deriving from interlacing between different time steps.

2.3.3 Experimental results

We wish to observe the transient subdiffusive regime of a disordered QW by analyzing the walker's behavior as a function of the disorder level. Given the disorder level p, there are several possible global coin configurations which can be generated by local random choices of the coin, as by Eq. (2.5). We refer to these configurations as *coin maps*, in analogy with the phase maps of the original p-diluted model. We experimentally implemented 400 coin maps for each disorder scenario under study $p \in \{0.0, 0.1, 0.2, 0.3, 0.5, 1.0\}$ and we averaged the output distributions $P(x, t)$ over all the disorder realization for each p. The resulting average probability distribution was measured for step numbers $t \in \{5, 8, 11, 14, 17, 20\}$. The total 2400 coin maps were generated by randomly creating initially static disordered coin configurations; this was achieved by randomly picking one coin value from three possible ones independently for each site of the line and setting the resulting static disorder patterns as the 2400 initial random configurations. This is a crucial difference with the original p-diluted model: there are three possible values for the disordering parameter, rather than two. The coin maps were then divided into six sets, each composed of 400 coin maps, and a different disorder level was imposed on each subset. Practically, the coin value at each position and time was changed

to another one, with a probability equal to p, in a p-diluted fashion. The new coin values were chosen with uniform probability among the remaining two. The result is a set of 400 different coin maps featuring the same average disorder level p, for each of the chosen ps. Since the initial static disorder is randomly implemented for each coin map, the final results do not depend on a particular static configuration but only on the disorder level p. Thus, we experimentally implemented such disorder configurations, measuring the output probability distributions. The resulting data allow to analyze both the spatial features of the average $P(x,t)$, following a certain exponential behavior with $1 < b < 2$ and the time-wise spreading pattern, crucial to certify anomalous diffusion, featuring $0 < 2d < 1$.

Spatial characterization

For a fixed step number t, and for $p = 0$, we expect the output probability distribution of light to be exponentially localized, as a consequence of an Anderson-like localization effect [27, 91]. By increasing disorder level p, we disrupt the static pattern of disorder, thus we expect a broadening of the distribution. Eventually, for $p = 1$, we expect the system to reach a diffusive propagation regime, showing a Gaussian spatial distribution typical of a classical random walk propagation. It is convenient to work with a modified expression of Eq. (2.3),

$$\ln(P) = \left(-\left|\frac{a}{\sigma}\right|^b\right)|x|^b - \ln\left(\sum_x e^{-|ax/\sigma|^b}\right), \tag{2.6}$$

in order to better represent the collected experimental data, after they have been analyzed by a non-linear fit. Measurements outcomes corresponding to $t = 20$ steps for different amounts of disorder are reported in the left column of Fig. 2.9. In the top-left plot, dots correspond to experimental average probability distributions. Dotted lines represent theoretical probability distributions, obtained from a numerical simulation. Experimental and theoretical distributions show a very good agreement, featuring similarities above 99%, even without considering unavoidable experimental imperfections in the simulation parameters.

The bottom-left picture in Fig. 2.9 shows data (dots) together with the fitted curves (dashed lines) according to Eq. (2.6), demonstrating the transition from a linear ($b \approx 1$) to a parabolic ($b \approx 2$) decay in this logarithmic depiction. Therefore, the presence of higher disorder p diminishes the probability to find the walker in the starting position $x = 0$ for $t > 0$, hindering the localization effect. As a consequence, the probability distributions broadens. It is worth noting that other imperfections may lead to an even broader range of parameters, such as $b > 2$ [109].

2.3.4 Temporal characterization

The second trait we focused our analysis on is the spatial distribution variance behavior as a function of the step number t, for different disorder levels. It is convenient again to use a logarithmic form of Eq. (2.4) to represent the data:

$$\ln(\sigma^2) = 2d\ln(t) + \ln(c^2), \tag{2.7}$$

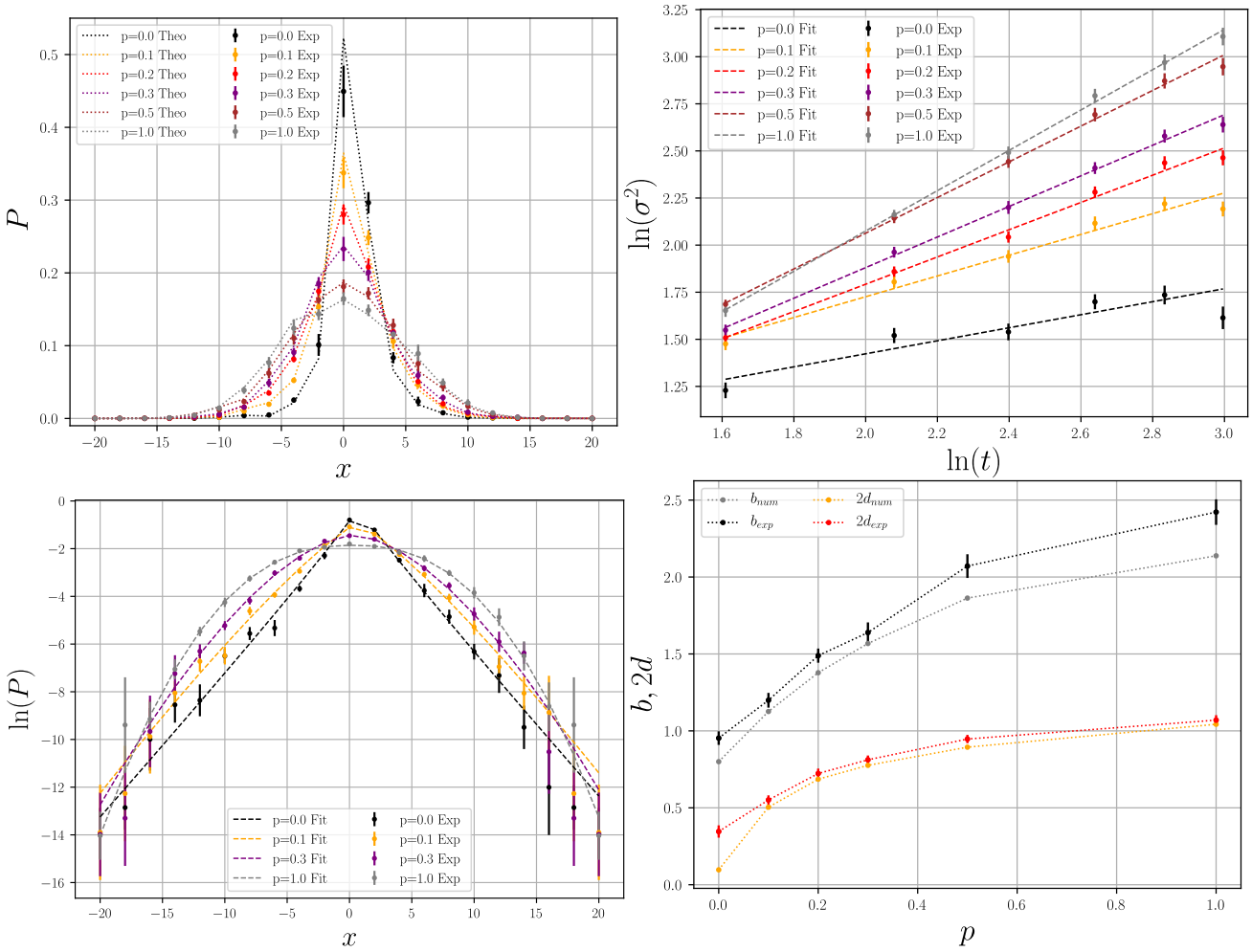

Figure 2.9: Experimental results for space and time behavior. *Top-left: Probability distribution P for a range of disorder values p. Experimental data (dots) agree within the uncertainties with the theoretical results (dotted lines). Error bars account for Poissonian statistics of the detection process and experimental imperfections of the setup. Bottom-left: Logarithm of the experimental probability distribution (dots) together with fitted function (dashed lines) according to Eq.* (2.6)*. We only show part of the analyzed p values to maintain clarity. Top-right: Logarithm of the variance as a function of the logarithm of the step number t for various disorder levels p. Dots correspond to experimental data and dashed lines represent the fitting functions according to Eq.* (2.7)*. The growth trend featuring slopes between zero and one in this doubly logarithmic graph for each value of p demonstrates an excellent agreement with the predicted subdiffusive behavior of the evolution. Bottom-right: Values of the exponents for the spatial (b) and temporal ($2d$) characteristics, obtained by fitting the theoretical predictions of Eqs.* (2.6) *and* (2.7) *to the measured data in bottom-left and top-right plots. Figures are borrowed from [111].*

in order to assess the presence of subdiffusive spreading. Results are reported in the top-right plot of Fig. 2.9 on a logarithmic scale for both axes. Dashed lines correspond to the curve in Eq. (2.7) which is fitted to the data (dots) for different p values. The transient subdiffusive propagation of the QW evolution is confirmed by the linear trends with slopes $0 \lesssim 2d \lesssim 1$ (see bottom-right depiction in Fig. 2.9 for the values). For $p = 0$, we would expect localization, hence a constant value of variance, corresponding to an absence of spreading in time. Indeed, this effect shall be considered as an asymptotic limit, which can be approached by enormously increasing the evolution time of the system. This is the reason for us denoting the phenomena we observe as corresponding to a transient regime. As in the previous spatial analysis, error bars on the experimental data have been computed considering a Poissonian statistic of counting as well as experimental imperfections. Beyond earlier studies, we analyzed both the spatial and temporal impact of the amount of disorder p. Our results confirm that such an approach enables the simulation of almost any subdiffusive behaviors, within the harmless restriction of a finite number of steps in experiments. Thus, the transient sublinear spread over time and the characteristic shapes of the spatial distributions that we were able to measure indicate that the interplay between a static disorder and completely random disorder, freely controlled and interpolated via p, can provide an accessible method to reproduce complex subdiffusion phenomena, modeled by the very general framework of discrete QWs.

2.3.5 Conclusion

The work we reviewed in this section was conceived as an additional tile on the path towards the implementation of a universal quantum simulator. We reported on the experimental demonstration of the capability of simulating a well-resolved range of subdiffusive propagation behaviors via disordered QWs. Indeed, the system was driven from Anderson-like localization to Gaussian distribution in a controllable fashion, and, at the same time, an exploration of the sublinear regime for a QW was performed for the first time. These results complete earlier investigations about superlinear propagation in QWs [110], providing with an experimental platform which can implement any regime from localized to ballistic.

Earlier works implied the possibility of subdiffusive dynamics in QWs by considering the presence of non-linearities in the coin operator [123, 124], an approach that requires high complexity and low efficiency as far as experimental demonstration is concerned [125], in addition to a complicated theoretical description. In contrast, we were able to realize subdiffusive QWs in a significantly more accessible manner, providing an efficient tool for the investigation of anomalous diffusion, as long as asymptotic limits are not considered. This was possible through a crossover between two disorder models: a static one, leading to Anderson-like localization, and a dynamical one, inducing diffusion. Thus, we were able to encode in a single parameter p a continuous transition from one model to the other, sweeping the entirety of the subdiffusive region.

This study exceeded a proof-of-principle experiment, providing a platform that could simulate a wide range of propagation phenomena, possibly for two walkers, as already demonstrated for the superdiffusive regime [110], by means of the very same setup [126].

The p-diluted disorder approach and the experimental platform we discussed in this section grant the ability to reproduce different spreading behaviours in a single, stable, and completely reconfigurable setup, which may foster further understanding of properties of quantum particles propagating in even more complex environments.

Personal contribution

I implemented the preliminary numerical simulations necessary to understand the feasibility of the subdiffusive QW transition and the experimental requirements for the actual realization of a visible subdiffusive transition.

2.4 Quantum metrology approach to anomalous diffusion

In the previous sections, we have reviewed a high number of studies about transport features in a QW. Quantum walks have only recently started being also explored in the context of quantum metrology [127], although some QW-like architectures, inspired by boson sampling, have been exploited to experimentally address the problem of multiphase estimation [128–130]. Indeed, the connection between QWs and quantum metrology is not straightforward, until we consider, for example, the p-diluted QW model: a network featuring a certain set of phases, that is explored by propagating quantum objects. In [112], we investigated the possibility of gathering information about the features of a QW network by the analysis of the quantum walker behavior. In particular, we were able to connect the Quantum Fisher Information (QFI),which quantifies the extractable information about an unknown parameter such as a phase ϕ, to the transport regime of a QW undergoing an evolution characterized by the parameter ϕ. This theoretical study revealed that disorder plays a significant role in the spreading behaviour of quantum information. In the following, we report on this work, showing that the step-wise trend of QFI allows one to recognize the disorder pattern imposed on the walker.

2.4.1 Quantum metrology

In this section we will review some basic concepts regarding Quantum Metrology (QM), in order to improve the readability of this section. The main reference we employ is the review from Polino et al. [131], because of the "photonic" framework we maintain throughout the following discussion.
The ability to precisely measure a physical quantity is of fundamental relevance, for instance in order to precisely test the predictions of a theory. Along with the measured value of a quantity, an uncertainty has to be provided, summarizing both the technical and fundamental errors. The first type of error mostly consists in accidental errors, due to imperfect control in the measurement process. The second type of error is of a different nature: it is the consequence of physical laws. Quantum mechanics provides an ultimate bound for the maximum achievable precision in the estimation of a physical quantity.
Metrology aims at developing the optimal protocol to measure an unknown physical parameter ϕ, characterizing a physical system, by means of an interaction between a probe and the system itself, after which the information is encoded in the probe state. In the quantum case, the probe is set to be a quantum object, provided with quantum features. Quantum metrology is meant to develop ways to enhance the accuracy of measurements by exploiting genuine quantum traits of the probe. The general scheme of a measurement process can be outlined as

- preparation of the probe state $\hat{\rho}_0$, which must be sensitive to variations of the parameter ϕ;
- interaction between the probe and the system through the unitary evolution $\hat{U}_\phi$ as $\hat{\rho}_\phi = \hat{U}_\phi \hat{\rho}_0 \hat{U}_\phi^\dagger$;
- extraction of information about ϕ by means of suitable operators acting on the probe;

- computation of a suitable estimator which provides an estimation $\Phi(x)$ of the unknown parameter ϕ based on the measurement result x.

Such a protocol has to be repeated M times in order to obtain a more and more accurate estimation of the value ϕ. An estimator Φ can have different properties, which determine its quality. An estimator can be:

- **consistent**: the estimator asymptotically converges to the actual value of the parameter
- **unbiased**: the estimator's mean value corresponds to the unknown parameter, i.e.

$$\langle \Phi \rangle = \sum_x P(x|\phi)\Phi(x) = \phi, \tag{2.8}$$

  where $P(x|\phi)$ is the output probability of obtaining a certain measurement result x, conditioned to a certain value of the parameter ϕ.

Accuracy of the measurement cam be evaluated in terms of the mean square error (MSE), defined as

$$\mathrm{MSE}(\phi) = \sum_x (\Phi(x) - \phi)^2 P(x|\phi) \tag{2.9}$$

which, for an unbiased estimator, yields an estimate of the variance of the parameter

$$\Delta\phi^2 = \sum_x (\Phi(x) - \bar{\Phi})^2 P(x|\phi). \tag{2.10}$$

Optimization of a measurement protocol can be pursued through different paths, aiming at increasing the accuracy of parameter estimation; the choice of estimator can be optimized, as well as the measurements performed on the probe or the initial state of the probe. We consider a fixed probe state and fixed measurement set; in order to optimize over the estimator choice, we define Fisher information (FI) as

$$F(\phi) = \sum_x P(x|\phi) \left(\frac{\partial \log(P(x|\phi))}{\partial \phi} \right)^2 = \sum_x \frac{1}{P(x|\phi)} \left(\frac{\partial P(x|\phi)}{\partial \phi} \right)^2 \tag{2.11}$$

FI quantifies the amount of information encoded in the output probabilities of the estimation protocol. We also introduce the symmetric logarithm derivative (SLD) $\hat{L}_\phi$ defined by the relation:

$$F(\phi) = \frac{\partial \hat{\rho}_\phi}{\partial \phi} = \frac{\hat{\rho}_\phi \hat{L}_\phi + \hat{L}_\phi \hat{\rho}_\phi}{2} \tag{2.12}$$

It is possible to rewrite FI as a function of the SLD:

$$F(\phi) = \sum_{x=1}^{M} \frac{\mathrm{Re}[\mathrm{Tr}[\hat{\rho}_\phi \hat{E}_x \hat{L}_\phi]]}{\mathrm{Tr}[\hat{\rho}_\phi \hat{E}_x]} \tag{2.13}$$

where $\hat{E}_x$ is an element of the chosen M measurements set $\{E_x\}_{x=1}^N$
The sensitivity of $F(\phi)$ to variations of the parameter ϕ is based on the dependence of $F(\phi)$ on

the derivative with respect to ϕ. Such dependence is framed by the Cramer Rao Bound (CRB), an inequality establishing the ultimate bound on precision achievable by any estimator, with fixed probes and measurements

$$\Delta\Phi^2 = \sum_x (\Phi(x) - \bar{\Phi})^2 P(x|\phi) \geq \frac{\partial\bar{\Phi}/\partial\phi}{MF(\phi)} \tag{2.14}$$

which, in the case of a local unbiased estimator ($\partial\bar{\Phi}/\partial\phi = 1$) becomes

$$\Delta\phi^2 \geq \frac{1}{MF(\phi)}. \tag{2.15}$$

This bound has been computed as the result of an optimization over the estimator choice, so that it can be overcome by optimizing the Fisher Information over the possible measurements performed on the probe after the interaction with the system. Indeed, we define as Quantum Fisher information (QFI) the maximum value of FI over any choice of measurements $\{\hat{E}_x\}_{x=1}^M$:

$$F_Q(\phi) = max_{\{\hat{E}_x\}_{x=1}^M} F(\phi). \tag{2.16}$$

By definition, $F_Q(\hat{\rho}_\phi) \geq F(\phi)$ and the CRB can be extended to a *quantum* CRB. The new bound for the maximum achievable accuracy holds:

$$\Delta\phi^2 \geq \frac{1}{MF(\phi)} \geq \frac{1}{MF_Q(\phi)}. \tag{2.17}$$

The right hand side of this equation represents the ultimate limit on the achievable precision value regardless of the measurement,although it depends on the particular choice of initial probe state $\hat{\rho}_0$.
QFI can be demonstrated to be associated with the symmetric logarithmic derivative $\hat{L}_\phi$ by the following relation:

$$F_Q(\phi) = Tr[\hat{\rho}_\phi \hat{L}_\phi^2]. \tag{2.18}$$

Maximization of QFI over any possible input probe state shall yield the ultimate bound for maximum achievable estimation accuracy. We consider n independent and at most classically correlated states. We get the so called Standard Quantum Limit (SQL):

$$\Delta\phi \geq \frac{1}{\sqrt{MnF_Q^{\max}}}$$

where $F_Q^{\max}$ is the maximum F_Q over the n states. If we allow the input states to share quantum correlations, such as entanglement, it is possible to further overcome this bound, leaving the Heisenberg limit as the only boundary to measurement accuracy. The Heisenberg limit is directly derived by Heisenberg's uncertainty principle and corresponds to a linear decrease in function of the amount of measurements $\Delta\phi \propto \frac{1}{M}$.

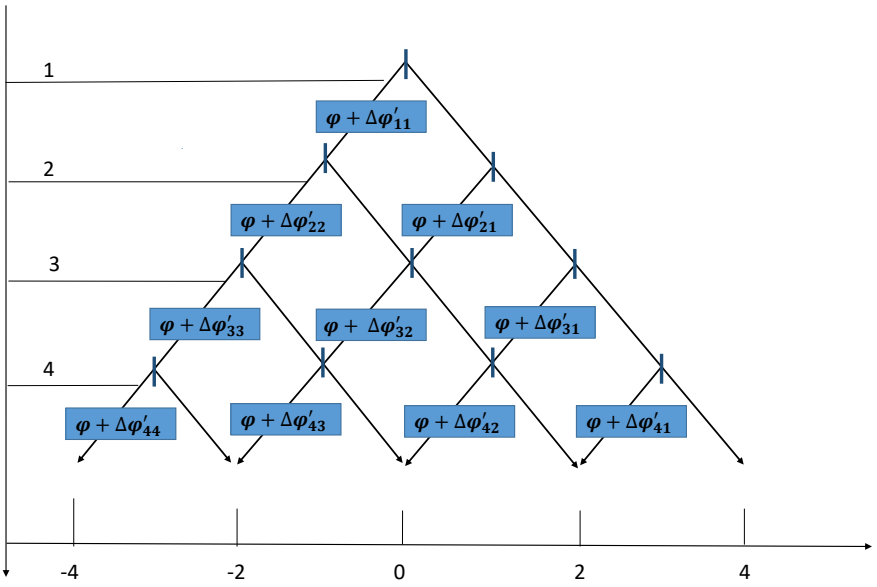

Figure 2.10: Representation of a quantum probing protocol using disordered quantum walk representation. *The parameter ϕ that we wish to estimate can be in principle affected by random noise, completely inhomogeneous in time and space. This picture is taken from [112].*

2.4.2 Theoretical proposal

We design a protocol in which a quantum walker acts as the probe and we observe how extractable information spreads through the corresponding QW network, analyzing the propagation behavior of the walker from a quantum estimation point of view.

A quantum estimation strategy aims at providing an estimate of the maximum extractable information about an unknown parameter ϕ through a set of repeated measurements on a probe state interacting with the system characterized by ϕ. In general, the interaction is formalized by a unitary operator featuring the parameter ϕ. In the present case of study, ϕ is encoded in the QW evolution through the global unitary operator of the QW evolution $\hat{U}(\phi) = \hat{S}(\hat{I} \otimes \hat{C})\hat{P}$, where $\hat{P}(t)$ is a phase-shift operator:

$$\hat{P}(t) = \sum_x |x\rangle \langle x| \otimes \left(|1\rangle_c \langle 1|_c + e^{i(\phi + \Delta\phi'(t,x))} |0\rangle_c \langle 0|_c \right). \tag{2.19}$$

As shown in Fig. 2.10, the phase-shift operator $\hat{P}$ produces a phase difference ϕ between the two different coin states $|1\rangle_c$ and $|0\rangle_c$ for any position. In particular, here we are interested in the condition in which the application of ϕ might come with unwanted time-position-dependent fluctuations $\Delta\phi'(t,x)$ that coherently affect the accuracy of encoding of the phase shift ϕ. Thus, our probing quantum walker will travel the QW network characterized by the phase ϕ, but the estimation process may be hindered by disorder, which may follow various patterns.
In a quantum metrology scenario, the measurement sensitivity of the parameter is given by the Cramér-Rao inequality $\Delta\phi \geq \Delta\phi_{min} = 1/\sqrt{MF_Q(\phi)}$ where $\Delta\phi$ is the mean square error in the measure of parameter ϕ and M is the number of measurements [40, 132–135]. The QFI is given by $F_Q(\phi) = Tr[\hat{L}^2\hat{\rho}]$, where, as we stated above, $\hat{\rho}$ and $\hat{L}$ satisfy the equation $d\hat{\rho}/d\phi = \{\hat{L}, \hat{\rho}\}/2$ and $\{.,.\}$ denotes the anticommutator. For a pure state, the corresponding density operator $\hat{\rho}$ is a projector, hence $\hat{\rho}^2 = \hat{\rho}$ holds and the SLD operator reduces to $\hat{L} = 2d\hat{\rho}/d\phi$. QFI can be computed

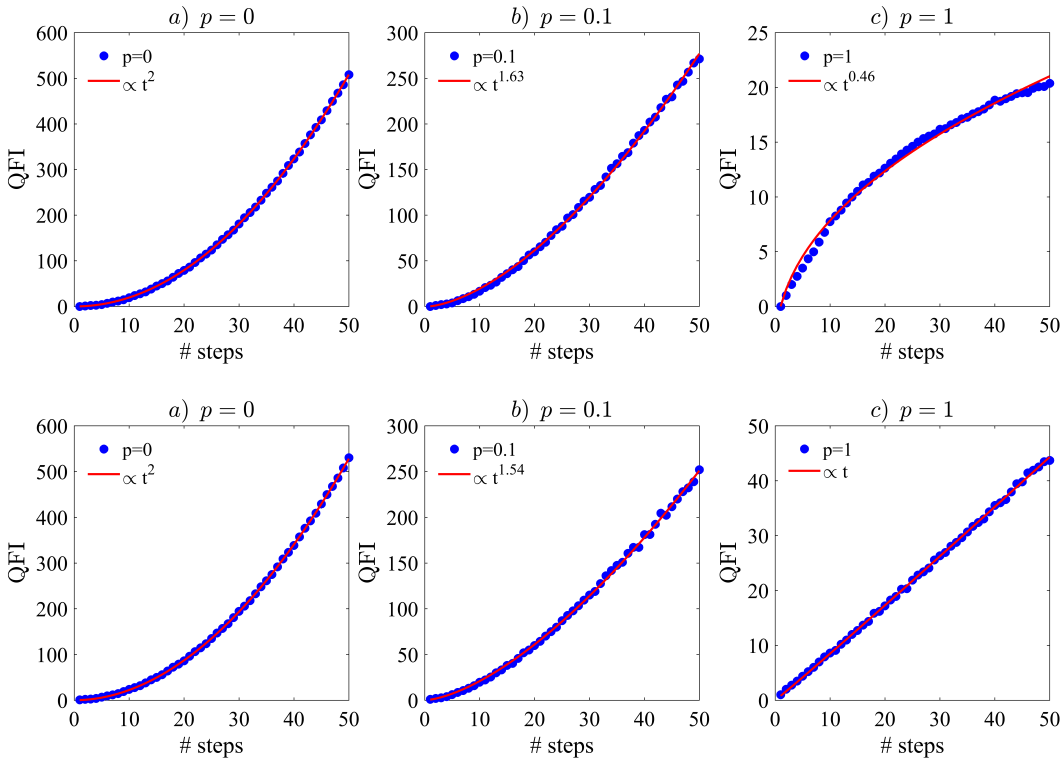

Figure 2.11: Quantum Fisher information trends for different disorder patterns. *Average QFI F_Q of a quantum walker (blue dots) as a function of the number of steps t for different values of disorder.* ***a)*** *$p = 0$,* ***b)*** *$p = 0.1$ and* ***c)*** *$p = 1$ for both static (**top**) and dynamic disorder (**bottom**). For each picture. we choose as the initial input the state $|\psi_0\rangle = |0\rangle_p \otimes |0\rangle$. Red lines correspond to a fitted curve $F \propto t^\alpha$. Figures borrowed from [112].*

numerically from the walker state at step t: $|\Psi_t\rangle = \hat{U}(\phi)\,|\Psi_{t-1}\rangle$. The derivative with respect to the parameter ϕ reads:

$$\left|\frac{\partial \psi_t}{\partial \phi}\right\rangle_t = \frac{\partial \hat{U}(\phi)}{\partial \phi}\,|\psi\rangle_{t-1} + \hat{U}(\phi)\left|\frac{\partial \psi_{t-1}}{\partial \phi}\right\rangle. \tag{2.20}$$

In the framework depicted in Fig. 2.10, we may expect the protocol to be more effective as we measure the probe at a later step: indeed, the probe interacts coherently with the parameter unitary a larger number of times as we let it evolve through the network for a longer time, hence collecting, in principle, more information. We are interested, in particular, to analyze how the QFI behaves when the ϕ parameter is affected by some random fluctuations. We focus our analysis on a p-diluted disorder scenario: random fluctuations $\Delta\phi'(t, x)$ can only be 0 or π and the degree of disorder p is on average the percentage of random phases that the walker finds throughout its propagation. These phases are also randomly distributed in time and position, as they are generated according to a p-diluted framework.

We used p-diluted to increase disorder from an ordered configuration as well as to scramble static disorder configurations, in order to investigate the disorder regime employed for the experiment discussed in Sec. 2.3. We slightly change here the generation of such disorder configurations: we do not scramble with time-position disorder an already statically disordered QW, but rather we apply static disorder with a certain probability p, so that the system becomes statically disordered

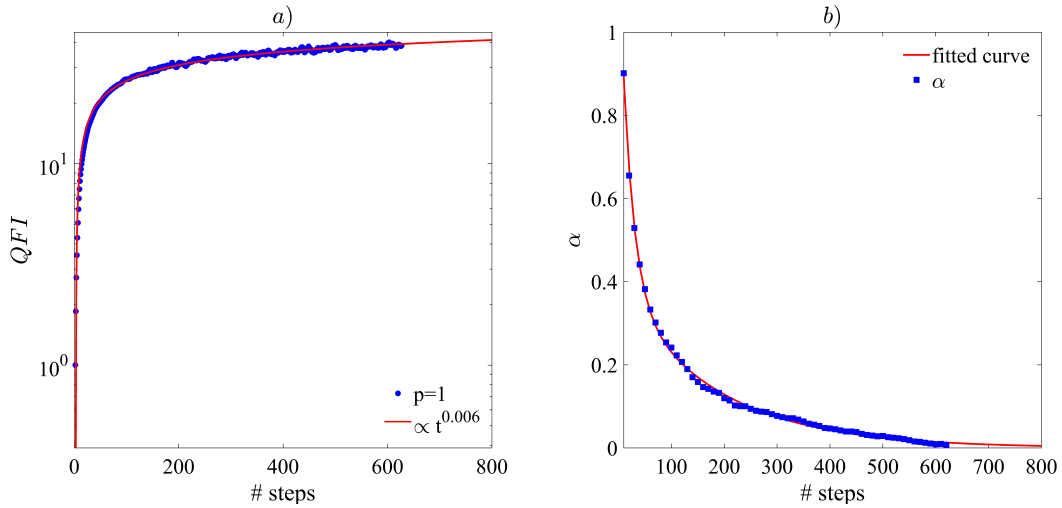

Figure 2.12: Quantum Fisher Information trend, logarithmic analysis ***a)*** *Logarithmic scale of the average QFI F_Q trend of a quantum walker (blue dots) in comparison with a fitted curve $F \propto t^{\alpha}$ (red line) in terms of the step number t for complete static disorder, corresponding to $p = 1$.* ***b)*** *Step-dependent coefficient $\alpha(t)$ (blue dots) in comparison with the corresponding theoretical fitted curve (red line) as a function of the step number. The decrease to the asymptotic vale of zero can be straightforwardly deduced. Figures appearing in [112].*

(affected by position-wise only inhomogeneity) with a certain percentage p of perturbed phases, thus deviating by the standard p-diluted model. As a consequence, the perturbations only depend on position, while the disorder pattern repeats in time. If the walker encounters a random fluctuation $\Delta\phi'$ for the first time from site x to $x-1$, it will experience that for any following evolution steps. In conclusion, when $p = 0$ an ordered QW is obtained while when $p = 1$ a completely statically disordered QW is retrieved. Despite the different approach to the the p-diluted technique, also this procedure yields a subdiffusive behavior of the walker. We also investigated the regime of dynamic disorder, which was implemented by the standard p-diluted method. In the following, we deliver the results of an investigation over average behavior of QFI in presence of a certain disorder level p, according to different disorder patterns.

2.4.3 Results

At first, we focus on the case of a quantum probe starting its QW evolution from site $x = 0$ with $|0\rangle_c$ coin state, hence featuring a global initial state $|\psi_0\rangle = |0\rangle \otimes |0\rangle_c$. We simulated the behavior in time of the average QFI regarding the parameter ϕ featured by the walker state, for different values of disorder p, according to either static or dynamic disorder. Simulation has been performed by averaging over 10000 different generated phase maps, analyzing the QW evolution up to the 50th step. The average QFI trends are reported in Fig. 2.11 as a function of the step number t. Numerical average QFI follows a power law with $F_Q \propto t^{\alpha}$, where α depends on p and $0 \leq \alpha \leq 2$ for the static disorder, while $1 \leq \alpha \leq 2$ for the dynamic disorder. In Fig. 2.11 a) we show that the QFI featured by the QW state grows quadratically in time, $F \propto t^2$, in analogy with the ballistic position spreading that we would expect for an ordered QW. In that case, the variance over the position state of the walker grows quadratically in time, as discussed in Sec 1.4 . As a consequence, we find a bound for the variance of the estimated phase value, that is proportional to the inverse of the number of steps, i.e $\Delta\phi \geq O(t^{-1})$.

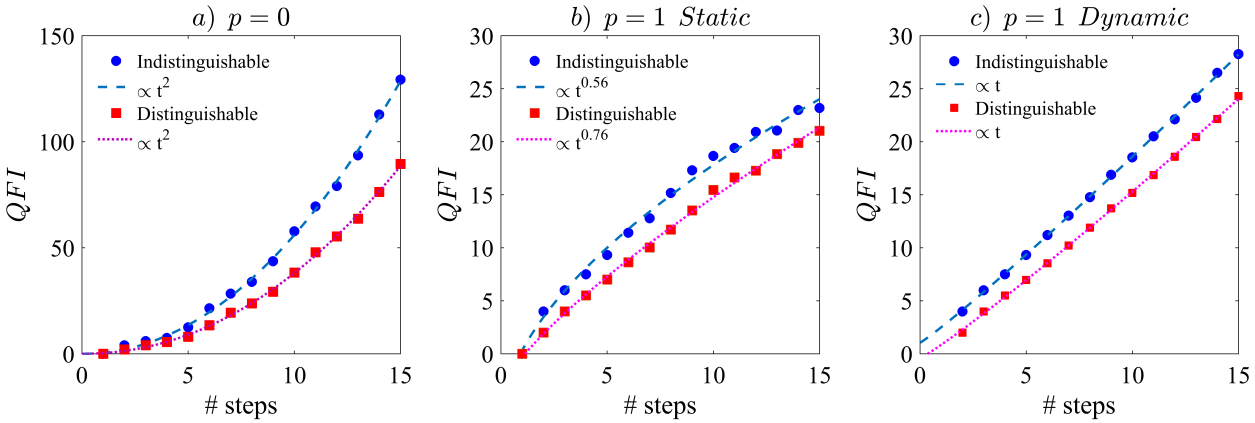

Figure 2.13: Quantum fisher information trends for the two-walkers case. *Average QFI F_Q trend for a pair of quantum walkers as a function of the number of steps t for* ***a)*** *the ordered case $p = 0$,* ***b)*** *complete static disordered case $p = 1$, and* ***c)*** *$p = 1$ complete dynamic disordered case. In the three plots, the blue circles and red squares correspond to indistinguishable and distinguishable two-particle inputs respectively. From these trends we can conclude that extractable information is generally higher for quantum correlated probes. Figure drawn from [112].*

As we insert disorder, a strong change in the QFI growth is noticeable. In the static disorder case (Fig. 2.11 top), a super-diffusive $\alpha > 1$ to sub-diffusive $\alpha < 1$ transition is achieved by increasing the value of disorder p, maintaining a stark analogy with the expected spatial spreading behavior of the quantum walker. The same phenomenon occurs in the case of dynamic disorder, where the average QFI trend turns from ballistic to superdiffusive, and eventually to diffusive (Fig. 2.11 bottom). As a consequence of this result we understand that the information which can be collected along the quantum network depends on the disorder strength: the higher the disorder, the lower the extractable information about the unknown parameter ϕ.

Here, we demonstrate that it is possible to use the QFI to probe the transition from the ballistic spreading regime with $p = 0$ (Fig. 2.11 a)), through the super-diffusive one with $p = 0.1$ (Fig. 2.11 b)) down to the diffusive spread with maximum degree of disorder $p = 1$ (Fig. 2.11 c)), analogous to the case of a classical probe. The presented results indicate that the output information, which is inferred trough measurements performed exclusively on the probe, show a super-diffusive to classical transition, such as the one for the transport pattern. Similarly to the variance of the position operator of the quantum walker [83, 110, 111], QFI provides us with a way to quantify the disorder pattern of the probed system. It is worth mentioning that the probing pattern depends on the number of steps that a walker takes. We consider the static disorder case, where we can see that the QFI growth slows down. In Anderson localization phenomena [87], which occur in statically disordered QWs [27, 91, 111], we have that the walker stops spreading after a reasonable amount of evolution time. Thus, in analogy with that, we would expect the QFI to have some upper bound for the static disorder case: indeed, this is highlighted by the logarithmic plot for 500 steps of the average QFI in Fig. 2.12 a), where the $\alpha(t)$ decreases dramatically with respect to the 50 step case. In conclusion, we may well expect the growth to slow down until average QFI reaches a maximum value. As an additional clarification, we fit QFI with a power function $F \propto t^{\alpha}(t)$, where $\alpha(t)$ is the step-dependent coefficient in a nonlinear fitting process. In Fig. 2.12 b), $\alpha(t)$ is reported in function of the step number of the QW process. We observe how the growth trend depends on the step number t, and how it significantly declines for higher t. This property shows that the walker stops

collecting useful information within the quantum network as an indicator of particle localization. Therefore, there is a well defined upper bound for the $\Delta\phi$ which can be obtained by this probing protocol, for the static disorder case.

Besides the single walker analysis, to enrich the physics of the phenomenon, we consider a probe of two quantum walkers either distinguishable or indistinguishable with initial opposite coin states. In the first case, the state can be written in a separable form in the first quantization formalism as $|\psi_0^s\rangle = |0\rangle_{1p}|\uparrow\rangle_{1c} \otimes |0\rangle_{2p}|\downarrow\rangle_{2c}$, while in the latter case, the state is entangled in coin state $|\psi_0^{\pm}\rangle = |0\rangle_{1p}|0\rangle_{2p} \otimes \left(\frac{1}{\sqrt{2}}(|\uparrow\rangle_{\mathbf{1c}}|\downarrow\rangle_{2c} \pm |\downarrow\rangle_{1c}|\uparrow\rangle_{2c})\right)$. The evolution can be studied by applying the two-particle unitary operator $\hat{U}(\phi) \otimes \hat{U}(\phi)$ to the states above. We plot the average QFI in terms of the step number t in Fig. 2.13 for the ordered case $p = 0$ and the completely disordered one $p = 1$, for both the cases of b) static and c) dynamic disorder. In general, the state of two indistinguishable particles exhibits a higher value of QFI compared to the distinguishable one. This property is explained by the fact that particle indistinguishability is an enriching resource for quantum information distribution within a composite system of identical particles [136, 137]. It is also interesting to note that both input states follow the same growth trend. In the case of ordered case $p = 0$, the increase is ballistic, while for the completely disordered one $p = 1$, the QFI follows a sub-diffusive pattern (Fig. 2.13 b)) or a diffusive one (Fig. 2.13 c)), due to static and dynamic disorder, respectively. It is worth noting that QFI, as a disorder pattern indicator, is independent of the number of quantum walkers, in contrast with the position variance dimension, which grows with the particle number [110].

2.4.4 Conclusion

In this section, we have discussed a quantum probing protocol that exploits QW processes to infer information about defects and perturbations occurring in both quantum and classical networks, such as reported in [112]. We applied quantum metrology techniques to a disordered QW framework, employing QFI to describe extractable information concerning an unknown phase ϕ that the quantum walker collects at each evolution step. Even though the framework is general, we have studied coherent static and dynamic disorder in the QW to describe the efficiency of information collection about the unknown parameter ϕ when it is prone to random fluctuations. We found that different disorder regimes, corresponding to different disorder percentages p in the QW process, lead to different QFI growth patterns in time, including ballistic, superdiffusive, classical, subdiffusive regimes, and Anderson localization, in complete analogy with spreading patterns of quantum walkers in the same disorder conditions. Thus, QFI can act as a spreading pattern indicator, and it is independent of the number of quantum walkers, in contrast with the position variance dimension, which grows according to the particle number [110]. Our results show how a QW can play the role of a readout device of information about the internal features of complex networks. Our results provide a general characterization of disorder level using the quantum probing scheme of QFI bound. Through the platform described in Sec. 2.2, it is possible to experimentally realize a QW evolution featuring the disorder configurations required by the scheme discussed above [110, 118, 119]. Nevertheless, it is challenging to implement an optimal estimation strategy with accuracy associated with QFI bound [135]. The quantum Cramér–Rao bound needs some prior knowledge to adopt a local approach and a large number of experimental observations. Also, the SLD operator itself may not represent

the optimal observable to be measured. One can compute the classical Fisher information (FI) by exploring all possible POVMs for a fixed input state and see if QFI is reached. To saturate the Cramér–Rao bound, one may also try to classically postprocess data using maximum likelihood, which is known to provide an asymptotically efficient estimator [40]. In addition, adaptive methods can be used to reduce the number of measurements [138] as well as machine learning methods [131, 139]. An experimental realization of this quantum probing protocol faces many challenges, but the most challenging one is probably utilizing phase-stable POVMs along multiple paths. Indeed, the experiment also depends on measurement devices featuring low noise and phase stability. In conclusion, the study we discussed in this section intimately links QW dynamics with quantum metrology theory, exploiting the usefulness of quantities as QFI in the analysis of QW dynamics. Due to the increasing interest in studying the spread of information in complex networks, the work we have presented here can be of pivotal importance for further investigations, that could involve a high-dimensional propagation space for the walker, as well as a higher number of walkers.

Personal contribution

I provided insights and expertise regarding QWs behavior and meaningful figures of merit, in addition to physical interpretation of the phenomenon.

Chapter 3

Enhancement of bosonic correlations through disordered Quantum Walks

In Subsec. 1.4.3, we have discussed how disordered QWs travelled by multiple particles feature some differences with respect to the single walker case, such as the possibility of co-localization. However, some open questions remain, such as whether, in the case of disorder patterns other then the static one, any unique effects arise or not. Indeed, an analysis focusing on the spreading behavior does not seem to reveal any [110].
As a matter of fact, single particle Quantum Walks can be effectively simulated by classical light [97] and do not feature genuine quantum effects. Indeed, as in the work reported in Sec. 2.3, a laser pulse can act as the walker, featuring an analogous behavior with respect to an actual single photon. This motivated further investigation, that we illustrate in the following. In this Chapter, we report on the results of our experimental study of bosonic correlations behavior through a disordered QW [119]. We experimentally observed the propagation of two indistinguishable photons (a *biphoton*) in a one-dimensional inhomogeneous Discrete Time Quantum Walk (1D DTQW). By numerical simulation, I found out that initial quantum correlations in the system feature a global and local decrease as the evolution proceeds, for the ordered case, while I was able to identify specific disorder configurations that partially preserve the initial quantum correlation of the biphoton, after some propagation time. The experimental demonstration of this effect was realized through the photonic setup described in Sec. 2.2, which can therefore be considered as an experimental platform capable of enhancing biphoton quantum correlation between two selected modes of the QW, thanks to the imposition of coherent disorder configurations, without any interaction with auxiliary systems or the environment.

3.1 Introduction

In [110], the spreading behavior of two walkers was investigated through the setup described in Sec. 2.2, revealing the possibility of driving a biphoton to superdiffusive propagation. In Sec. 2.4, we discuss how this effect can be useful for the collection of Quantum Information in complex systems, thanks to the exploitation of bosonic indistinguishability. Indeed, indistinguishability of quantum identical particles can be considered as a useful nonclassical resource [140, 141]. From an operational point of view, particles are denoted as indistinguishable if they are in the same mode

with respect to a given characterization via two-particle interference [142]. From a broader perspective, the indistinguishability concept is related to a given set of quantum measurements [136]. In fact, indistinguishability underlies various quantum processes, such as many-body interference [142, 143], entanglement generation [137, 140, 141, 144–146], quantum teleportation [137], quantum metrology [147, 148], quantum coherence [149–151], quantumness protection [136, 152, 153], quantum key distribution [154, 155], and the high state complexity exploited by Boson Sampling algorithms [156, 157]. In this context, it can be crucial to understand how quantum features relying on indistinguishability behave in a dynamical framework, specifically in the case of bosons propagating through a non-homogeneous system. For a large variety of systems, disorder plays a detrimental role because it drives the system into decoherence [158]. On the other hand, for some systems, disorder can enhance physical properties such as coherent transport [74], quantum algorithms speedup [80], and quantum correlations [159–162]. These effects commonly appear due to the interaction with an external environment, though not always featuring a back-action mechanism [163, 164].
A suitable theoretical platform to perform such a study can be Quantum Walks, which provide with a very general coherent propagation model: indeed, QWs allow to preserve genuine nonclassical features such as superposition, interference, and entanglement [68, 71, 78], while classical RWs do not. We wish to stress again how QWs provide powerful models to describe energy transport phenomena in different types of systems like photosynthetic complexes [74, 165], or solid state ones, as in the case of Luttinger Liquids [166]. We have already discussed how adjustable disorder can play a significant role in the evolution of quantum walkers in which the ballistic growth can become anomalous, classical, or localized [27, 83, 110, 111, 167]. Moreover, the dynamics of a quantum walker is intimately connected to its nonclassical features. The way quantum-correlated walkers, realized by photon pairs, evolve in a homogeneous optical lattice has been investigated, highlighting the different behavior of distinguishable or indistinguishable photons [26, 98, 100, 101, 168]. On the other hand, the analysis carried in [110] does not directly yield information about non-classical correlations behavior in a disordered medium, but rather their effect on propagation properties. Some previous studies [162] tried to achieve the manipulation of correlations among different degrees of freedom of the same particle through disorder; nonetheless, strategies employing disorder control for enriching two-particle quantum correlations, hence actual non-local quantum correlations, were still missing.

3.2 Theoretical framework

We apply the p-diluted disorder model we already discussed in Sec. 2.1 to a 1D DTQW. We give here a brief summary: the single step evolution of the quantum state of the system can be written as

$$|\Psi(t+1)\rangle = \sum_k e^{i\phi_k(t)} \hat{U} \alpha_k(t) \, |k\rangle \, , \tag{3.1}$$

where step-position dependent phases $\phi_k(t)$ are chosen out of two values 0 or π. We assume that the phases experienced by the quantum walker are independently and randomly generated. Thus, a sequence of Bernoulli processes depending on p generates a phase map $\{\Phi_p(t)\}_{t=0,\dots t_{max}}$, such as described in Sec. 2.1. In the following, we especially focus on the single phase maps that enhance

the quantum correlation between the walkers: in that case, the average level of disorder p is no more a relevant quantity.

We wish to study the effect of disorder over nonclassical bosonic correlations in a QW dynamics, thus we consider two indistinguishable photonic walkers as input. Indeed, the state of the so-called biphoton: $\left|\Psi^{(2)}\right\rangle = |k_1, k_2\rangle$ (where $|k_i\rangle = |x_i\rangle\,|\sigma_i\rangle$) exhibits intrinsic quantum correlations even without any particular state engineering; two bosonic indistinguishable particles, can be seen as occupying the symmetrical entangled state:

$$\left|\Psi^{(2)}\right\rangle = |k_1, k_2\rangle = \frac{1}{\sqrt{2}}\big(\,|k_1\rangle^{(1)}\,|k_2\rangle^{(2)} + |k_2\rangle^{(1)}\,|k_1\rangle^{(2)}\,\big) \tag{3.2}$$

where the different particles are here identified by different superscripts. This approach feature an inherent contradiction: indistinguishable particles are treated as distinguishable objects by means of fictitious labels. However, a recent alternative approach demonstrates that indistinguishable particles can unequivocally feature "intrinsic" non-local entanglement, when they spatially overlap [169, 170]. In this sense, the generation of an entangled NOON state as the output of an HOM effect between two indistinguishable bosons may be regarded as some kind of entanglement translation. The two-particle QW evolution is simply described by the application of $\hat{U} \otimes \hat{U}$ to the initial state, besides the local phase factors $e^{i\phi_k(t)} \otimes e^{i\phi_k(t)}$. One way to detect the nonclassicality of the correlation between two outputs, such as two QW modes, is by violating the inequality, reported in [98, 100]:

$$V_{ij} = \frac{2}{3}\sqrt{P_{ii}P_{jj}} - P_{ij} < 0, \tag{3.3}$$

where P_{ij} is the probability of finding a photon in mode i and the other one in j, namely the probability of measuring a coincidence between modes i and j. Inequality (3.3), which is inspired by the detection of classical Hanbury, Brown and Twiss correlations [20], stands for classically correlated light and its violation, corresponding to a positive V_{ij}, is assumed to witness and quantify the presence of quantum correlations, as a signature of photon bunching [98, 100, 101]. It is worth trying to provide some interpretation of this V_{ij} value. Eq. (3.3) links three experimentally measurable quantities, i.e. $P_{i,i}, P_{j,j}$, and $P_{i,j}$, to the amount of quantum correlations between modes i and j or, more precisely, to the degree of indistinguishability of the photons travelling along those modes.

To clarify the meaning of Eq. (3.3), it is convenient to refer to a HOM effect framework. We recall here that this effect, which we discussed in Sec. 1.2.6, is visible when two indistinguishable photons (i. e. photons with exactly the same features) impinge at the same time on a BS from the two input ports. In an ideal case, the state of the system at the output of the BS reads:

$$|\psi\rangle_{ind} = \frac{i}{2}(\hat{a}^{\dagger 2} + \hat{b}^{\dagger 2})\,|0\rangle = \frac{i}{\sqrt{2}}(|2,0\rangle + |0,2\rangle)$$

where the ket states are written as $|n_a, n_b\rangle$. We remark we are considering now a second quantization framework, where we describe the system in terms of the number of particles occupying its possible modes. In this case, the two possible modes are the output ports of a BS.

This straightforward computation shows that the probability to find the particles travelling along two different modes, i.e. $P_{a,b}$, drops to 0, while the probability to find them travelling along the same mode, namely $P_{a,a}$ and $P_{b,b}$ is 1/2. If we compute the quantity from Eq. 3.3 with these

values we get a value $V_{a,b} = \frac{1}{3} > 0$.
On the other hand, in the case of distinguishable photons, the output state after the interaction with the BS reads

$$|\psi\rangle_{dist} = \frac{1}{2}(i \cdot \hat{a}^\dagger \hat{a'}^\dagger + \hat{a}^\dagger \hat{b'}^\dagger - \hat{b}^\dagger \hat{a'}^\dagger + i \cdot \hat{b}^\dagger \hat{b'}^\dagger)\,|0\rangle = \frac{1}{2}(i \cdot |1,1,0,0\rangle + |1,0,0,1\rangle - |0,1,1,0\rangle + i \cdot |0,0,1,1\rangle)$$

where the ket states are written as $\left|\hat{a}^\dagger, \hat{a'}^\dagger, \hat{b}^\dagger, \hat{b'}^\dagger\right\rangle$, and the different creation and destruction operators represent the two distinguishable particles. The total probability $P_{a,b} = P_{a,b'} + P_{b,a'}$ of the two particles travelling two different modes results to be $\frac{1}{2}$ while, for $P_{a,a'}$ and $P_{b,b'}$ we get $\frac{1}{4}$. Thus, the resulting value of $V_{a,b}$ is $-\frac{1}{3} < 0$. In the indistinguishable photons case, a positive value witnesses the presence of non classical correlation between the two modes under study, namely they are correlated in a way that can not be described in classical terms. On the contrary, in the distinguishible case, we obtain a value < 0 which corresponds to correlations that can be interpreted as originating from a classical state.
For our purposes, it is interesting to understand how this kind of correlations can be influenced by phase shiftings in an interferometrical framework such as the one of an optical 1D QW (such as the one described in Sec. 2.2). We consider a MZI, such as the one depicted in Fig. 1.4, travelled by two photons. We observe now the output modes of the interferometer, denoted as a and b. If we insert a phase shift ϕ along one of the two arms of the MZ, we obtain the following analytic expression for the value of $V_{a,b}$ as a function of the phase ϕ, in the case of indistinguishable photons.

$$V_{a,b} = -\frac{1}{3} - \frac{2}{3}\cos(2\phi)$$

In the distinguishable photons case, we obtain the following relation

$$V_{a,b} = -\frac{2}{3} - \frac{1}{3}\cos(2\phi)$$

In the distinguishable photons case, the 0 "non-classical threshold" value is never reached, while in the indistinguishable case it is possible to obtain larger values than 0 that witness the presence of a quantum input travelling the network.
It is worth understanding how the amount of violation V from Eq. (3.3) featured by a biphoton state can be trusted to quantify the amount of indistinguishability of the two particles. It is possible to establish a link between this value and the state of the system, in the case of two partially indistinguishable photons entering the QW. This framework can be addressed as an imperfect process of generation of indistinguishable photon pairs, featuring a known probability q of generating a distinguishable pair instead of an indistinguishable one. The initial state can be written as:

$$\hat{\rho}_0 = (1-q)\hat{a}^\dagger \hat{b}^\dagger\,|0\rangle\,\langle 0|\,\hat{a}\hat{b} + q\hat{a}^\dagger \hat{b'}^\dagger\,|0\rangle\,\langle 0|\,\hat{a}\hat{b'} = \tag{3.4}$$

$$(1-q)\,|1,1\rangle_{ind}\,\langle 1,1|_{ind} + q\,|1,1\rangle_{dist}\,\langle 1,1|_{dist} \tag{3.5}$$

where q can be also interpreted as the overlap of the two photon wave-functions, so that the

photons are distinguishable with classical probability q. The two modes correspond to the input ports of a BS. After impinging from different directions on the BS, we have a mixture of two terms, the indistinguishable output, featuring HOM effect, and the distinguishable one:

$$\hat{\rho}_1 = (1-q)\left(i \cdot \frac{|2,0\rangle + |0,2\rangle}{\sqrt{2}}\right)\left(...\right)^T + \tag{3.6}$$

$$+ q\left(\frac{i \cdot |1,1,0,0\rangle + |1,0,0,1\rangle - |0,1,1,0\rangle + i \cdot |0,0,1,1\rangle}{2}\right)\left(...\right)^T. \tag{3.7}$$

We can evaluate the inequality Eq. (3.3) for the output state of the process, considering $P_{a,a} = P_{b,b} = \frac{1-q}{2} + \frac{q}{4}$ and $P_{a,b} = \frac{q}{2}$. We get:

$$\frac{2}{3}(\frac{1}{2} - \frac{q}{4}) - \frac{q}{2} < 0 \tag{3.8}$$

which, in order to be violated, requires a value $q > \frac{1}{2}$, corresponding to photons which are more likely to be indistinguishable than distinguishable. Hence, the inequality (3.3) provides a straightforward quantifier of the effective indistinguishability of photons, in the operative context of boson bunching occurrence.
In the general case of a BS network, such as the one exploited in the present work, a value of $V_{ij} > 0$ can be subject to multiple interpretations. For a pure initial state, after a n step propagation, the system will be in a superposition state which can be written considering the number of photons travelling in the modes of interest:

$$|\Phi\rangle = \sqrt{1-\Pi}\big(...\big) + \sqrt{\Pi}\big(\alpha_{k_1k_1}\,|2\rangle_{k_1}\,|0\rangle_{k_2} + \tag{3.9}$$

$$+\alpha_{k_1k_2}\,|1\rangle_{k_1}\,|1\rangle_{k_2} + \alpha_{k_2k_2}\,|0\rangle_{k_1}\,|2\rangle_{k_2}\,\big) \tag{3.10}$$

where Π is the overall probability of having both photons in the selected modes, which normalizes the α_{ij} coefficients, while $\{|k_1\rangle, |k_2\rangle\}$ are the two output modes under observation, corresponding to combined states of position and coin of the form $|k\rangle := |x\rangle\,|\sigma\rangle$. We do not consider contributions of other modes, included in the first term (...). It is also possible to have single photon states of the two modes, but they would be invisible to coincidence-like measurements. In this case, the amount of violation between modes k_1 and k_2 can be computed as:

$$V_{k_1k_2} = \Pi \times \left(\frac{2}{3}\sqrt{|\alpha_{k_1k_1}|^2|\alpha_{k_2k_2}|^2} - |\alpha_{k_1k_2}|^2\right) \tag{3.11}$$

Therefore, the violation amount depends on two factors:

- the actual non-classicality of the correlation determining a positive or negative value;
- the global probability of the selected output modes (given by Π).

The first factor is the one pointing out the form of a hypothetically post-selected state of the two photons emerging from the considered modes. The higher this factor, the cleaner is the distillation of NOON states by post-selection, since it necessarily corresponds to a low $|\alpha_{k_1k_2}|^2$. The second factor is an amplification parameter, which gives the probability of actually finding two photons

in the two-modes selected subsystem, hence it gives the efficiency of the NOON states distillation. In conclusion, the violation value provides with information regarding the composite effect of the two parameters, hence its maximization can be related to either one or the other. Therefore, this aspect needs to be taken into account in hypothetical applications of this protocol. For instance, the most external output modes will provide the purest NOON states, since they are the mere propagation of the first HOM resulting state, but with a very low probability. On the other hand, by means of inhomogeneous phase configurations, we will show that it is possible to manipulate the probability for central modes and get an higher efficiency, although at the cost of a non-zero chance of extracting a useless state.
All of this discussion was inspired by a very thorough numerical study I performed, which took into account the behavior of these correlations in an ordered case as well as in the average disordered case. As we will show in the next sections, non-classical correlations are bound to disperse and decrease in these cases, while the only way to preserve them and even focus them is by imposing a specific disorder configuration on the evolution. In the following, we discuss these findings and the experimental results they led to.

3.3 High brilliance SPDC source of indistinguishable photon pairs

In order to implement disordered QW evolution of a biphoton, we employed the all-optical setup described in Sec. 2.2. The input indistinguishable photon pairs are produced through SPDC by a PPKTP crystal embedded in a phase-stable bulk optics triangular Sagnac Interferometer, realized with two broadband dielectric mirrors on its vertices and a dual wavelength Polarizing Beam Splitter (PBS) as the input/output vertex (see Fig. 3.1). This setup was directly inspired by the one designed and realized by Fedrizzi et al. in [171].

A single-mode continuous wave laser at a wavelength of 405nm, coherence time $\sim 0.33\mu$s, acts as the pump, entering the SI after being reflected by an external dichroic mirror (DM). The pump is then reflected and redirected towards the dual wavelength PBS. The polarization of the pump can be tuned by means of a quarter wave plate QWP_{λ_p} and an half wave plate HWP_{λ_p}, working at the pump wavelength λ_p and placed along its path before entering the SI. As an example, the pump can be prepared in a diagonal polarization state $|\psi\rangle = \frac{1}{\sqrt{2}}(|H\rangle + |V\rangle)$. After encountering the dual wavelength PBS, the $|H\rangle$ component is transmitted along the counter-clockwise trajectory, while the $|V\rangle$ one is reflected along the clockwise one.
A non-linear PPKTP crystal is positioned in the middle of the SI path. The pump laser interacts with the PPKTP, yielding photon pair generation by SPDC. Since the crystal is uniaxial negative, the type II quasi-phase matching (QPM) condition has to be fulfilled:

$$n_e(\omega_p)\omega_p = (n_e(\frac{\omega_p}{2}) + n_o(\frac{\omega_p}{2}))\frac{\omega_p}{2}$$

where $n_e(\omega_p)$ is the extraordinary refractive index and $n_o(\omega_p)$ is the ordinary one, both depending on the pump laser frequency ω_p.
The crystal is placed inside an oven that keeps it at fixed temperature, since temperature fluctuations can produce thermal expansion of the crystal, changing the QPM condition. Due to the linear superposition of the polarization state of the pump, two SPDC processes take place in superposition. The H polarized part of the pump can generate two degenerate photons at 810nm in a $|H\rangle\,|V\rangle$ state.

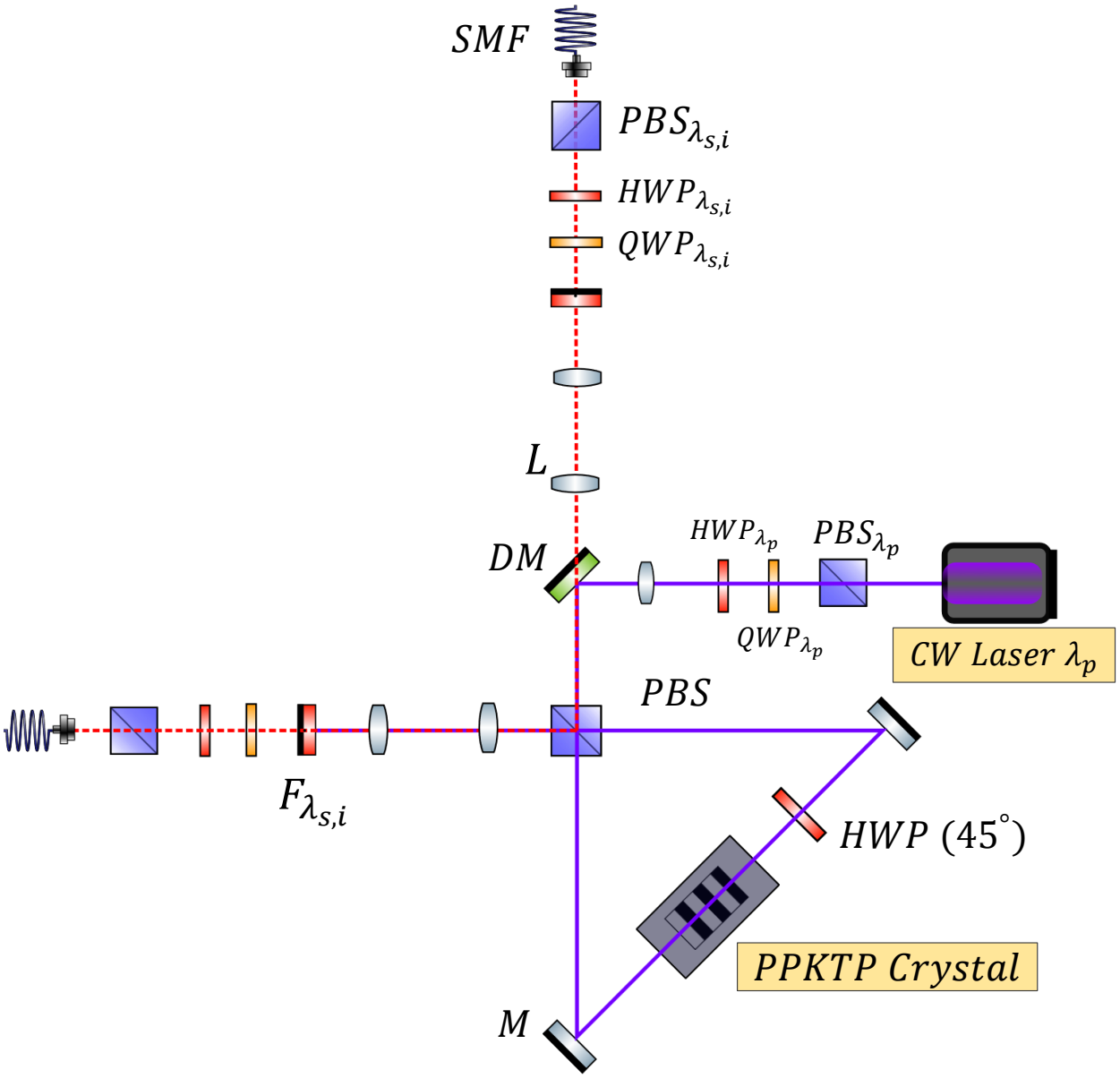

Figure 3.1: Sketch of the photon pair source. *The pump laser (wavelength $\lambda_p = 405nm$) is represented as a violet-coloured beam. Its polarization state is prepared by an Half Waveplate (HWP) and a Quarter Waveplate (QWP), designed to properly work at wavelength λ_p. The pump is directed by a Dichroic Mirror (DM) into the Sagnac Inteferometer, made of a Polarizing BeamSplitter (PBS) and two mirrors (M). The laser impinges on the PPKTP crystal from two directions (in one of them, polarization is rotated by a HWP). The produced photons (wavelength $\lambda_{s,i} = 808nm$) are sent into two different paths depending on their polarization, where their polarization state is processed in turn by the sequence QWP, HWP and PBS, before collection by a Single Mode optical Fiber (SMF). An interferential filter F centered on $\lambda_{s,i}$ is also inserted on both paths, to filter out residual laser signal. The beams are suitably collimated by lenses (L), in order to guarantee efficient pumping and photon collection.*

The V polarized part of the pump, circulating clockwise, needs to be rotated into $|H\rangle$ in order to fulfill the QPM relation and to produce photon pairs. To this aim, a broadband HWP is placed right before the crystal on the $|V\rangle$ component trajectory, rotating the pump polarization to $|H\rangle$ and fulfilling QPM. At the same time, photons generated by the $|H\rangle$ pump will be accordingly rotated by the HWP. The resulting state of down-converted photon pairs is a superposition of two possible

generation events, where the photons are separated in polarization and spatially distributed by the dual wavelength PBS to two output spatial modes that we identify as the *system* (s) and the *ancilla* (a):

$$|\psi\rangle = \alpha\,|H\rangle_s\,|V\rangle_a + \beta e^{i\phi}\,|V\rangle_s\,|H\rangle_a \tag{3.12}$$

where $|\alpha|^2 + |\beta|^2 = 1$ and ϕ represents the total phase factor between the two parallel SPDC processes. The balance between α and β (thus between the populations of the two states) can be tuned by means of an external HWP applied on the pumping state $|\psi\rangle$. In turn, the phase ϕ can be controlled by a Quarter Wave Plate (QWP) acting on the pumping state or, in order to achieve a better control, by a liquid crystal (LC) positioned along the trajectory of the signal/idler mode. Indeed, LCs feature a different refraction index depending on the polarization of traversing light [172], and this refractive index can be tuned by the application of an electric field, allowing to precisely set the phase shift between the two terms. The state generated in this way is entangled, and the two photons are always found with opposite polarization states. For the experiment we are discussing, we only employed indistinguishable photons, without any path-polarization entanglement. On this purpose, the pump polarization was prepared in a completely H(or V)-polarized state, so that a single possible generation event was produced. The resulting state reads $|H_s, V_i\rangle$, thus, imposing a polarization rotations on one of the two output modes we get a final state of two identical photons. After preparation, the photons are injected into the setup of Sec. 2.2 through Single Mode Fibers (SMFs). In order to have two actually indistinguishable photons propagating through the QW evolution, we have to ensure that they enter the setup at the same time, i.e. they travel the same distance from the source to the first collision with the BS. To this aim, a motorized *optical cage* is inserted along the fiber line carrying one of the two photons; in this way, one of the two photon paths features a segment in air, the length of which is tunable with an accuracy of $O(\mu m)$. Thus, we can achieve maximum photon indistinguishability by observing the visibility of HOM effect among the two photons (see Subsec. 1.2.6) as a function of the tunable time delay and deduce the optimal one. In order to perform this optimization, photons were injected in the setup, hitting the central BS of the platform and reproducing the traditional HOM scheme. Then, they were collected by the Moving Mirrors and sent to detectors via SMFs. The detectors were connected to a correlator, measuring the number of coincidence events. For indistinguishable photons we expect to register no simultaneous counts on the detectors, because of HOM effect. Thus, we tuned the path in air provided by the cage, so that the HOM dip resulted as low as possible. An experimental scanning of the Hong-Ou-Mandel dip as a function of the tunable length is shown in Fig. 3.2. After correction of accidental coincidences, the visibility of HOM effect resulted to be $V \sim 93\%$. This high value of photon indistinguishability is also the result of a thorough optimization in function of the temperature degree of freedom: as we mentioned above, crystal temperature changes the QPM condition, so that there is, in general, a temperature leading to the generation of more indistinguishable photon pairs in terms of wavelength and polarization. In Fig. 3.3, we show the HOM dips for various temperature, which led to the resulting optimal temperature $T = 109.8°C$.

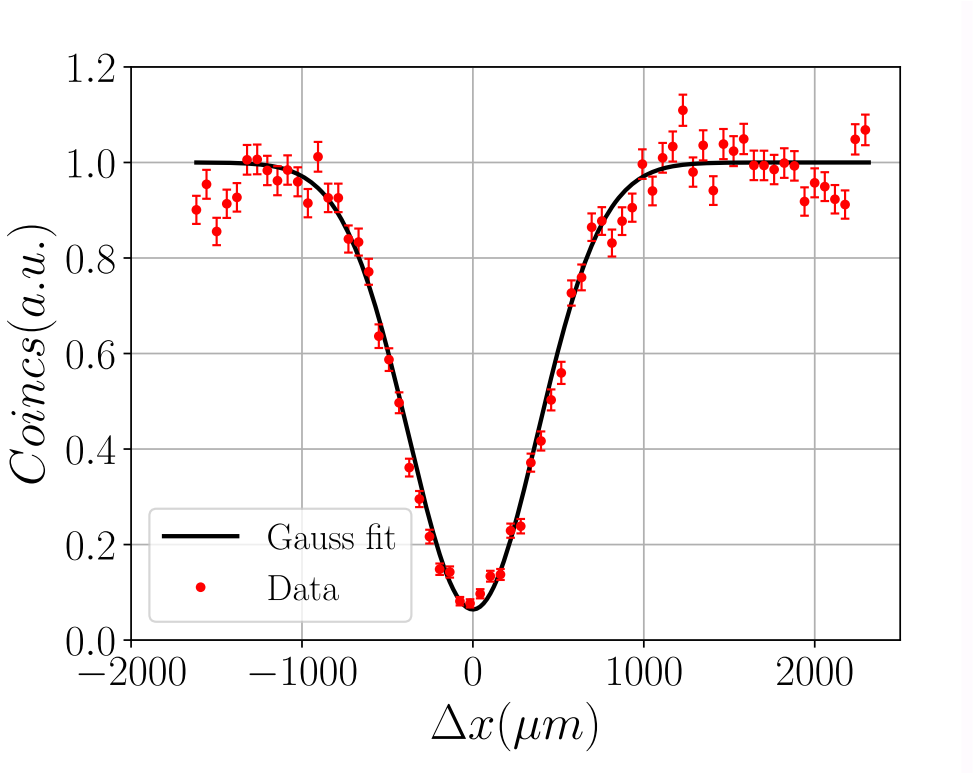

Figure 3.2: Normalized HOM coincidences as a function of the optical delay between photons. *Red dots represent experimental data with error bars computed considering poissonian distributed coincidences. The black solid line represents a gaussian fit of the experimental data. Photon indistinguishability is confirmed by the high dip visibility* $V \sim 93\%$.

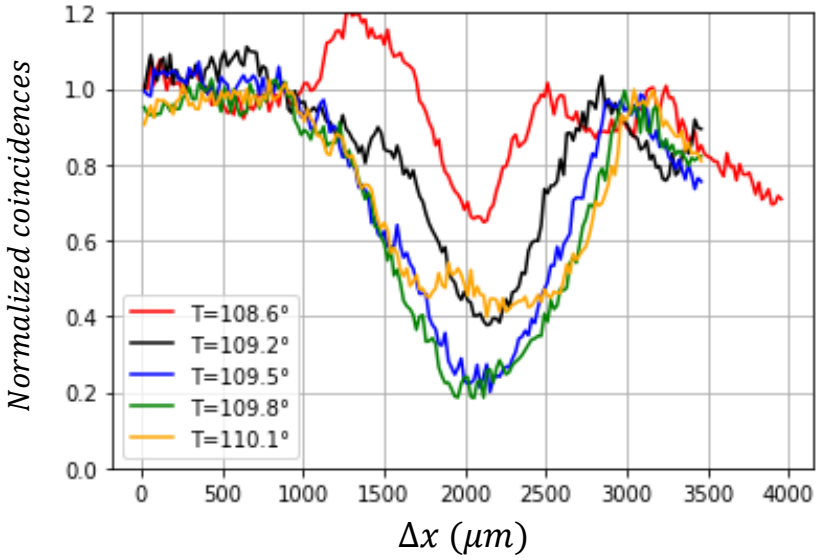

Figure 3.3: Normalized HOM dip as a function of the optical delay for various temperatures (reported in $°C$**).** *The indistinguishability of photons generated by our source changes depending on the crystal temperature. The best photon indistinguishability (thus the best QPM condition) is achieved around a temperature of* $109.8°C$.

3.4 Numerical Results

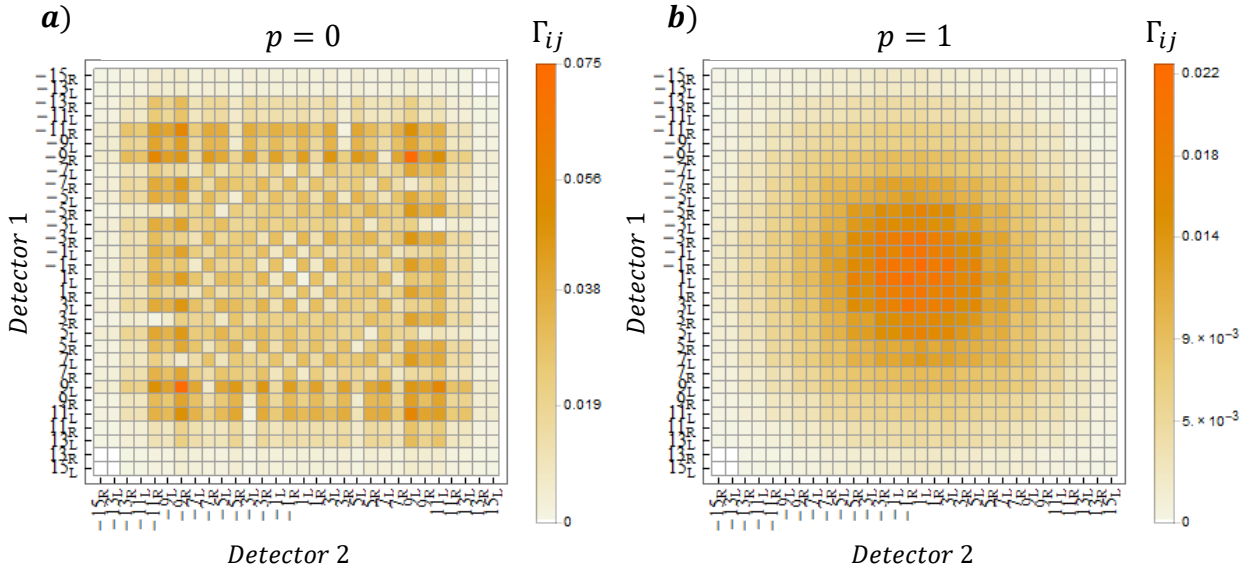

Figure 3.4: Numerical simulation of coincidences matrices. *Step 15 output distributions of indistinguishable photons in the* ***a)*** *ordered case ($p = 0$) and the completely* ***b)*** *disordered one ($p = 1$). The disordered matrix has been computed by averaging over 10^4 disorder configurations. Figures reported in [119].*

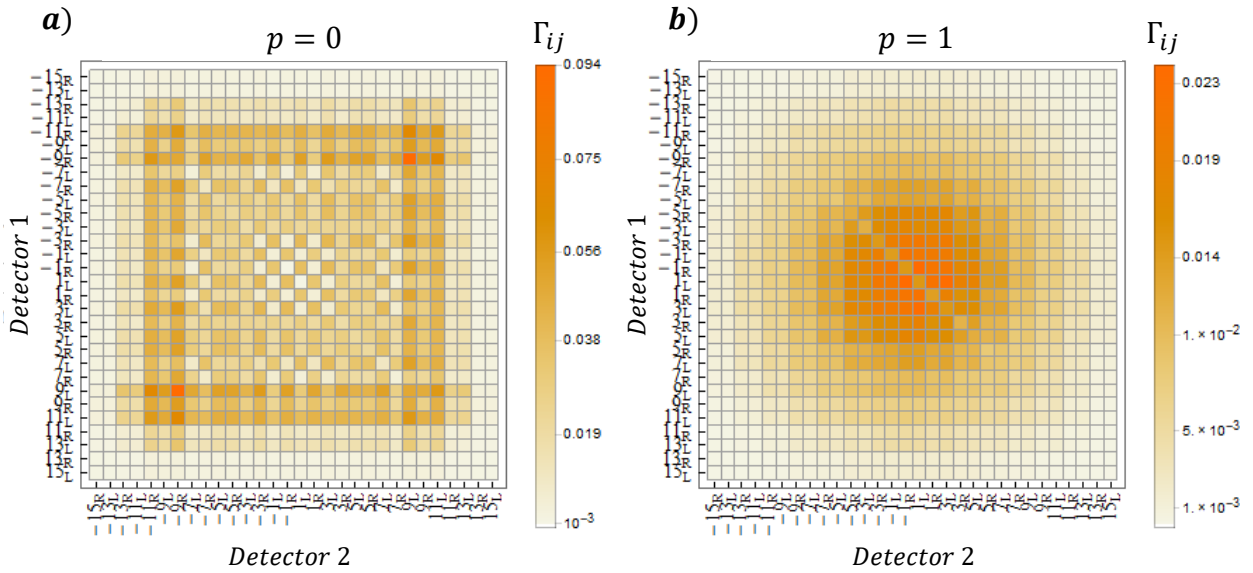

Figure 3.5: Numerical simulation of coincidences matrices. *Step 15 output distributions of distinguishable photons in the* ***a)*** *ordered case ($p = 0$) and the completely* ***b)*** *disordered one ($p = 1$). The disordered matrix has been computed by averaging over 10^4 disorder configurations. Pictures reported in [119].*

I carried preliminary simulations in an ideal p-diluted framework: two indistinguishable photons travelling a bulk-optics 1D DTQW, provided with space-time disorder. As we discussed in the introductory section, there are no examples of studies regarding the behavior of biphoton non-classicality evolving in a disordered medium. The first step in our analysis is understanding how the QW output distribution is affected by p-diluted disorder. We compare the output distributions of an ordered evolution $p = 0$ and a completely disordered one for the case of perfectly indistinguishable photons (Fig. 3.4) and distinguishable ones (Fig. 3.5). These matrices show the values of probability P_{ij} of finding a coincidence between two photons emerging from mode i and j. As the disorder increases, the output coincidences distributions for the indistinguishable and distinguishable case become more and more similar. This is also highlighted by the similarity $S(P^{ind}, P^{dist}) = \sum_{i,j} \frac{\sqrt{P_{ij}^{ind} P_{ij}^{dist}}}{\sqrt{P_{ij}^{ind}}\sqrt{P_{ij}^{dist}}}$ between the two distribution, reported in function of the disorder level p in Fig. 3.6. Indeed, the output coincidences distribution does not yield direct information regarding the way quantum correlations are affected by a disordered evolution.

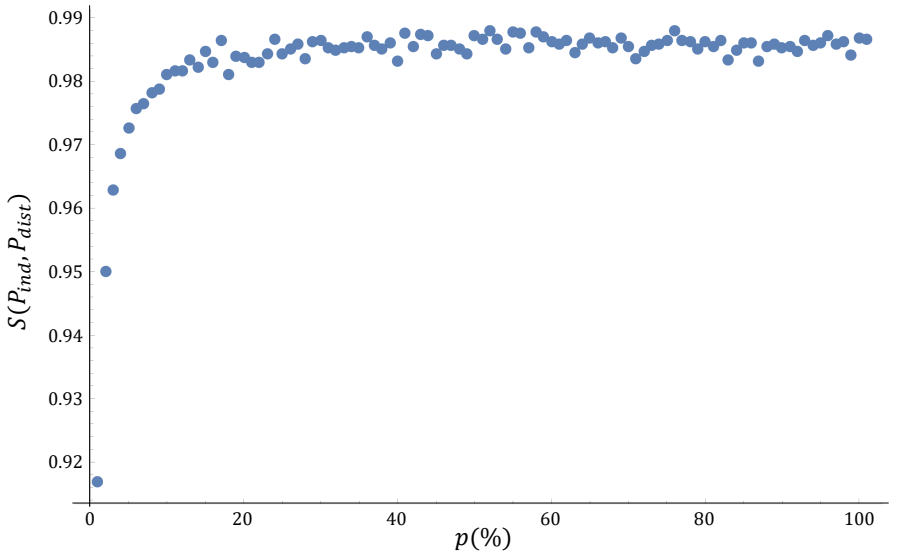

Figure 3.6: Similarity between output distributions at 15 steps of indistinguishable and distinguishable photons for variable p. *The output distributions for indistinguishable and distinguishable photons are practically identical for highlevel of disorder. This is compatible with the notion that a disordered QW features a classical-like behavior.*

In turn, we can use the average probability coincidences distributions to obtain the output violation matrices. We show the violation matrices corresponding to the output distributions reported in Figures 3.4 and 3.5: the output violation matrix for an indistinguishable photon pair after 15 steps is shown in Fig. 3.7, both for the ordered case (**a**), and the completely disordered one (**b**) featured by maximal randomness $p = 1$. In this case, the disorder level p is a relevant quantity, since it indicates the average quantity of disorder imposed on the evolution. It is straightforward to notice that violations are present both in the ordered and in the disordered case, though there is an evident migration of the violating values towards the matrix tails as disorder is inserted. On the other hand, for distinguishable photons no violations are present at all (Fig. 3.8).

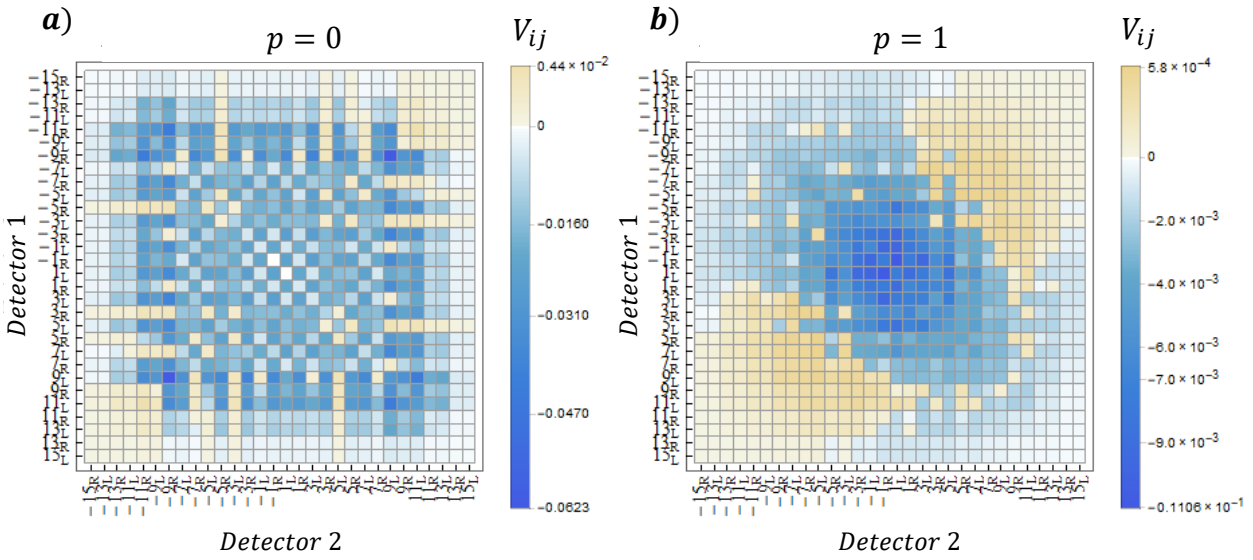

Figure 3.7: Numerical simulation of coincidences matrices. *Step 15 output distributions of indistinguishable photons in the* ***a)*** *ordered case ($p = 0$) and the completely* ***b)*** *disordered one ($p = 1$). The disordered matrix has been computed by averaging over 10^4 disorder configurations. Figures from [119].*

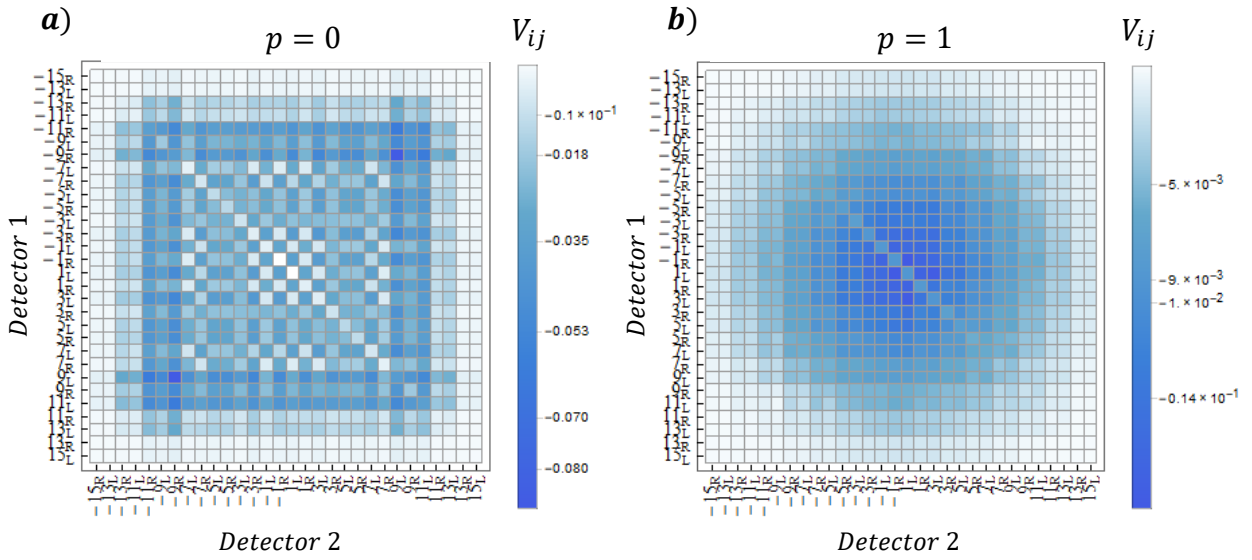

Figure 3.8: Numerical simulation of coincidences matrices. *Step 15 output distributions of indistinguishable photons in the* ***a)*** *ordered case ($p = 0$) and the completely* ***b)*** *disordered one ($p = 1$). The disordered matrix has been computed by averaging over 10^4 disorder configurations. Figures from [119].*

It is worth comparing the coincidence and violation matrices for the indistinguishable case: indeed, in the completely disordered case, a strong funneling of population towards central modes is present, while quantum correlations disappear in the central region. Non-classical correlations tend

to appear between modes which have low coincidences (and less population). This phenomenon may nourish the idea that correlations specifically generated by the QW dynamics are classical and may even smother the underlying non-classical correlations [97, 173], especially in the completely disordered case, when the QW dynamic emulates the one of a Classical Random Walk [80, 83, 110].

In order to describe the dynamical average behavior of violation-quantified non-classicality, we define a quantity capable of displaying the amount of non-classicality exhibited by a violation matrix, i.e. the total non-classicality which the correlations of the system feature at a given evolution step for a given disorder level p. We define the Total Violation (Tot V) of the system as the sum of all the positive $V_{i,j}$, namely the ones corresponding to non-classical correlations, that we deem as a measure of the total quantum correlation present in the system. Its normalized trend in function of the disorder level is reported in Fig. 3.9, for different evolution time lengths. Total Violation has

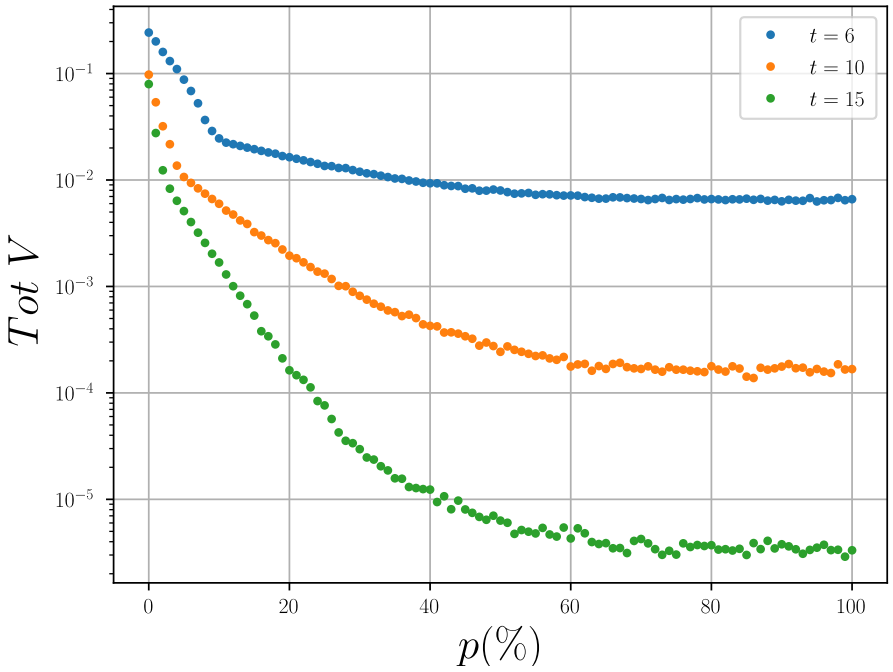

Figure 3.9: Numerical simulation of Total Violation trends. *Step 15, step 10 and step 6 plot of the average Total Violation, computed over* 10^4 *disorder configurations, as a function of the disorder level p. Figure taken from [119].*

a decreasing trend as p increases, which can be explained as a consequence of the migration picture described above. Since violations are bound to appear only between scarcely populated modes, the global quantum correlation diminishes.

On the other hand, the average evolution seems to feature a decrease of global non-classicality in time, regardless of the disorder level. Nevertheless, this property only stands for average quantities. Global and local quantifiers of quantum correlations can exhibit quite a different trend as we observe the output distributions of specific disorder realizations rather than the average ones. There may be, indeed, some individual phase configurations which do not lead to decrease of quantum correlations, although this is the case on average. I investigated in this direction both from a global point of view, analyzing Total Violation, and focusing on local quantities. In particular, I aimed at finding the maximum value of V_{ij} which could be achieved at any given step number for any disorder con-

figuration and considering any modes pair $\{i, j\}$, which we define as Maximum Achievable Violation (MAV). In order to check for the existence of such phase maps, I adopted a random search protocol: I simulated the evolution with 10^4 different phase maps for each step number t up to 30 steps, for a total amount $3 \cdot 10^5$ of explored configurations. These configurations were generated for a fixed level of disorder, but, since we focused on individual phase maps, the average level of disorder was not relevant anymore. We computed the V_{ij} between each pair of output modes for each simulated probability distribution, obtaining the corresponding violation matrices. The resulting entire set of V_{ij} elements corresponding to any combination of i and j modes was reported and I compared the values for any pair (i, j) and for each simulated phase map at a given step, to find the MAV and the maximum achievable Total Violation after a certain number of evolution steps, i.e. the maximum positive value of V_{ij} which could be achieved at that given evolution time. In this way, we can also record the individual phase maps producing the MAVs and the maximum values of Total Violation, which are generally different.

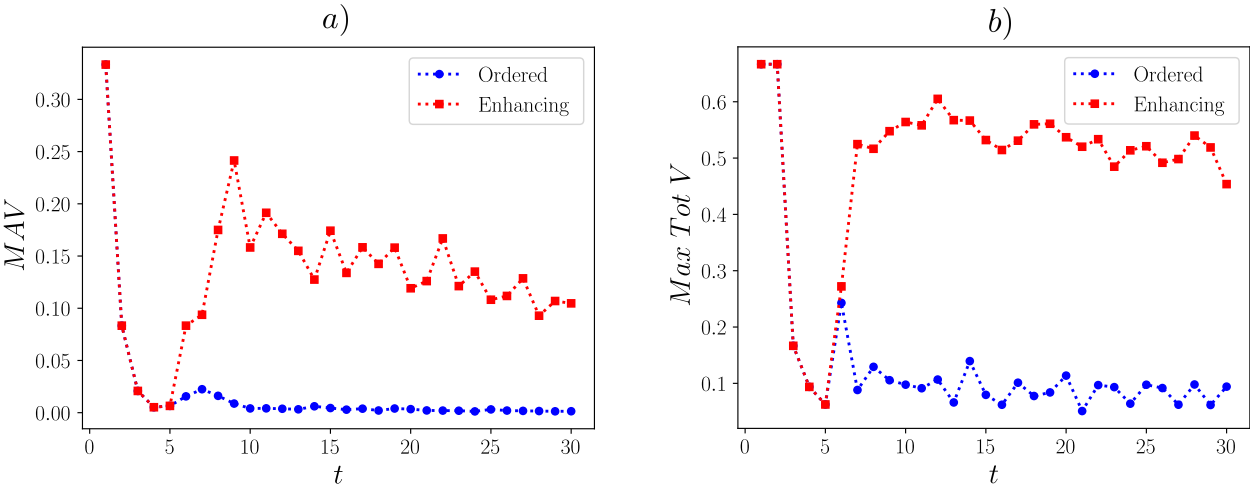

Figure 3.10: Numerical simulation compression between ordered and enhancing disordered QW. ***a)*** *Maximum Achievable Violation (MAV) and* ***b)*** *maximum achievable Total Violation versus the number of steps (discrete time) t for the ordered (blue circles) and enhancing disordered (red squares) QW. Figures appearing in [119].*

Summarizing, for each configuration the procedure consists of comparing maximum positive violations of inequality (3.3) at step t. This also allows to know where and when it is beneficial to apply the π phase shift within the quantum walk network so to identify and select enhancing phase maps. Simulation results are shown in Fig. 3.10 **a)** and **b)**, respectively. We report the MAV as a function of the number of steps, and the step-wise trend of the maximum achievable Total Violation. The highest MAV, besides the first step, is achieved at the output of the 9th step: the MAV for each modes pair (i, j) of the 9th step output distribution was computed, by analyzing 10^6 different phase maps each. The resulting landscape in Fig. 3.11 shows that this maximum can be achieved in different positions, depending on the chosen enhancing disorder configuration. In particular, it suggests that the proper MAV can be achieved only in "central" modes pairs: the MAV can be induced between different mode pairs by imposing different (yet equally enhancing) phase maps, although that is not possible in modes which have not interfered enough. In fact, photons emerging from central modes will have the most interfering paths, getting to be more affected by

inhomogeneities along the evolution. This phenomenon is quite understandable if we consider the underlying network structure of a QW evolution (as depicted in Fig. 2.7). Indeed, central modes are subject to more complex interference phenomena with respect to the ones close to the boundaries, even more complex when their correlations are considered. This can be directly linked to the amount of MZIs jointly travelled by photons emerging from the two selected modes, i.e. the amount of phase shifts that are imposed over both photons. Therefore, the manipulation of non-classicality results more powerful and effective as central modes are considered.

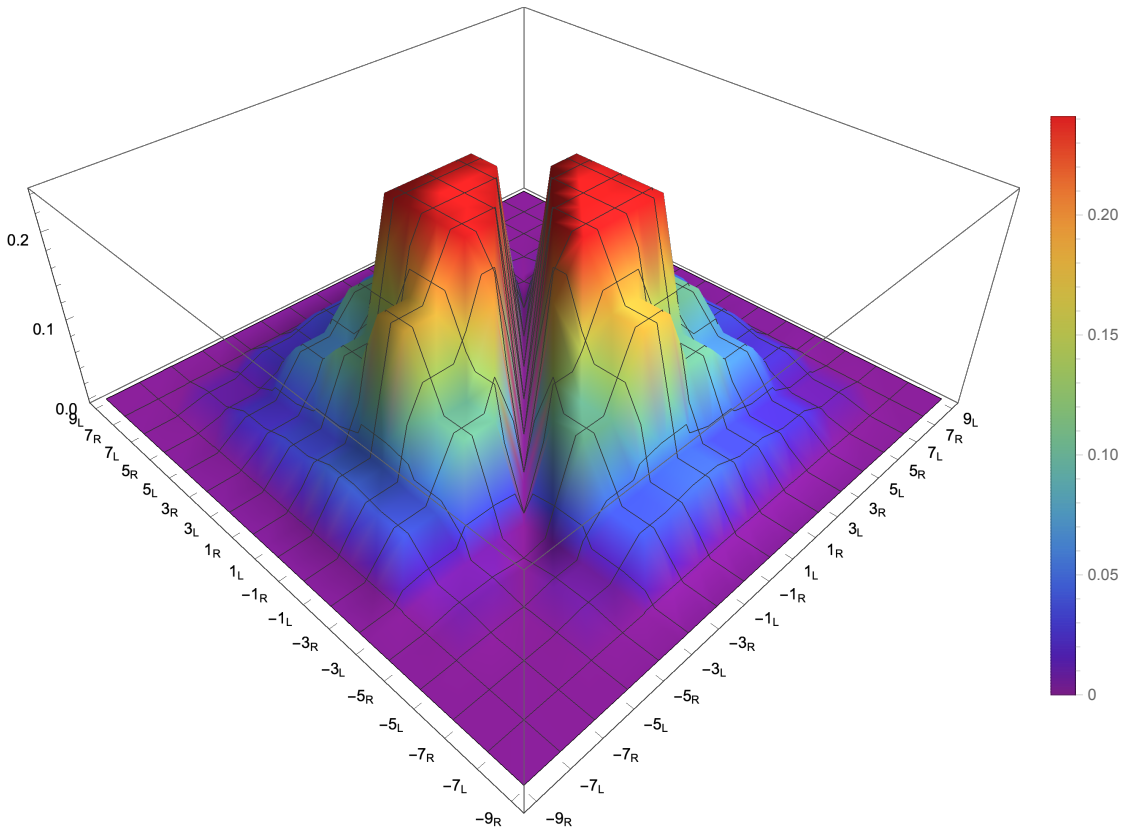

Figure 3.11: Numerical simulation of 9 step MAV landscape. *Plot of the maximum violation achievable for each output modes pair at step 9, obtained by comparing* 10^6 *different disorder realizations.Figure appearing in [119].*

Since the explored configurations may not cover the entire set of possible disorder patterns, the results can not be considered absolutely optimal, but rather enhancing in comparison with the ordered case. Nevertheless, the analysis highlights that disorder helps to retrieve quantum correlations after a specific step of QW, both for MAV and Total Violation, suggesting that the two quantities are related although not bound to be maximized together. From numerical results, we can conclude that disorder, acting through mere interference, significantly modifies the evolution of the walker, not only reshaping the probability distribution but also affecting the amount of quantum correlation between the photons. As a consequence, disorder may enable enhancement of the quantum correlation of a bipartite system. We stress again the fact that no violations are observed, whatever the phase map, when a state of distinguishable photons is employed, as shown above and also demonstrated in [100]. The numerical analysis we reported in this section represented the preliminary work for an experimental demonstration of the enhancement effect due to inhomoge-

neous evolution, which was implemented thanks to the completely bulk-optics setup we described in Sec. 2.2, which is capable of actually implementing any p-diluted phase configurations both for single or double walkers.

3.5 Experimental results

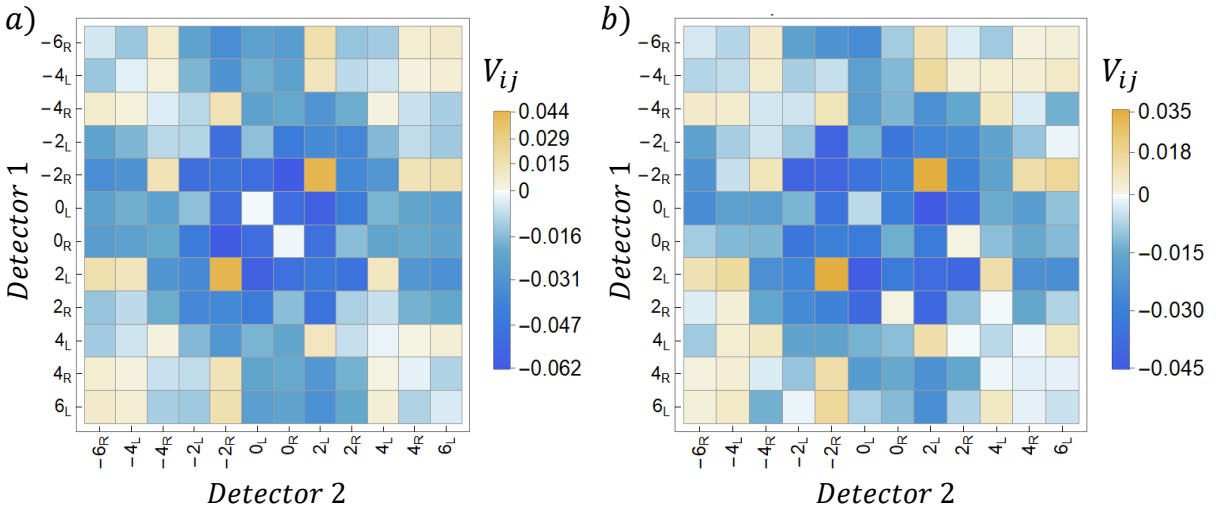

Figure 3.12: Comparison between the theoretical and experimental violation matrices at the 6th step. ***a)*** *Numerical simulation of the violation matrix corresponding to the 6th step output distribution of a Quantum Walk evolution featured by an enhancing disorder configuration. Simulation was performed taking into account experimental parameters. In* ***b)****, the corresponding experimental violation matrix is reported: the expected peak in the value of V is experimentally confirmed, and the measured output coincidence distribution reach a similarity value of* $97.5(\pm 1.3)\%$ *in comparison with the one expected by numerical simulation. Figures drawn from [119].*

To experimentally verify disorder-induced changes in the violation matrix, we measured both ordered and disordered evolution QW output distributions. Indeed, according to the simulation results displayed in Fig. 3.10, we expect the first unquestionable occurrence of the quantum correlation enhancement effect due to disorder to appear at the 6th step of QW. Therefore, the output violation matrices for optimal phase maps were measured up to the 6th step. Since there is no enhancement until the 5th step, the corresponding optimal phase maps can be considered equivalent to the ordered one, while for the 6th step it is possible to find many specific disorder configurations enhancing the non-classicality in the correlation between two chosen output modes, both for the ideal case and accounting for experimental parameters. The phase map selected for the experimental implementation features phase shifters at step $t = 4$, position $x = -2$ with coin $\sigma = L$ and $x = 2$ with coin $\sigma = R$ set to π, while all the others are set to 0. The BS network underlying the disordered evolution we picked was straightforwardly implemented by the multi-pass SI of Sec. 2.2. The experimental output violation matrix for a biphoton travelling such an inhomogeneous network is shown in Fig. 3.12, compared with the expected one, where a mode $|k\rangle = |x\rangle\,|\sigma\rangle$ is represented by the notation x_σ. A strong quantum correlation peak appears at modes $(2_L, -2_R)$ and $(-2_R, 2_L)$

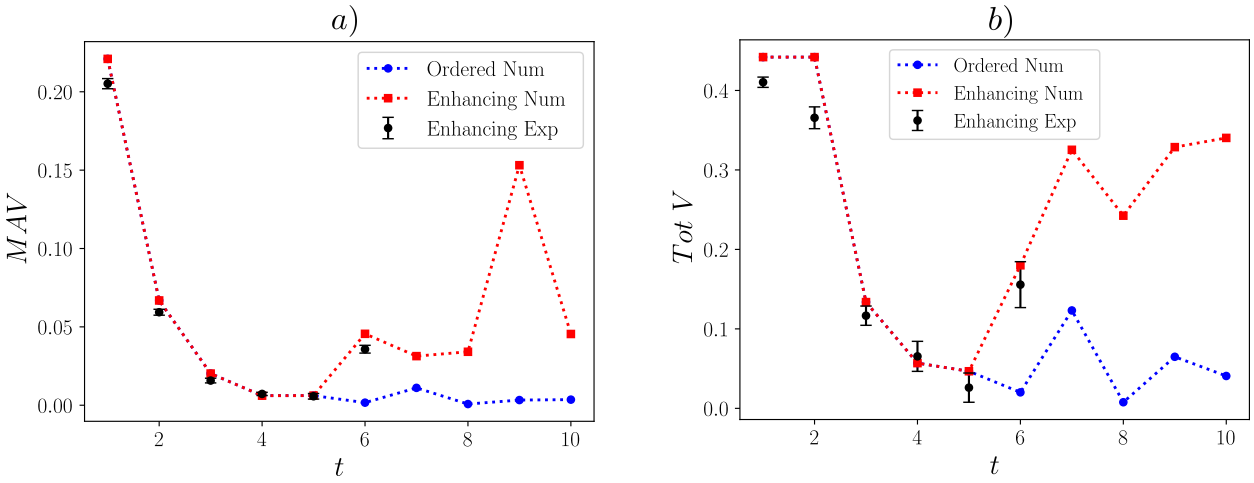

Figure 3.13: Experimental results compression between the order and the enhancing disordered configuration QW. *Experimental results for (dark dots)* ***a)*** *Maximum Achievable Violation (MAV) and* ***b)*** *corresponding Total Violation versus the number of steps. The trends are compared with the simulation for enhancing disorder (red squares) and ordered evolution (blue circles). The expected results are obtained by numerical simulations performed accounting for experimental parameters and asymmetries, so that the theoretical trends show some discrepancies with respect to the ones in Fig. 3.10. Images drawn from [119].*

confirming the expectation.

It is interesting to compare these violation matrices with output violation distributions corresponding to the 5th step, reported in Fig. 3.14. Since there is no optimal configuration for this step number, we chose a random phase map to demonstrate the dependence of quantum correlation distributions from the disorder pattern imposed on the evolution, although any kind of quantitative enhancement is absent. It is also useful to observe the corresponding coincidence matrices for the ordered 5th step and the optimal 6th step (Fig. 3.15). Evolution inhomogeneities, as we mentioned above and as demonstrated in several previous works [27, 83, 110, 171], determine an effect of spread hindering, for multiparticle systems as well. This effect can be noticed even in the case of a single disorder configuration (Fig. 3.15). The manipulation of this localization effect can change the non-classicality pattern in the output distribution in many different fashions, changing the probability of finding coincident photons between the output modes. Indeed, the corresponding experimental coincidences distributions result in good agreement with the expected ones. It is also worth mentioning the experimental method of measurement of the autocorrelation terms P_{ii} for each i, that correspond to the diagonal terms in the coincidence matrices: a BS placed at the output of the setup allows to split two photons travelling the same mode with probability $2RT$ with R (T) being the reflectivity (transmissivity) of the BS. By carefully characterizing the BS we can weigh the measured coincidences in order to compare them with the values of P_{ij} for $j \neq i$.

From the violation matrices we can compute the experimental step-wise trend for MAV, which is shown in Fig. 3.13a), in comparison with the expected enhanced one obtained by numerical analysis, taking into account experimental constraints. They are plotted together with the ordered case trend to provide a clear display of the beneficial effect of the non-homogeneous evolution. Theoretical patterns are shown up to the 10th step, as a reference. The corresponding trends for the Total Violation computed over the same output distributions are also reported in Fig. 3.13b). Simulations of the MAV values in the ordered case show that the quantum correlation spreads in a homogeneous

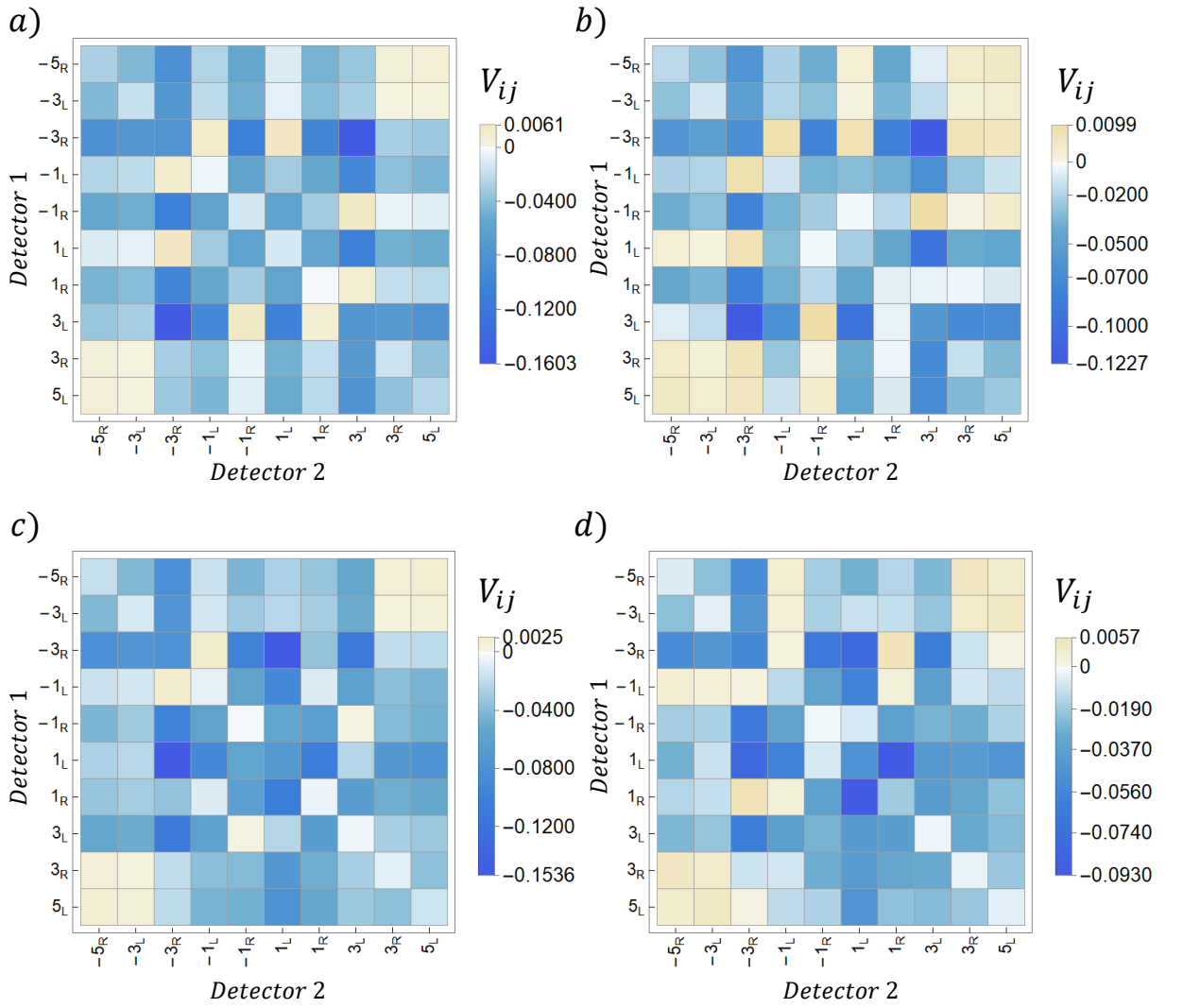

Figure 3.14: Violation matrices at the 5th step. *Ordered evolution: theoretical* ***a)*** *and experimental* ***b)*** *violation matrices at the 5th step. Disordered evolution: theoretical* ***c)*** *and experimental* ***d)*** *violation matrices at the 5th step. The disorder configuration has been chosen randomly. Figure taken from [119].*

network, so that the values of V_{ij} and the Total Violation are going to decline as the propagation proceeds. However, as can be seen in Fig. 3.13a), inhomogeneity enriches the quantum correlation between two indistinguishable photons at the selected modes. Experimental evidences, reported in Fig. 3.13b), show that the very same configuration also enhances the total quantum correlation of the Quantum Walk. Experimental errors are derived from the Poissonian statistics of the measured coincidences. Deviations from the expected results are mainly due to modest drops in photons indistinguishability along the evolution. Nevertheless, the indistinguishability decline slightly affects the exact violation values, while not changing the overall trend. Our QW implementation is limited to a six steps evolution because of the internal losses in each unit passage (nearly 17%) and because of both the geometrical structure and the length of the QW that make it difficult to guarantee a high quality spatial overlap of the two photons at each passage of light through the central BS of the platform. On the other hand, the main advantages of this QW configuration consist of both phase stability and a flexible disorder reconfigurability, and also by the fact that the output distribution

for any step of the QW is directly accessible and measurable. An evolution of six steps through this setup is enough to investigate on the photon correlation enhancement effect. Indeed, the numerical analysis reported in the main text indicates that a larger number of steps would have not brought any further physical insight to the experiment.

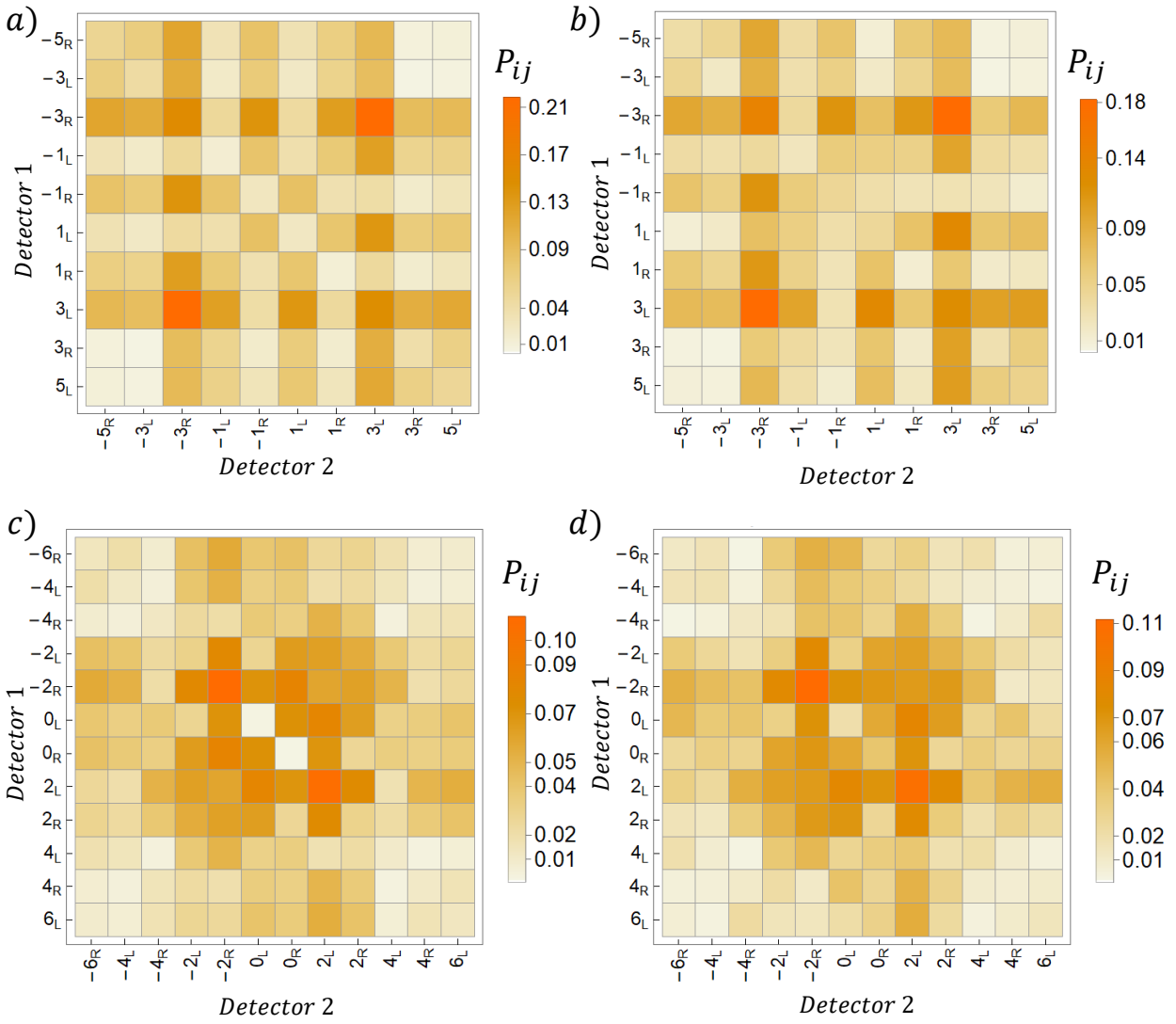

Figure 3.15: Numerical and experimental coincidences matrices. *5th step* ***a)*** *theoretical coincidences matrix and* ***b)*** *corresponding experimental measurement output for the ordered quantum walk. 6th step* ***c)*** *theoretical coincidences matrix and* ***d)*** *corresponding experimental measurement output for the optimal disordered configuration. The similarities between theoretical and experimental coincidences distributions are* $98(\pm1)\%$ *for the 5th step case (**a-b**) and* $97.5(\pm1.3)\%$ *for the 6th step case (**c-d**). Errors are computed accounting for Poissonian statistics of measured coincidences. Figures appearing in [119].*

3.6 Conclusion

Two indistinguishable particles evolving through some kind of homogeneous lattice are bound to feature less and less quantum correlations as they propagate through the medium. On average, the same behavior occurs as inhomogeneities are inserted in the evolution. In this Chapter, we have discussed a technique for the retrieval of these correlations and their localization by the imposi-

tion of suitable inhomogeneous phase configurations on the evolution, that has been experimentally demonstrated and reported in [119]. The experiment relied on a sophisticate bulk optics setup and a very bright photon pairs source, which allowed to realize a six step two particle disordered QW, with great flexibility and the possibility of measuring the output distributions at every step number. At the time of the experiment realization, this was the highest step number ever achieved for a biphoton QW with such disorder tunability features. We observed that by the imposition of different phase configurations, it is possible to tune the two-mode and total enhancement of non-classicality in position and intensity; this corresponds to implementing an adaptive network whose parameters evaluation determines the focusing of nonclassical resources in selected modes. These results deliver a method for enriching quantum correlation through controlling unitary evolution (effective Hamiltonian engineering) of the biphoton. In conclusion, two-mode quantum correlation diminishes in the case of random phase disorder in the system, which can be interpreted as a manifestation of detrimental classical noise, but this quantum correlation degradation can be challenged by single realizations of disorder. These results supply a conceptual and practical advance compared to previous studies limited to single-photon disorder-assisted quantum correlation enhancement between two degrees of freedom of the photon [162]. In fact, since violations of Eq. (3.3) witness biphoton quantum correlations between two modes, our method may well be interesting for applications requiring the distribution of Quantum Correlations among nodes of a network. Further research on the topic should focus on understanding whether this enhancement procedure can be generalized to systems with $N > 2$ photons or not; if so, our results would pave the way for the development of new methods and tools for the generation and distribution of NOON states, crucial, among the other Quantum Information tasks, for Quantum Metrology ones. The same problem may be interesting to investigate for a fermionic system, although it would be necessary to develop a new witness and quantifier of non-classicality, possibly related to the fermionic antibunching effect in a HOM context. Indeed, the same experimental platform may even be employed for such an experimental study, using indistinguishable photons in a fermionic entangled state, as mentioned in Subsec. 1.2.6.

Personal contribution

I personally studied the problem of indistinguishable particles travelling a disordered QW from a theoretical and numerical point of view. Not conclusive preliminary material was not reported here for sake of clarity and brevity. After analyzing the average behavior of indistinguishable biphotons and the effect of disorder on their spreading, I decided to switch to individual disorder configurations. As a consequence, I developed the idea for the experiment reported in this Chapter. Thus, I performed the numerical simulations aimed at finding the enhancing disorder configuration to employ for the experimental demonstration. I also worked to the actual implementation of the experiment thanks to the preexisting setup described in Sec. 2.2 after some improvements.

Chapter 4

Time-binning approach for efficient Quantum State Discrimination through a network-like receiver

In the previous Chapters, we have dealt with explicit applications of the QW model, as we aimed at analyzing the effect of disorder in systems that could be described as coherently propagating excitations. Indeed, we have already seen how a discrete QW dynamic features an inherent network structure. This property has been exploited to develop an approach based on Quantum Walks to the issue of Quantum State Discrimination [61]. In this case, a QW-like evolution is employed as a tool to dynamically process a quantum system in order to identify its state among a given number of possible ones. In collaboration with Prof. Caruso from University of Florence, we realized the first experimental demonstration of this dynamical approach to QSD [174], and we exploited the same strategy to implement a further very powerful protocol, capable of discriminating the state of high-dimensional systems [175]. We report on both works in this Chapter.

4.1 Quantum Stochastic Walk dynamics for Quantum State Discrimination through a network receiver

In Section 1.3, we described the basics of Quantum State Discrimination. We also mentioned the many different approaches that are possible while developing QSD protocols. In particular, there are some of them that feature the application of the Quantum Walk model. In [176–178] the application of Quantum Walks as quantum state measurement devices is investigated and demonstrated, with some reminiscence of weak measurements protocols [179, 180]. A recent work suggested the employment of a generalized model of Quantum Walk as a tool for Quantum State Discrimination [181], a quantum evolution pattern known as Quantum Stochastic Walk (QSW) [182]. This generalized model interpolates Quantum and Classical Random Walk evolution as a function of a real parameter. In [61], a quantum receiver with a neural network structure is conceived and studied, featuring QSW dynamics. We briefly review the methods and results of this work, in order to gain some useful insights for the following discussion. We consider a QSW on a graph $\mathcal{G} = (\mathcal{N}, \mathcal{E})$, where $\mathcal{N}$ is the set of nodes of the graph and $\mathcal{E}$ is the set of edges connecting the nodes and outlining the graph. We denote the edges as node pairs $(\mathcal{N}_i, \mathcal{N}_j)$. We can summarize the edges set as the

adjacency matrix A:

$$A_{j,i} = \begin{cases} w_{j,i}, \text{if } (\mathcal{N}_i, \mathcal{N}_j) \in \mathcal{E} \\ 0, \text{if } (\mathcal{N}_i, \mathcal{N}_j) \notin \mathcal{E} \end{cases} \tag{4.1}$$

where $w_{j,i} \in \mathbb{R}$ is the weight of the corresponding edge. We consider equal weights and an undirected graph, such that $A_{j,i} = A_{i,j}$. In a random walk on a graph, the dynamics are defined by a transition matrix $T = AD^{-1}$, where $D = \sum_j A_{j,i}$ represents the number of nodes connected to i. T makes the distribution of occupation probability $\vec{q}(t)$ evolve in time, $\vec{q}(t+1) = T\vec{q}(t)$. In the quantum case, the nodes are the basis vectors of the Hilbert space describing the graph and the evolution is driven by the system Hamiltonian H and the Schrödinger equation. We can interpolate between the two scenarios considering the general case of both a quantum and classical evolution. We consider the density matrix ρ describing the state of the system and and the evolution driven by the Gorini-Kossakowski-Sudarshan-Lindblad master equation:

$$\frac{d\rho}{dt} = -(1-p)i[H,\rho] + p\sum_{i,j}\left(L_{i,j}\rho L_{i,j}^{\dagger} - \frac{1}{2}\{L_{i,j}^{\dagger}L_{i,j},\rho\}\right) \tag{4.2}$$

that is the equation regulating a Quantum Stochastic Walk evolution, where $\{L_{i,j}\}$ are the Lindblad operators [183]. In practice, we interpolate between the quantum evolution driven by H and the classical, incoherent evolution driven by the $L_{i,j} = \sqrt{T_{i,j}}\,|i\rangle\langle j|$, through the parameter p representing the probability of classical "noise" occurring in the quantum dynamics, hence the probability of the quantum walk collapsing into a classical random walk. In [61], H and T are optimized independently of the adjacency matrix, that is only used to define the topology of the considered graph, while accounting for the constraints on T:

$$\begin{cases} 0 \leq T_{i.j} \leq 1 \ \forall i,j \\ \sum_i T_{i,j} = 1 \end{cases} \tag{4.3}$$

and taking a symmetrical H, such that $H_{i,j} = H_{j,i}$. Nodes of the graph may have different characterizations: in the network, they are divided among *input nodes*, where the initial state is prepared at the start of the dynamics, *sink nodes*, where the system is trapped, i.e. if if the system reaches this nodes its evolution stops, and *sinker nodes*, sites from which it is possible to be sent to a sink node. In particular, sink nodes are conveniently considered as external nodes, attached by means of directed edges to the sinker nodes, so that the symmetrical properties of the remaining graph are not hindered (without any drawback, since the system in the sink nodes does not follow any dynamics). This addition to the network evolution can be expressed through a further term in Eq. 4.2, featuring an additional Lindblad operator $L_n = |n\rangle\langle s_n|$, where $|n\rangle$ represents the sink node and $|s_n\rangle$ the corresponding sinker one:

$$\sum_{n=1}^{\mathcal{M}} \Gamma(2\,|n\rangle\langle s_n|\,\rho\,|s_n\rangle\langle n| - \{|s_n\rangle\langle s_n|,\rho\} \tag{4.4}$$

where $\mathcal{M}$ is the number of sink nodes, and Γ is a timescale factor. It is worth stressing that L_n is the only operator involving the sink nodes $\{|n\rangle\}$, since the Lindblad operators $\{L_{i,j}\}$ only act on internal nodes of the network. Thus, there is no way of evolving back from the sink nodes to

the network. In conclusion, the dynamics of a Quantum Stochastic Walks on a graph featuring additional sink nodes can be written as:

$$\frac{d\rho}{dt} = -(1-p)i[H,\rho] + p\sum_{i,j}\left(L_{i,j}\rho L_{i,j}^{\dagger} - \frac{1}{2}\{L_{i,j}^{\dagger}L_{i,j},\rho\}\right) + |n\rangle\langle s_n|\rho|s_n\rangle\langle n| - \{|s_n\rangle\langle s_n|,\rho\} \quad (4.5)$$

in the continuous time case. In general, the sink nodes represent the measurement apparatus, where the system exits the network and is detected. We are interested in the population of these sinks at a certain time τ: $\rho_{n,n}(\tau) = \langle n|\rho(\tau)|n\rangle = 2\Gamma\int_0^\tau \rho_{s_n,s_n}(\tau)$. This result provides us with the fact that the population of the sinks is proportional to that of the sinker nodes, which depends in turn on the evolution parameters.
The method employed in [61] to harness QSWs for Quantum State Discrimination stems from this considerations: they conceive a quantum receiver with a neural network structure, composed of an input layer (where the states to be discriminated are encoded), an intermediate layer that contains the sinker nodes, and an output layer made of the sink nodes. The number of sink nodes equals the number of states to be discriminated, and each of them $|n\rangle$ is associated to a state $|\psi_n\rangle$. The Hamiltonian H is set in such a way that, at the end of the measurement time τ, the cumulative probability $\rho_{n,n}(\tau)$ is maximum for an initial state of the network $|\psi_n\rangle$. They show that by their method, the authors are able to achieve optimal results corresponding to the theoretical bounds mentioned in Sec. 1.3. We established a collaboration with Professor Caruso of the University of Florence (one of the author of [61]), aiming at the experimental realization of a simple network-like receiver; we were able to even exceed this goal, by devising a protocol that employs the network for a more powerful task than it was initially foreseen.

4.2 Experimental realization of a network-like receiver

We were interested in the $p = 0$ and discrete time case of the model described above; this required a new formalization of the problem, that is described in detail in the following. In particular, some operators and parameters are neglected or completely redefined, in order to make the discussion linear and provide a better adherence between theoretical model and experimental implementation.

4.2.1 Theoretical model

We aimed at experimentally realizing a network featured by a 2 nodes-2 nodes-2 nodes topology, characterized by 2 nodes in the input layer, 2 sinker nodes and 2 sink nodes. In particular, we wished to realize a network without connections between nodes of the same layer, as depicted in Fig. 4.1 for binary QSD. In compliance with the nomenclature adopted in [61], we refer to such topology as 2r-2r-2 in the following discussion. The network features six nodes and six edges; in particular we denote as $\{1,2\}$ the input layer's nodes, which are connected in an undirected way to the nodes $\{3,4\}$ of the intermediate layer. In turn, the intermediate layer nodes share directed links with nodes $\{5,6\}$, that form the output layer, composed of the sink nodes.

Though our theoretical scheme is undoubtedly derived from [61], we propose a slightly different model, where the evolution is time discrete and the system can not linger on the same state after an evolution step. Thus, the evolution of the system can be pictured as follows: the state of the network switches from a superposition of the input nodes to a superposition of the intermediate

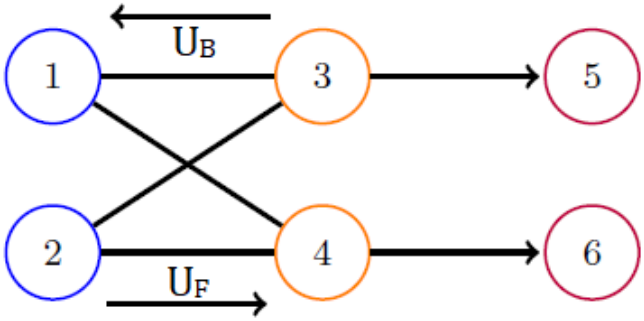

Figure 4.1: 2r-2r-2 model of the quantum network. *The system goes from a superposition state of input layer nodes* $\{1,2\}$ *to one of* $\{3,4\}$*, evolving according to the unitary evolution* $\hat{U}_F$*. Then, the population of the system which has not been trapped in the sinks evolves through* $\hat{U}_B$ *to a new general state of the input layer nodes, starting a new evolution loop. This figure is drawn from [174].*

ones. Then, it has a certain probability of getting caught in a superposition of the sink nodes or to turn again into a combination of the input nodes. Hence, the loop evolution starts again, although the dynamics necessary vanishes as time progresses, since all the population will be eventually lost to the sinks. Through this model, we achieved both the dynamical binary discrimination suggested in [61] and a novel protocol, that extend the employment of the time degree of freedom.

4.2.2 Experimental implementation

We developed a bulk optical setup reproducing the network described above in the polarization and position degrees of freedom of single photons, reported in Fig. 4.2. The nodes of each layer correspond to the orthogonal polarization states $\{|H\rangle, |V\rangle\}$, while the different layers correspond to different positions along the photon path. First of all, the initial state $|\psi\rangle$ of the system has to be set by a unitary preparation stage $\hat{U}_P$. We apply unitary operations to the photon polarization through waveplates sets composed by a sequence of a quarter waveplate (QWP), a half waveplate (HWP) and a further QWP; we remind here that by means of this waveplates sequence it is possible to apply any unitary operator to the polarization degree of freedom of light. Since the state of the photon coming from the source is $|H\rangle$, we can easily transform it into any superposition $|\psi\rangle = \alpha|H\rangle + \beta|V\rangle$ we require through such a waveplates set. After preparation, we can consider the system to be in the input layer of the network in Fig. 4.1, where the superposition of polarization states $|H\rangle$ and $|V\rangle$ corresponds to a superposition of the nodes 1 and 2. The evolution begins then, and the single photons undergo the first evolution stage by the application of the *forward unitary operator* $\hat{U}_F$ that brings the system from nodes $\{1,2\}$ to $\{3,4\}$, that act as the sinker nodes, encoded again in polarization. Since the nodes in each layer are encoded in the same degree of freedom, different layers are identified by different positions in the setup. After this first evolution step, a Beam Splitter (BS) is placed along the path. Then, the photon can be transmitted to the sink nodes with probability p_s or sent back into the network with probability $1 - p_s$, where it continues the evolution from the input layer. In the first case, the photon travels towards the sinks and impinges on a Polarizing Beam Splitter (PBS) which separates the $|H\rangle$ and $|V\rangle$ components of the photon state, corresponding to the sink nodes $\{5,6\}$, and then it is measured by Avalanche Photodiodes (APD) detectors. If, instead, the photon is driven again into the network, it is subject to the *backward unitary operator* $\hat{U}_B$, the operator describing the propagation of the system from nodes $\{3,4\}$ to

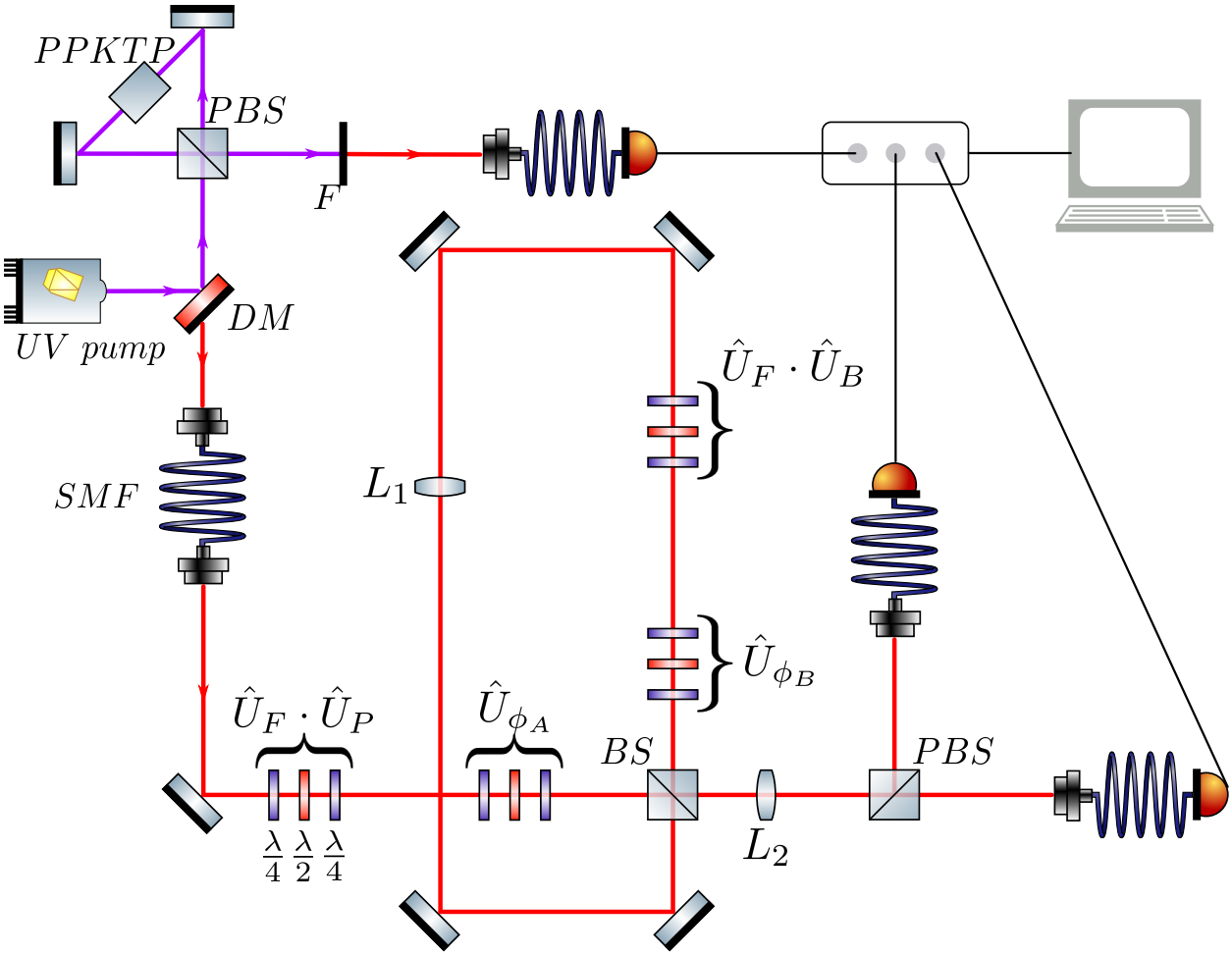

Figure 4.2: Experimental implementation the 2r-2r-2 network. *The total unitary operator $\hat{U} = \hat{U}_F \cdot \hat{U}_P$ is actually encoded in a single QWP-HWP-QWP set, in order to reduce losses and systematic errors. Each of the optical elements imposes a phase shift ϕ_x between the different polarization components. The phase shifts are compensated by the supplemental waveplates sets $\hat{U}_{\phi_{A/B}}$. One lens, identified by L_1, is positioned along the loop to prevent losses due to beam divergence; a second one, L_2, is located along the extraction path to allow photon collection through multi-mode fibers. This figure is drawn from [174].*

$\{1, 2\}$. The system is again in a superposition of the input nodes, where the evolution can start again, by another application of $\hat{U}_F$. In this way, the system evolves from a state of nodes $\{3, 4\}$ to $\{1, 2\}$ and then again to nodes $\{3, 4\}$. It is worth mentioning that, in our setup, we use a single set of waveplates QWP-HWP-QWP to apply the joint operator $\hat{U}_F \cdot \hat{U}_B$. At this point, the walker passes again through the BS, beginning another loop evolution or being detected in the sinks. Clearly, this setup provides an experimental realization of a 2r-2r-2 network, where we have the ability to gather how many loop evolution the system has performed before being detected. That is possible because the detection of photons that have travelled through the network is performed in coincidence with another photon produced by the same generation event. Indeed, we generate photon pairs through the high brilliance SPDC source described in Section 3.3: their initial state of polarization is $|H\rangle_s \otimes |H\rangle_a \equiv |H, H\rangle$, where we use the subscript s to denote the *system* photon, which undergoes the network evolution, while the subscript a indicates the *ancilla* photon, which is directly sent to detection and is exploited as an external trigger. After both photons are collected, we process their detection event by an ID-Quantique time tagger ID800: this device features the possibility of setting

a narrow coincidences window (up to 81 ps), the capability of recording the relative detection time of a photon, hence the possibility of electronically setting any delay between two photon counters with the aim of computing coincidences and also to perform high-resolved time scanning of the delay between two detecting channels. In this way, we can set as contemporary the events corresponding to the detection of the ancilla and the photon extracted after the first step of the evolution (0 loops completed) and, in general, we can find out the number of loops travelled by the system photon by analyzing the delay between its detection and the ancilla's. In order to perform this kind of operation, we need to have a negligible contribution from successive photon generations. The flux rate of pairs of photons generated by the source is $N_p/s \sim 100000/s$. Therefore, the mean time between the generation of one photon and the subsequent one is $t = 1s/100000 = 10^{-5}s$, corresponding to a mean space separation between two consecutive photon pairs of $l = t \cdot c \sim 3000m$. Therefore, we set the length of the optical loop to $x \sim 2m$, corresponding to a travel time of $\sim 7ns$, which grants on average a time distance corresponding to around 1500 loops between one photon generation and the next. We focused on the observation of the first 20 steps of the evolution, which we estimated as a good compromise between feasibility and data significance, considering a net loss of signal per loop completion $L = 0.057\%$. The probability that a second photon pair is generated in the time interval corresponding to these 20 steps is $(x \times 20/c)/t \sim 0.02$, which is far under other systematic errors. Thus, the experiment is barely affected by spurious coincidences, even employing a CW source such as ours. It is worth mentioning that we didn't take into account the first extraction step, but we rather started from the second one. Indeed, the first step features a different extraction probability with respecte to the following: we employed an unbalanced Beamsplitter (BS) for the extraction of signal, characterized by a transmittivity $T \sim 70\%$ and a reflectivity $R \sim 30\%$. Therefore, as understandable from Fig. 4.2, the first extraction step features R as the p_s mentioned above, while for the remaining ones the rate corresponds to T. Because of that, we chose to neglect the coincidences of photons extracted at the first step. This experimental scheme was at first exploited to demonstrate the binary discrimination protocol proposed in [184].

4.2.3 Experimental binary quantum state discrimination with a network-like receiver

In order to test its capabilities, we used the receiver described above to perform a simple binary quantum state discrimination scheme that relies on dynamical processing of the input states. We considered two non-orthogonal states $\{|\psi_1\rangle, |\psi_2\}\rangle$ encoded in the input layer of the network in Fig. 4.1; we tailored the unitary evolution regulating the network so as to associate the detection of the system in one of the two sinks with the presence of one of the two possible input states rather than the other, with the minimum probability of error. As a consequence, detection in the other sink reveals the other input state. In general, the one-shot protocol for the optimal discrimination of two states consists of the simple projection of the system onto two orthogonal basis states. Suitably choosing the basis, it is possible to achieve the maximum theoretical probability of successful guess, corresponding to the Helstrom bound [40]. Therefore, we can straightforwardly extend this method to a multi-step scheme: we perform an optimal binary discrimination at any step, i.e. each time the system is sent to the output layer. To do that, we only need to present an "optimal" output state at the first extraction step, through the tuning of operator $\hat{U}_F$, and then

tailoring $\hat{U}_B$ to produce the same state at any extraction step. In conclusion, $\hat{U}_F$ must be the optimally discriminating projector and $\hat{U}_B$ must be such that the product $\hat{U}_F \cdot \hat{U}_B = \hat{I}$. Such an optimal network can discriminate among two states up to the Helstrom bound, by the computation of the cumulative population of the sinks in time. The states experimentally exploited for the protocol were $|\psi_1\rangle = \cos\left(\frac{\pi}{8}\right)|H\rangle + \sin\left(\frac{\pi}{8}\right)|V\rangle$ and $|\psi_2\rangle = \cos\left(\frac{\pi}{8}\right)|H\rangle - \sin\left(\frac{\pi}{8}\right)|V\rangle$, setting a direct correspondence with the case studied in [61]. The optimal unitary matrix for the realization of a suitable dynamical discrimination protocol was analytically found by maximizing or minimizing the output probability of each sink with respect to the corresponding input state. The result of this optimization led to the evolution matrix $U = U_F = U_B = \frac{1}{\sqrt{2}}\begin{pmatrix} 1 & 1 \\ 1 & -1 \end{pmatrix}$, which has some analogy to the one computed in [61], besides some peculiar property. Indeed, employing this evolution matrix, the discrimination protocol consists of a repeated optimal single-shot discrimination protocol: the network periodically brings the system in the state of the sinker nodes that allows optimal two state discrimination. In this way, after each round trip through the network, the information on the state is optimally extracted, leading to the output probabilities in time P_5 and P_6 reported in Fig.4.3, where the sink node 5 is associated to the detection of state $|\psi_1\rangle$, while sink 6 to the detection of $|\psi_2\rangle$. It is now interesting to understand the dynamical behaviour of the probability of correct guess (as well as the dynamics of the extracted information). To this aim, the cumulative probability of correct discrimination in time is computed, for both states: $C_1 = \sum_\tau^t p_5^{(1)}(\tau)$, $C_2 = \sum_\tau^t p_6^{(2)}(\tau)$, where $p_k^{(i)}(\sigma)$ is the population of sink k, with input state $|\psi_i\rangle$, measured after the σth loop.

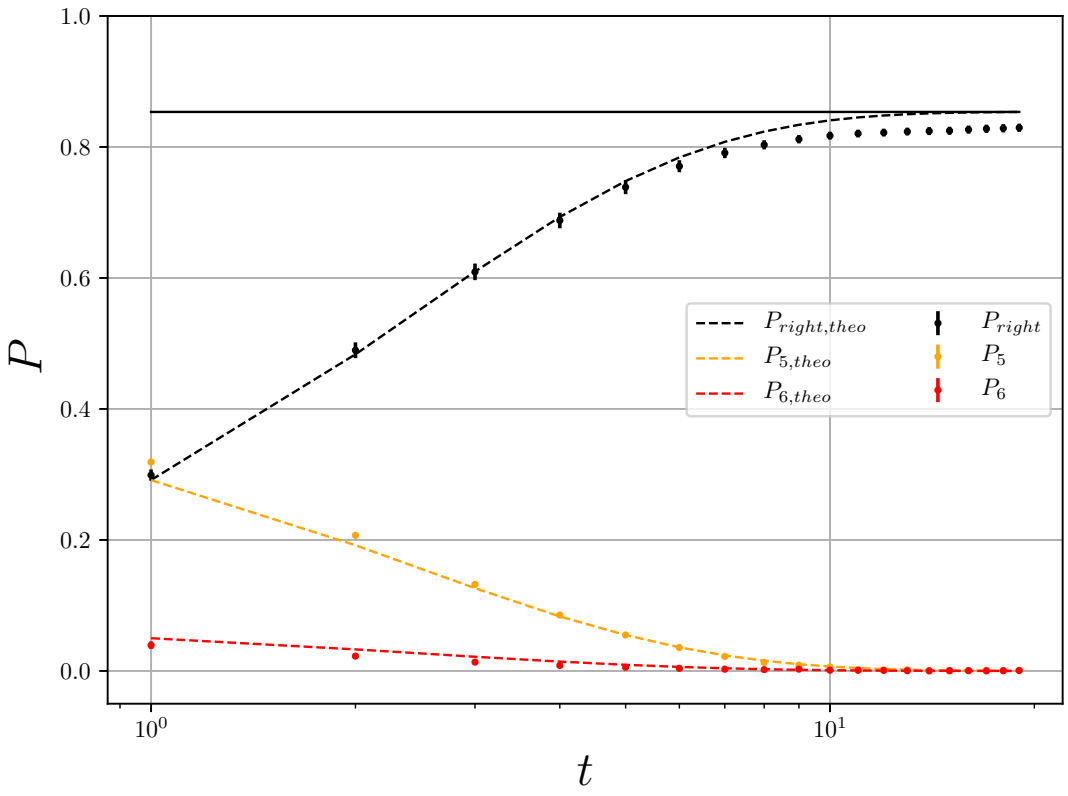

Figure 4.3: Cumulative curve and output probability in time *Temporal evolution of the experimental output probability $P_{5(6)}$ in sink 5(6) for the input state $|\psi_1\rangle$, together with the experimental average cumulative curve P_{right}, corresponding to the total probability of correct discrimination. The experimental results are reported in comparison with the numerical expectations. Black solid line represents the Helstrom Bound computed for the two selected states. A systematic error in the state preparation leads to an imperfect match of the bound, as the extracted information saturates. Figure appearing in [174].*

The curve resulting from the average between C_1 and C_2, normalized to the total cumulative probability, is exhibited in Fig. 4.3 as P_{right}, in comparison with the numerical expectations. The experimental analysis proved the effectiveness of this protocol to achieve Helstrom level binary quantum state discrimination in a dynamical context. These positive results paved the way towards the exploitation of these dynamical features in more complex and powerful protocols, fully taking advantage of a time-binned extraction of information. The following section clarifies this idea and reports on the results of a protocol I designed as another, more powerful, application of the optical network receiver in Fig- 4.2 to a four-state quantum discrimination problem in dimension $D = 2$, in a minimum error probability scenario.

4.3 Multi-state minimum error discrimination protocol via time-binning approach

As we have highlighted in Sec. 1.3, the discrimination of $N > 2$ non-orthogonal states, encoded in a D-dimensional space where $N > D$, is not a problem for which a general solution is known [38]. In particular, we focus on the problem of discriminating sets of four states encoded in the two-dimensional space of photon polarization and we use our network-like receiver to realize a protocol for this task that employs time-multiplexing as a decoding tool. Our method can be applied to

different sets of states and doesn't require auxiliary systems for decoding of information while featuring a clear saving of equipment resources.

4.3.1 Theoretical approach

The protocol consists of a mapping of the quantum features of states in time-wise probability distributions by means of the dynamical features of the network-like receiver. We exploit the time degree of freedom as a supplemental resource in this QSD strategy and, in order to clarify this, we provide a rigorous mathematical discussion of our framework. The network in Fig. 4.1 can be described in terms of two separate subspaces: the first one represents the two layers connected in an undirected way, i.e. the input and intermediate layers, while the second one represents the sink nodes. We write the state of the first subsystem as a 4-dimensional vector, where the first two dimensions represent the input layer and the remaining two stand for the intermediate one. The same framework is adopted in [61]. The state of this subspace, that we denote as *network space*, evolves according to a unitary evolution, determined by the network parameters. On the other hand, we address the subspace of the sink nodes as *sink space*, where no evolution runs, but measurement only. We focus initially on the evolution of a particle (photon polarization) that is prepared in a state of the network space. In our model, the system can not occupy a superposition state of the input and intermediate layers, the only possible states have the form $\begin{pmatrix} \alpha \\ \beta \\ 0 \\ 0 \end{pmatrix}$ or $\begin{pmatrix} 0 \\ 0 \\ \gamma \\ \delta \end{pmatrix}$. Therefore, the one-step evolution of the system is described by a $4x4$ unitary matrix, composed of two antidiagonal blocks $U = \begin{pmatrix} 0 & 0 & a & b \\ 0 & 0 & c & d \\ a' & b' & 0 & 0 \\ c' & d' & 0 & 0 \end{pmatrix}$. We remind here that also the permanence of the system in the same layer after an evolution step is not allowed by our model. The left-bottom block represents U_F, the forward evolution of the system from input layer nodes $\{1, 2\}$ towards the sinker nodes $\{3, 4\}$, while the right-top block stands for U_B, the backward evolution of the system from sinker nodes $\{3, 4\}$ to the input layer nodes $\{1, 2\}$. In the actual implementation, as sketched in Fig. 4.2, both layers are encoded in the polarization degree of freedom, but they are well distinguished one from the other in terms of time and space. This is why, notwithstanding the four dimensional description, we can practically describe the evolution as an alternate application of operators $\hat{U}_F$ and $\hat{U}_B$ to the same 2-D vector. These two matrices can be identically or differently set, producing a symmetric or asymmetric network. We have discussed how we are able to discriminate the extraction time of photons, i.e. the number of round trips the photon has completed through the network before being sent to the sinks. This supplemental degree of freedom, which is crucial in our protocol, can be formally addressed as an auxiliary system, featuring two subspaces: one for the photon travelling through the network, representing the evolution step of the system, and one for the sinks, representing the extraction time. In the following discussion, we label with the subscript n the vector state of the network subspace and with subscript s that of the sinks subspace, both for the actual nodes and the corresponding time degree of freedom. The unitary evolution operators $\hat{U}_F$ and $\hat{U}_B$, which only act on the network subspace, represent now the joint operator $\hat{U}_{F/B} \otimes \hat{I}_s$, being

$\hat{I}_s$ the identity over the sink subspace. Moreover, we define as $\hat{I}_N$ the identity over the joint space of network and sinks, while the identity over the time auxiliary system will be I_t. In conclusion, the evolution of the system in terms of its state in the network subspace n and in the sink subspace s, besides the time degree of freedom, can be divided in three different segments, given the initial state $|\psi_0\rangle_{n,s} = (\alpha_0 |1\rangle_n + \beta_0 |2\rangle_n) |t_0\rangle_n$. In the first one, the initial state evolves from input to intermediate layer through $\hat{U}_F$:

$$\left|\psi_0^{(1)}\right\rangle_{n,s} = (\hat{U}_F \otimes \hat{I}_t) |\psi_0\rangle_{n,s} = (\gamma_0 |3\rangle_n + \delta_0 |4\rangle_n) |t_0\rangle_n \,, \tag{4.6}$$

The second step consists of the extraction to the sink nodes, which corresponds to the generation of a superposition state of the system being in the network or in the sinks at a certain time step, through a projector from the network to the sinks:

$$\begin{aligned} \left|\psi_0^{(2)}\right\rangle_{n,s} &= \Big[\sqrt{T}(\hat{I}_N \otimes \hat{I}_t) + \\ +\sqrt{1-T}\big(|5\rangle_s \langle 3|_n + |6\rangle_s \langle 4|_n\big) \otimes \Big(\sum_{k=0}^{\infty} |t_k\rangle_s \langle t_k|_n\Big)\Big] \left|\psi_0^{(1)}\right\rangle &= \\ = \sqrt{T}\big(\gamma_0 |3\rangle_n + \delta_0 |4\rangle_n\big) |t_0\rangle_n + \sqrt{1-T}\big(\gamma_0 |5\rangle_s + \delta_0 |6\rangle_s\big) |t_0\rangle_s \,, \end{aligned} \tag{4.7}$$

where T is the probability that the system stays in the network and $1-T$ the probability of it being extracted towards the sinks. The last step leads again the network to a state of the input layer, while the sinks do not evolve at all:

$$\begin{aligned} |\psi_1\rangle_{n,s} &= \Big(\hat{U}_B \otimes \sum_{k=0}^{\infty} |t_{k+1}\rangle_n \langle t_k|_n\Big) \left|\psi_0^{(2)}\right\rangle_{n,s} = \\ = \sqrt{T}\big(\alpha_1 |1\rangle_n + \beta_1 |2\rangle_n\big) |t_1\rangle_n + \sqrt{1-T}\big(\gamma_0 |5\rangle_s + \delta_0 |6\rangle_s\big) |t_0\rangle_s \,, \end{aligned} \tag{4.8}$$

where the "time state" of the network has been updated, because a forward and backward evolution has been completed. The evolution continues as a repetition of these three steps, leading to a general state, after M completed loops:

$$\begin{aligned} |\psi_M\rangle = \sqrt{T}^M \big(\alpha_M |1\rangle_n + \beta_M |2\rangle_n\big) |t_M\rangle_n + \\ + \sum_{k=1}^{M} \sqrt{T}^{k-1} \sqrt{1-T}\big(\gamma_{k-1} |5\rangle_s + \delta_{k-1} |6\rangle_s\big) |t_{k-1}\rangle_s \,, \end{aligned} \tag{4.9}$$

where $\alpha_k, \beta_k, \gamma_k, \delta_k$ with $k = 0, .., M$ are the coefficients for each basis state of the network after a k steps evolution. The measurement we are able to perform, in the end, corresponds to a projection on both the sink state and the time step, which determines the probability of finding the system in a given sink, hence a certain polarization state $|\pi\rangle \in \{|H\rangle, |V\rangle\}$, at a certain time t^k:

$$P(\{\pi_s, t_s^k\}) = \left|\langle\pi|_s \left\langle t^k\right|_s |\phi\rangle_s\right|^2 \tag{4.10}$$

where $|\phi\rangle_s$ is a general joint state of the sinks and the associated extraction time. The whole evolution is completely deterministic until the measurement, so that the initial state determines the output probability distribution: $P(\{\pi_s, t_s^k\}) = P(\{\pi_s, t_s^k\} | |\psi_0\rangle_n)$. This formalism allows us to

intuitively describe the capability of our setup to exploit time as a further degree of freedom for discrimination, while the actual realization is implemented through a set of subsequent post-selection procedures.
The exploitation of a globally asymmetrical network unitary, with $U_F \neq U_B$, is at the basis of the four state discrimination protocol I devised. In particular, this method is effective for a set of geometrically uniform states [38], since we consider the network parameters to be fixed in time. Indeed, the first implementation of our model for four state discrimination involved a set of geometrically uniform states (GUSs), i.e. a set of equally likely states that feature a particular symmetry with respect to a given transformation $\hat{U}$; specifically, they form a finite Abelian commutative group [42]. We took into account the case of the geometrically uniform *quantum* states:

$$\begin{aligned} |+\rangle &= 1/\sqrt{2}\,(|H\rangle + |V\rangle), \\ |-\rangle &= 1/\sqrt{2}\,(|H\rangle - |V\rangle), \\ |R\rangle &= 1/\sqrt{2}\,(|H\rangle + i\,|V\rangle), \\ |L\rangle &= 1/\sqrt{2}\,(|H\rangle - i\,|V\rangle). \end{aligned} \tag{4.11}$$

The unitary representing the network evolution is tailored with the aim of producing the most different output probability distributions as the four different states occur in the input layer. That was achieved selecting one of the two sinks and requesting that each different input state featured the relative highest probability of extraction in one of the first four time bins. This corresponds to associate an output polarization-time pair $\{\pi_i, t_i\}$ with one of the states $|\psi_i\rangle$ and to maximize the conditional probability $P(\{\pi_i, t_i\}|\,|\psi_i\rangle)$. We aim at guessing correctly the input state from the outcome of our measurements: hence we need to associate each state $|\psi_i\rangle$ with a pair $\{\pi_i, t_i\}$ and we want to maximize the conditional probability $P(|\psi_i\rangle\,|\{\pi_i, t_i\})$. By Bayes' rule:

$$P(|\psi_i\rangle\,|\{\pi_i, t_i\}) = \frac{P(\{\pi_i, t_i\}|\,|\psi\rangle_i) \times P(|\psi\rangle_i)}{P(\{\pi_i, t_i\})} \tag{4.12}$$

where $P(\{\pi_i, t_i\}) = \sum_{j=1}^{4} P(\{\pi_i, t_i\}|\,|\psi_j\rangle) \times P(|\psi_j\rangle)$. Therefore, thanks to the optimization performed above on the network parameters, we shall also get the optimal guessing probability.

The optimal evolution matrices that were found following our maximization method were $U_F = \frac{1}{\sqrt{2}}\begin{pmatrix} 1 & 1 \\ 1 & -1 \end{pmatrix}$ and $U_B = \frac{1}{\sqrt{2}}\begin{pmatrix} \frac{1+i}{2} & \frac{1+i}{2} \\ \frac{1-i}{2} & \frac{-1+i}{2} \end{pmatrix}$. The product matrix, representing the loop evolution of the system between two distinct extraction steps, resulted then $U_L = U_F U_B = \frac{1}{\sqrt{2}}\begin{pmatrix} 1 & i \\ i & 1 \end{pmatrix}$. It is worth noting that $U_L^4 = I$, from which a four steps-periodicity of the output probability distributions derives. Therefore, the first four time bins contain all of the information on the input state, while the experimental exploitation of the further ones is only useful for collecting a greater amount of meaningful signal. Actually, the information extracted in one of the sinks is complementary to that extracted in the other one, so that even the first two time bins would suffice. Indeed, in the experimental realization of the protocol, this would correspond to a heavy waste of signal, as we discuss in the following. From an analytical point of view, if we consider only one of the two sinks, e.g. the one corresponding to horizontal light polarization, the measurement at each time step t represents the application of the POVM $U_L^t \circ |H\rangle\langle H|$. Hence, our setup is capable of reproducing

the families of POVM identified by the global unitary of the loop and depending on the evolution step parameter $\{U_L^t \circ |H\rangle\langle H| \,|t \in \mathbb{N}\}$ and $\{U_L^t \circ |V\rangle\langle V| \,|t \in \mathbb{N}\}$, although the actually distinct POVMs for each set are only four. Since the states we are considering are geometrically uniform, separated by a $\frac{\pi}{2}$ rotation around the same axis, this kind of procedure yields an optimal output. Indeed, without changing the network parameters in time, it is possible to achieve a $P_{err} = 0.5$, which is the analytical bound for a set of four GUSs, as we demonstrated in Sec. 1.3. This is understandable by looking at Fig. 4.4a), where the numerical probability of detection in the first four time bins is displayed for the geometrically uniform set. The distributions are normalized in such a way that, given a certain polarization and time outcome, the total probability equals to 1; we are indeed considering the $P(|\psi_i\rangle \,|\{\pi, t\})$ for each $i = 1, ..., 4$. In this way, the error probability of guess can be straightforwardly computed considering the right time and polarization pairs:

$$\bar{P}_{guess} = \frac{1}{4}\sum_i P(|\psi_i\rangle \,|\{t_i, \pi_i\}) \tag{4.13}$$

In this theoretical analysis, we are not considering that in the experimental framework the total signal decreases as the system experiences an extraction step, as well as the fact that some of the signal will be detected at further step of the evolution. These aspects are discussed in the following.

The theoretical probability distributions of Fig. 4.4, each of which provides an unambiguous "time signature" of a given input state, clearly show the four step-periodicity of the probability trajectory in time that we anticipated above. This feature relies on the network structure of our receiver and is intimately connected to the number of its intermediate layers. In this particular case of study, we considered two pairs of orthogonal states, providing an intrinsic advantage in producing maximally different time dependent distributions. The same protocol was also applied to the set known as Tetrad set [51], consisting of four mutually maximally distant states on the Poincaré sphere:

$$\begin{aligned}
|\psi_1\rangle &= 1/\sqrt{3}\,(-|H\rangle + \sqrt{2}e^{-2\pi i/3}\,|V\rangle)\\
|\psi_2\rangle &= 1/\sqrt{3}\,(-|H\rangle + \sqrt{2}e^{2\pi i/3}\,|V\rangle)\\
|\psi_3\rangle &= 1/\sqrt{3}\,(-|H\rangle + \sqrt{2}\,|V\rangle)\\
|\psi_4\rangle &= |H\rangle
\end{aligned} \tag{4.14}$$

featuring several interesting properties for quantum communication and cryptography [51]. The results of the theoretical analysis for the Tetrad set are shown in Fig. 4.4b). For this latter set, the network optimization was carried according to the same method as for the other set, that practically corresponds to the maximization of the discrimination probability between different pairs of states at each extraction step. The resulting evolution matrices, resulting from a numerical maximization, were

$$U_F = \frac{1}{\sqrt{2}}\begin{pmatrix} 0.953 & 0.303 \\ -0.303 & 0.953 \end{pmatrix} \text{ and } U_B = \frac{1}{\sqrt{2}}\begin{pmatrix} -0.675 + 0.217i & 0.212 - 0.673i \\ -0.212 - 0.673i & -0.675 - 0.217i \end{pmatrix} \tag{4.15}$$

which, again, produce a loop evolution $U_L \sim \frac{1}{\sqrt{2}}\begin{pmatrix} 1 & i \\ i & 1 \end{pmatrix}$. In this case, the method produces a theoretical $P_{err} > 0.5$, therefore the protocol is slightly suboptimal. Indeed, the distribution

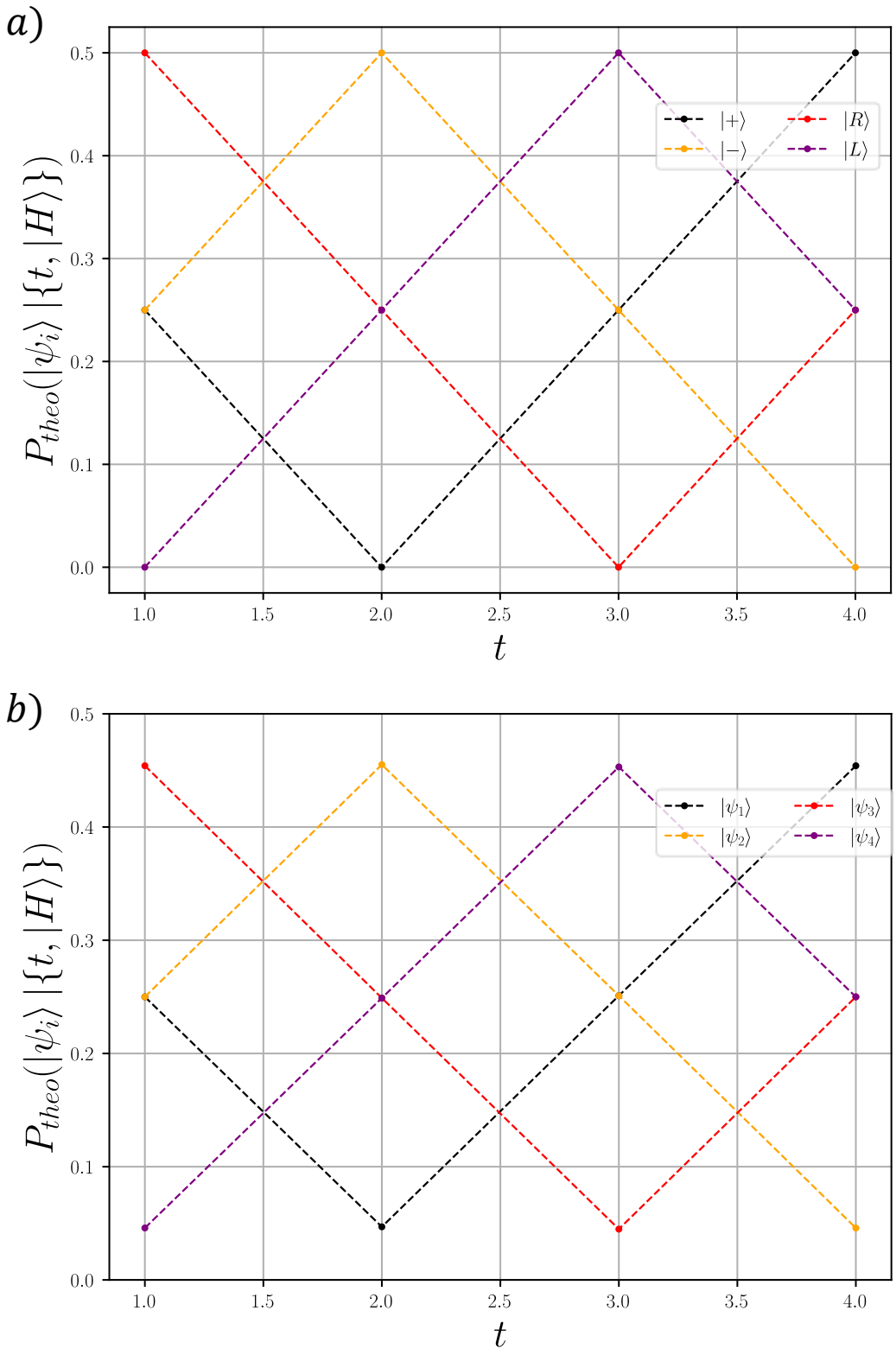

Figure 4.4: Theoretical output probability distributions for both states sets. *Time-wise output probability of the first four extraction steps when a) the geometrically uniform states and b) the Tetrad states circulate in the network. Figure taken from [174]*

minima are not vanishing (see Fig. 4.4b)), but a more powerful optimization procedure may return more effective results. Nevertheless, as discussed below, as the number of available copies increases,

the error probability scales down exponentially.

4.3.2 Experimental results

In our experiment, we focused on the observation of the information dynamics rather than on the actual performances of our receiver. Therefore, we measured the population for as many time steps as possible, considering one sink only, i.e. a single one of the two output polarizations, namely $|H\rangle$. We were interested in observing the differences among the probability dynamics we imposed and we quantified them by different figures of merit. First of all, we considered the probability that a photon featuring a given initial polarization state left the network, function of the evolution step, $P(\{|H\rangle, t\}||\psi_i\rangle)$, normalized in such a way that $P(|H\rangle) = 1$ and $P(|\psi_i\rangle) = 1$, since we knew the initial state of the photon. Such experimental detection probability distributions in time for both sets of states are reported in Fig. 4.5, in comparison with the numerical ones, computed accounting for signal decrease after each evolution step and experimental parameters. These probability distributions were reconstructed recording the number of photons extracted in the $|H\rangle$ sink after any number of travelled loops up to $t = 20$; this was possible thanks to the heralding procedure described in Subsec. 4.2.2. The measured coincidences had to be cleaned off the background noise: as we discussed above, the first actual detection step, not taken into account in the analysis, featured a much higher signal with respect to the following ones. Therefore, it caused a high rate of spurious coincidences for any considered delay. A measurement of the background noise due to the first extraction photons was performed for the delays corresponding to output time bins and directly subtracted to the time-binned measurements, in order to get time-wise coincidences profiles which only displayed actual coincidences.
In conclusion, clean step-wise coincidences counts were obtained, for each input state of both the considered sets. Because of the high number of detected coincidences, the resulting output was considered as an average result per se. Therefore, the output probability distribution for each input state, displayed in Fig 4.5, were directly deduced by the normalization of the clean coincidences profiles. The time dependent distributions show a good agreement with the numerical expectations computed accounting for actual parameters, demonstrating a reliable procedure of multi-state discrimination, without the exploitation of any supplementary system, or spreading the states in multi-mode configurations which would require an abundance of detecting devices. Specifically, by combining Eq. 4.21 and Eq. 4.13, the average probabilities of guess which can be computed by such experimental distributions are $\bar{P}_{guess}^{compass} = 0.483 \pm 0.027$ and $\bar{P}_{guess}^{tetrad} = 0.444 \pm 0.021$.
The discrepancy with the ideal case values can be understood in terms of the losses and imperfect phase-compensation, which produce small but significant polarization rotations, hence slightly lower maxima and higher minima in the distributions. The losses are considered by the simulation results reported in Fig. 4.5, where the experimental errors are computed according to a Montecarlo procedure, considering a Gaussian uncertainty of 0.5° on every wave-plate angular position. It is worth noting that error bars computed according to this procedure yield larger uncertainties on values that are not minimum nor maximum values of the distributions, while they are smaller on maxima and minima, that are practically used to estimate the effectiveness of our protocol: we can provide little insight regarding this matter, apart from a possible resilience to internal noise of the joint POVMs-states chosen set, which may deserve further investigation. Indeed, the normalization we impose to data reported in Fig. 4.5 also plays a part in the error propagation process leading to

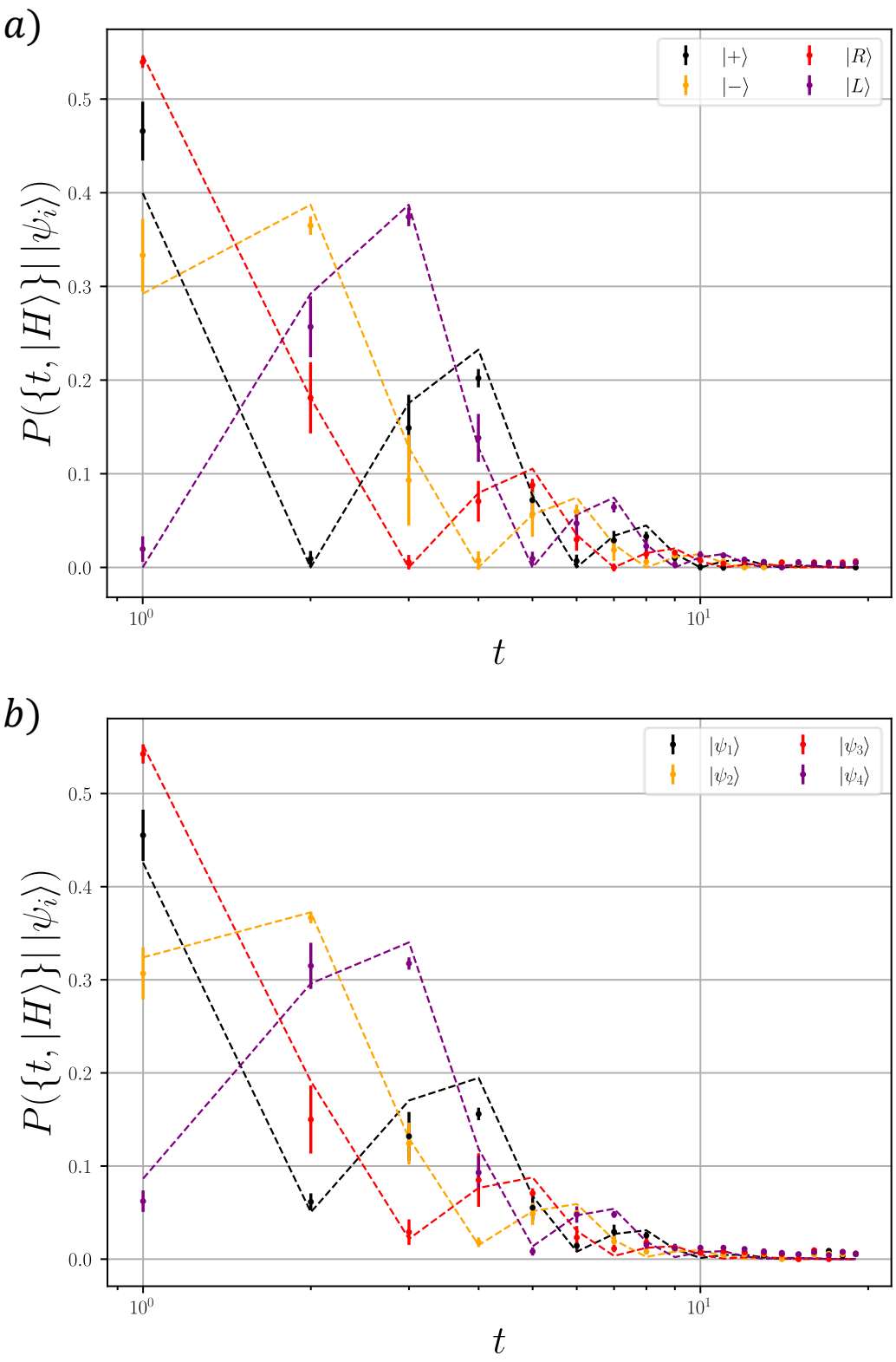

Figure 4.5: Step-wise output probability for a) geometrically uniform states and b) the Tetrad set, sink 5 (horizontal polarization). *Experimental output probability as a function of the number of round trips travelled by photons when a) the geometrically uniform states and b) the Tetrad states circulate in the network. Normalization of each distribution is performed summing over the total output probability for each single state, in order to account for the experimental signal decrease as the observed time bin grows. Data are reported in comparison with corresponding numerical results (dashed lines). Figure taken from [174].*

the aforementioned behavior. Another very important source of noise consists of the background coincidence counts, which are only partially removed by the procedure described above.
By our scheme, we need half the photon-counting detectors which would be needed if we were to actually apply separately each projective measurement, together with the capability of discriminating the arrival time of photons without strict precision requirements. In this case, we were able to do that by an additional APD detector performing coincidence measurements, but this issue may be easily addressed by using a pulsed pump single photon source, so that the presence of a trigger photon could be simply replaced by a suitable synchronization procedure.
In order to verify the effectiveness of the multi-state discrimination protocol in an actual scenario, we tuned the photon source depicted in Sec. 3.3 to a low average photon number regime: through this source, it is not possible to deterministically generate photons, but it is rather possible to set an average rate of generation of single photons. Nevertheless, through this procedure, it was possible to test the average quality of the protocol by computing the average error probability P_{err} as a single copy of the system is available and how this quantity scales as the average available number of copies grows. The experimental strategy to compute the average P_{err} starts by setting the average rate of photon generation per second of the source. An average rate of 1-2 total observed coincidences per second was set, and a higher average photon number was straightforwardly obtained by integrating for a longer time. In this regime, the same time-binned measurements exploited to evaluate the step-wise output distributions were performed, registering n-seconds events for different integration time intervals n. We address as *n-seconds event* a time-binned measurement performed for n seconds. The events measured in this way still had to be cleaned off the accidental coincidences, as mentioned in the previous section. Hence, it was not possible to consider single instances of n-seconds events, but rather an average n-seconds event had to be taken into account, to get the chance of subtracting background noise (which is only meaningful as an average quantity).
We considered the temporal probability distributions sampled in the previous section: for each of the two sets, we had four time-wise sampled probability distributions $P_i(t|\,|\psi_i\rangle)$, one for each of the states in the set, describing the conditional probability of a photon being extracted at time t, given a certain input state $|\psi_i\rangle$. We normalized these probability distributions to 1 without particular consequences, since we were considering the case of equally likely states and we limited observation to one sink only. Indeed, we ignored events from the $|V\rangle$ polarized output because they represented complementary data with respect to the ones yielded by the other output port. In application cases, the corresponding signal must naturally be taken into account, since it carries meaningful information. Thus, if we have an average m-photon event $\bar{E}_m$, measured as described above and cleaned off the noise, we can compute the probability of this event, given the input state we set, as $P(\bar{E}_m|\psi_i) = \prod_t P_i(n_t^{(m)})$ where $n_t^{(m)}$ is the number of photon detected at time t for the event $\bar{E}_m$. As a consequence, the probability of error in guessing the input state can be computed as:

$$P_{err}(\psi_i, m) = 1 - P(\psi_i|\bar{E}_m) = 1 - \frac{P(\bar{E}_m|\psi_i)}{\sum_{\psi_j} P(\bar{E}_m|\psi_j)} \tag{4.16}$$

exploiting Bayes' rule. The resulting trends of P_{err} in function of the average number of detected photons, which act as the available amount of copies of the system, are shown in Fig. 4.6, for both sets of states.

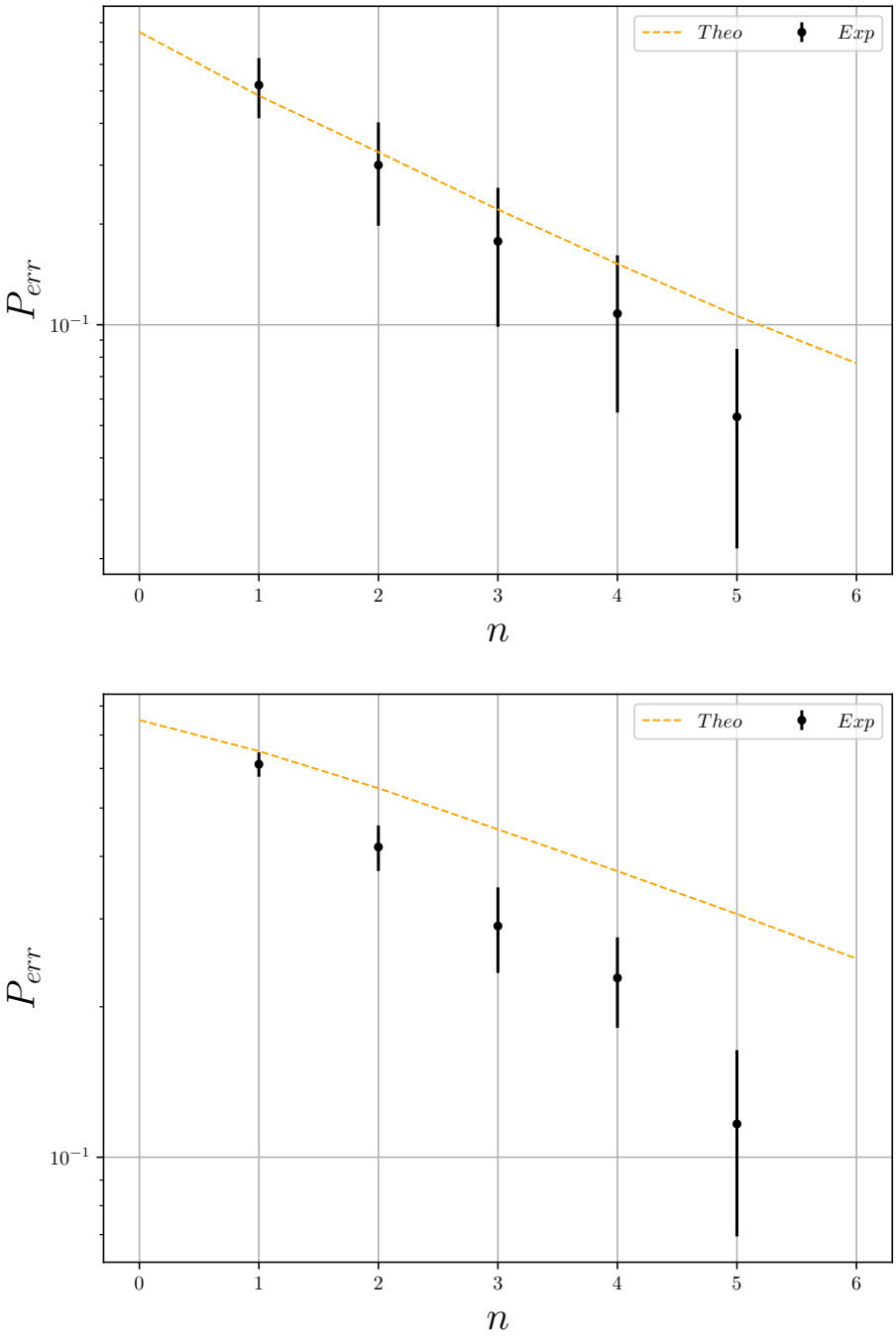

Figure 4.6: Error probability scaling for both states sets. *Scaling of the error probability as a function of the number of analyzed copies of the system, for the geometrically homogeneous states (top) and the Tetrad states (bottom). It is worth noting that, in our specific framework, experimental asymmetries appear to produce a scaling of the probability of correct detection as the number of employed photons grow which deviates from theoretical expectations. In addition to the experimental uncertainty over the y-axis, the photon number n has to be considered as affected by a Poissonian uncertainty equal to* $\sqrt{n}$. *Figure taken from [174].*

4.3.3 Noise-robustness: preliminary analysis

We investigated the robustness of the protocol to the kind of noise which is most likely in application scenarios: the receiver is usually easy to isolate from the environment, while, if the exchange of qubits is remote, the transmission channel may be prone to environmental noise. In particular, we perform an experimental simulation in order to understand how the protocol would perform if the initial state were to be affected by some degree of decoherence before reaching the receiver. We simulated this behaviour by measuring the output time-wise distribution of photons featuring initial state $|H\rangle$ and $|V\rangle$ and suitably mixing it to the experimental outcome of the GUS or Tetrad set in the analysis step. Indeed, we can describe a photon which was prepared in a polarization state $|\psi\rangle$ and has undergone decoherence as represented by the state:

$$\rho_0 = (1-d)\,|\psi\rangle\langle\psi| + d(A\,|H\rangle\langle H| + B\,|V\rangle\langle V|) \tag{4.17}$$

where d is the intensity of the decoherence effect, namely the probability for the system to be in a completely classical state, and $A = \langle H|\psi\rangle\langle\psi|H\rangle, B = \langle V|\psi\rangle\langle\psi|V\rangle$. The evolution through the network receivers applies in parallel to the two terms in Eq. 4.17, without any interplay among them. We want to compute the average P_{guess} for different sets of initial states as a function of the level of decoherence affecting the system before analysis. Without accounting for the losses, we have that the probability for the system to be found at a certain time in the sink $|H\rangle$ corresponds to:

$$\begin{aligned} P(\{t,|H\rangle\}|\,|\rho_0\rangle) = \langle H|\,\rho(t)\,|H\rangle = (1-d)\,\langle H|\,U^t\,|\psi\rangle\langle\psi|\,(U^+)^t\,|H\rangle + \\ +d(\alpha\,\langle H|\,U^t\,|H\rangle\langle H|\,(U^+)^t\,|H\rangle + \beta\,\langle H|\,U^t\,|V\rangle\langle V|\,(U^+)^t\,|H\rangle) = \\ = (1-d)\times P(\{t,|H\rangle\}|\,|\psi\rangle) + d\times(\alpha P(\{t,|H\rangle\}|\,|H\rangle) + \beta P(\{t,|H\rangle\}|\,|V\rangle)). \end{aligned} \tag{4.18}$$

Thus we can simply evaluate the three contributions separately and mix them according to the level of decoherence we wish to simulate. In this way, we obtain different trends of the average P_{guess} in function of the decoherence level, depending on the states set we employ. We show the behavior of the GUS set, the Tetrad set and we compare them to the pure numerical results corresponding to the employment of another possible set of GUS states $\{|+\rangle, |-\rangle, |H\rangle, |V\rangle\}$, that we address as **Compass** set, because of the particular way the states are distributed on the Bloch sphere. We report the results in Fig. 4.7.

We can conclude, by observing Fig. 4.7, that the GUS set we considered in the experiment described above is the worst set in terms of noise resilience, although this is a mere consequence of the noise model we chose: indeed, the disruption of coherence would lead all the states in the set to the same $\rho = \frac{1}{2}(|H\rangle\langle H| + |V\rangle\langle V|)$, while the Tetrad and Compass sets would maintain a certain amount of distinguishability. As a consequence, we decided to employ the set $\{|+\rangle, |-\rangle, |H\rangle, |V\rangle\}$ for further application and extension of the protocol, since it does feature the nice symmetry properties of a GUS set, while being more resilient to decoherence.

4.3.4 Remarks regarding experimental time-binning strategy for QSD

Optimal strategies for Quantum State Discrimination of actual quantum states have a great deal of relevance and a wide range of applications: Quantum Communication [185], Quantum Key Dis-

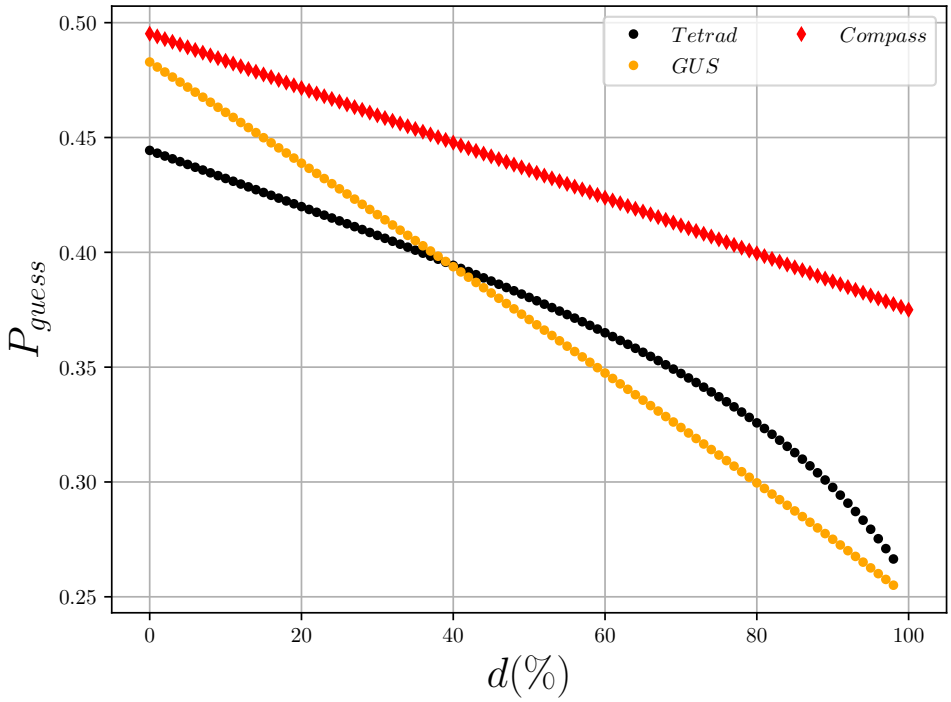

Figure 4.7: Probability of correct guess as a function of decoherence *Experimental simulation scaling of the probability of correct guess in function of the amount of decoherence in the state preparation, for the geometrically uniform states (yellow), the Tetrad states (black) and the Compass set (red), that is marked by diamonds to highlight the theoretical nature of the corresponding trend. The comparison is a mere qualitative analysis, thus we don't report experimental error bars.*

tribution [186] and also Quantum Sensing, in the case of distinguishing different external fields affecting the system dynamics (such as in NV-center noise spectroscopy [187] or avian magnetoreception [188]). In recent years, the development of actual single-photon protocols for QSD has been generally set aside, in favour of protocols requiring the exploitation of coherent states (adaptive strategies, Quantum Phase Shift Keying [54–56, 58]). However, it is well known that the use of coherent states in Quantum Communication protocols does not grant equal security as compared to the exploitation of actual quantum states [189, 190].

In the work reported in this section, as well as in the next one, we exploited actual single-photon states and we achieved a nearly optimal protocol featuring a clear spare of resources, in terms of auxiliary systems and physical measurement devices. For clarity's sake, we stress here that the same protocol can be straightforwardly implemented by means of weak laser pulses, rather than single photons. Anyway, the aim of our work was indeed to realize a protocol that could achieve optimal and effective results without needing to resort to coherent states of light, hence reduced transmission security. The spare of auxiliary physical systems is achieved by the network structure of our receiver, which allows us to implement strategies based on time-binning of information extraction, in the case of binary and multi-state discrimination, without the need for an individual physical implementation for all of the projective measurements; that is a relevant property for applications. This scenario shares some similarities with the weak-measurement framework developed in [179] and [180]; in stark contrast with that, we were able to develop a protocol applying to a higher number of states, to the problem of minimum error probability and with a completely novel the-

oretical and experimental quantum network approach. The exploitation of actual quantum states in this protocol makes it quite interesting for the application to secure Quantum Communication tasks and Quantum Key Distribution, tightly relying on the quantum nature of the implementing platforms for their effective realization. The results we reported in this section represent on one side a basic proof of the effectiveness of our protocol, but they also potentially pave the way to further extensions, such as the adoption of adaptive methods for more general tasks, or the implementation of more complex networks, in order to increase the maximum possible number of states which could be discriminated.
With some improvements,this simple model may be turned in a proper Quantum Neural Network [191], with a potential which is yet to be uncovered in the QSD field. Noise-robustness analysis of the protocol still needs to be thoroughly carried out, consistently with the approach of [61], in order to reveal possible usefulness for Quantum Computing in NISQ devices. Even Machine Learning techniques may be applied to our framework, aiming at the development of quantum machine learning protocols in which quantum information is classified as in classical supervised deep learning schemes. This approach in experimental realizations of QSD protocols features some practical and theoretical advantages for the applications and leaves a lot of room for improvement and generalization. For instance, it is possible to extend the same protocol to more than one degree of freedom in parallel, in order to implement a more complex network and gain the ability to discriminate among a larger set of states. This is the best and most feasible way to scale up our approach: the addition of further layers, hence further concatenated optical loops, may be challenging and would involve a large amount of losses. Moreover, there would not be any increase in the encoding system dimensionality, so that we may be able to discriminate among more states, but with lower accuracy. Therefore, I developed an extended protocol based on the exploitation of photon energy, that led to the realization of a network-like receiver capable of discriminating at the optimal level among eight states encoded in the four-dimensional joint space of energy and polarization of single photons. We report on the experimental demonstration of this protocol in the following section.

Personal contribution

I helped developing and building the experimental setup. I personally designed the four state time-binning protocol and found the optimal configurations for discrimination. I also worked to the realization of the experiment and to data analysis.

4.4 Frequency embedding for enhancement of time-binning QSD strategies

The quest for more powerful QSD protocols is inevitably linked to the search for high-dimensional carriers of quantum information. In general, it is important for quantum communication applications that each carrier that is sent can be filled with as much information as possible, i.e., that high-dimensional systems are exploited [192]. Indeed, *qudits*, d-dimensional quantum bits, can carry much more information than both *qubits* and classical bits [193]. For example, it has been demonstrated that entangled *qudits* allow to get further the capacity of a classical channel [194–196]. As an additional favourable property, high-dimensional quantum states are robust to noise, either

environmental or due to eavesdropping, providing a greater security for Quantum Communication purposes [186, 197, 198].
Thus, the increase in dimensionality of systems employed for Quantum Information tasks represents in any case an advancement towards more powerful and secure Quantum Communication [192]. Quantum State Discrimination is no exception, and the development of protocols harnessing high-dimensional systems is crucial in order to extend their effectiveness and range of application.
We have already discussed how single photons represent one of the best candidates for the role of flying qubits and feature several fundamental properties such as resistance to decoherence, ease of manipulation with bulk linear optic elements, possibility of encoding information in their several degrees of freedom [199]. In Sec. 1.2.7 we have described the working principles of semiconductor quantum dots (QDs), that are emerging as one of the most promising candidates in the wide landscape of single-photon emitters. They can emit single and entangled photons on-demand [200, 201], with high level of indistinguishability [202] and high degree of entanglement, ultra-low multiphoton emission probability [203] and their properties can be enhanced with the combination of photonic cavities [204–207] and strain-tuning [208]. The possibility to successfully employ quantum light from semiconductors QD has been already demonstrated for quantum communication protocols such as quantum teleportation [209, 210], entanglement swapping [211, 212] and their use in quantum key distribution [34, 213, 214]. The increasing performance of QDs in terms of brightness and indistinguishability [205, 215] are drawing interest on this class of emitters for applications in quantum cryptography. Indeed, the simultaneous emission of two photons with a different energy in the biexciton-exciton cascade has already been exploited for spectral multiplexing in quantum cryptography [216]. This is an example of how increasing the Hilbert space dimension of a quantum state can be useful, combining the frequency degrees of freedom with single photon polarization.
As we highlighted in Sec. 1.3, light polarization has been the first and main degree of freedom exploited for experimental Quantum State Discrimination and the only one to be employed in actual single photon experimental attempts [50, 217–219], while, in a coherent state experimental framework, it is possible to increase the system dimensionality in different ways, such as by Quantum Phase Shift Keying (QPSK) [54, 55, 57, 58, 220] or the employment of complex modal structures [221]. Another viable way is represented by the exploitation of multiple copies of the system to increase effectiveness of QSD protocols and allowing for adaptive measurements [49, 54, 56, 222, 223].
The time multiplexing scheme that is described in Sec. 4.3, which led to the experimental demonstration in [174], is flexible to an extension to further photonic degrees of freedom. In the following, I present a protocol exploiting such time-multiplexing method as a tool to achieve a benchmarking result in the framework of single-photon QSD protocols: we implemented an experimental MED protocol for the discrimination of eight non-orthogonal states, using single photons generated by a QD. We harnessed the photon energy as an additional degree of freedom to realize a 4D encoding space. In particular, the eight states were vectors of the joint 4D Hilbert space obtained composing the photon polarization degree of freedom and the 2D space spanned by the two different possible frequencies of photons produced by a biexciton-exciton cascade.

4.4.1 Protocol description

We aim at the discrimination of eight non-orthogonal states encoded in a four-dimensional *qudit* with the maximum probability of success. Our approach focuses again on saving resources, in terms

of hardware and signal, and also on the conservation of a fundamental-level security that could only be guaranteed by the employment of single photons, as we pointed out repeatedly throughout the manuscript.
In this sense, the MED framework is again the best choice, since we wished each measurement outcome to be useful. We wished to perform discrimination among N states of a D-dimensional system, achieving the highest possible average probability of correct guess. This time we only consider a set of geometrically uniform states (GUSs). We stress again that we are taking into account the case of geometrically uniform *quantum* states in a discrete variable framework, rather than their coherent continuous variable counterpart. In any case, we know that for GUSs the minimum error probability of guess (averaged over all the initial states) that is achievable is $P_{err} = 1 - \frac{D}{N}$ [44]. In particular, we are interested in the $N = 8$, $D = 4$ case, which yields again a minimum $P_{err} = 0.5$, that is in turn equal to the successful guess maximum probability $P_{guess} = 1 - P_{err} = 0.5$.
The space we consider is the composition of the one spanned by the orthogonal polarization basis $|H\rangle, |V\rangle$ and the one spanned by a basis of two different frequencies $|\omega_1\rangle, |\omega_2\rangle$. In principle, light frequency could span an infinite dimensional space, but we limited to the two possible distinguishable frequencies that we were able to prepare our input states into and that we were able to discriminate. Hence, we had a joint basis $\{|H\rangle|\omega_1\rangle, |V\rangle|\omega_1\rangle, |H\rangle|\omega_2\rangle, |V\rangle|\omega_2\rangle\}$.
We chose eight states that are globally non-orthogonal, although some subsets of them are:

$$\begin{cases} |\psi_1\rangle = |+\rangle|\omega_1\rangle \\ |\psi_2\rangle = |-\rangle|\omega_1\rangle \\ |\psi_3\rangle = |H\rangle|\omega_1\rangle \\ |\psi_4\rangle = |V\rangle|\omega_1\rangle \\ |\psi_5\rangle = |+\rangle|\omega_2\rangle \\ |\psi_6\rangle = |-\rangle|\omega_2\rangle \\ |\psi_7\rangle = |H\rangle|\omega_2\rangle \\ |\psi_8\rangle = |V\rangle|\omega_2\rangle \end{cases} \tag{4.19}$$

This set is not properly a geometrical uniform one but, in practice, we can treat it as such, since it is composed of two orthogonal subsets that are, in turn, geometrically uniform. The eight states set is indeed a "frequency embedding" of the Compass set defined in Subsec. 4.3.3.
Our discrimination strategy can be summarized as a four state discrimination analogous to the one discussed in Sec. 4.3 as well as in [174], followed by a binary discrimination among the two orthogonal frequency subspaces.

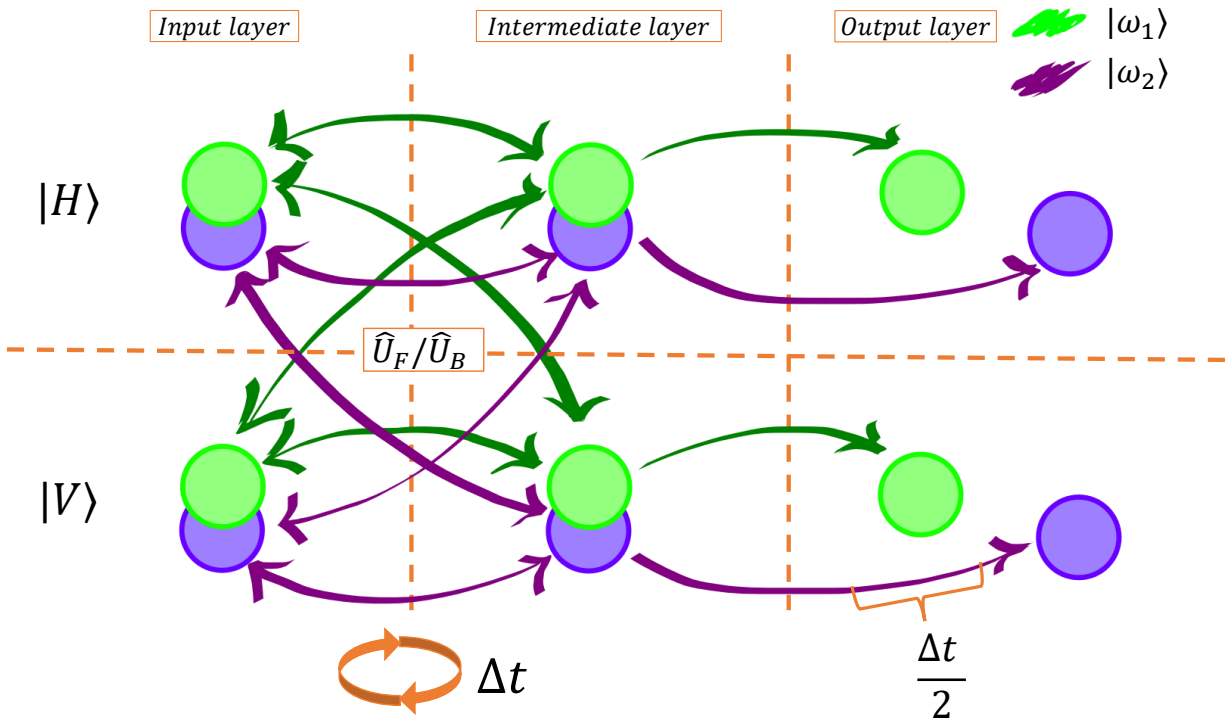

Figure 4.8: Model of the network-like receiver. *The system is prepared in a certain frequency and polarization state, that corresponds to a superposition state of input layer nodes. The system evolves back and forth from the input layer to the intermediate one of two parallel networks, according to the unitary operators $\hat{U}_F$ and $\hat{U}_B$, with a chance of being sent to the output when in the intermediate layer. There, the two identical networks become different, since the output with ω_2 frequency is delayed with respect to the one featuring ω_1. Specifically, this delay is half the travel time of the back and forth evolution between the intermediate and input layers. In this way, signal featuring one of the two frequencies is maximally distinguishable from the other in time. Figure taken from [175].*

This was performed thanks to the imposition of a periodical dynamic on the polarization state of the system. Such an evolution pattern made possible to associate the detection of a photon after a certain evolution step and in a certain polarization state with the presence of a specific input state among the possible eight given in Eq. 4.19.

Our protocol can be described as the processing of the input state through the network depicted in Fig. 4.8, which corresponds to two parallel networks, each analogous to the one in Fig. 4.1 employed for the four states case, inspired by [224]. The polarization state is sent forward and backward through the input and intermediate layers of the network, with a certain probability of being sent to the output layer. The frequency degree of freedom, on the other hand, does not evolve throughout the process and it is globally discriminated by a final projection. There is no way that the two frequencies are mistaken; therefore, states in different frequency subspaces can be regarded as processed through different networks. The evolution from the input layer to the intermediate layer follows again the *forward* unitary evolution $\hat{U}_F$, while the *backward* unitary $\hat{U}_B$ describes evolution from the intermediate layer back to the input one. These are 2x2 unitary matrices acting on the polarization degree of freedom only. These operators act on both frequency subspaces in

parallel, so that the global forward and backward operators $\hat{U}_F^G$ and $\hat{U}_B^G$ are:

$$\hat{U}_F^G = \begin{pmatrix} \hat{U}_F & \begin{pmatrix} 0 & 0 \\ 0 & 0 \end{pmatrix} \\ \begin{pmatrix} 0 & 0 \\ 0 & 0 \end{pmatrix} & \hat{U}_F \end{pmatrix} \text{ and } \hat{U}_B^G = \begin{pmatrix} \hat{U}_B & \begin{pmatrix} 0 & 0 \\ 0 & 0 \end{pmatrix} \\ \begin{pmatrix} 0 & 0 \\ 0 & 0 \end{pmatrix} & \hat{U}_B \end{pmatrix}, \tag{4.20}$$

since in our model switching from a frequency to the other is not allowed. After the application of $\hat{U}_F$ the system is in the intermediate layer. With a certain probability, it is either sent to the output layer, where the frequency discrimination takes place, or it keeps evolving, as in the four state protocol.

We now consider the polarization-wise discrimination, briefly repeating for clarity's sake some of the discussion of Sec. 4.3: in the output layer, we can detect the system in one of two states of polarization, $|H\rangle$ or $|V\rangle$, that from now on we denote as $|H\rangle = \pi_1$ and $|V\rangle = \pi_2$. The probability of finding the system in π_1 or π_2 depends on the initial state and the dynamics it is subject to. The dynamics we impose are such that if the system does not travel towards the output, it may return at a larger evolution step after propagating back and forth through the network. At this point, the probability for the system to be found in one of the two polarization states may have changed. Therefore, we consider the conditional probabilities $P(\{t, \pi\}|\psi_i)$ and manipulate them by tailoring the evolution parameters. In particular, we can associate a specific duple $\{t_i, \pi_i\}$ to each state $|\psi_i\rangle$ and set the evolution unitary so as to maximize the probabilities $P(\{t_i, \pi_i\}|\psi_i)$. If the initial state is $|\psi_i\rangle$, the probability that the system is detected at the chosen time bin t_i with chosen polarization π_i is maximum. This kind of strategy is the same that produces an optimal protocol for four geometrically uniform states, as we demonstrated in Sec. 4.3.

In order to apply the same method to the eight states defined in Eq. 4.19, we need to split the time bins we are considering: for each time bin t_i we consider two sub-bins, one for each frequency. We apply a delay line to one of the two frequencies ($|\omega_2\rangle$ arbitrarily), imposing a time delay to the detection of states in the $|\omega_2\rangle$ subspace. We set the delay as half of the cycle time of the network. This is schematically depicted in Fig. 4.8. We can consider all the time bins and renumber them, so that detection in even time bins $\{t_0, t_2, t_4, ...\}$ corresponds to an initial state in the $|\omega_1\rangle$ subspace while detection in odd time bins $\{t_1, t_3, t_5, ...\}$ reveals that the system features an $|\omega_2\rangle$ frequency. Thanks to this strategy, we can in principle produce a discrimination protocol for eight polarization-frequency GUSs featuring the optimal probability of correct guess $P_{guess} = 0.5$.

4.4.2 Single photon source: GaAs QD in a cavity

For this experiment, we established a collaboration with the Nanophotonics group of Sapienza University, that allowed us to employ their Quantum Dot (QD) sources, which we briefly describe here. The source of single photons we used was specifically a single GaAs/AlGaAs QD placed in a circular Bragg resonator (CBR) cavity (also known as bullseye cavity) [225]. This kind of sample is grown with the Al-droplet etching technique on a GaAs commercial wafer [226]. The sample is then subject to several processing steps to fabricate positioned and size-tailored CBR around selected QDs, following a procedure similar to previously developed ones [204, 227]. Afterwards, the sample is processed with the aim of isolating the AlGaAs membrane containing the QDs. A

broadband mirror (made of a layer of aluminum oxide and a layer of gold) is placed at the bottom of the membrane [204, 206] and the whole membrane is eventually glued to a substrate with SU8 photoresist. The positions of single QDs with respect to reference markers are gathered by means of computer analysis of microscope images of the surface of the sample at cryogenic temperature (5K), under illumination with uncollimated blue LED [227]. A mask is tailored by means of electron beam lithography on the surface of the sample and the photonic cavities are etched around single QDs using a chlorine-based inductive coupled plasma reactive ion etching machine. The CBR cavity is designed to have the main resonant mode in the vicinity of the X-XX energies. In this way, the lifetimes of the excitations are critically reduced. In order to work as an emitter, the sample must be placed in a cryostat at low temperature (5K) and it is possible to excite a single QD by suitably focusing laser light by an aspheric lens placed inside the cryostat in a confocal configuration, as depicted in Fig. 4.2a). The signal coming from the QD is collected by the same lens and directed to the optical table. In our case, the XX level of the QD was resonantly excited by tuning the energy of a Ti:Sapphire pulsed laser at half of the transition energy from the ground state inducing a two-photon absorption. In order to activate the transition, the QD charge environment had to be stabilized with the aid of an uncollimated halogen lamp with blackbody spectrum [228, 229]. It is worth noting, that no heralding procedures were needed in this case, because of the pulsed pump we employed.

4.4.3 Experimental realization

The time-multiplexing scheme we describe above can be experimentally implemented by a linear optics setup which consists of an extension and improvement of the one employed in the four state discrimination experiment, employing again two Single Photon Avalanche Diodes (SPADs) only, connected to a time tagger.

The input states from Eq. 4.19 can be encoded in the polarization and frequency degrees of freedom of single photons generated by a Quantum Dot source, driven under resonant two-photon excitation by a Ti:sapphire laser at frequency $781.2\,nm$. This excitation leads to the production of two photon at different wavelengths via the biexciton-exciton cascade we discussed in Sec. 1.2.7. The setup can be divided in two parts: the first one, in Fig. 4.9 a), is the single photon source, while the second one (Fig. 4.9 b)) is the quantum receiver. The system is prepared in one of the states in Eq. 4.19 as follows: the chosen frequency was selected by sending to the receiver in Fig. 4.2b) the single photons generated by an exciton-to ground transition (exciton or X for brevity) or a biexciton-to-exciton one (biexciton or XX). As shown in Fig. 4.9 a), this selection is performed by two optical Volume Bragg Filter (VBG) filters. The VBGs feature a wavelength tunable narrow-band reflection, the tunability of which is obtained by changing the incoming light angle of incidence. Thus, by suitably setting the angular positon of the two VBGs we can select only the frequency corresponding to the biexciton and the exciton respectively. An additonal VBG filters out the pump laser backreflection. The exciton wavelength is 780.3 nm and the biexciton one is 782.3 nm. The FWHM of the emission, obtained with a Gaussian fit of the peaks, are 22.3 ± 6 pm for the exciton and 37.3 ± 7 pm for the biexciton, while an individual VBG filter has a bandwidth < 60 pm and an extinction ratio $OD3$ as stated by the manufacturer. Therefore, the filter bandwidth is much wider than the QD linewidth, which allows to collect a specific emission line avoiding losses, while still effectively separating different emission lines. This approach features some limitations: if the linewidth of the photons

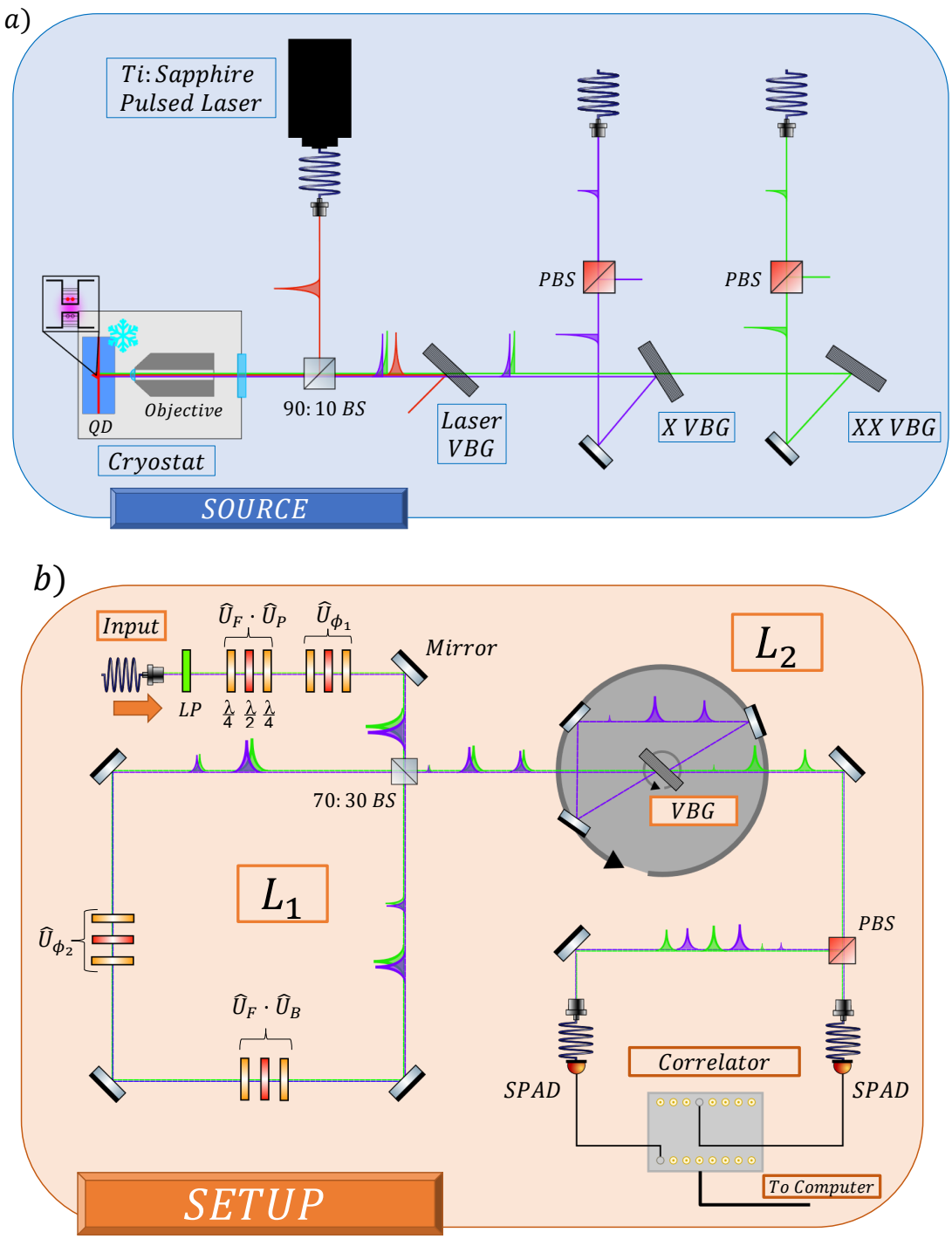

Figure 4.9: Experimental scheme of the a) source setup and the b) optical receiver. *A Ti:Sa Pulsed Laser pumps a Quantum Dot (QD), that generates single photons at different frequencies. The residual laser light is filtered out by an optical volume Bragg grating (VBG) filter suitably oriented. The $|H\rangle$ output of the exciton (purple) or the biexciton (green) light is used as an input for the b) actual discriminator, depending on the state we wish to prepare. Polarization state is prepared through a Linear Polarizer (LP) and a waveplates set QWP-HWP-QWP ($\frac{\lambda}{4} - \frac{\lambda}{2} - \frac{\lambda}{4}$ in the picture) that also drive the first evolution step, globally applying $\hat{U}_F \cdot \hat{U}_P$. Along the loop L_1, a set of waveplates imposes the transformation $\hat{U}_F \cdot \hat{U}_B$ on photon polarization. Further sets are employed for phase compensation through the unitaries $\hat{U}_{\phi_1}, \hat{U}_{\phi_2}$. After escaping L_1, the signal arrives on a VBG set to reflect photons at the exciton frequency ω_2, sending them in a second optical loop L_2. The signal is reflected again, after travelling for a length $l_{L_2} = l_{L_1}/2$, so that ω_1 and ω_2 are time delayed and perfectly distinguishable. Eventually, photons are coupled to multimode fibers and sent to Single Photon Avalanche Diodes (SPADs), connected to a correlator and interfaced to a computer. Figure taken from [175].*

is larger than the spectral bandwidth of the VBG filter, the preparation of the frequency state may be unreliable. To this aim, we cleaned the band around the X and XX emissions with two additional suitably positioned VBG filters. After the photon is prepared in the frequency subspace we require, a single mode fiber directs it into the second part of the setup, sketched in Fig. 4.9 b), where the polarization state is prepared by a linear polarizer and a waveplate (WP) set composed of the sequence of a Quarter-Wave Plate (QWP), a Half-Wave Plate (HWP), and a QWP. The application of the WPs sequence corresponds to the preparation of the polarization state by the unitary operation $\hat{U}_P$ and the discrimination protocol begins right after.
The application of unitary $\hat{U}_F$ bringing the system from the initial to the intermediate network layer, is practically performed by the same WP set as the preparation stage, as highlighted in Fig. 4.9 b). Photons find then an unbalanced BS on their path, featuring an average reflectivity $R \approx 27.5\%$. This reflectivity value was chosen to maximize the amount of signal collected throughout the protocol and to make population in the different time bins as homogeneous as possible, in order for them to feature similar uncertainties. In particular, without considering the losses, this value of R allows to collect approximately the 98.5% of the input signal by measuring the output of the first four passages through the L_1 loop (corresponding to the first eight time bins). If photons are reflected by the BS, they travel a loop of mirrors, propagating through a second WP set, that applies the unitaries $\hat{U}_B$ and $\hat{U}_F$, so that the system has completed a back and forth evolution through the network before encountering again the BS. If the photon is reflected again, another loop evolution begins and the polarization state changes accordingly. In this way, we are able to apply a dynamic on the single photon polarization degree of freedom. The frequency-wise discrimination takes place after the extraction from the first optical loop, addressed as L_1: single photons impinge on a VBG filter along their path, which is set to reflect the ones originating from exciton transition at ω_2. Then, reflected photons travel a supplemental optical loop, called L_2, after which they impinge again on the VBG and are redirected on the same path as the ω_1 photons, but provided with a delay in time, which is tailored to be half the loop evolution time of L_1. In this way, we end up with doubled time bins, one for each possible frequency. The pump pulses have a 80 MHz repetition rate, meaning that the narrowest time interval between two consecutive photon generations is around 12.5 ns. We engineered the length of the optical loops in order to fit eight detection time bins in the 12.5 ns laser repetition period, one for each of the possible input states. To this aim, the two loops lengths were set to $l_{L_1} = 90\,\text{cm}$ and $l_{L_2} = 45\,\text{cm}$. It is evident that very narrow time distributions of the photon generation are required from the Quantum Dot, that are achieved through the fast recombination of GaAs/AlGaAs nanostructures further enhanced by Purcell effect, leading to the very short lifetime of 22±4 ps for the XX transition and 41±2 ps for the X transition. This guarantees an emission time distribution after each laser pulse which is much shorter than the period of the pulse train, minimizing in this way the cross-talking between two subsequent pulses. The L_2 optical loop, also because of its relatively short length, had to be aligned very carefully: the VBG reflects only a small band around a certain wavelength depending on the angle of incidence with a very high angular selectivity (circa 0.4 mrad). Thus, in order to close the loop, it is necessary not only to impinge on the VBG with the same angle at the second reflection, but also to hit the same spot in order to align with the trasmitted beam.
To make the whole system flexible to wavelength changes, for example when using a different QD, the VBG was placed on a rotating mount that allows for a precise and flexible angular alignment.

In order to adapt the setup to different angles of reflection of the VBG filter, the optical loop L_2 was placed on a platform that can rotate independently from the VBG filter. We collected signal for the first eight time bins, corresponding to four L_1 trips with the L_2 doubling, both for the $|H\rangle$ and $|V\rangle$ polarized output. In Fig. 4.10, we report histograms of the sampled probabilities $P(|\psi_i\rangle\,|\{t,\pi\})$ of having an input state $|\psi_i\rangle$ if the photon is detected at $\{t,\pi\}$. From these quantities we can estimate the performance of our receiver, and we can rest assured that they will yield the best result achievable since they are proportional to the probabilities $P(\{t,\pi\}|\,|\psi_i\rangle)$ we considered in our optimization procedure. This can be deduced by Bayes' rule:

$$P(|\psi_i\rangle\,|\{t,\pi\}) = \frac{P(\{t,\pi\}|\,|\psi\rangle_i) \times P(|\psi\rangle_i)}{P(\{t,\pi\})} \tag{4.21}$$

where $P(\{t,\pi\}) = \sum_{j=1}^{8} P(\{t,\pi\}|\,|\psi_j\rangle) \times P(|\psi_j\rangle)$.

In Fig. 4.10, we can recognize the expected periodical dynamics, featuring a different time shift depending on the input state. The maximum probabilities are achieved at a different $\{t_i,\pi_i\}$ for each $|\psi_i\rangle$. It can be useful to analyze one specific instance: let us consider the input state $|\psi_1\rangle = |+\rangle\,|\omega_1\rangle$. The corresponding probability values are represented by blue bars in Fig. 4.10: we have XX frequency, thus the system can end up in even time bins only, corresponding to transmission through the VBG of L_2; our receiver is designed in such a way that if an event is detected at $t = 2$ and $\pi = \pi_1$, we can guess that the input state was $|+\rangle\,|\omega_1\rangle$ with a success probability that is maximum time-wise and state-wise. In fact, the bars in Fig. 4.10 are normalized so as to have the total probability $P(\{t,\pi\}) = 1$ for any $\{t,\pi\}$, that corresponds to a situation in which a detection event has been recorded and a guess about the input state has to be made. Since we consider the case of equally likely input states, it is clear by Eq. 4.21 that the probability distributions in figure are proportional to the $P(\{t,\pi\}|\,|\psi\rangle_i)$ representing the evolution of the system depending on its initial state. Hence, a time-wise pattern medium-maximum-medium-minimum of probability values arises, clearly noticeable in Fig. 4.10 a), representing the fixed polarization rotation imposed by passage through L_1. Indeed, the time evolution is always fixed, but the initial point changes, so that the periodical probability dynamics is shifted in time, depending on the input state. This can be understood by means of a comparison between Fig. 4.10 a) and c) (H polarized output): an initial polarization state $|+\rangle$ produces an output time-wise distribution featuring a two time bins shift (corresponding to one trip through L_1) with respect to an initial $|H\rangle$ or $|V\rangle$. The same behaviour can be observed for the other frequency, but for a global one time-bin shift. On the other hand, the dynamics of the V polarized output (reported in Fig. 4.10 b) and d)) are complementary, yielding the same information as the H polarized one. Thus, since we measure eight time bins, we actually measure two probability maxima for each state, one for the H output and another for the V one. The experimental data are shown in comparison with the expected ones, represented as scattered symbols, which were produced by a simulation performed taking into account experimental parameters. Data were taken over the eight time bins at the same time, with a count rate oscillating around $\approx 3 - 3.5 \cdot 10^3$/s, and each measurement take lasting 3 minutes. Right after collection, data were cleaned off background noise, due to dark counts of the SPADs, spurious signal from the QD due to white light illumination, and environmental noise.
Nonetheless, in Fig. 4.10 it is possible to notice the effect of some parasite counts in the output

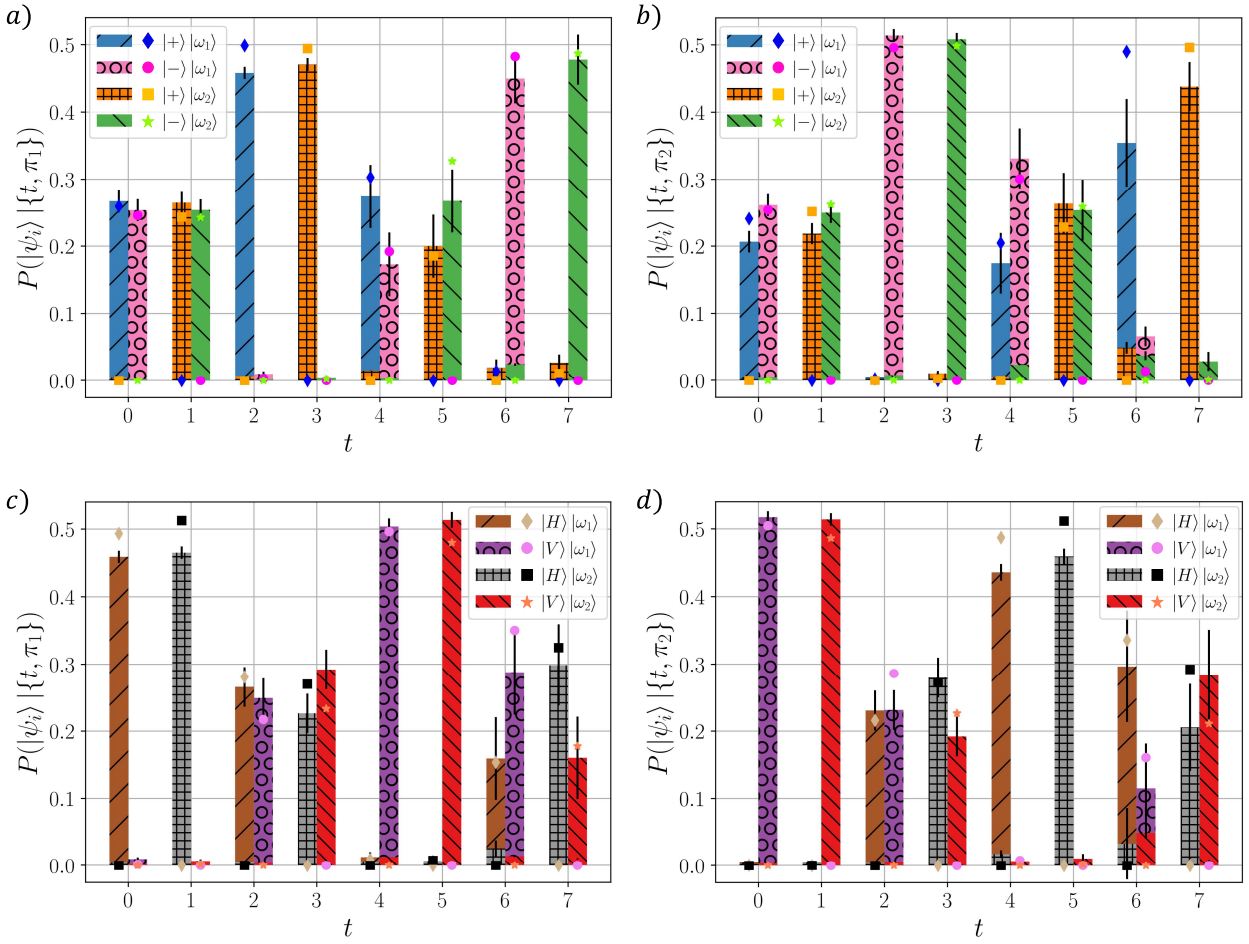

Figure 4.10: Probabilities for each of the eight states conditioned to the detection of a photon in each time bin and in the a)-c) $|H\rangle$ polarization or b)-d) $|V\rangle$ polarization. *The data are normalized so as to have $P(\{t,\pi\}) = 1$ for any $\{t,\pi\}$. They are compared to their expected values, that are the results of a simulation run accounting for experimental parameters, here represented by symbols of similar colours with respect to their experimental counterpart. Some discrepancies are present, that are extensively discussed in the text, together with the error computation. For each state, it is possible to recognize the same "triangular wave" dynamics (medium-maximum-medium-minimum) with a different time shifting. Some asymmetries can be ascribed to the slight unbalanced behavior of the Beam Splitter with respect to polarization. Figure taken from [175].*

distributions corresponding to X frequency: photons featuring ω_1 should end up in odd time bins only, while, especially for larger delays where the proper signal is lower, there are some counts that occurred also at even times. This means that some of the photons which should be reflected by the VBG in L_2 loop were transmitted instead; it is possible to ascribe this issue to the finite extinction ratio of the VBG, which is supposed to be $OD3$. From the experimental counts, we can estimate an actual extinction ratio of 0.0125 for H polarization and 0.0055 for V polarization corresponding to the double reflection on the VBG in L_2. This discrepancy with respect to the constructor's indications, as well as to the flawless working of the VBGs employed in the source setup, can be straightforwardly attributed to an imperfect angular positioning of the frequency-discriminating VBG filter and, above all, an imperfect angle of the second impingement of photons after traveling the L_2 loop. Indeed, the setting of the latter is a challenging task to achieve with high precision and we estimate that an error of 0.1% in the angle of incidence on the VBG can result in a decrease of one order of magnitude in the extinction ratio. Nevertheless, we did not include this effect in our statistical error computation, since, although it may appear relevant from Fig. 4.10, it did not significantly affect the performance of the receiver, as we show below. Indeed, the experimental parameters we had to account for in our simulations consisted of asymmetries and imperfections in the optical components. These features affect the protocol performance, and the most relevant among them is the uneven response to polarization of the unbalanced BS in L_1: specifically, it features $R_H = 0.26 \pm 0.02$ and $R_V = 0.29 \pm 0.02$ together with losses of $\approx 21\%$, that sum up with another 11% of losses for every loop completion. Moreover, these asymmetries can apparently yield an over-performance of the protocol for some input states: for instance, in Fig. 4.10 d), the expected maximum guessing probability for the state $|V\rangle |\omega_1\rangle$ is higher than the theoretical maximum 0.5. Indeed, this effect is compensated by under-performance for other states, so that the two contributions compensate when considering the average probability of correct guess, hence the average performances of the receiver. Since the BS and the loop L_1 are travelled repeatedly, the asymmetry and the losses heavily condition the performance of the receiver; as a result the theoretical probability of correct guess we expected was $P_{guess} = 0.488$ instead of the ideal 0.5.
The experimental errors we supply in Fig. 4.10 have been computed by considering possible errors in the parameters setting and evaluation: indeed, the waveplates angles positioning and calibration are subject to random errors, that we estimated jointly as a $\pm 1^\circ$ uncertainty on their angular position, and the BS reflectivities feature the uncertainty reported above. The errors are computed through a Montecarlo procedure and then summed in quadrature to the Poissonian error computed on the raw counts.
From the experimental samples, we can compute the average probability of correct guess, where we guess the input state to be $|\psi\rangle_i$ if the system is detected in the corresponding $\{t_i, \pi_i\}$, weighing with the total probability for the system to be found in $\{t_i, \pi_i\}$:

$$\bar{P}_{guess} = \frac{1}{2}\frac{1}{8}\sum_i P(|\psi_i\rangle |\{t_i, \pi_i\}) P(\{t_i, \pi_i\}) \tag{4.22}$$

where we consider equally likely input states (hence the 1/8 factor), and we sum two terms for each state, as mentioned above (hence the 1/2 factor). The result of this computation delivered a $\bar{P}_{guess} = 0.486 \pm 0.002$ which is in agreement with the expected value $\bar{P}^{sim}_{guess} = 0.488$, thus confirming that the BS asymmetry was our main limiting factor.

4.4.4 Conclusion and perspectives

All of the considerations reported in Subsec. 4.3.4 also apply to the protocol discussed in this section, especially concerning the employment of single photons and the clear experimental advantages of our time-binning strategy. In addition to that, we employed a solid state source, featuring excellent efficiency and control over different aspects of the emission process, to experimentally realize a scheme for discrimination among eight quantum states of actual single photons, encoded in their polarization and frequency degrees of freedom. The protocol was implemented through a time-multiplexing dynamic that allows the achievement of optimal results using linear optics, with no feedback mechanisms and only two photodetectors.
The importance of our results resides not only in the fact that, to the best of our knowledge, this is the largest alphabet ever implemented with a single photon platform for QSD, but also from the novel employment of photon energy as an encoding variable. Energy is very robust to environmental noise and, in principle, it can even be used to span spaces with dimension $D > 2$.
The possibility of writing information into photon frequency with such reliability derives from the exceptional properties of our solid state source: not only the source is nearly deterministic, but the generated photons also feature a convenient trade-off between fast emission and narrow bandwidth, granting reliable encoding and decoding effectiveness. There are, naturally, some limits to additional developments with this approach: the preparation of a superposition state in frequency as well as its possible manipulation inside the receiver are not trivial. However, some recent efforts have been successfully devolved to efficient frequency conversion and manipulation [230–232].
Moreover, we delivered a novel experimental method for frequency-wise delay lines, that may feature a wide applicability. For these reasons, the work reported here represents a relevant step in the implementation of high-dimensional quantum communication protocols and the start for further promising investigations.

Personal contribution

I had the idea of using frequency as a photon encoding variable for QSD, and exploiting energy non-degeneration of photon pairs generated by a Quantum Dot. I designed the eight-state discrimination protocol and personally realized the double loop quantum receiver. Eventually, I collaborated to perform the experiment and the data analysis.

Chapter 5

A protocol for multipartite entanglement distribution via separable carriers

In Sec. 2.4, we reported on the employment of a quantum walker as a probe in a quantum metrology scenario. The idea that a flying quantum system, a photon for instance, could perform some task by travelling through a network and interacting with nodes, has a wide range of applicability. In particular, this is the main concept behind Entanglement Distribution via Separable Systems (EDSS): this approach aims at generating entanglement between remote nodes without actually exchanging entangled particles, but rather employing an uncorrelated quantum "walker" acting as some sort of spool, travelling from one node to the other, entangling them while never getting entangled. Thanks to a fruitful collaboration with Prof. Mauro Paternostro at Queen's University of Belfast (UK), I was able to design a powerful protocol for multipartite EDSS. This work [233] delivers the first generalization of this kind of protocol to N entangled nodes in such a way that the carrier system is actually separable at all times. In this Chapter, we briefly review the topic of EDSS and we report on the results of our analysis, which is completely theoretical, although including proposals for experimental demonstration.

5.1 Entanglement Distribution via Separable States (EDSS)

Entanglement is a crucial ingredient in quantum networking and communication, as several benchmarking protocol and experimental demonstrations have established since long [5, 234–240]. Therefore, the development of efficient methods to build entanglement among the nodes of a network is mandatory, in the quest for real-life application of quantum technologies. Specifically, it is important that entanglement distribution protocols account for the inherent fragility of entanglement. One way to deal with this, would be to create this resource right before it is needed for some task. Typical entanglement distribution protocols involve two parties, Alice and Bob, who wish to share some entanglement. A direct way to set entanglement between them would involve Alice creating an entangled state of two particles in her laboratory and then sending one to Bob through some quantum channel. An alternative to this would be to make use of an ancillary particle: this ancilla would interact with Alice's particle first and then it would travel to Bob. In general, in this latter kind of process, the entanglement carrier must become entangled itself with the two systems. These two general methods, that summarize most of the specific entanglement distribution protocols cur-

rently in use, feature both a critical issue: entanglement can be easily damaged by environmental noise, thus the transmission of one entangled system through a channel, that is generally affected by noise, can jeopardize the success of the protocol. Indeed, there exists a third way to address the problem of entanglement distribution, which also exploits an ancillary system (known as a *carrier* system) that interacts with the parties to entangle while, on the other hand, never getting entangled itself with any part of the total system into account. This is possible thanks to a particular tailoring of the initial state of the remote particles and the carrier, together with a suitable choice of the interaction among them. The first analysis of this kind of protocol was reported in [241] by Cubitt et al.: in this work, the possibility of establishing entanglement between two remote particles *without* sending entanglement is demonstrated in a general fashion, and an explicit protocol is also exhibited as an example. The crucial point resides in allowing the system to occupy a non-pure state: if we consider three systems A, B and C, where A and B are the two systems we wish to get entangled at the end of the protocol, that we address as the *nodes*, through the interaction with the carrier system C, and we allow them only to be in a pure state such as $|a\rangle_A |b\rangle_B |c\rangle_C$, it is possible to demonstrate that no entanglement can be generated among A and B with local interactions of the two systems with C, without the latter becoming entangled with them during the process. We consider an evolution Hamiltonian corresponding to the interaction having the form $H_{AC} \otimes \mathbb{I}_B + \mathbb{I}_{ABC}$, thus the condition for the carrier separability is:

$$(\mathbb{I} + \delta t(H_{AC} + H_{BC}))\,|a\rangle_A |b\rangle_B |c\rangle_C = (|a\rangle_A |b\rangle_B + \delta t\,|\psi\rangle_{AB})(|c\rangle_C + \delta t\,|\phi\rangle_C) \tag{5.1}$$

where $|\psi\rangle_{AB}$ and $|\phi\rangle_C$ are unnormalized states. The condition for entanglement between A and B is that $|a\rangle_A |b\rangle_B + \delta t\,|\psi\rangle_{AB}$ has a non-vanishing overlap with the state $|a^\perp\rangle_A |b^\perp\rangle_B$, which can be readily demonstrated to be unfulfilled by multiplying the first term of Eq. (5.1) by $\langle a^\perp|_A \langle b^\perp|_B$. Therefore, if we require the total system of the nodes and the carrier to be separable and pure, we can not distribute entanglement via LOCC while not getting the mediating particle entangled. The intuition of Cubitt et al. consists of observing that in an entanglement distribution process, two nodes can be made strongly entangled by multiple repetition of distribution protocol in which the carrier is indeed barely entangled with the two nodes. Thus, accounting for the fact that noise can disrupt entanglement in a way proportional to its intensity, it should be in principle possible to insert in the system an amount of noise that dissolves entanglement between C and the two nodes, while maintaining (at least partially) entanglement among A and B. In particular, in [241] the authors provide an explicit example for the discrete case and some general bounds for the continuous one that show the possibility to achieve distillable entanglement distribution through interaction with a separable system thanks to the preparation of the system in an initial mixed state, imposing a sufficient amount of noise for weak carrier entanglement to be waived while the nodes remain entangled. However, the idea of weak entanglement being disrupted while cumulative strong one is preserved suits well continuous processes, but does not fit discrete, one-shot protocols, such as the one the authors even yielded in their seminal work. Indeed, we dare say that the results delivered in [241] feature some dark spots and lack of fundamental insight, namely there is little discussion regarding the physics underlying the protocol, in terms of quantum resources. Nevertheless, their contribution deserves enormous credit for the discovery of this exciting phenomenon and for paving the way for further studies and generalization to the continuous variable

framework [242]. A thorough characterization of Entanglement Distribution via Separable Systems (EDSS) in terms of quantum resources, explaining from a theoretical point of view, rather than an operational one, how entanglement could be generated without any direct interaction between the entangled systems, or any transmission of entangled ancillas, came out many years later: in [243] the connection between generation of entanglement and the presence of a preexisting amount of quantum correlations, quantifiable by Quantum Discord [244], is discussed for the first time. Indeed, from [241], it can be implied that the amount of distributed entanglement is not bounded by the entanglement initially shared by the carrier and the sender. Since entanglement can not be generated by local node-carrier interactions and classical communication only [245], there must be some pre-existing quantum correlation between the nodes or some genuine quantum features in the carrier system. This idea had been suggested in [246, 247], but in [243], Chuan et al. achieved the formulation of a general bound for entanglement distribution involving pre-existing quantum correlations quantified by Quantum Discord. We consider again the case of two remote agents, Alice and Bob, holding two quantum systems A and B, respectively. They wish to increase the entanglement that they share by sending an auxiliary quantum system—the carrier C—with which they interact locally. The whole system features a certain global state ρ. The entanglement residing in the bipartitions $A : BC$ and $AC : B$, corresponding to the cases of the carrier being in Alice's or Bob's lab, can be quantified by the relative entropy of entanglement $\mathcal{E}(\rho)$ [9, 248] and the following bound stands [243]:

$$|\mathcal{E}_{A:BC}(\rho) - \mathcal{E}_{AC:B}(\rho)| \leq \mathcal{D}_{AB|C}(\rho) \tag{5.2}$$

where $\mathcal{D}_{AB|C}(\rho)$ is the relative entropy of discord [249, 250] for the bipartition $AB|C$ of the total state ρ. A very similar relation was also reported in the parallel work by Streltsov et al. [251]. We can now apply this bound to a practical protocol for entanglement distribution between two nodes with a separable carrier: the initial state of the total system is α. We perform then a so-called *encoding* operation, a local map $\mathcal{M}_{AC}$ that drives an interaction between the node A and the carrier C and leads to the new state $\beta = \mathcal{M}_{AC}(\alpha)$. By a local operation on AC it is not possible to increase entanglement in the $AC : B$ bipartition, hence $\mathcal{E}_{AC:B}(\beta) \leq \mathcal{E}_{AC:B}(\alpha)$. The carrier is then transferred to Bob's laboratory, where a *decoding* local operation on BC is used to localize on B the entanglement built between the labs [252]. Applying Eq. (5.2), we have that:

$$\mathcal{E}_{A:BC}(\beta) \leq \mathcal{E}_{AC:B}(\alpha) + \mathcal{D}_{AB|C}(\beta). \tag{5.3}$$

Thus, entanglement increase between the nodes is bound by the amount of quantum discord shared by the nodes with the carrier system. It is very interesting to review here further considerations reported in [243], before specifically addressing actual protocols for EDSS. First of all, if no quantum discord is present in the state β, considering the cut $AB|C$: the state then has the quantum-classical form $\beta = \sum_i p_i \rho^i_{AB} \otimes |i\rangle_C \langle i|$. In this case, the carrier system stores only classical information, hence we reduce to the case of a protocol based completely on LOCC, which can not increase entanglement [245]. So, Eq. (5.3) represents an extension of the monotonicity of entanglement with respect to LOCC, since it implies that entanglement can be increased by LOCC and *quantum communication*. In conclusion, it is worth understanding which conditions have to be implemented in order to make

an EDSS protocol possible, namely a protocol fulfilling the following requirements:

$$\begin{aligned} &\text{a) } \mathcal{E}_{AC:B}(\alpha) = 0 \\ &\text{b) } \mathcal{E}_{AB:C}(\beta) = 0 \\ &\text{c) } \mathcal{E}_{A:BC}(\beta) > 0 \end{aligned} \tag{5.4}$$

We consider Eq. (5.3), exchanging the role of B and C:

$$\mathcal{E}_{A:CB}(\beta) \leq \mathcal{E}_{AB:C}(\beta) + \mathcal{D}_{AC|B}(\alpha). \tag{5.5}$$

If we apply the condition Eq. (5.5) b), we see that entanglement which can be created by an EDSS protocol is only bounded by the initial amount of quantum discord $\mathcal{E}_{A:CB}(\beta) \leq \mathcal{D}_{AC|B}(\alpha)$. In particular, the carrier can be chosen as completely uncorrelated at the start of the protocol, so that the creation of entanglement between the nodes only relies on their initial quantum correlation $\mathcal{D}_{A|B}(\alpha)$, and the generation of entanglement in this framework consists of some sort of translation of discord into entanglement. Other possibilities involve particle exchange but eventually reduce to the one mentioned above. As discord is way more resilient to noise than entanglement [253–257], protocols that rely on discord presence rather than entanglement feature an inherent advantage. This kind of protocols requires suitable and interdependent choices of initial nodes state, initial carrier state and quantum encoding and decoding operations, as we review in the following.

5.2 Binary EDSS protocols

After the seminal work from Cubitt et al. [241], various protocols for EDSS have been designed both for discrete variable encoding [258] or continuous variable platforms [242, 259, 260], addressing the problem of binary EDSS, i.e. distribution of entanglement between two nodes via a separable carrier system. Binary EDSS was also experimentally demonstrated in the following years [261–263]. We take as a reference scheme Kay's EDSS protocol for qubits [258], which will provide the framework for our analysis. The protocol can be described as follows: at the start, Alice and Bob initially share a separable state of their systems A and B, though featuring some quantum correlations quantified by quantum discord. Afterwards, Alice introduces an ancilla system K which is uncorrelated from AB. Then, Alice performs the *encoding operation*, that is, a unitary operation U_{AK} on her system and the carrier and sends K to Bob. In Ref. [258] it is shown that when AB is in an initial Bell-diagonal state and U_{AK} is a controlled-phase gate, it is possible to choose a suitable initial state for K so that the state of the total system at the end of the protocol is entangled in the bipartition $A|BK$ and K remains separable from A and B throughout the process. In the following, we will build on a slightly different scheme, adding a supplemental step to the protocol: Bob performs a *decoding operation* on his particle and the carrier after he receives K from Alice. This leads to entanglement in both the $A|BK$ and $B|AK$ bipartitions while the ancilla remains separable with no entanglement in the partition $K|AB$. This version of the protocol for entanglement distribution with separable states has been employed for the experimental demonstration in Ref. [261] such as illustrated in Fig. 5.1. In this section, we thoroughly review this scheme, which is crucial for the generalization I developed.

As we mentioned, the initial state of the two nodes A and B is set as separable, yet featuring

non-classical correlations (quantified by quantum discord [243]). Specifically, we prepare the mixed state:

$$\begin{aligned}\alpha_{AB} = \frac{1}{4}\left(|00\rangle\langle 00| + |11\rangle\langle 11|\right)_{AB} + \frac{1}{8}\left(|DD\rangle\langle DD|\right. \\ \left. + |AA\rangle\langle AA| + |RL\rangle\langle RL| + |LR\rangle\langle LR|\right)_{AB},\end{aligned} \tag{5.6}$$

where $|D\rangle = \frac{1}{\sqrt{2}}(|0\rangle + |1\rangle)$, $|A\rangle = \frac{1}{\sqrt{2}}(|0\rangle - |1\rangle)$, $|R\rangle = \frac{1}{\sqrt{2}}(|0\rangle + i\,|1\rangle)$ and $|L\rangle = \frac{1}{\sqrt{2}}(|0\rangle - i\,|1\rangle)$. We use here the notation $|D/A\rangle$ rather than $|+/-\rangle$ in order to keep homogeneity with the rest of related literature. While α_{AB} is invariant under partial transposition, it is endowed with non-zero quantum discord, as quantified by the relative entropy of discord [250, 264]

$$\mathcal{D}(\alpha_{AB}) = \min_{\Pi_B}[S(\Pi_B(\alpha_{AB}))] - S(\alpha_{AB}), \tag{5.7}$$

where $S(\rho)$ is the von Neumann entropy of state ρ and $\Pi_B(\rho) = \sum_{j=0}^{1}\pi_j\rho\pi_j$ is a rank-one projective measurement of ρ with $\pi_{0,1}$ two orthogonal projectors on qubit B. We have $\mathcal{D}(\alpha_{AB}) = 0.0612781$.

The state of the nodes then undergoes encoding and decoding operations, each consisting of a controlled-phase (CPHASE) gate acting on the joint state of either A or B and the carrier K:

$$\text{CPHASE} := |0\rangle\langle 0|_{A/B} \otimes \mathbb{I}_K + |1\rangle\langle 1|_{A/B} \otimes \sigma_{z,K} \tag{5.8}$$

where $\mathbb{I}$ is the two-dimensional identity matrix and σ_z is the z Pauli matrix. This gate sets a relative phase between the two states of the computational basis of the target qubit K, depending on the state of control one A/B. The initial state of the carrier system must be a mixture of orthogonal vectors that are maximally distant from the eigenstates of σ_z, in order to amplify the effect of the encoding and decoding operations. We thus choose

$$\alpha_K = \frac{1}{4}\left(|D\rangle\langle D| + 3\,|A\rangle\langle A|\right)_K, \tag{5.9}$$

although a mixture of $|R\rangle$ and $|L\rangle$ would also be suitable. These mixing probabilities are chosen so as to guarantee that the carrier does not get entangled throughout the process, while achieving the largest possible entanglement between the two nodes at the end of the protocol. In this sense, a mixture with balanced probabilities would be suitable too, although less effective. Adding more weight on the heavier term will lead to entanglement with the carrier, while lowering its probability would lead to lower entanglement between the nodes.
The protocol first involves the encoding step, where the CPHASE gate is applied to qubit A and the carrier. That is followed by a decoding step, consisting of the application of the CPHASE to node B and carrier. The first step reads

$$\beta_{ABK} = \mathcal{P}_{AK}(\alpha_{AB} \otimes \alpha_K)\mathcal{P}_{AK}^{\dagger} \tag{5.10}$$

where

$$\mathcal{P}_{AK} = |0\rangle\langle 0|_A \otimes \mathbb{I}_K + |1\rangle\langle 1|_A \otimes \sigma_{z,K} \tag{5.11}$$

is the CPHASE gate between A and the carrier K. The decoding step then yields

$$\gamma_{ABK} = \mathcal{P}_{BK}\beta_{ABK}\mathcal{P}_{BK}^{\dagger}. \tag{5.12}$$

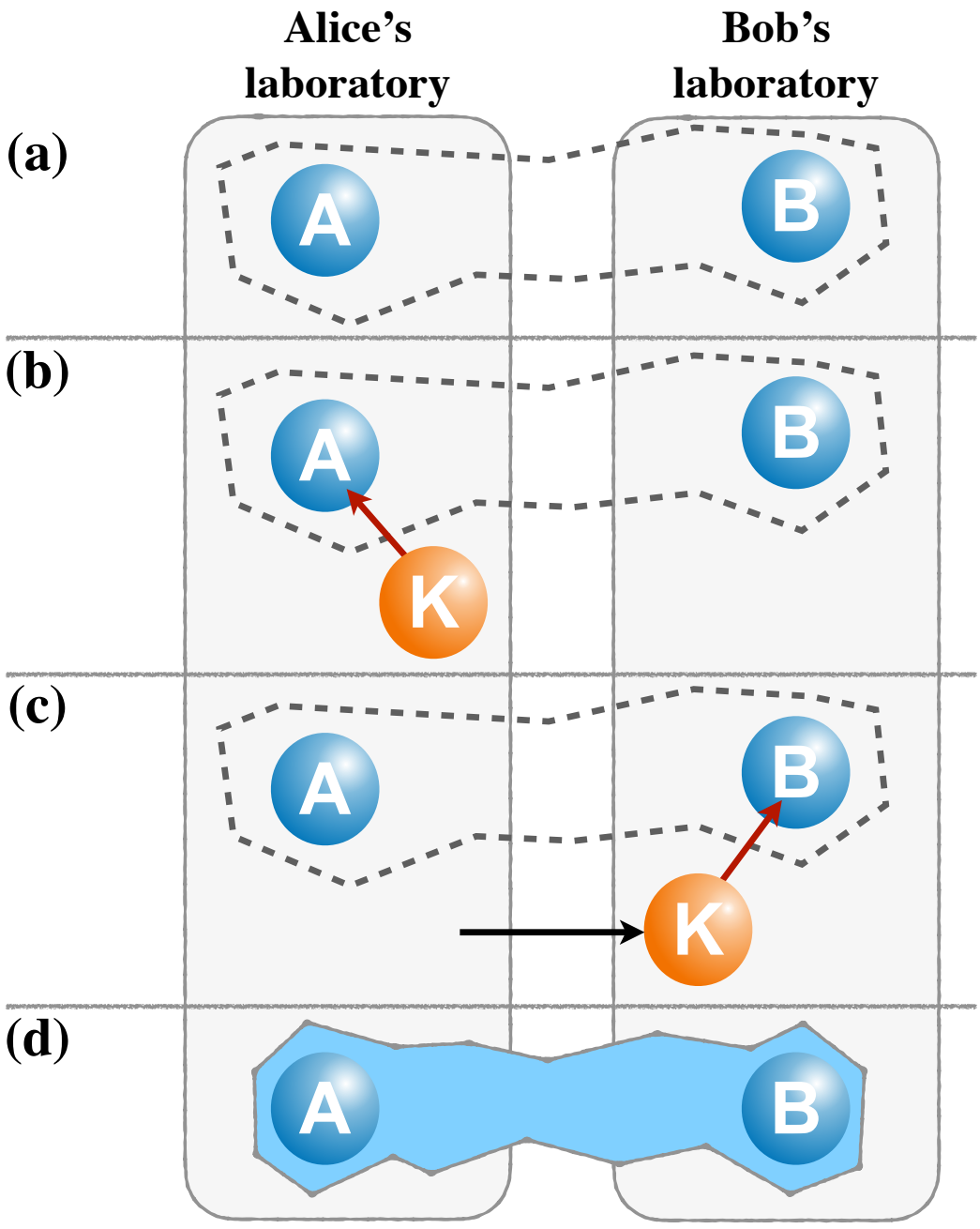

Figure 5.1: Sketch of the two-qubit protocol. **(a)** *Nodes A and B are initially separable and they share quantum discord (dashed line).* **(b)** *The auxiliary system K (the carrier) is prepared in such a state that K is completely uncorrelated from AB. The encoding operation, that we consider as a controlled-phase gate in this case, is performed between A and K.* **(c)** *The carrier K is sent to Bob and B and K interact via the decoding operation, which is again a controlled-phase gate.* **(d)** *At the end of the protocol nodes A and B share quantum entanglement. Picture from [233].*

The resulting state γ_{ABK} features distillable entanglement in the bipartitions $A|BK$ and $B|AK$ with the carrier K being in a separable state with respect to the state of the nodes (either collectively or individually taken). In particular, entanglement can be witnessed by the minimum eigenvalues $\lambda_{A|BK}$ ($\lambda_{B|AK}$) of the partial transpose of γ_{ABK} with respect to the bipartition $A|BK(B|AK)$, according to Peres-Horodecki criterion [11]. This witness is tightly related to the negativity of entanglement $\mathcal{N}$ [10], that we defined in Subsec. 1.1.4: $\mathcal{N}_{\mathcal{X}|\mathcal{Y}} = (|\lambda_{X|Y}| - \lambda_{X|Y})/2$. For this binary protocol, they obtained $\mathcal{N}_{\mathcal{A}|\mathcal{BK}} = 0.0625$ as well as for the $B|AK$ bipartion, which is the maximum achievable entanglement with binary EDSS [258], while $\mathcal{N}_{\mathcal{AB}|\mathcal{K}}$ remains zero throughout the protocol. Although the generation of entanglement is inherently probabilistical, Ref. [261] demonstrates with a thorough analysis of noise robustness, that there exists a consistent range of noise parameters for which EDSS is the optimal way to distribute entanglement between two remote qubits.

5.3 Scheme for multipartite EDSS

In this section, directly based on our work [233], we report the generalization of the protocol in Ref. [258] to the distribution of multipartite entanglement through EDSS, specifically focusing on the conditions of its experimental demonstration in Ref. [261]. Multipartite EDSS had been previously addressed in Ref. [265], where a systematic method was proposed based on the EDSS protocol by Cubitt et al. [241]. In this case, AB and K are initially correlated (yet unentangled), but the bipartition $K|AB$ does not remain unentangled at all times. Entanglement must be wiped out after each interaction with the nodes, in a way that the carrier may remain entangled more likely in their proposal and extra effort must be made to ensure its prevention. As the initial state of K in Refs. [258, 261] shares no classical or non-classical correlations with A or B, we avoided this problem and we exhibited that favouring this type of protocol offers a promising avenue for successful EDSS with fewer restrictions.

5.3.1 General protocol

I employed the same encoding and decoding mechanisms illustrated for the binary case to design a generalization of the two-qubit protocol to a multipartite set of nodes. The resource being exploited is a mixed state that features initial non-classical correlations between each of the node pairs. The aim of the process is to entangle the elements of the network according to a chosen entanglement pattern. We review here the protocol in its general formulation.

Initial state of network and carrier, encoding and decoding operation

We consider the case of a network of N nodes $\{Q_i\}$ ($i = 1, \ldots, N$) and we need to devise a way to establish a pattern of entangled links between such nodes, according to a desired structure. Thus, we require the definition of a state which features non-classical correlations between the nodes we wished to get entangled. In order to do that, we use the two-qubit state featuring quantum discord

that was employed in the two-qubit case of Eq. (5.6).

$$\begin{aligned}\rho^0_{Q_iQ_j} = \frac{1}{4}\left|00\right\rangle_{Q_iQ_j}\left\langle 00\right| + \frac{1}{4}\left|11\right\rangle_{Q_iQ_j}\left\langle 11\right| + \\ + \frac{1}{8}\left|DD\right\rangle_{Q_iQ_j}\left\langle DD\right| + \frac{1}{8}\left|AA\right\rangle_{Q_iQ_j}\left\langle AA\right| + \\ + \frac{1}{8}\left|RL\right\rangle_{Q_iQ_j}\left\langle RL\right| + \frac{1}{8}\left|LR\right\rangle_{Q_iQ_j}\left\langle LR\right|\end{aligned} \tag{5.13}$$

As we discussed in the previous section, this state has been shown to be optimal for the two qubit EDSS protocol, in terms of the amount of entanglement created while always keeping the carrier in a separable state.

Proceeding in analogy with the bipartite case, we generalize this state to N qubits by imposing a mixed initial state, consisting of a balanced mixture of terms featuring non-classicality between every pair of nodes targeted by our protocol. Each of such terms features a correlated state of a given pair of nodes, while the other nodes are set in an eigenstate of the encoding and decoding operation. We define a list of two-element sets containing the M pairs we wish to entangle, labelling them as $\{\mathcal{C}_k\}_{k=1}^{M}$, where each $\mathcal{C}_k = \{Q_i, Q_j\}$ represents a different node pair $\{i, j\}$ among the chosen ones. The initial state of the network α_N has thus the form

$$\alpha_N = \frac{1}{M}\sum_{k=1}^{M}\rho^0_{\mathcal{C}_k}\left(\bigotimes_{Q_i\notin\mathcal{C}_k}\alpha^0_{Q_i}\right), \tag{5.14}$$

where $\alpha^0_{Q_i} = \left|0\right\rangle\left\langle 0\right|_{Q_i}$ and $\rho^0_{\mathcal{C}_k}$ is the initial state in Eq. (5.6), but for the pair $\mathcal{C}_k$. For instance, we can choose to distribute entanglement according to a chain-like structure, namely a linear network in which each node is entangled with its closest neighbours. The initial state can be written in the compact form as

$$\alpha_N^{linear} = \frac{1}{N-1}\sum_{k=1}^{N-1}\rho^0_{Q_k,Q_{k+1}}\left(\bigotimes_{Q_i\neq\{Q_k,Q_{k+1}\}}\alpha^0_{Q_i}\right). \tag{5.15}$$

Such an initial state is necessary to keep the carrier in a separable state with respect to the network. Basically, in this way we are able to carry the two-qubit protocol in parallel over any node pair we want to entangle, without interference between the various terms. As we will see later on, this has some interesting implications for the features of the final state.

The encoding and decoding operations consist of CPHASE gates $\mathcal{P}_{Q_iK}$ acting on the state of node Q_i and the carrier K, which can be written as:

$$\mathcal{P}_{QK} = \left|0\right\rangle_Q\left\langle 0\right|\otimes\mathbb{I}_K + \left|1\right\rangle_Q\left\langle 1\right|\otimes\sigma_{Z,K} \tag{5.16}$$

that is just the general expression for the CPHASE gate in Eq. (5.11).

The initial state of the carrier is chosen again as in Eq. (5.9).

$$\alpha_K = \frac{1}{4}\left|D\right\rangle\left\langle D\right| + \frac{3}{4}\left|A\right\rangle\left\langle A\right| \tag{5.17}$$

since the choice of the most suitable carrier state is tightly related to the choice of the encoding and decoding gate. Other equivalent gate-carrier initial state pairings exist, though they do not result

in better performance of the protocol. The scheme consists of the application of the local encoding and decoding operations to each of the node qubits and the carriers. Indeed, I also developed a variation of the protocol involving a multi-qubit or qudit carrier, featuring some slight differences in procedure and performance.

Single qubit carrier

In this case, we only have one carrier K and the total initial state of the system can be set as

$$\alpha_T = \alpha_N \otimes \alpha_K \tag{5.18}$$

so that the preparation of the network system and the carrier can be independently addressed. As the carrier is the same for each pair of nodes, a single encoding and decoding step for each qubit is enough for weaving multiple entanglement links. The effect of the local CPHASE gate on the total state is

$$\mathcal{P}_{Q_l K} \alpha_T \mathcal{P}_{Q_l K}^\dagger = \frac{1}{M} \sum_{k=1}^{M} \chi_{k,Q_l} \left(\bigotimes_{Q_i \notin \mathcal{C}_k} \alpha_{Q_i}^0 \right), \tag{5.19}$$

where

$$\chi_{k,Q_l} = \begin{cases} \rho_{\mathcal{C}_k}^0 \otimes \alpha_K & \text{for } Q_l \notin \mathcal{C}_k, \\ \mathcal{P}_{Q_l K} \left(\rho_{\mathcal{C}_k}^0 \otimes \alpha_K \right) \mathcal{P}_{Q_l K}^\dagger & \text{for } Q_l \in \mathcal{C}_k. \end{cases} \tag{5.20}$$

The CPHASE gate on qubit Q_l acts as an encoding operation on the terms involving Q_l as a target or a decoding one, while acting as the identity on the others.

Multiple qubit carriers

It is possible to tailor the above protocol to work with multiple carriers. We investigated this case in order to understand which beneficial effects or costs may derive from this choice. We consider a compound of n qubits $\{K_i\}_{i=1}^n$ and choose α_K in Eq. (5.9) as the initial state for each of them. Therefore, the total product state of the carrier compound results

$$\alpha_{\bar{K}} = \bigotimes_{i=1}^{n} \alpha_K^i = \bigotimes_{i=1}^{n} \left(\frac{1}{4} |D\rangle \langle D|_{K_i} + \frac{3}{4} |A\rangle \langle A|_{K_i} \right), \tag{5.21}$$

so that the total initial state is simply

$$\alpha_T = \alpha_N \otimes \alpha_{\bar{K}}. \tag{5.22}$$

The main difference with respect to the one qubit carrier protocol is that, in the present case, we proceed to entangle each qubit pair making them interact with a different carrier. Therefore, node qubit Q_i is subject to encoding via the carrier qubit K_i, which also mediates the local decoding at Q_{i+1}. Then, the encoding between Q_{i+1} and Q_{i+2} is mediated by carrier K_{i+1}. As a consequence, separate encoding and decoding operations are needed.
In general, the final state of the nodes will have the form of a mixture of terms stemming from the various two-qubit processes, which could take place in parallel, and an incoherent term Ω_N, thus

reading

$$\rho_N^f = P\ \Omega_N + (1-P)\sum_{k=1}^{M} \left|\phi^+\right\rangle \left\langle\phi^+\right|_{\mathcal{C}_k} \left(\bigotimes_{Q_i \notin \mathcal{C}_k} \alpha_{Q_i}^0\right), \tag{5.23}$$

where $|\phi^+\rangle = \frac{1}{\sqrt{2}}(|00\rangle + |11\rangle)$ is a Bell state and, as stated previously, $\{\mathcal{C}_k\}_{k=1}^M$ is the list of node pairs we aim to entangle. The mixing coefficient P is determined by the terms we insert in the initial mixed states, hence the number of entangled links we wish to establish. For each contribution, an incoherent residual term appears in the final state, forming the global incoherent term Ω_N. Therefore, the final state is a mixture of terms featuring bipartite entanglement, one for each of the initially non-classically correlated node pairs. Clearly, that implies a probabilistic generation of entanglement. Nevertheless, as we explicitly show in the following examples, the final state of the system unambiguously exhibit multipartite entanglement, namely the network is entangled with respect to any possible bipartition.

5.4 Performance analysis

In this section, we report the analysis of the performance of both single- and multiple-carrier protocols by addressing two explicit examples.

5.4.1 Four nodes example: Ring configuration

Single carrier

We consider a four-node case where the qubits $Q_{1,..,4}$ are entangled as a result of the application of the protocol illustrated before. As we request explicitly that Q_1 and Q_4 are entangled, we would thus realize a *ring-like* structure [cf. Fig. 5.2 **(a)**]. The initial state of the nodes, then, must include non-classical correlations between every possible pair $\{\mathcal{C}_k\}_{k=1}^4$, where $\mathcal{C}_k = \{Q_k, Q_{k+1}\}$ and we set $Q_5 = Q_1$, so that

$$\begin{aligned}\alpha_4 = \frac{1}{4}\big(&\rho_{Q_1,Q_2}^0 \otimes \alpha_{Q_3}^0 \otimes \alpha_{Q_4}^0 + \rho_{Q_2,Q_3}^0 \otimes \alpha_{Q_1}^0 \otimes \alpha_{Q_4}^0 + \\ &+\rho_{Q_3,Q_4}^0 \otimes \alpha_{Q_1}^0 \otimes \alpha_{Q_2}^0 + \rho_{Q_4,Q_1}^0 \otimes \alpha_{Q_2}^0 \otimes \alpha_{Q_3}^0\big)\end{aligned} \tag{5.24}$$

where $\rho_{\mathcal{C}_k}^0$ and $\alpha_{Q_i}^0$ are the same as in Eq. (5.14). The protocol consists of only four steps, taking the initial state α_4 to the final one as

$$\eta_4 = \left(\Pi_{j=1}^4 \mathcal{P}_{Q_j K}\right)(\alpha_4 \otimes \alpha_K)\left(\Pi_{j=1}^4 \mathcal{P}_{Q_j K}^\dagger\right). \tag{5.25}$$

In particular, the amount of entanglement in each of the one-vs-four bipartitions of the form $Q_j|\mathcal{G}_K$ with $\mathcal{G}_K = \{Q_1, Q_2, Q_3, Q_4, K\} \setminus Q_j$ that can be identified in state η_4 is the same: the corresponding partially transposed density matrices $\eta^{\mathrm{PT}_{Q_j}}$ all have a single negative eigenvalue equal to -0.0175206, so that the entanglement $\mathcal{E}_{Q_j|\mathcal{G}_K}$ does not depend on $j = 1, .., 4$. On the other hand, the entanglement $\mathcal{E}_{K|Q_{1,..,4}}$ between the carrier K and the network is identically zero, thus achieving a successful distribution of entanglement without involving the carrier. It is worth noting that after projecting the carrier system onto state $|A\rangle$ and tracing the carrier system away we obtain a reduced matrix of the network only which exhibit the same entanglement values. In

State label	Description of evolution	Encoder/ Decoder
β_T	$\mathcal{P}_{Q_1K_1}\alpha_T\mathcal{P}^+_{Q_1K_1}$	K_1
γ_T	$\mathcal{P}_{Q_2K_1}\beta_T\mathcal{P}^+_{Q_2K_1}$	K_1
δ_T	$\mathcal{P}_{Q_2K_2}\gamma_T\mathcal{P}^+_{Q_2K_2}$	K_2
η_T	$\mathcal{P}_{Q_3K_2}\delta_T\mathcal{P}^+_{Q_3K_2}$	K_2
ζ_T	$\mathcal{P}_{Q_3K_3}\eta_T\mathcal{P}^+_{Q_3K_3}$	K_3
κ_T	$\mathcal{P}_{Q_4K_3}\zeta_T\mathcal{P}^+_{Q_4K_3}$	K_3
χ_T	$\mathcal{P}_{Q_4K_4}\kappa_T\mathcal{P}^+_{Q_4K_4}$	K_4
ω_T	$\mathcal{P}_{Q_1K_4}\chi_T\mathcal{P}^+_{Q_1K_4}$	K_4

Table 5.1: *Description of the steps required in a multi-qubit carrier protocol. We provide the label of the state achieved at each step of the scheme, the corresponding encoding (decoding) operation and the associated encoder (decoder).*

order to demonstrate that the system actually features multipartite entanglement, we check the eigenvalues of the partial transpose with respect to any possible bipartition of the system From the Peres-Horodecki separability criterion [11, 266], we know that a negative eigenvalue of the partially transposed density matrix of a bipartite system witnesses entanglement between the parties and we have negative eigenvalues for any bipartition apart from $ABCD|K$, as reported in Tab. 5.2.

Multi-qubit carrier

We now focus on the study of a multi-carrier configuration, and how this might affect the effectiveness of the protocol. Since in the ring pattern we have to weave four entanglement links, we define a 16-dimensional qudit $\bar{K}$, that we can consider as a compound carrier system of 4 qubits K_j $(j = 1, .., 4)$. The protocol differs from the single-carrier one in the exploitation of different carrier subspaces for the encoding and decoding operations affecting different node pairings. This implies that each operation will only act on a certain link, depending on the nodes that are involved. Therefore, the protocol needs twice the number of steps required in the single-qubit carrier scheme. Such steps are explicitly illustrated in Table 5.1.

We report a sketch of the procedure in Fig. 5.2 **(b)**. We compute again the eigenvalues for any possible bipartition of the system, reporting them in Tab. 5.2. The results of our analysis show that also a qudit carrier approach produces multipartite entanglement, since the eigenvalues of the partially transposed density matrix are negative with respect to any bipartition of the nodes system.A main drawback comes from the fact that, although the carrier is in a separable state, tracing it away presents some complications. Since each of the different entanglement links is mediated by a different subspace, the projection of the qubit carrier on the state $|A\rangle$ will result in the preservation of that link in the reduced network state. Unfortunately, that can't be done simultaneously for all the node pairs: by projecting every qubit carrier on their respective $|A\rangle$ state, we get a separable reduced state of the network. Therefore, the final state for the system remains multipartite entangled as far as the carrier state is not further manipulated. The carrier can be only traced away in case we wish to observe a specific entanglement link between two nodes.

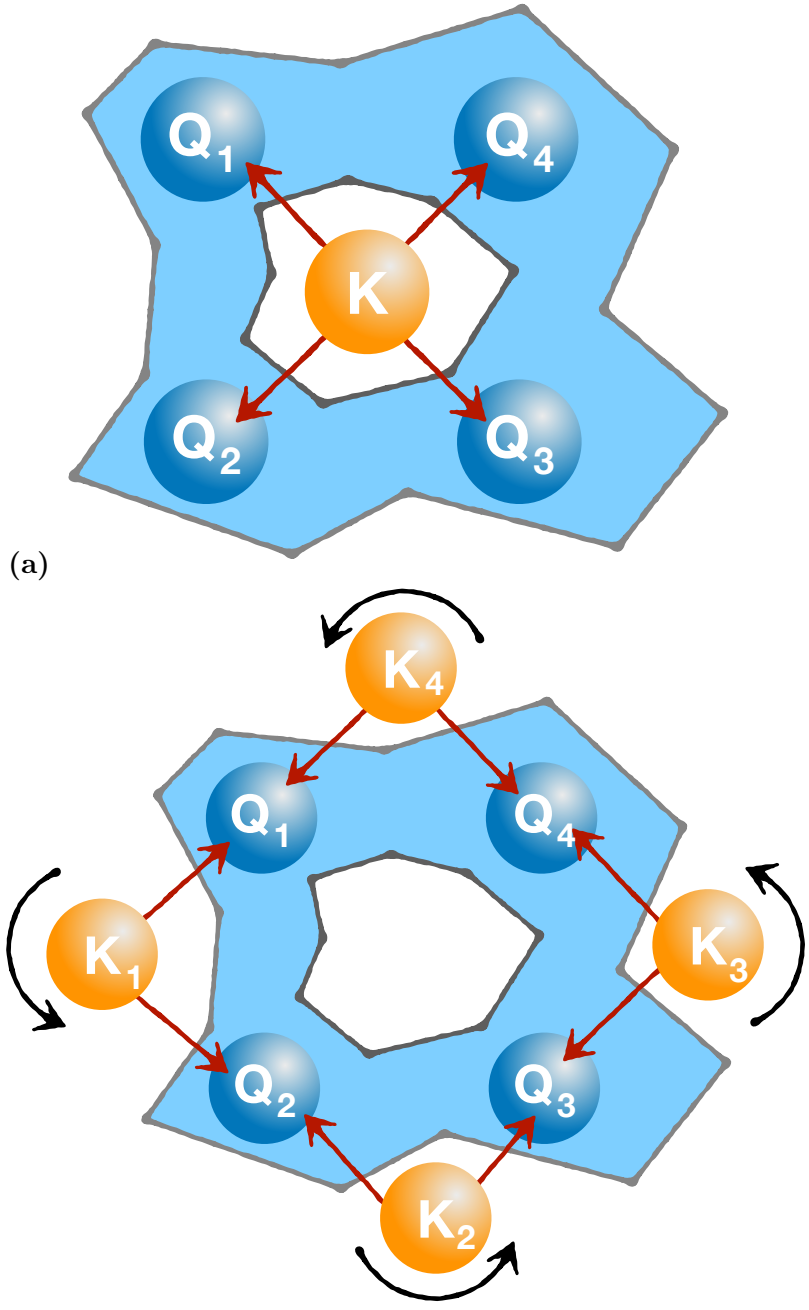

Figure 5.2: Ring topology protocols. **(a)** *Single-carrier protocol: the carrier qubit K interacts once with each node;* **(b)** *qudit carrier case: the carrier proceeds in one direction, interacting twice with each node, once for encoding and the second time for decoding, since different subspaces of the carrier system are involved in each encoding and decoding operation. Picture from [233].*

Bipartition	Single-carrier	Multiple-carrier
$Q_1\|Q_2Q_3Q_4K$	-0.0175206	$\{-0.011786, -0.00392868, -0.00392868, -0.001309565\}$
$Q_2\|Q_1Q_3Q_4K$	-0.0175206	$\{-0.011786, -0.00392868, -0.00392868, -0.001309565\}$
$Q_3\|Q_1Q_2Q_4K$	-0.0175206	$\{-0.011786, -0.00392868, -0.00392868, -0.001309565\}$
$Q_4\|Q_1Q_2Q_3K$	-0.0175206	$\{-0.011786, -0.00392868, -0.00392868, -0.001309565\}$
$Q_1Q_2\|Q_3Q_4K$	$\{-0.0078125,$ $-0.0078125\}$	$\{-0.00769043, -0.00769043, -0.00286949, -0.00256348,$ $-0.00256348, -0.00256348, -0.00256348, -0.000956497,$ $-0.000956497, -0.000854492, -0.000854492, -0.000318832\}$
$Q_1Q_3\|Q_2Q_4K$	-0.03125	$\{-0.0117871, -0.0117871, -0.00395737, -0.00395737,$ $-0.00395737, -0.00395737, -0.00195313\}$
$Q_1Q_4\|Q_2Q_3K$	$\{-0.0078125,$ $-0.0078125\}$	$\{-0.00769043, -0.00769043, -0.00286949, -0.00256348,$ $-0.00256348, -0.00256348, -0.00256348, -0.000956497,$ $0.000956497, -0.000854492, -0.000854492, -0.000318832\}$

Table 5.2: *Negative eigenvalues of every possible partition, ring pattern, qubit and qudit carrier protocols*

General remarks on ring topology protocols

In order to compare the effectiveness of the two protocols we compute the average negativity of the final state for both cases. Given a certain partition p of a composite state ρ, we have defined negativity as in [10]

$$\mathcal{N}_p(\rho) = \frac{||\rho^{T_p}|| - 1}{2} \tag{5.26}$$

which is equal to the sum of all negative eigenvalues of the transposition of ρ with respect to the partition p. We consider the geometrical average of the negativity values for all the possible partitions of the system, denominating this value $\mathcal{N}$. We obtain a $\mathcal{N} = 0.0184179$ ($\mathcal{N} = 0.0261631$) for the single qubit carrier (multi-qubit carrier) protocol. These results show some advantage coming from the employment of a high-dimensional carrier in terms of entanglement production, though implying, in the perspective of an experimental realization, far heavier efforts and drawbacks.

It is worth noting that the amount of entanglement produced on average for a single link is lower than in the binary case of [261]. This is understandable considering the fact that the four-nodes initial mixed state contains many more terms which generate “noise" contributions in the final state, with respect to the two nodes case. Indeed, we expect the average produced negativity to decrease as the number of nodes increases, together with the number of terms to be included in the initial state. It may even be possible that, after a certain size of the network, entanglement between the nodes is no longer detectable.

Nonetheless, we can define the total negativity as the sum of all the negative eigenvalues over any bipartition Tot$\mathcal{N} = \sum_{\{p\}} \mathcal{N}_p$, and this quantity is not bound to decrease, since the initial state features the same amount of initial quantum correlation disregarding of the number of nodes. Specifically, the quantum correlation remains the same as the two qubit case in [261], even if split among a larger number of terms in the total initial mixture. The ring pattern case was investigated up to $N = 10$ nodes, in order to understand the trend of negativity in function of the size of the network, and the results are reported in Fig. 5.3. My simulations confirmed the expected decrease of the average negativity, but also highlighted that the total negativity remains constant as we increase the number of entangled nodes; therefore, the addition of more nodes does not seem to jeopardize the protocol efficiency in converting discord into entanglement.

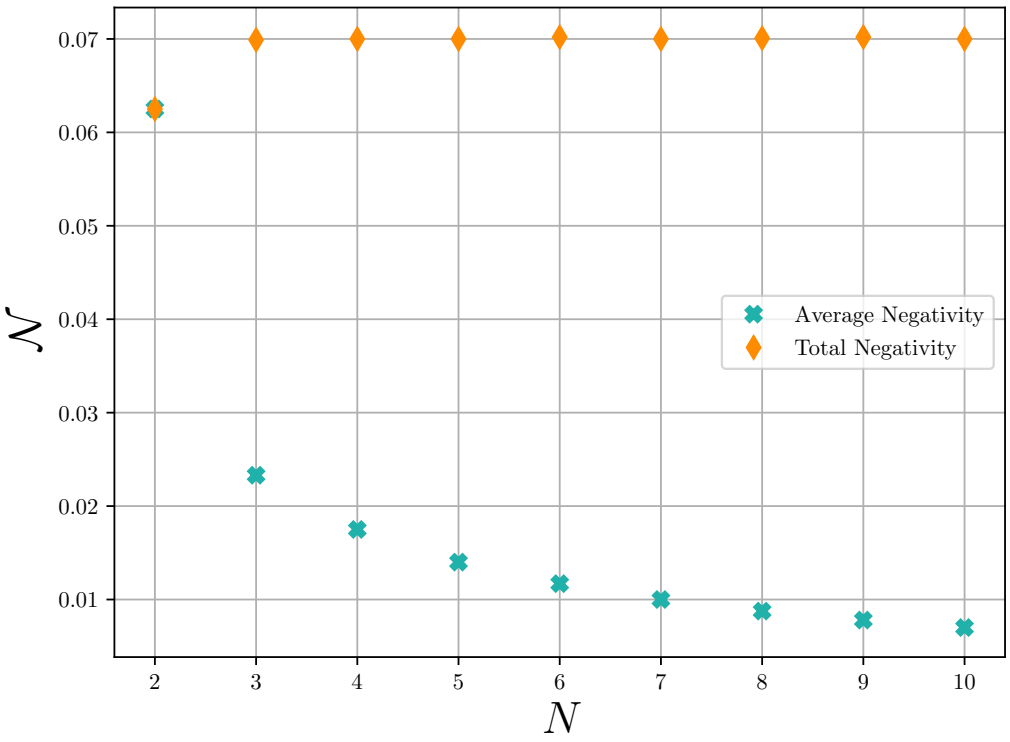

Figure 5.3: Negativity vs number of network nodes. *The average negativity $\mathcal{N}$, computed over any bipartition, is plotted in function of the number of nodes N in the entangled network, together with the corresponding total negativity. The results correspond to the single qubit carrier case, in the ring pattern scenario. Picture from [233].*

5.4.2 Four nodes example: Star Topology

In order to provide a more thorough analysis of the potentialities of our approach, we tailored the protocol to generate a star-like entanglement pattern. We designed the initial state and the protocol steps with the aim of producing a final state in which one central node is entangled with all the others. In this case, the final state results in entanglement with respect to any possible bipartition of the system. We briefly report on this analysis, because of the many analogies with the ring pattern case. We consider four nodes $\mathcal{Q} = \{Q_1, Q_2, Q_3, Q_4\}$, with Q_1 as the central node. Hence, our initial state needs to be the mixture of three terms, each featuring non-classical correlation between qubit Q_1 and the others:

$$\alpha_4 = \frac{1}{3}\sum_{j=2}^{4} \rho^0_{Q_1,Q_j} \otimes \left(\bigotimes_{\overline{j}\in\overline{\mathcal{Q}}} \rho_{Q_{\overline{j}}} \right) \tag{5.27}$$

with $\overline{\mathcal{Q}} = \mathcal{Q}\backslash\{Q_1, Q_j\}$. In this case, the single qubit carrier protocol proceeds identically to the ring case: the carrier interacts at first with the central node and then once with each other qubit, as depicted in Fig. 5.4, since the first operation acts as encoding for every entanglement link. The only difference consists of the initial state preparation of the network, a remarkable feature in terms of flexibility of our strategy.

The qudit carrier case is more complex: each encoding and decoding operation have to be addressed separately, having the nodes interact with different sub-qubits of the carrier. Therefore, the carrier has to travel back and forth from the central node to the periferic qubits, until each link

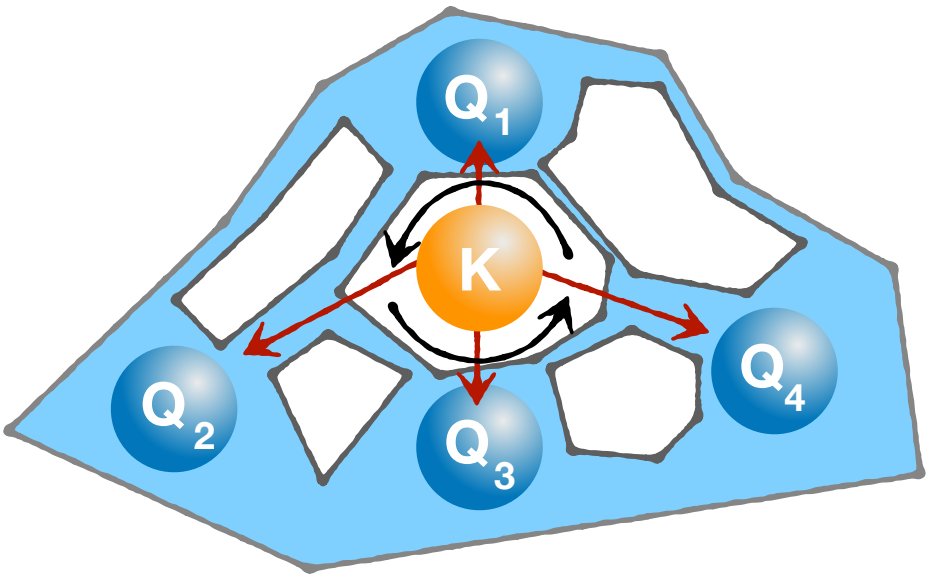

Figure 5.4: Star topology protocol. *Single qubit carrier case: the qubit travels in one direction, interacting once with each node. We leave the description of the qudit carrier case to the main body of text, as it is quite complex to illustrate graphically. Picture from [233].*

has been woven. Considering a eight-dimensional qudit carrier and three qubit subsystems K_1, K_2 and K_3, we can explicitly write down the protocol:

$$\begin{aligned}
\beta_T &= \mathcal{P}_{Q_1K_1}\alpha_T\mathcal{P}^+_{Q_1K_1}\text{encoding mediated by } K_1\\
\rightarrow \gamma_T &= \mathcal{P}_{Q_2K_1}\beta_T\mathcal{P}^+_{Q_2K_1}\text{decoding mediated by } K_1\\
\rightarrow \delta_T &= \mathcal{P}_{Q_1K_2}\gamma_T\mathcal{P}^+_{Q_1K_2}\text{encoding mediated by } K_2\\
\rightarrow \eta_T &= \mathcal{P}_{Q_3K_2}\delta_T\mathcal{P}^+_{Q_3K_2}\text{decoding mediated by } K_2\\
\rightarrow \zeta_T &= \mathcal{P}_{Q_1K_3}\eta_T\mathcal{P}^+_{Q_1K_3}\text{encoding mediated by } K_3\\
\rightarrow \kappa_T &= \mathcal{P}_{Q_4K_3}\zeta_T\mathcal{P}^+_{Q_4K_3}\text{decoding mediated by } K_3.
\end{aligned} \tag{5.28}$$

We report in Tab. 5.3 the negative eigenvalues relative to every bipartition of the system for both methods. The average negativity computed from these results reads $\mathcal{N} = 0.019268$ for the qubit carrier protocol and $\mathcal{N} = 0.0262659$ for the qudit carrier one. In this case, the gap in entanglement production due to the exploitation of a high-dimensional carrier is slightly lower with respect to the ring pattern case, while the other issues remain. In general, the comparison between the usage of a qubit or a qudit carrier may provide different answers according to the application case and, more importantly, the actual experimental situation we are dealing with.

5.4.3 Explicit decomposition for the four-qubit protocol

In general, the Peres-Horodecki criterion is sufficient to witness entanglement but for composite systems of joint dimension $D > 6$, such as the cases we took into account, it is not enough to establish the separability of a system with respect to a given bipartition. In particular, for N nodes systems, we can not demonstrate the separability of the carrier system K by computing the eigenvalues of the partially transposed density matrix only. We have to exhibit an explicit

Bipartition	Single-carrier	Multiple-carrier
$Q_1\|Q_2Q_3Q_4K$	-0.0342865	$\{-0.0291511, -0.00642872, -0.00642872, -0.00642872\}$
$Q_2\|Q_1Q_3Q_4K$	-0.0121071	$\{-0.00681022, -0.00227007, -0.00227007, -0.000756691\}$
$Q_3\|Q_1Q_2Q_4K$	-0.0121071	$\{-0.00681022, -0.00227007, -0.00227007, -0.000756691\}$
$Q_4\|Q_1Q_2Q_3K$	-0.0121071	$\{-0.00681022, -0.00227007, -0.00227007, -0.000756691\}$
$Q_1Q_2\|Q_3Q_4K$	-0.0245719	$\{-0.0235657, -0.00681022, -0.00460722,$ $-0.00460722, -0.00460722, -0.00227007\}$
$Q_1Q_3\|Q_2Q_4K$	-0.0245719	$\{-0.0235657, -0.00681022, -0.00460722,$ $-0.00460722, -0.00227007\}$
$Q_1Q_4\|Q_2Q_3K$	-0.0245719	$\{-0.0235657, -0.00681022, -0.00460722,$ $-0.00460722, -0.00460722, -0.00227007\}$

Table 5.3: *Negative eigenvalues of every possible partition, star pattern, qubit and qudit carrier protocols*

decomposition, as it is done in the Supplementary material to [261] for the two qubits-one carrier qubit case. Indeed, the situation we treat here is a direct generalization of the two qubit protocol: in practice, we run in parallel the binary scheme over different and non interacting terms. Nonetheless, we report here an explicit decomposition for the four qubit case (easily generalizable to the N qubit case), demonstrating the separability of the carrier throughout the process. We consider the two-qubit protocol in Sec. 5.2, acting on the initial state $\alpha_{AB}\otimes\alpha_K$ with the encoding operation produces state β_{ABK}, which can be written as [261]

$$\begin{aligned}
\beta_{ABK} &= \frac{3}{16}\left|00\right\rangle\left\langle 00\right|\otimes\left|A\right\rangle\left\langle A\right| + \frac{3}{16}\left|11\right\rangle\left\langle 11\right|\otimes\left|D\right\rangle\left\langle D\right| \\
&+ \frac{1}{8}\left|\phi^+\right\rangle\left\langle\phi^+\right|\otimes\left|0\right\rangle\left\langle 0\right| + \frac{1}{8}\left|\phi^-\right\rangle\left\langle\phi^-\right|\otimes\left|1\right\rangle\left\langle 1\right| \\
&+ \frac{1}{16}\left|01\right\rangle\left\langle 01\right|\otimes\left|A\right\rangle\left\langle A\right| + \frac{1}{16}\left|10\right\rangle\left\langle 10\right|\otimes\left|D\right\rangle\left\langle D\right| \\
&+ \frac{1}{16}\left|\phi^{+i}\right\rangle\left\langle\phi^{+i}\right|\otimes\left|L\right\rangle\left\langle L\right| + \frac{1}{16}\left|\phi^{-i}\right\rangle\left\langle\phi^{-i}\right|\otimes\left|R\right\rangle\left\langle R\right| \\
&+ \frac{1}{32}\left|01\right\rangle\left\langle 01\right|\otimes\left|L\right\rangle\left\langle L\right| + \frac{1}{32}\left|10\right\rangle\left\langle 10\right|\otimes\left|L\right\rangle\left\langle L\right| \\
&+ \frac{1}{32}\left|\psi^+\right\rangle\left\langle\psi^+\right|\otimes\left|R\right\rangle\left\langle R\right| + \frac{1}{32}\left|\psi^-\right\rangle\left\langle\psi^-\right|\otimes\left|R\right\rangle\left\langle R\right|,
\end{aligned} \tag{5.29}$$

where $\{\left|\phi^\pm\right\rangle, \left|\psi^\pm\right\rangle\}$ is the Bell basis and $\left|\phi^{\pm i}\right\rangle = \frac{1}{\sqrt{2}}(\left|00\right\rangle \pm i\left|11\right\rangle)$. Therefore, the state β_{ABK} is separable with respect to the carrier at this point. After the decoding operation, we have the state γ_{ABK} where

$$\begin{aligned}
\gamma_{ABK} &= \frac{1}{4}\left|\phi^+\right\rangle\left\langle\phi^+\right|\otimes\frac{\mathbb{I}}{2} + \frac{3}{16}\left|00\right\rangle\left\langle 00\right|\otimes\left|A\right\rangle\left\langle A\right| \\
&+ \frac{3}{16}\left|11\right\rangle\left\langle 11\right|\otimes\left|A\right\rangle\left\langle A\right| + \frac{1}{16}\left|01\right\rangle\left\langle 01\right|\otimes\left|D\right\rangle\left\langle D\right| \\
&+ \frac{1}{16}\left|10\right\rangle\left|10\right\rangle\otimes\left|D\right\rangle\left\langle D\right| + \frac{1}{16}\left|\phi^+\right\rangle\left\langle\phi^+\right|\otimes\left|A\right\rangle\left\langle A\right| \\
&+ \frac{1}{16}\left|\phi^-\right\rangle\left\langle\phi^-\right|\otimes\left|D\right\rangle\left\langle D\right| + \frac{1}{16}\left|01\right\rangle\left\langle 01\right|\otimes\frac{\mathbb{I}}{2} \\
&+ \frac{1}{16}\left|10\right\rangle\left\langle 10\right|\otimes\frac{\mathbb{I}}{2},
\end{aligned} \tag{5.30}$$

which demonstrates that this state too is separable with respect to K. We can move now to the four-qubit case in Sec. 5.4. The ring structure has initial state as in Eq. (5.24). Each element of the sum takes the form

$$\frac{1}{4}\rho_{Q_iQ_j} \otimes |0\rangle\langle 0|_{Q_l} \otimes |0\rangle\langle 0|_{Q_m} \otimes \alpha_K. \tag{5.31}$$

A CPHASE gate with Q_l or Q_m as the control qubit will have no effect on this term. However, with Q_i as the control qubit, $\beta_{Q_iQ_jK} \otimes |0\rangle\langle 0|_{Q_l} \otimes |0\rangle\langle 0|_{Q_m}$ is generated. Alternatively, acting on Q_jK will give $\beta'_{Q_iQ_jK} \otimes |0\rangle\langle 0|_{Q_l} \otimes |0\rangle\langle 0|_{Q_m}$ where

$$\begin{aligned}\beta' =& \beta - \frac{1}{16}|01\rangle\langle 01| \otimes |A\rangle\langle A| - \frac{1}{16}|10\rangle\langle 10| \otimes |D\rangle\langle D| \\ &+ \frac{1}{16}|01\rangle\langle 01| \otimes |D\rangle\langle D| + \frac{1}{16}|10\rangle\langle 10| \otimes |A\rangle\langle A|,\end{aligned} \tag{5.32}$$

and therefore we are still left with a separable decomposition with respect to the carrier. When the CPHASE gate on Q_iK acts on the state $\beta'_{Q_iQ_jK}$, we retrieve $\gamma_{Q_iQ_jK}$. As a consequence, after the four CPHASE gates have been applied, the final state of the total system is

$$\begin{aligned}\rho_{\text{final}} =& \gamma_{Q_1Q_2K} \otimes |0\rangle\langle 0|_{Q_3} \otimes |0\rangle\langle 0|_{Q_4} \\ &+ \gamma_{Q_2Q_3K} \otimes |0\rangle\langle 0|_{Q_4} \otimes |0\rangle\langle 0|_{Q_1} \\ &+ \gamma_{Q_3Q_4K} \otimes |0\rangle\langle 0|_{Q_1} \otimes |0\rangle\langle 0|_{Q_2} \\ &+ \gamma_{Q_4Q_1K} \otimes |0\rangle\langle 0|_{Q_2} \otimes |0\rangle\langle 0|_{Q_3}.\end{aligned} \tag{5.33}$$

We can proceed similarly for the star structure case; starting from the initial state in Eq. (5.27), we achieve the final state

$$\rho_{\text{final}} = \frac{1}{3}\sum_{j=2}^{4} \gamma_{Q_1Q_jK} \left(\bigotimes_{\bar{j}\in\bar{\mathcal{Q}}} |0\rangle\langle 0|_{Q_{\bar{j}}} \right), \tag{5.34}$$

where $\bar{\mathcal{Q}} = \mathcal{Q}\backslash\{Q_1, Q_j\}$. Therefore, the carrier is separable from all other subsystems at each stage of the protocol. The multi-qubit case can be addressed following similar lines, that we omit as they do not add consequential material to the global discussion.

5.5 Variations on the theme

In order to better exhibit the flexibility and effectiveness of our protocol, we report here some modified schemes that were at first proposed in [233], addressing different possible scenarios of entanglement distribution.

5.5.1 Simultaneously entangled pairs

At the end of Section 5.3.1, we described the form of the final state of the network as a mixture of terms featuring entanglement between a single node pair each. Clearly, the initial state can be tailored to obtain different mixtures. We show this via a ring pattern example, where we consider a network of N nodes $\{Q_i\}_{i=1}^N$ and we take an even N for sake of simplicity. We want to obtain a final state of the network featuring multipartite entanglement and the possibility of having simultaneously

entangled node pairs in the system. We set the initial state as the mixture of two terms

$$\alpha_N = \frac{1}{2}\left(\bigotimes_{k=1}^{N/2}\rho_{Q_{2k-1},Q_{2k}} + \bigotimes_{j=0}^{N/2-1}\rho_{Q_{2j},Q_{2j+1}}\right) \tag{5.35}$$

where we consider $Q_0 = Q_N$. In this case, simply applying the single qubit carrier protocol, we would obtain a final state of the network fulfilling our initial requirements, but the carrier would end up being entangled during the process. Therefore, we mix these two terms with the initial state for a N nodes ring-like entanglement distribution pattern

$$\begin{aligned}\alpha_N = \frac{1}{N+2}\Bigg[&\bigotimes_{k=1}^{N/2}\rho_{Q_{2k-1},Q_{2k}} + \bigotimes_{j=0}^{N/2-1}\rho_{Q_{2j},Q_{2j+1}} + \\ &+ \sum_{k=1}^{N}\left(\bigotimes_{i=1}^{k}|0\rangle\langle 0|_{Q_i}\right)\otimes\rho^0_{Q_k,Q_{k+1}}\otimes\left(\bigotimes_{j=k+2}^{N}|0\rangle\langle 0|_{Q_j}\right)\Bigg]\end{aligned} \tag{5.36}$$

where we consider $Q_{N+1} = Q_1$. In this way, we are inserting "noise" in the state of the system, which helps keep the carrier separable, while diminishing the probability of finding the network in a final state featuring simultaneously entangled node pairs. After the application of the single-qubit carrier protocol, the final state will be

$$\begin{aligned}\rho^f_N = p\Omega_N + q&\left(\sum_{k=1}^{N}|\phi^+\rangle\langle\phi^+|_{Q_i,Q_{i+1}}\right)\otimes\left(\bigotimes_{j=1,j\neq i,i+1}^{N-1}\alpha^0_{Q_j}\right) \\ &+ r\left(\bigotimes_{k=1}^{N/2}|\phi^+\rangle\langle\phi^+|_{Q_{2k-1},Q_{2k}} + \bigotimes_{j=0}^{N/2-1}|\phi^+\rangle\langle\phi^+|_{Q_{2j},Q_{2j+1}}\right)\end{aligned} \tag{5.37}$$

where $p, q, r \in \mathcal{R}$ with $p + q + r = 1$, and Ω_N is again a completely diagonal contribution to the state of the network, hence classical. Therefore, we have a certain probability of actually finding the system in the state we desire. Alternatively, if we relax the request of complete multipartite entanglement, we can use the initial state $\alpha = \bigotimes_{k=1}^{N/2}\rho_{Q_{2k-1},Q_{2k}}$, relatively increasing the probability of finding the network in a product state of entangled node pairs, although the system shall remain separable with respect to some bipartitions.

5.5.2 Relay scheme for single qubit carrier

In the perspective of an experimental realization, the protocols that we described above can be very demanding from a practical point of view. If we consider the optical framework, photonic control-phase gates require the photons to be indistinguishable in order to work. The request of producing and holding N indistinguishable photons, even for low $N > 3$, may actually be difficult to comply with. There is another suitable way to demonstrate the protocol in an experimental implementation and it is reported in the following: indeed, I devised a variation of the protocol, a single qubit carrier "relay" scheme, where the carrier system is measured and replaced with another after a certain number of protocol steps. This scheme is less efficient than the standard one, but possesses some interesting features as we face experimental realization. We explicitly show the

details of this relay scheme in a four nodes ring pattern example. We have four nodes A, B, C, D and a carrier qubit K. The initial state of the network and carrier is the same as in the standard ring pattern case α_T, as well as the encoding and decoding operations. The only difference consists in the fact that after two interactions, we project the qubit system on the $|A\rangle\langle A|$ state, we trace it away and we insert a new qubit carrier in the initial state α_K

$$\begin{aligned}
\beta_T &= \mathcal{P}_{AK}\alpha_T\mathcal{P}^{+}_{AK} \\
\rightarrow \gamma_T &= \mathcal{P}_{BK}\beta_T\mathcal{P}^{+}_{BK} \\
\rightarrow \gamma_T^{'} &= |A\rangle_K \langle A|\, \gamma_T\, |A\rangle_K \langle A| \\
\rightarrow \gamma_N &= Tr_K(\gamma_T^{'}) \\
\rightarrow \gamma_T^{''} &= \gamma_N \otimes \alpha_K^{\prime} \\
\rightarrow \delta_T &= \mathcal{P}_{CK'}\gamma_T^{''}\mathcal{P}^{+}_{CK'} \\
\rightarrow \eta_T &= \mathcal{P}_{DK'}\delta_T\mathcal{P}^{+}_{DK'}
\end{aligned} \tag{5.38}$$

At the end of the protocols, we get the following negative eigenvalues from the partial transpositions of η_T

$$\begin{cases}
\mathcal{E}_{A-BCDK'} = \{-0.00986842, -0.00328947\} \\
\mathcal{E}_{B-ACDK'} = -0.00986842 \\
\mathcal{E}_{C-ABDK'} = \{-0.00986842, -0.00328947\} \\
\mathcal{E}_{D-ABCK'} = -0.00986842 \\
\mathcal{E}_{K'-ABCD} = 0
\end{cases} \tag{5.39}$$

and, by analyzing all the partitions, the system exhibits multipartite entanglement. It is quite evident that the average negativity produced is lower than in the standard case, although the requested multipartite entanglement and carrier separability are achieved. Therefore, the relay scheme provides with a weaker yet effective protocol for EDSS, which may prove to be useful in practical applications.

5.6 Experimental proposals

We present here some feasible experimental ways of demonstrating the effectiveness of our protocol in an optical framework, that were proposed in [233]. It is important to mention that such proposals can be regarded as suitable platforms for mere proof-of-principle demonstrations. Indeed, the required initial state of the system, although disentangled, is quite complicated to prepare, since it involves the controlled setting of a statistical mixture of many parties, which is generally demanding.

Single qubit carrier

The direct experimental implementation of the single qubit carrier may well be a direct generalization of the apparatus of [261]: N single photons are employed, one as a carrier qubit, while the others act as the network nodes. The state of the network is encoded in the polarization degree of freedom of photons. All photons have to be indistinguishable with the carrier (hence recipro-

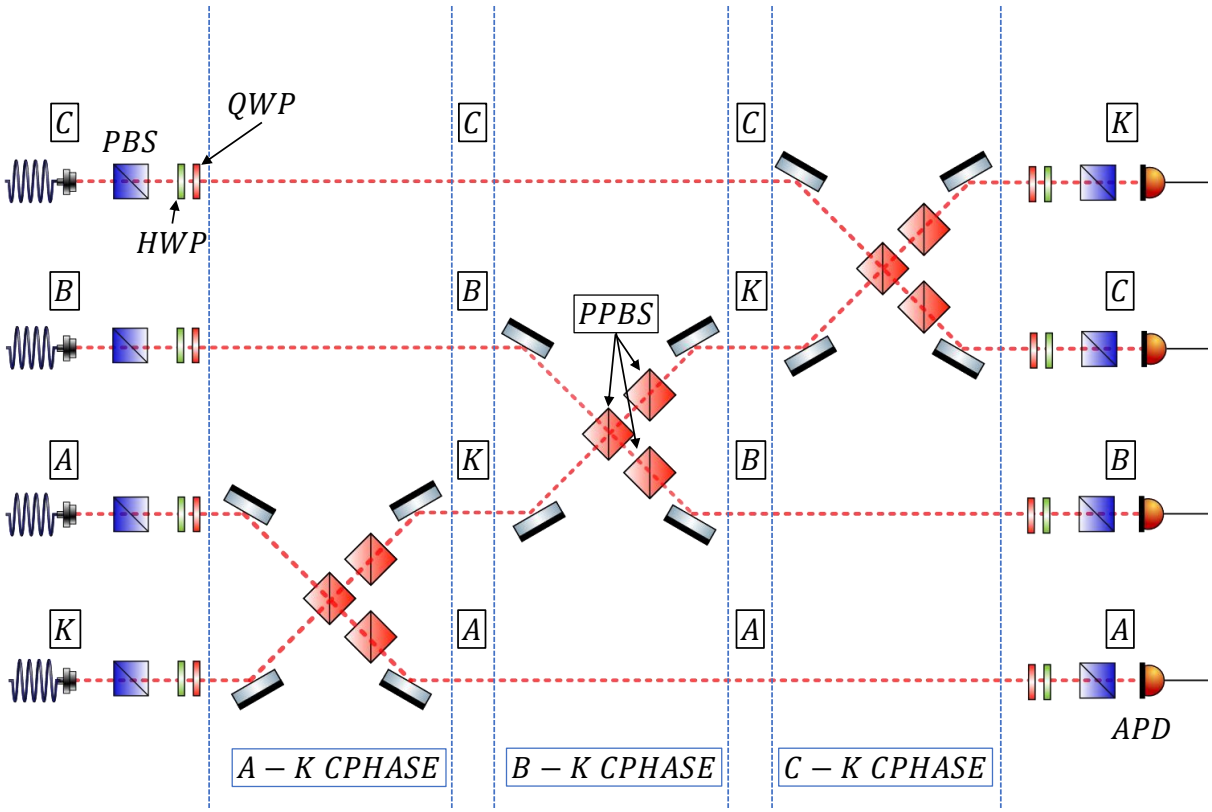

Figure 5.5: Experimental scheme for the Distribution Protocol, 3 nodes ring pattern case. *Four indistinguishable photons are necessary, possibly with a further one for heralding. Three of them act as nodes and interact in turn with the fourth photon, that represents the carrier qubit. Initial state preparation in the degree of freedom of polarization can be addressed through the following set of optical elements: Polarizing Beamsplitter/Polarizer, Half-wave Plate and Quarter-wave plate. The interaction between photonic qubits can be realized via the optical CPHASE gate described in [261, 267]. The sequence of physical interactions depicted here results in a ring-like multipartite entanglement pattern among the photons, or a star-like pattern, depending on the initial state of the system. Picture from [233].*

cally indistinguishable) in order to implement the optical quantum CPHASE gate as described in [261, 267], which acts as the encoding/decoding operation. That may be very difficult to obtain for a high number of photons: they have to be synchronized and identical in any degree of freedom. Indeed, it is possible to build sources with a such a control on the photon generation, which allow many photons interaction [268]. In Fig. 5.5, we report a sketch of the possible experimental implementation of the protocol for the ring pattern for three nodes. After each encoding/decoding operation the photon acting as carrier is sent to the next node and interacts with the corresponding photon, until it has interacted with all the network nodes and it can be projected and measured, leaving, in principle, an entangled state of the network. As mentioned above, the most complex part of the protocol resides in the state preparation, but, if we wish to provide a mere experimental demonstration of the protocol effectiveness, the mixing probabilities of the various terms in the initial state may be simulated by different sampling times, as already done in [261]. That could not be the case in actual application scenarios.

Single qubit carrier, relay scheme

Indeed, the relay strategy implies that the carrier needs only to be indistinguishable with the qubit nodes it interacts with. In particular, we consider the case in which a new qubit carrier is employed after the previous one has interacted with two nodes. Therefore, again in an optical framework, we only need to generate three indistinguishable photons, plus a triggering one, which corresponds to what has been already realized in [261] for the binary protocol. The N nodes protocol may be realized by exploiting $N/2$ sources in an actual scenario.
In case of a proof-of-principle framework, it would be even possible to use the same photon source, since the different parts of the systems remain completely isolated throughout the protocol. It would only be necessary to suitably set the photons' state as the qubit pair which is simulated to be under observation. A sketch of the possible experimental implementation of the scheme for the case of the ring pattern and four nodes is reported in Fig. 5.6.

5.7 Discussion and conclusion

In this Chapter, we have reported on a scheme for the achievement of mutlipartite EDSS in a network. In contrast with the proposal in Ref. [265], where the carrier is made separable by additional operations, our strategy is a generalization of the protocol employed in [261], the carrier is always separable throughout the procedure and supplemental manipulation of the carrier system, aimed at disentangling it, are not needed. It is also characterized by a remarkable flexibility in terms of feasible distribution patterns and possible variations of the standard scheme. Indeed, our strategy may be extended to a continuous-variable framework, as in the binary case, in order to make experimental implementations easier to realize. The results of our work provide a very general alternative approach to direct protocols in the problem of entanglement distribution, although, as highlighted in the text, it is a probabilistic approach. Nevertheless, the advantages of using a separable state carrier in some environmental conditions [261], may be eventually extended to the N qubits scenario, where noise can play a very relevant part. Therefore, these results may pave the way to the development of the general and useful application of EDSS protocols in actual multiparty Quantum Communication and Information tasks. For instance, an application of this work worth mentioning is quantum conference key agreement (QCKA) [269], namely the problem of harnessing properties of quantum states to securely share secret keys between $N > 2$ parties. Quantum key distribution is becoming increasingly important as we approach the realization of quantum computers which would render existing security protocols useless. In particular, QCKA is growing in relevance as quantum networks of many nodes are being developed for the purpose of secure communication (for instance, see Refs. [270–272]). Remarkably, the resources for QCKA are precisely states with the entanglement structure achieved through the protocol illustrated here [273]. Once the entangled state has been shared among the desired N nodes according to the protocol in Sec. 5.3, the N-BB84 protocol [269, 274] for QCKA could then be used to establish a secret key. Therefore, not only can we distribute keys securely between N parties without needing to send, for instance, fragile Green-Horn-Zeilinger (GHZ) states [275] to several nodes, but we show that it is in fact possible without sending any entanglement at all. A natural drawback of our approach is the current experimental unfeasibility, due to two main issues:

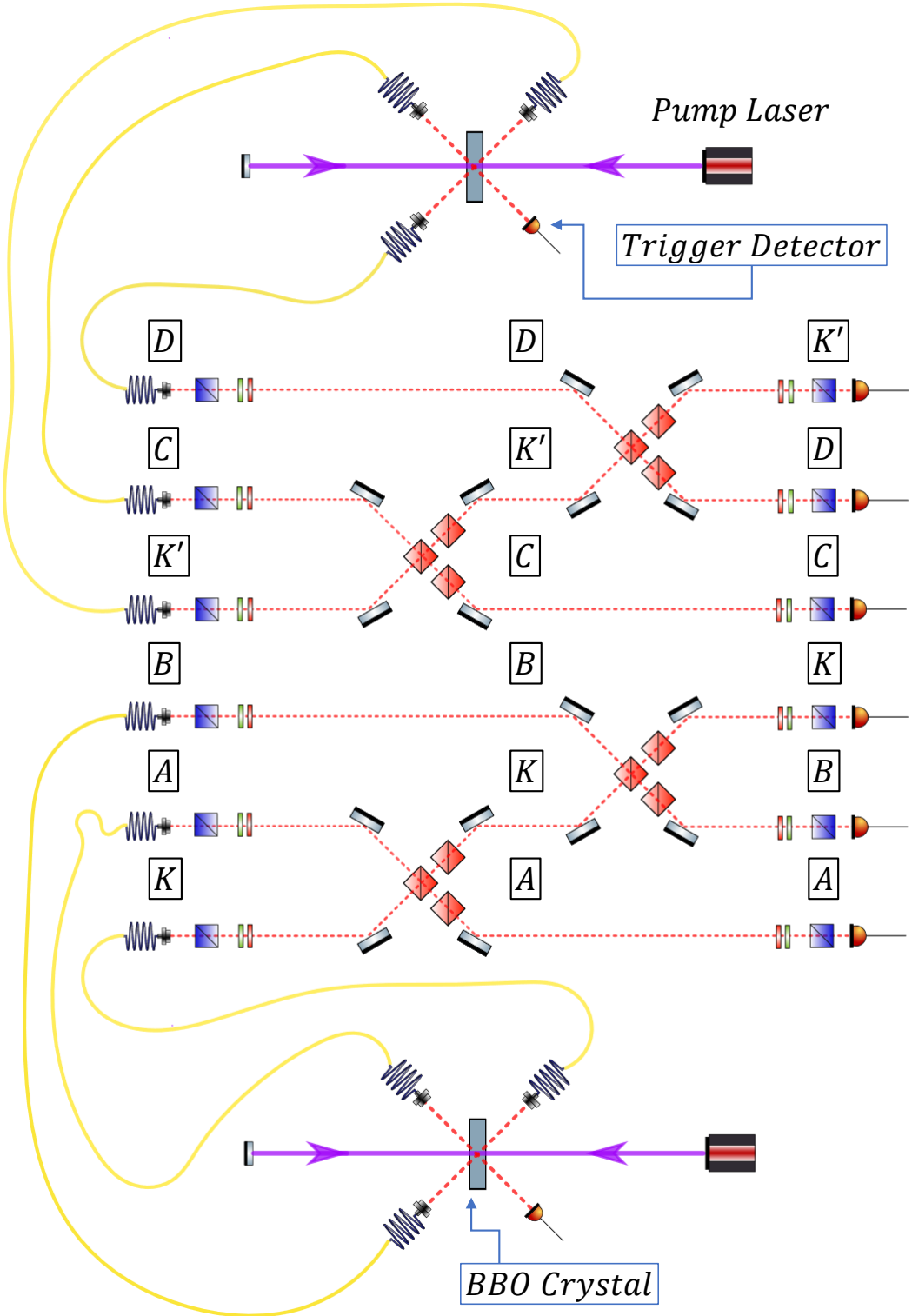

Figure 5.6: experimental scheme for the Relay Protocol, 4 nodes ring pattern case. *Two BBO crystals pumped by pulsed laser are synchronized to generate four indistinguishable photons at the same time. Three of them are sent into the setup, while the fourth is used as a herald for photon generation. Two photon sources allow to generate two triplets of indistinguishable photons, each of which can be used to address two nodes and one carrier. The photons are prepared in the requested initial state after traveling through an optical fiber, then three of them are used to perform the encoding and decoding of entanglement between A and B via K. After the measurement of K, a second triplet can be used to generate entanglement between C and D via K' and, in parallel, between B and C and D and A. Picture from [233].*

- challenging initial state preparation, since it is hard to tailor multipartite mixed states
- low efficiency for photonic implementations, since photonic quantum gates are currently probabilistic

Nonetheless, the solution to these problems is of general interest for experimental quantum information and the pace of technical enhancement in this field is such that thinking of improvements in the very next years is far from preposterous.

Personal contribution

I personally devised the generalized entanglement distribution protocol and all of its variations, run the numerical analyses, and designed the experimental proposals.

Conclusive remarks

He who has come only in part to a freedom of reason cannot feel on earth otherwise than as a wanderer - though not as a traveler towards a final goal, for this does not exist. But he does want to observe, and keep his eyes open for everything that actually occurs in the world; therefore he must not attach his heart too firmly to any individual thing; there must be something wandering within him, which takes its joy in change and transitoriness.

Human, All Too Human, Friedrich W. Nietzsche

It is worth summarizing the varied material we have provided in this thesis: first of all, we deal here with quantum objects and their stark difference with respect to classical ones. To genuine quantum features, such as superposition, indistinguishability and entanglement, can be associated corresponding problems and tasks. In Chapter 1, we have briefly reviewed some of these traits and we have focused on selected issues deriving from them. We have thoroughly described the problem of Quantum State Discrimination as well as the Quantum Walk model, both tightly related to the superposition principle which is applied to quantum states. The topic of Quantum Walks, as we anticipated in the foreword, is spread across the various Chapters, sometimes as the object of investigation, some other times as a tool or an inspiration. In addition to this, we provided a concise description of relevant quantum optics phenomena and quantum optical elements, in order to establish the experimental framework we refer to throughout this work, even when reporting on mere theoretical results. A proper discussion of the activities developed during the PhD course starts in Chapter 2: we establish the p-diluted disorder model, which is pivotal to introduce the contents of both Chapter 2 and 3, and we describe an experimental setup that realizes coherent disordered 1D Quantum Walks, with a great amount of flexibility, such as the one needed to implement p-diluted disorder. A report follows on two works that we partook in as providers of the necessary theoretical ground. The first one consists of a collaboration with the Univeristy of Paderborn, an experiment that realized an optical Quantum Walk simulating subdiffusive propagation by suitable application of disorder. The second one represents the first step of a collaboration with the University of Palermo, an all-theoretical analysis aiming at understanding how disorder can affect the ability to extract information out of a Quantum Walk network. In this Chapter, the duality of Quantum Walks, both interesting objects *per se* and useful tool for quantum information related tasks, clearly emerges. In the third Chapter, we report the results of the first experiment in this manuscript that we actually realized, as the main outcome of the collaboration with University of Palermo mentioned above. Right at the start of the Covid-19 pandemic, I started studying indistinguishable bosons undergoing a disordered but coherent evolution, such as the one dictated by a p-diluted Quantum

Walk, and the way they featured changes in their quantum correlation depending on the disorder configurations they found along their propagation. I found out that it is possible to spatially manipulate the correlation of bosons emerging out of a Quantum Walk evolution, by imposing suitable disorder realizations and we experimentally demonstrated this effect on the optical platform described in Chapter 2. Chapter 4 apparently features an abrupt change of topic: we step from quantum correlation and disordered Quantum walks to Quantum State Discrimination protocols. As a matter of fact, we move from Quantum Walks as the object under investigation to Quantum Walks as an approach for problem solving. This transition is actually smoother than it looks: since Chapter 2 even, we have regarded Quantum Walks as a platform, rather than a phenomenon. Thus, we have a Quantum Walk-based simulator, a Quantum Walk-based probing scheme for phase estimation in a disordered environment and a Quantum Walk-based protocol for enriching bosonic correlation. In Chapter 4, we illustrate a quantum receiver for discrimination of quantum states that is based on coherent propagation on a graph, which is, by definition, described by a Quantum Walk evolution. This quantum discriminator was designed in collaboration with the University of Florence and realized at Sapienza University. We achieved benchmarking experimental results for an actual single particle protocol thanks to this platform, managing to apply it to the states of four-dimensional qudits encoded in single photon's polarization and energy degrees of freedom. In the last and the most "standalone" Chapter, I report on the work I developed during a visiting period at the Queen's University of Belfast, under the supervision of Prof. Mauro Paternostro. In this case, I was asked to try and formulate a Quantum Walk-inspired solution to an open problem: the N-nodes generalization of a protocol for Entanglement Distribution via Separable Systems.I was able to address this issue, devising a protocol for the distribution of multipartite entanglement throughout a network composed of any number of nodes, by local interaction of the parties with an always separable carrier system. This scheme is reported in Chapter 5, together with ideas for experimental implementation.

We have mentioned in the foreword how the thread sewing together the variety of concepts and frameworks employed in this thesis is represented by the quest for dynamical approaches to quantum information problems, approaches that are mainly based on the Quantum Walk model. Nonetheless, we understand that the resulting landscape can not avoid resembling some kind of patchwork. This thesis demonstrates the wide range of problems that can be addressed by dynamical methods based on the Quantum Walk model, as well as it bolsters the notion of quantum optics as the most suitable platform for associated experimental implementations. The manifold subject we have displayed and discussed in this thesis has also led to some impact for the research community, represented by the corresponding publications, that we have cited throughout the body of this work. Nonetheless, in the end, little remains of these results to the authors: projects conclude, setups are dismantled, old ideas are pushed into the shadow by new and compelling commitments. What really is bound to last is the acquaintance with a wide range of topics in the quantum information spectrum, and the practical and intellectual abilities deriving from working on different experimental setups (different light sources even), from addressing different theoretical frameworks and, crucially, from dealing with different people.

List of Papers

The following list reports the works that were developed as a result of my PhD activities. These papers represent the main source of the present manuscript. The first paper I featured in as an author, namely *Experimental investigation of superdiffusion via coherent disordered quantum walks* [110] has not been included in this list, neither extensively reported in the text, since the development and publishing of that work dates back to my master thesis activity.

Publications

- *A scheme for multipartite entanglement distribution via separable carriers*, **Laneve A.**, McAleese H., and Paternostro M., New Journal of Physics **24** 123003, Ref. [233]
- *Experimental multi-state quantum discrimination through optical networks*, **Laneve A.**, Geraldi A., Hamiti F., Mataloni P., and Caruso F., Quantum Science and Technology **7** (2), 025028 (2022), Ref. [174]
- *Enhancing nonclassical bosonic correlations in a quantum walk network through experimental control of disorder*, **Laneve A.**, Nosrati F., Geraldi A., Shadfar M. K., Pegoraro F., Mahdavipour K., Lo Franco R., and Mataloni P., Phys. Rev. Research **3**, 033235 (2021), Ref. [119]
- *Readout of quantum information spreading using a disordered quantum walk*, Nosrati F., **Laneve A.**, Shadfar M. K., Geraldi A., Mahdavipour K., Pegoraro F., Mataloni P., and Lo Franco R., JOSA B, **38**(9), 2570-2578 (2021), Ref. [112]
- *Transient subdiffusion via disordered quantum walks*, Geraldi A., De S. **Laneve A.**, Barkhofen S., Sperling J., Mataloni P., and Silberhorn C., Physical Review Research **3** (2), 023052 (2021), Ref. [111]

Preprints

- *Experimental Multi-state Quantum Discrimination in the Frequency Domain with Quantum Dot Light*, **Laneve A.**, Rota M.B., Basso Basset F. Fiorente N. P., Krieger T.M., Covre da Silva S.F., Buchinger Q., Stroj S., Hoefling S., Huber-Loyola T., Rastelli A., Trotta R., and Mataloni P., arxiv preprint arXiv:2209.08324 (2022), Ref. [175]

Bibliography

[1] Michael A Nielsen and Isaac L Chuang. *Quantum Computation and Quantum Information: 10th Anniversary*. Cambridge University Press, Cambridge, England, 2011.

[2] Albert Einstein, Boris Podolsky, and Nathan Rosen. Can quantum-mechanical description of physical reality be considered complete? *Physical review*, 47(10):777, 1935.

[3] Charles H Bennett and Stephen J Wiesner. Communication via one-and two-particle operators on einstein-podolsky-rosen states. *Physical review letters*, 69(20):2881, 1992.

[4] Artur K Ekert. Quantum cryptography based on bell's theorem. *Physical Review Letters*, 67(6):661, 1991.

[5] Charles H Bennett, Gilles Brassard, Claude Crépeau, Richard Jozsa, Asher Peres, and William K Wootters. Teleporting an unknown quantum state via dual classical and einstein-podolsky-rosen channels. *Phys. Rev. Lett.*, 70(13):1895, 1993.

[6] Eric Chitambar, Debbie Leung, Laura Mančinska, Maris Ozols, and Andreas Winter. Everything you always wanted to know about locc (but were afraid to ask). *Communications in Mathematical Physics*, 328(1):303–326, 2014.

[7] Ryszard Horodecki, Paweł Horodecki, Michał Horodecki, and Karol Horodecki. Quantum entanglement. *Rev. Mod. Phys.*, 81(2):865, 2009.

[8] Otfried Gühne and Géza Tóth. Entanglement detection. *Physics Reports*, 474(1-6):1–75, 2009.

[9] Vlatko Vedral, Martin B Plenio, Michael A Rippin, and Peter L Knight. Quantifying entanglement. *Phys. Rev. Lett.*, 78(12):2275, 1997.

[10] Guifré Vidal and Reinhard F Werner. Computable measure of entanglement. *Physical Review A*, 65(3):032314, 2002.

[11] Asher Peres. Separability criterion for density matrices. *Physical Review Letters*, 77(8):1413, 1996.

[12] Rodney Loudon. *The quantum theory of light*. OUP Oxford, 2000.

[13] Marcos Curty, Maciej Lewenstein, and Norbert Lütkenhaus. Entanglement as a precondition for secure quantum key distribution. *Physical review letters*, 92(21):217903, 2004.

[14] Antonio Acin, Serge Massar, and Stefano Pironio. Efficient quantum key distribution secure against no-signalling eavesdroppers. *New Journal of Physics*, 8(8):126, 2006.

[15] Charles H Bennett and Gilles Brassard. An update on quantum cryptography. In *Workshop on the theory and application of cryptographic techniques*, pages 475–480. Springer, 1984.

[16] Feihu Xu, Xiongfeng Ma, Qiang Zhang, Hoi-Kwong Lo, and Jian-Wei Pan. Secure quantum key distribution with realistic devices. *Reviews of Modern Physics*, 92(2):025002, 2020.

[17] Grant R Fowles. *Introduction to modern optics*. Courier Corporation, 1989.

[18] Jeremy L O'brien. Optical quantum computing. *Science*, 318(5856):1567–1570, 2007.

[19] Anthony Mark Fox, Mark Fox, et al. *Quantum optics: an introduction*, volume 15. Oxford university press, 2006.

[20] R Brown and Richard Q Twiss. Correlation between photons in two coherent beams of light. *Nature*, 177(4497):27–29, 1956.

[21] Bahaa EA Saleh and Malvin Carl Teich. *Fundamentals of photonics*. John Wiley & Sons, 2019.

[22] Max Born and Emil Wolf. *Principles of optics: electromagnetic theory of propagation, interference and diffraction of light*. Elsevier, 2013.

[23] Robert W Boyd. *Nonlinear optics*. Elsevier, 2003.

[24] JA Armstrong, N Bloembergen, J Ducuing, and PS Pershan. Interactions between light waves in a nonlinear dielectric. *Physical review*, 127(6):1918, 1962.

[25] Chong-Ki Hong, Zhe-Yu Ou, and Leonard Mandel. Measurement of subpicosecond time intervals between two photons by interference. *Physical review letters*, 59(18):2044, 1987.

[26] Linda Sansoni, Fabio Sciarrino, Giuseppe Vallone, Paolo Mataloni, Andrea Crespi, Roberta Ramponi, and Roberto Osellame. Two-particle bosonic-fermionic quantum walk via integrated photonics. *Phys. Rev. Lett.*, 108(1):010502, 2012.

[27] Andrea Crespi, Roberto Osellame, Roberta Ramponi, Vittorio Giovannetti, Rosario Fazio, Linda Sansoni, Francesco De Nicola, Fabio Sciarrino, and Paolo Mataloni. Anderson localization of entangled photons in an integrated quantum walk. *Nat. Photonics*, 7(4):322, 2013.

[28] Daniel Huber, Marcus Reindl, Johannes Aberl, Armando Rastelli, and Rinaldo Trotta. Semiconductor quantum dots as an ideal source of polarization-entangled photon pairs on-demand: a review. *Journal of Optics*, 20(7):073002, 2018.

[29] Neil W Ashcroft and N David Mermin. *Solid state physics*. Cengage Learning, 2022.

[30] Go Dresselhaus. Effective mass approximation for excitons. *Journal of Physics and Chemistry of Solids*, 1(1-2):14–22, 1956.

[31] John H Davies. *The physics of low-dimensional semiconductors: an introduction*. Cambridge university press, 1998.

[32] Radim Hošák, Ivo Straka, Ana Predojević, Radim Filip, and Miroslav Ježek. Effect of source statistics on utilizing photon entanglement in quantum key distribution. *Physical Review A*, 103(4):042411, 2021.

[33] Peter Michler. *Quantum dots for quantum information technologies*, volume 237. Springer, 2017.

[34] Daniel A Vajner, Lucas Rickert, Timm Gao, Koray Kaymazlar, and Tobias Heindel. Quantum communication using semiconductor quantum dots. *Advanced Quantum Technologies*, page 2100116, 2022.

[35] Chao-Yang Lu and Jian-Wei Pan. Quantum-dot single-photon sources for the quantum internet. *Nature Nanotechnology*, 16(12):1294–1296, 2021.

[36] Matthew S Leifer and Owen JE Maroney. Maximally epistemic interpretations of the quantum state and contextuality. *Physical review letters*, 110(12):120401, 2013.

[37] Anthony Chefles. Quantum state discrimination. *Contemporary Physics*, 41(6):401–424, 2000.

[38] Joonwoo Bae and Leong-Chuan Kwek. Quantum state discrimination and its applications. *Journal of Physics A: Mathematical and Theoretical*, 48(8):083001, 2015.

[39] Stephen Boyd, Stephen P Boyd, and Lieven Vandenberghe. *Convex optimization*. Cambridge university press, 2004.

[40] Carl W Helstrom and Carl W Helstrom. *Quantum detection and estimation theory*, volume 84. Academic press New York, 1976.

[41] Y.C. Eldar, A. Megretski, and G.C. Verghese. Optimal detection of symmetric mixed quantum states. *IEEE Transactions on Information Theory*, 50(6):1198–1207, 2004.

[42] Yonina C Eldar and G David Forney. On quantum detection and the square-root measurement. *IEEE Transactions on Information Theory*, 47(3):858–872, 2001.

[43] Carlos Mochon. Family of generalized "pretty good" measurements and the minimal-error pure-state discrimination problems for which they are optimal. *Phys. Rev. A*, 73:032328, Mar 2006.

[44] Horace Yuen, Robert Kennedy, and Melvin Lax. Optimum testing of multiple hypotheses in quantum detection theory. *IEEE Transactions on Information Theory*, 21(2):125–134, 1975.

[45] Anthony Chefles. Unambiguous discrimination between linearly independent quantum states. *Physics Letters A*, 239(6):339–347, 1998.

[46] János A. Bergou, Ulrike Futschik, and Edgar Feldman. Optimal unambiguous discrimination of pure quantum states. *Phys. Rev. Lett.*, 108:250502, Jun 2012.

[47] Y.C. Eldar. A semidefinite programming approach to optimal unambiguous discrimination of quantum states. *IEEE Transactions on Information Theory*, 49(2):446–456, 2003.

[48] Alexander Semenovich Holevo. Remarks on optimal quantum measurements. *Problemy Peredachi Informatsii*, 10(4):51–55, 1974.

[49] Antonio Acín, Emili Bagan, Maria Baig, Ll Masanes, and Ramon Munoz-Tapia. Multiple-copy two-state discrimination with individual measurements. *Physical Review A*, 71(3):032338, 2005.

[50] Roger BM Clarke, Anthony Chefles, Stephen M Barnett, and Erling Riis. Experimental demonstration of optimal unambiguous state discrimination. *Physical Review A*, 63(4):040305, 2001.

[51] Roger BM Clarke, Vivien M Kendon, Anthony Chefles, Stephen M Barnett, Erling Riis, and Masahide Sasaki. Experimental realization of optimal detection strategies for overcomplete states. *Physical Review A*, 64(1):012303, 2001.

[52] Samuel L Braunstein and Peter Van Loock. Quantum information with continuous variables. *Reviews of modern physics*, 77(2):513, 2005.

[53] Dany-Sebastien Ly-Gagnon, Satoshi Tsukamoto, Kazuhiro Katoh, and Kazuro Kikuchi. Coherent detection of optical quadrature phase-shift keying signals with carrier phase estimation. *Journal of lightwave technology*, 24(1):12, 2006.

[54] FE Becerra, J Fan, G Baumgartner, JTKJ Goldhar, JT Kosloski, and A Migdall. Experimental demonstration of a receiver beating the standard quantum limit for multiple nonorthogonal state discrimination. *Nature Photonics*, 7(2):147–152, 2013.

[55] FE Becerra, Jingyun Fan, and Alan Migdall. Implementation of generalized quantum measurements for unambiguous discrimination of multiple non-orthogonal coherent states. *Nature communications*, 4(1):1–6, 2013.

[56] AR Ferdinand, MT DiMario, and FE Becerra. Multi-state discrimination below the quantum noise limit at the single-photon level. *npj Quantum Information*, 3(1):1–7, 2017.

[57] IA Burenkov, MV Jabir, A Battou, and SV Polyakov. Time-resolving quantum measurement enables energy-efficient, large-alphabet communication. *PRX Quantum*, 1(1):010308, 2020.

[58] Jasminder S Sidhu, Shuro Izumi, Jonas S Neergaard-Nielsen, Cosmo Lupo, and Ulrik L Andersen. Quantum receiver for phase-shift keying at the single-photon level. *PRX Quantum*, 2(1):010332, 2021.

[59] Shuro Izumi, Masahiro Takeoka, Kazuhiro Ema, and Masahide Sasaki. Quantum receivers with squeezing and photon-number-resolving detectors for m-ary coherent state discrimination. *Physical Review A*, 87(4):042328, 2013.

[60] Shuro Izumi, Jonas S Neergaard-Nielsen, and Ulrik L Andersen. Adaptive generalized measurement for unambiguous state discrimination of quaternary phase-shift-keying coherent states. *Prx Quantum*, 2(2):020305, 2021.

[61] Nicola Dalla Pozza and Filippo Caruso. Quantum state discrimination on reconfigurable noise-robust quantum networks. *Physical Review Research*, 2(4):043011, 2020.

[62] Andrew Patterson, Hongxiang Chen, Leonard Wossnig, Simone Severini, Dan Browne, and Ivan Rungger. Quantum state discrimination using noisy quantum neural networks. *Physical Review Research*, 3(1):013063, 2021.

[63] Marco Fanizza, Andrea Mari, and Vittorio Giovannetti. Optimal universal learning machines for quantum state discrimination. *IEEE Transactions on Information Theory*, 65(9):5931–5944, 2019.

[64] Matthew F Pusey, Jonathan Barrett, and Terry Rudolph. On the reality of the quantum state. *Nature Physics*, 8(6):475–478, 2012.

[65] Carlton M. Caves, Christopher A. Fuchs, and Rüdiger Schack. Conditions for compatibility of quantum-state assignments. *Phys. Rev. A*, 66:062111, Dec 2002.

[66] Somshubhro Bandyopadhyay, Rahul Jain, Jonathan Oppenheim, and Christopher Perry. Conclusive exclusion of quantum states. *Phys. Rev. A*, 89:022336, Feb 2014.

[67] G. M. D'Ariano and P. Lo Presti. Quantum tomography for measuring experimentally the matrix elements of an arbitrary quantum operation. *Phys. Rev. Lett.*, 86:4195–4198, May 2001.

[68] Yakir Aharonov, Luiz Davidovich, and Nicim Zagury. Quantum random walks. *Phys. Rev. A*, 48(2):1687, 1993.

[69] Andrew M Childs. Universal computation by quantum walk. *Physical review letters*, 102(18):180501, 2009.

[70] Neil B Lovett, Sally Cooper, Matthew Everitt, Matthew Trevers, and Viv Kendon. Universal quantum computation using the discrete-time quantum walk. *Physical Review A*, 81(4):042330, 2010.

[71] Salvador Elías Venegas-Andraca. Quantum walks: a comprehensive review. *Quantum Information Processing*, 11(5):1015–1106, 2012.

[72] Vivien M Kendon and Christino Tamon. Perfect state transfer in quantum walks on graphs. *Journal of Computational and Theoretical Nanoscience*, 8(3):422–433, 2011.

[73] Taira Giordani, Emanuele Polino, Sabrina Emiliani, Alessia Suprano, Luca Innocenti, Helena Majury, Lorenzo Marrucci, Mauro Paternostro, Alessandro Ferraro, Nicolò Spagnolo, et al. Experimental engineering of arbitrary qudit states with discrete-time quantum walks. *Physical review letters*, 122(2):020503, 2019.

[74] Masoud Mohseni, Patrick Rebentrost, Seth Lloyd, and Alan Aspuru-Guzik. Environment-assisted quantum walks in photosynthetic energy transfer. *The Journal of chemical physics*, 129(17):11B603, 2008.

[75] Rodney Coleman. *Stochastic processes*, volume 14. Springer Science & Business Media, 2013.

[76] David A Meyer. From quantum cellular automata to quantum lattice gases. *Journal of Statistical Physics*, 85(5-6):551–574, 1996.

[77] Ashwin Nayak and Ashvin Vishwanath. Quantum walk on the line. *arXiv preprint quant-ph/0010117*, 2000.

[78] Andris Ambainis, Eric Bach, Ashwin Nayak, Ashvin Vishwanath, and John Watrous. One-dimensional quantum walks. In *Proceedings of the thirty-third annual ACM symposium on Theory of computing*, pages 37–49, New York, NY, USA, 2001. Association for Computing Machinery.

[79] Norio Konno. Quantum random walks in one dimension. *Quantum Information Processing*, 1(5):345–354, 2002.

[80] Viv Kendon and Ben Tregenna. Decoherence can be useful in quantum walks. *Phys. Rev. A*, 67(4):042315, 2003.

[81] Markus Gräfe, René Heilmann, Maxime Lebugle, Diego Guzman-Silva, Armando Perez-Leija, and Alexander Szameit. Integrated photonic quantum walks. *Journal of Optics*, 18(10):103002, 2016.

[82] Fulvio Flamini, Lorenzo Magrini, Adil S Rab, Nicolò Spagnolo, Vincenzo D'ambrosio, Paolo Mataloni, Fabio Sciarrino, Tommaso Zandrini, Andrea Crespi, Roberta Ramponi, et al. Thermally reconfigurable quantum photonic circuits at telecom wavelength by femtosecond laser micromachining. *Light: Science & Applications*, 4(11):e354–e354, 2015.

[83] A Schreiber, KN Cassemiro, V Potoček, A Gábris, I Jex, and Ch Silberhorn. Decoherence and disorder in quantum walks: from ballistic spread to localization. *Phys. Rev. Lett.*, 106(18):180403, 2011.

[84] Filippo Cardano, Francesco Massa, Hammam Qassim, Ebrahim Karimi, Sergei Slussarenko, Domenico Paparo, Corrado de Lisio, Fabio Sciarrino, Enrico Santamato, Robert W Boyd, et al. Quantum walks and wavepacket dynamics on a lattice with twisted photons. *Science advances*, 1(2):e1500087, 2015.

[85] Chiara Esposito, Mariana R Barros, Andrés Durán Hernández, Gonzalo Carvacho, Francesco Di Colandrea, Raouf Barboza, Filippo Cardano, Nicolò Spagnolo, Lorenzo Marrucci, and Fabio Sciarrino. Quantum walks of two correlated photons in a 2d synthetic lattice. *npj Quantum Information*, 8(1):1–7, 2022.

[86] Andrew M Childs and Jeffrey Goldstone. Spatial search by quantum walk. *Physical Review A*, 70(2):022314, 2004.

[87] Philip W Anderson. Absence of diffusion in certain random lattices. *Phys. Rev.*, 109(5):1492, 1958.

[88] Matthew A Broome, Alessandro Fedrizzi, Benjimain P Lanyon, Ivan Kassal, Alan Aspuru-Guzik, and Andrew G White. Discrete single-photon quantum walks with tunable decoherence. *Physical review letters*, 104(15):153602, 2010.

[89] Diederik S Wiersma, Paolo Bartolini, Ad Lagendijk, and Roberto Righini. Localization of light in a disordered medium. *Nature*, 390(6661):671, 1997.

[90] Hefei Hu, A Strybulevych, JH Page, Sergey E Skipetrov, and Bart A van Tiggelen. Localization of ultrasound in a three-dimensional elastic network. *Nature Physics*, 4(12):945, 2008.

[91] Mordechai Segev, Yaron Silberberg, and Demetrios N Christodoulides. Anderson localization of light. *Nat. Photonics*, 7(3):197, 2013.

[92] SS Abdullaev and F Kh Abdullaev. On propagation of light in fiber bundles with random parameters. *Radiofizika*, 23(6):766–767, 1980.

[93] Hans De Raedt, AD Lagendijk, and Pedro de Vries. Transverse localization of light. *Physical review letters*, 62(1):47, 1989.

[94] Tal Schwartz, Guy Bartal, Shmuel Fishman, and Mordechai Segev. Transport and anderson localization in disordered two-dimensional photonic lattices. *Nature*, 446(7131):52, 2007.

[95] Yoav Lahini, Assaf Avidan, Francesca Pozzi, Marc Sorel, Roberto Morandotti, Demetrios N Christodoulides, and Yaron Silberberg. Anderson localization and nonlinearity in one-dimensional disordered photonic lattices. *Physical Review Letters*, 100(1):013906, 2008.

[96] Alán Aspuru-Guzik and Philip Walther. Photonic quantum simulators. *Nature physics*, 8(4):285, 2012.

[97] Hyunseok Jeong, Mauro Paternostro, and Myungshik S Kim. Simulation of quantum random walks using the interference of a classical field. *Phys. Rev. A*, 69(1):012310, 2004.

[98] Yaron Bromberg, Yoav Lahini, Roberto Morandotti, and Yaron Silberberg. Quantum and classical correlations in waveguide lattices. *Phys. Rev. Lett.*, 102(25):253904, 2009.

[99] Yoav Lahini, Rami Pugatch, Francesca Pozzi, Marc Sorel, Roberto Morandotti, Nir Davidson, and Yaron Silberberg. Observation of a localization transition in quasiperiodic photonic lattices. *Physical review letters*, 103(1):013901, 2009.

[100] Alberto Peruzzo, Mirko Lobino, Jonathan CF Matthews, Nobuyuki Matsuda, Alberto Politi, Konstantinos Poulios, Xiao-Qi Zhou, Yoav Lahini, Nur Ismail, Kerstin Wörhoff, et al. Quantum walks of correlated photons. *Science*, 329(5998):1500–1503, 2010.

[101] Konstantinos Poulios, Robert Keil, Daniel Fry, Jasmin DA Meinecke, Jonathan CF Matthews, Alberto Politi, Mirko Lobino, Markus Gräfe, Matthias Heinrich, Stefan Nolte, et al. Quantum walks of correlated photon pairs in two-dimensional waveguide arrays. *Phys. Rev. Lett.*, 112(14):143604, 2014.

[102] Vadim Oganesyan and David A Huse. Localization of interacting fermions at high temperature. *Physical review b*, 75(15):155111, 2007.

[103] Yoav Lahini, Yaron Bromberg, Demetrios N Christodoulides, and Yaron Silberberg. Quantum correlations in two-particle anderson localization. *Phys. Rev. Lett.*, 105(16):163905, 2010.

[104] Andre Ahlbrecht, Holger Vogts, Albert H Werner, and Reinhard F Werner. Asymptotic evolution of quantum walks with random coin. *Journal of Mathematical Physics*, 52(4):042201, 2011.

[105] AM Jayannavar and N Kumar. Nondiffusive quantum transport in a dynamically disordered medium. *Physical Review Letters*, 48(8):553, 1982.

[106] Leonardo Golubović, Shechao Feng, and Fan-An Zeng. Classical and quantum superdiffusion in a time-dependent random potential. *Physical Review Letters*, 67(16):2115, 1991.

[107] Marshall N Rosenbluth. Comment on "classical and quantum superdiffusion in a time-dependent random potential". *Physical review letters*, 69(12):1831, 1992.

[108] Yevgeny Krivolapov, Liad Levi, Shmuel Fishman, Mordechai Segev, and Michael Wilkinson. Super-diffusion in optical realizations of anderson localization. *New Journal of Physics*, 14(4):043047, 2012.

[109] Liad Levi, Yevgeny Krivolapov, Shmuel Fishman, and Mordechai Segev. Hyper-transport of light and stochastic acceleration by evolving disorder. *Nat. Phys.*, 8(12):912, 2012.

[110] Andrea Geraldi, Alessandro Laneve, Luis Diego Bonavena, Linda Sansoni, Jose Ferraz, Andrea Fratalocchi, Fabio Sciarrino, Álvaro Cuevas, and Paolo Mataloni. Experimental investigation of superdiffusion via coherent disordered quantum walks. *Phys. Rev. Lett.*, 123(14):140501, 2019.

[111] Andrea Geraldi, Syamsundar De, Alessandro Laneve, Sonja Barkhofen, Jan Sperling, Paolo Mataloni, and Christine Silberhorn. Transient subdiffusion via disordered quantum walks. *Phys. Rev. Research*, 3:023052, Apr 2021.

[112] Farzam Nosrati, Alessandro Laneve, Mahshid Khazaei Shadfar, Andrea Geraldi, Kobra Mahdavipour, Federico Pegoraro, Paolo Mataloni, and Rosario Lo Franco. Readout of quantum information spreading using a disordered quantum walk. *JOSA B*, 38(9):2570–2578, 2021.

[113] Robert B Griffiths. Nonanalytic behavior above the critical point in a random ising ferromagnet. *Physical Review Letters*, 23(1):17, 1969.

[114] Jianwei Wang, Fabio Sciarrino, Anthony Laing, and Mark G Thompson. Integrated photonic quantum technologies. *Nature Photonics*, 14(5):273–284, 2020.

[115] Caterina Taballione, Reinier van der Meer, Henk J Snijders, Peter Hooijschuur, Jörn P Epping, Michiel de Goede, Ben Kassenberg, Pim Venderbosch, Chris Toebes, Hans van den Vlekkert, et al. A universal fully reconfigurable 12-mode quantum photonic processor. *Materials for Quantum Technology*, 1(3):035002, 2021.

[116] Emanuele Pelucchi, Giorgos Fagas, Igor Aharonovich, Dirk Englund, Eden Figueroa, Qihuang Gong, Hübel Hannes, Jin Liu, Chao-Yang Lu, Nobuyuki Matsuda, et al. The potential and global outlook of integrated photonics for quantum technologies. *Nature Reviews Physics*, 4(3):194–208, 2022.

[117] Álvaro Cuevas, Andrea Geraldi, Carlo Liorni, Luís Diego Bonavena, Antonella De Pasquale, Fabio Sciarrino, Vittorio Giovannetti, and Paolo Mataloni. All-optical implementation of collision-based evolutions of open quantum systems. *Scientific reports*, 9(1):3205, 2019.

[118] Andrea Geraldi, Luís Diego Bonavena, Carlo Liorni, Paolo Mataloni, and Álvaro Cuevas. A novel bulk-optics scheme for quantum walk with high phase stability. *Condensed Matter*, 4(1):14, 2019.

[119] Alessandro Laneve, Farzam Nosrati, Andrea Geraldi, Kobra Mahdavipour, Federico Pegoraro, Mahshid Khazaei Shadfar, Rosario Lo Franco, and Paolo Mataloni. Enhancing nonclassical bosonic correlations in a quantum walk network through experimental control of disorder. *Physical Review Research*, 3(3):033235, 2021.

[120] Andreas Schreiber, Katiuscia N Cassemiro, Václav Potoček, Aurél Gábris, Peter James Mosley, Erika Andersson, Igor Jex, and Ch Silberhorn. Photons walking the line: a quantum walk with adjustable coin operations. *Physical review letters*, 104(5):050502, 2010.

[121] Thomas Nitsche, Sonja Barkhofen, Regina Kruse, Linda Sansoni, Martin Štefaňák, Aurél Gábris, Václav Potoček, Tamás Kiss, Igor Jex, and Christine Silberhorn. Probing measurement-induced effects in quantum walks via recurrence. *Science advances*, 4(6):eaar6444, 2018.

[122] H Eduardo Roman and Massimiliano Giona. Fractional diffusion equation on fractals: three-dimensional case and scattering function. *Journal of Physics A: Mathematical and General*, 25(8):2107, 1992.

[123] A. S. Pikovsky and D. L. Shepelyansky. Destruction of anderson localization by a weak nonlinearity. *Physical Review Letters*, 100(9):094101, 2008.

[124] Ihor Vakulchyk, Mikhail V. Fistul, and Sergej Flach. Wave packet spreading with disordered nonlinear discrete-time quantum walks. *Physical Review Letters*, 122(4):040501, 2019.

[125] Carlos Navarrete-Benlloch, Armando Pérez, and Eugenio Roldán. Nonlinear optical galton board. *Physical Review A*, 75(6):062333, 2007.

[126] T Nitsche, S De, S Barkhofen, E Meyer-Scott, J Tiedau, J Sperling, Gábris A, I Jex, and C Silberhorn. Local versus global two-photon interference in quantum networks. *arXiv:2005.07219*.

[127] Mostafa Annabestani, Majid Hassani, Dario Tamascelli, and Matteo GA Paris. Multiparameter quantum metrology with discrete-time quantum walks. *Physical Review A*, 105(6):062411, 2022.

[128] Emanuele Polino, Martina Riva, Mauro Valeri, Raffaele Silvestri, Giacomo Corrielli, Andrea Crespi, Nicolò Spagnolo, Roberto Osellame, and Fabio Sciarrino. Experimental multiphase estimation on a chip. *Optica*, 6(3):288–295, 2019.

[129] Mauro Valeri, Emanuele Polino, Davide Poderini, Ilaria Gianani, Giacomo Corrielli, Andrea Crespi, Roberto Osellame, Nicolò Spagnolo, and Fabio Sciarrino. Experimental adaptive bayesian estimation of multiple phases with limited data. *npj Quantum Information*, 6(1):1–11, 2020.

[130] Seongjin Hong, Yong-Su Kim, Young-Wook Cho, Seung-Woo Lee, Hojoong Jung, Sung Moon, Sang-Wook Han, Hyang-Tag Lim, et al. Quantum enhanced multiple-phase estimation with multi-mode n00n states. *Nature communications*, 12(1):1–8, 2021.

[131] Emanuele Polino, Mauro Valeri, Nicolò Spagnolo, and Fabio Sciarrino. Photonic quantum metrology. *AVS Quantum Science*, 2(2):024703, 2020.

[132] Alexander S Holevo. *Probabilistic and statistical aspects of quantum theory*, volume 1. Springer Science & Business Media, 2011.

[133] Dénes Petz and Csaba Sudár. Geometries of quantum states. *Journal of Mathematical Physics*, 37(6):2662–2673, 1996.

[134] Dénes Petz. Covariance and fisher information in quantum mechanics. *Journal of Physics A: Mathematical and General*, 35(4):929, 2002.

[135] Matteo GA Paris. Quantum estimation for quantum technology. *International Journal of Quantum Information*, 7(supp01):125–137, 2009.

[136] Farzam Nosrati, Alessia Castellini, Giuseppe Compagno, and Rosario Lo Franco. Robust entanglement preparation against noise by controlling spatial indistinguishability. *npj Quantum Inf.*, 6(1):1–7, 2020.

[137] Kai Sun, Yan Wang, Zheng-Hao Liu, Xiao-Ye Xu, Jin-Shi Xu, Chuan-Feng Li, Guang-Can Guo, Alessia Castellini, Farzam Nosrati, Giuseppe Compagno, et al. Experimental quantum entanglement and teleportation by tuning remote spatial indistinguishability of independent photons. *Opt. Lett*, 45(23):6410–6413, 2020.

[138] Dominic W Berry and Howard M Wiseman. Optimal states and almost optimal adaptive measurements for quantum interferometry. *Physical review letters*, 85(24):5098, 2000.

[139] Alexander Hentschel and Barry C Sanders. Machine learning for precise quantum measurement. *Physical review letters*, 104(6):063603, 2010.

[140] Howard Mark Wiseman and John A Vaccaro. Entanglement of indistinguishable particles shared between two parties. *Phys. Rev. Lett.*, 91(9):097902, 2003.

[141] Rosario Lo Franco and Giuseppe Compagno. Indistinguishability of elementary systems as a resource for quantum information processing. *Phys. Rev. Lett.*, 120(24):240403, 2018.

[142] ZY Ou, CK Hong, and L Mandel. Relation between input and output states for a beam splitter. *Opt. Commun*, 63(2):118–122, 1987.

[143] Taira Giordani, Fulvio Flamini, Matteo Pompili, Niko Viggianiello, Nicolò Spagnolo, Andrea Crespi, Roberto Osellame, Nathan Wiebe, Mattia Walschaers, Andreas Buchleitner, et al. Experimental statistical signature of many-body quantum interference. *Nat. Photonics*, 12(3):173–178, 2018.

[144] F Benatti, R Floreanini, F Franchini, and U Marzolino. Entanglement in indistinguishable particle systems. *Phys. Rep.*, 878:1–27, 2020.

[145] S Bose and D Home. Generic entanglement generation, quantum statistics, and complementarity. *Phys. Rev. Lett.*, 88(5):050401, 2002.

[146] Mariana R Barros, Seungbeom Chin, Tanumoy Pramanik, Hyang-Tag Lim, Young-Wook Cho, Joonsuk Huh, and Yong-Su Kim. Entangling bosons through particle indistinguishability and spatial overlap. *Opt. Express*, 28(25):38083–38092, 2020.

[147] Jonathan P Dowling. Quantum optical metrology–the lowdown on high-n00n states. *Contemporary physics*, 49(2):125–143, 2008.

[148] Vittorio Giovannetti, Seth Lloyd, and Lorenzo Maccone. Advances in quantum metrology. *Nat. Photonics*, 5(4):222, 2011.

[149] Leonard Mandel. Coherence and indistinguishability. *Opt. Lett*, 16(23):1882–1883, 1991.

[150] Jan Sperling, Armando Perez-Leija, Kurt Busch, and Ian A Walmsley. Quantum coherences of indistinguishable particles. *Phys. Rev. A*, 96(3):032334, 2017.

[151] Alessia Castellini, Rosario Lo Franco, Ludovico Lami, Andreas Winter, Gerardo Adesso, and Giuseppe Compagno. Indistinguishability-enabled coherence for quantum metrology. *Phys. Rev. A*, 100(1):012308, 2019.

[152] Armando Perez-Leija, Diego Guzmán-Silva, Roberto de J León-Montiel, Markus Gräfe, Matthias Heinrich, Hector Moya-Cessa, Kurt Busch, and Alexander Szameit. Endurance of quantum coherence due to particle indistinguishability in noisy quantum networks. *npj Quantum Inf.*, 4(1):1–12, 2018.

[153] Farzam Nosrati, Alessia Castellini, Giuseppe Compagno, and Rosario Lo Franco. Dynamics of spatially indistinguishable particles and quantum entanglement protection. *Phys. Rev. A*, 102(6):062429, 2020.

[154] Hoi-Kwong Lo, Marcos Curty, and Bing Qi. Measurement-device-independent quantum key distribution. *Phys. Rev. Lett.*, 108(13):130503, 2012.

[155] Yang Liu, Teng-Yun Chen, Liu-Jun Wang, Hao Liang, Guo-Liang Shentu, Jian Wang, Ke Cui, Hua-Lei Yin, Nai-Le Liu, Li Li, et al. Experimental measurement-device-independent quantum key distribution. *Phys. Rev. Lett.*, 111(13):130502, 2013.

[156] Scott Aaronson and Alex Arkhipov. The computational complexity of linear optics. In *Proceedings of the forty-third annual ACM symposium on Theory of computing*, pages 333–342, New York, NY, USA, 2011. Association for Computing Machinery.

[157] Han-Sen Zhong, Hui Wang, Yu-Hao Deng, Ming-Cheng Chen, Li-Chao Peng, Yi-Han Luo, Jian Qin, Dian Wu, Xing Ding, Yi Hu, et al. Quantum computational advantage using photons. *Science*, 370(6523):1460–1463, 2020.

[158] Viv Kendon. Decoherence in quantum walks–a review. *Math. Struct. Comput. Sci.*, 17(6):1169–1220, 2007.

[159] Rafael Vieira, Edgard PM Amorim, and Gustavo Rigolin. Dynamically disordered quantum walk as a maximal entanglement generator. *Phys. Rev. Lett.*, 111(18):180503, 2013.

[160] Rafael Vieira, Edgard PM Amorim, and Gustavo Rigolin. Entangling power of disordered quantum walks. *Phys. Rev. A*, 89(4):042307, 2014.

[161] Meng Zeng and Ee Hou Yong. Discrete-time quantum walk with phase disorder: localization and entanglement entropy. *Sci. Rep.*, 7(1):1–9, 2017.

[162] Qin-Qin Wang, Xiao-Ye Xu, Wei-Wei Pan, Kai Sun, Jin-Shi Xu, Geng Chen, Yong-Jian Han, Chuan-Feng Li, and Guang-Can Guo. Dynamic-disorder-induced enhancement of entanglement in photonic quantum walks. *Optica*, 5(9):1136–1140, 2018.

[163] R Lo Franco, Bruno Bellomo, Erika Andersson, and Giuseppe Compagno. Revival of quantum correlations without system-environment back-action. *Phys. Rev. A*, 85(3):032318, 2012.

[164] Jin-Shi Xu, Kai Sun, Chuan-Feng Li, Xiao-Ye Xu, Guang-Can Guo, Erika Andersson, Rosario Lo Franco, and Giuseppe Compagno. Experimental recovery of quantum correlations in absence of system-environment back-action. *Nat. Commun*, 4(1):1–7, 2013.

[165] M B Plenio and Susana F Huelga. Dephasing-assisted transport: quantum networks and biomolecules. *New Journal of Physics*, 10(11):113019, 2008.

[166] Vir B Bulchandani, Christoph Karrasch, and Joel E Moore. Superdiffusive transport of energy in one-dimensional metals. *PNAS*, 117(23):12713–12718, 2020.

[167] Francesco De Nicola, Linda Sansoni, Andrea Crespi, Roberta Ramponi, Roberto Osellame, Vittorio Giovannetti, Rosario Fazio, Paolo Mataloni, and Fabio Sciarrino. Quantum simulation of bosonic-fermionic noninteracting particles in disordered systems via a quantum walk. *Phys. Rev. A*, 89(3):032322, 2014.

[168] Yoav Lahini, Mor Verbin, Sebastian D Huber, Yaron Bromberg, Rami Pugatch, and Yaron Silberberg. Quantum walk of two interacting bosons. *Phys. Rev. A*, 86(1):011603, 2012.

[169] Rosario Lo Franco and Giuseppe Compagno. Quantum entanglement of identical particles by standard information-theoretic notions. *Sci. Rep.*, 6:20603, 2016.

[170] Giuseppe Compagno, Alessia Castellini, and Rosario Lo Franco. Dealing with indistinguishable particles and their entanglement. *Phil. Trans. R. Soc. A*, 376(2123):20170317, 2018.

[171] Alessandro Fedrizzi, Thomas Herbst, Andreas Poppe, Thomas Jennewein, and Anton Zeilinger. A wavelength-tunable fiber-coupled source of narrowband entangled photons. *Opt. Express*, 15(23):15377–15386, 2007.

[172] Shin-Tson Wu. Birefringence dispersions of liquid crystals. *Physical Review A*, 33(2):1270, 1986.

[173] Peter L Knight, Eugenio Roldán, and JE Sipe. Propagating quantum walks: the origin of interference structures. *J. Mod. Opt.*, 51(12):1761–1777, 2004.

[174] Alessandro Laneve, Andrea Geraldi, Frenkli Hamiti, Paolo Mataloni, and Filippo Caruso. Experimental multi-state quantum discrimination through optical networks. *Quantum Science and Technology*, 2022.

[175] Alessandro Laneve, Michele B Rota, Francesco Basso Basset, Nicola P Fiorente, Tobias M Krieger, Saimon F Covre da Silva, Quirin Buchinger, Sandra Stroj, Sven Hoefling, Tobias Huber-Loyola, et al. Experimental multi-state quantum discrimination in the frequency domain with quantum dot light. *arXiv preprint arXiv:2209.08324*, 2022.

[176] Paweł Kurzyński and Antoni Wójcik. Quantum walk as a generalized measuring device. *Physical review letters*, 110(20):200404, 2013.

[177] Yuan-yuan Zhao, Neng-kun Yu, Paweł Kurzyński, Guo-yong Xiang, Chuan-Feng Li, and Guang-Can Guo. Experimental realization of generalized qubit measurements based on quantum walks. *Physical Review A*, 91(4):042101, 2015.

[178] Zihao Li, Haoyu Zhang, and Huangjun Zhu. Implementation of generalized measurements on a qudit via quantum walks. *Physical Review A*, 99(6):062342, 2019.

[179] Janos Bergou, Edgar Feldman, and Mark Hillery. Extracting information from a qubit by multiple observers: Toward a theory of sequential state discrimination. *Physical review letters*, 111(10):100501, 2013.

[180] Min Namkung and Younghun Kwon. Analysis of optimal sequential state discrimination for linearly independent pure quantum states. *Scientific reports*, 8(1):1–13, 2018.

[181] Nicola Dalla Pozza and Filippo Caruso. Quantum stochastic walk models for quantum state discrimination. *Physics Letters A*, 384(9):126195, 2020.

[182] James D Whitfield, César A Rodríguez-Rosario, and Alán Aspuru-Guzik. Quantum stochastic walks: A generalization of classical random walks and quantum walks. *Physical Review A*, 81(2):022323, 2010.

[183] Goran Lindblad. On the generators of quantum dynamical semigroups. *Communications in Mathematical Physics*, 48(2):119–130, 1976.

[184] Nicola Dalla Pozza and Filippo Caruso. Quantum state discrimination on reconfigurable noise-robust quantum networks. *Phys. Rev. Research*, 2:043011, Oct 2020.

[185] Mikio Fujiwara, Masahiro Takeoka, Jun Mizuno, and Masahide Sasaki. Exceeding the classical capacity limit in a quantum optical channel. *Physical review letters*, 90(16):167906, 2003.

[186] Nicolas J Cerf, Mohamed Bourennane, Anders Karlsson, and Nicolas Gisin. Security of quantum key distribution using d-level systems. *Physical review letters*, 88(12):127902, 2002.

[187] C.L. Degen, F. Reinhard, and P. Cappellaro. Quantum sensing. *Rev. Mod. Phys.*, 89:035002, 2017.

[188] Neill Lambert, Yueh-Nan Chen, Yuan-Chung Cheng, Che-Ming Li, Guang-Yin Chen, and Franco Nori. Quantum biology. *Nature Physics*, 9(1):10, 2013.

[189] Gilles Brassard, Norbert Lütkenhaus, Tal Mor, and Barry C Sanders. Limitations on practical quantum cryptography. *Physical review letters*, 85(6):1330, 2000.

[190] Alexios Beveratos, Rosa Brouri, Thierry Gacoin, André Villing, Jean-Philippe Poizat, and Philippe Grangier. Single photon quantum cryptography. *Physical review letters*, 89(18):187901, 2002.

[191] Maria Schuld, Ilya Sinayskiy, and Francesco Petruccione. The quest for a quantum neural network. *Quantum Information Processing*, 13(11):2567–2586, 2014.

[192] Daniele Cozzolino, Beatrice Da Lio, Davide Bacco, and Leif Katsuo Oxenløwe. High-dimensional quantum communication: benefits, progress, and future challenges. *Advanced Quantum Technologies*, 2(12):1900038, 2019.

[193] Thomas M Cover. *Elements of information theory*. John Wiley & Sons, 1999.

[194] Julio T Barreiro, Tzu-Chieh Wei, and Paul G Kwiat. Beating the channel capacity limit for linear photonic superdense coding. *Nature physics*, 4(4):282–286, 2008.

[195] Xiao-Min Hu, Yu Guo, Bi-Heng Liu, Yun-Feng Huang, Chuan-Feng Li, and Guang-Can Guo. Beating the channel capacity limit for superdense coding with entangled ququarts. *Science advances*, 4(7):eaat9304, 2018.

[196] P Ben Dixon, Gregory A Howland, James Schneeloch, and John C Howell. Quantum mutual information capacity for high-dimensional entangled states. *Physical review letters*, 108(14):143603, 2012.

[197] Lana Sheridan and Valerio Scarani. Security proof for quantum key distribution using qudit systems. *Physical Review A*, 82(3):030301, 2010.

[198] Helle Bechmann-Pasquinucci and Wolfgang Tittel. Quantum cryptography using larger alphabets. *Physical Review A*, 61(6):062308, 2000.

[199] Fulvio Flamini, Nicolo Spagnolo, and Fabio Sciarrino. Photonic quantum information processing: a review. *Reports on Progress in Physics*, 82(1):016001, 2018.

[200] Peter Michler, Alper Kiraz, Christoph Becher, WV Schoenfeld, PM Petroff, Lidong Zhang, Ella Hu, and A Imamoglu. A quantum dot single-photon turnstile device. *science*, 290(5500):2282–2285, 2000.

[201] Harishankar Jayakumar, Ana Predojević, Tobias Huber, Thomas Kauten, Glenn S. Solomon, and Gregor Weihs. Deterministic photon pairs and coherent optical control of a single quantum dot. *Phys. Rev. Lett.*, 110:135505, Mar 2013.

[202] Liang Zhai, Giang N Nguyen, Clemens Spinnler, Julian Ritzmann, Matthias C Löbl, Andreas D Wieck, Arne Ludwig, Alisa Javadi, and Richard J Warburton. Quantum interference of identical photons from remote gaas quantum dots. *Nature Nanotechnology*, pages 1–5, 2022.

[203] Lucas Schweickert, Klaus D Jöns, Katharina D Zeuner, Saimon Filipe Covre da Silva, Huiying Huang, Thomas Lettner, Marcus Reindl, Julien Zichi, Rinaldo Trotta, Armando Rastelli, et al. On-demand generation of background-free single photons from a solid-state source. *Applied Physics Letters*, 112(9):093106, 2018.

[204] Jin Liu, Rongbin Su, Yuming Wei, Beimeng Yao, Saimon Filipe Covre da Silva, Ying Yu, Jake Iles-Smith, Kartik Srinivasan, Armando Rastelli, Juntao Li, et al. A solid-state source of strongly entangled photon pairs with high brightness and indistinguishability. *Nature nanotechnology*, 14(6):586–593, 2019.

[205] Hui Wang, Yu-Ming He, T-H Chung, Hai Hu, Ying Yu, Si Chen, Xing Ding, M-C Chen, Jian Qin, Xiaoxia Yang, et al. Towards optimal single-photon sources from polarized microcavities. *Nature Photonics*, 13(11):770–775, 2019.

[206] Hui Wang, Hai Hu, T-H Chung, Jian Qin, Xiaoxia Yang, J-P Li, R-Z Liu, H-S Zhong, Y-M He, Xing Ding, et al. On-demand semiconductor source of entangled photons which simultaneously has high fidelity, efficiency, and indistinguishability. *Physical review letters*, 122(11):113602, 2019.

[207] Niccolo Somaschi, Valerian Giesz, Lorenzo De Santis, JC Loredo, Marcelo P Almeida, Gaston Hornecker, S Luca Portalupi, Thomas Grange, Carlos Anton, Justin Demory, et al. Near-optimal single-photon sources in the solid state. *Nature Photonics*, 10(5):340–345, 2016.

[208] Daniel Huber, Marcus Reindl, Saimon Filipe Covre Da Silva, Christian Schimpf, Javier Martín-Sánchez, Huiying Huang, Giovanni Piredda, Johannes Edlinger, Armando Rastelli, and Rinaldo Trotta. Strain-tunable gaas quantum dot: A nearly dephasing-free source of entangled photon pairs on demand. *Physical review letters*, 121(3):033902, 2018.

[209] J Nilsson, RM Stevenson, KHA Chan, J Skiba-Szymanska, M Lucamarini, MB Ward, AJ Bennett, CL Salter, I Farrer, DA Ritchie, et al. Quantum teleportation using a light-emitting diode. *Nature Photonics*, 7(4):311–315, 2013.

[210] Marcus Reindl, Daniel Huber, Christian Schimpf, Saimon F Covre da Silva, Michele B Rota, Huiying Huang, Val Zwiller, Klaus D Jöns, Armando Rastelli, and Rinaldo Trotta. All-photonic quantum teleportation using on-demand solid-state quantum emitters. *Science Advances*, 4(12):eaau1255, 2018.

[211] F Basso Basset, Michele B Rota, Christian Schimpf, Davide Tedeschi, Katharina D Zeuner, SF Covre Da Silva, Marcus Reindl, Val Zwiller, Klaus D Jöns, Armando Rastelli, et al. Entanglement swapping with photons generated on demand by a quantum dot. *Physical Review Letters*, 123(16):160501, 2019.

[212] Michael Zopf, Robert Keil, Yan Chen, Jingzhong Yang, Disheng Chen, Fei Ding, and Oliver G Schmidt. Entanglement swapping with semiconductor-generated photons violates bell's inequality. *Physical review letters*, 123(16):160502, 2019.

[213] Timm Kupko, Martin von Helversen, Lucas Rickert, Jan-Hindrik Schulze, André Strittmatter, Manuel Gschrey, Sven Rodt, Stephan Reitzenstein, and Tobias Heindel. Tools for the performance optimization of single-photon quantum key distribution. *npj Quantum Information*, 6(1):1–8, 2020.

[214] Francesco Basso Basset, Mauro Valeri, Emanuele Roccia, Valerio Muredda, Davide Poderini, Julia Neuwirth, Nicolò Spagnolo, Michele B Rota, Gonzalo Carvacho, Fabio Sciarrino, et al.

Quantum key distribution with entangled photons generated on demand by a quantum dot. *Science advances*, 7(12):eabe6379, 2021.

[215] Natasha Tomm, Alisa Javadi, Nadia Olympia Antoniadis, Daniel Najer, Matthias Christian Löbl, Alexander Rolf Korsch, Rüdiger Schott, Sascha René Valentin, Andreas Dirk Wieck, Arne Ludwig, et al. A bright and fast source of coherent single photons. *Nature Nanotechnology*, 16(4):399–403, 2021.

[216] Thomas Aichele, Gaël Reinaudi, and Oliver Benson. Separating cascaded photons from a single quantum dot: Demonstration of multiplexed quantum cryptography. *Physical Review B*, 70(23):235329, 2004.

[217] Roger BM Clarke, Vivien M Kendon, Anthony Chefles, Stephen M Barnett, Erling Riis, and Masahide Sasaki. Experimental realization of optimal detection strategies for overcomplete states. *Physical Review A*, 64(1):012303, 2001.

[218] Masoud Mohseni, Aephraim M Steinberg, and János A Bergou. Optical realization of optimal unambiguous discrimination for pure and mixed quantum states. *Physical review letters*, 93(20):200403, 2004.

[219] MA Solis-Prosser, P González, J Fuenzalida, S Gomez, GB Xavier, A Delgado, and G Lima. Experimental multiparty sequential state discrimination. *Physical Review A*, 94(4):042309, 2016.

[220] FE Becerra, Jingyun Fan, Gerald Baumgartner, SV Polyakov, Julius Goldhar, JT Kosloski, and Alan Migdall. M-ary-state phase-shift-keying discrimination below the homodyne limit. *Physical Review A*, 84(6):062324, 2011.

[221] MA Solís-Prosser, MF Fernandes, O Jiménez, A Delgado, and L Neves. Experimental minimum-error quantum-state discrimination in high dimensions. *Physical review letters*, 118(10):100501, 2017.

[222] Antonio Assalini, Nicola Dalla Pozza, and Gianfranco Pierobon. Revisiting the dolinar receiver through multiple-copy state discrimination theory. *Physical Review A*, 84(2):022342, 2011.

[223] Sergei Slussarenko, Morgan M Weston, Jun-Gang Li, Nicholas Campbell, Howard M Wiseman, and Geoff J Pryde. Quantum state discrimination using the minimum average number of copies. *Physical review letters*, 118(3):030502, 2017.

[224] Nicola Dalla Pozza and Filippo Caruso. Quantum state discrimination on reconfigurable noise-robust quantum networks. *Physical Review Research*, 2(4):043011, 2020.

[225] Marcelo Davanco, Matthew T Rakher, Dieter Schuh, Antonio Badolato, and Kartik Srinivasan. A circular dielectric grating for vertical extraction of single quantum dot emission. *Applied Physics Letters*, 99(4):041102, 2011.

[226] YH Huo, A Rastelli, and OG Schmidt. Ultra-small excitonic fine structure splitting in highly symmetric quantum dots on gaas (001) substrate. *Applied Physics Letters*, 102(15):152105, 2013.

[227] Jin Liu, Marcelo I Davanço, Luca Sapienza, Kumarasiri Konthasinghe, José Vinícius De Miranda Cardoso, Jin Dong Song, Antonio Badolato, and Kartik Srinivasan. Cryogenic photoluminescence imaging system for nanoscale positioning of single quantum emitters. *Review of Scientific Instruments*, 88(2):023116, 2017.

[228] Hai Son Nguyen, Gregory Sallen, Marco Abbarchi, Robson Ferreira, Christophe Voisin, Philippe Roussignol, Guillaume Cassabois, and Carole Diederichs. Photoneutralization and slow capture of carriers in quantum dots probed by resonant excitation spectroscopy. *Physical review B*, 87(11):115305, 2013.

[229] Tobias Huber, Ana Predojević, Glenn S Solomon, and Gregor Weihs. Effects of photoneutralization on the emission properties of quantum dots. *Optics Express*, 24(19):21794–21801, 2016.

[230] Paritosh Manurkar, Nitin Jain, Michael Silver, Yu-Ping Huang, Carsten Langrock, Martin M Fejer, Prem Kumar, and Gregory S Kanter. Multidimensional mode-separable frequency conversion for high-speed quantum communication. *Optica*, 3(12):1300–1307, 2016.

[231] Sachin Kasture, Francesco Lenzini, Ben Haylock, Andreas Boes, Arnan Mitchell, Erik W Streed, and Mirko Lobino. Frequency conversion between uv and telecom wavelengths in a lithium niobate waveguide for quantum communication with yb+ trapped ions. *Journal of Optics*, 18(10):104007, 2016.

[232] Nils T Otterstrom, Shai Gertler, Eric A Kittlaus, Michael Gehl, Andrew L Starbuck, Christina M Dallo, Andrew T Pomerene, Douglas C Trotter, Peter T Rakich, Paul S Davids, et al. Nonreciprocal frequency domain beam splitter. *Physical review letters*, 127(25):253603, 2021.

[233] Alessandro Laneve, Hannah McAleese, and Mauro Paternostro. A scheme for multipartite entanglement distribution via separable carriers. *New Journal of Physics*, 24:123003, 2022.

[234] Artur K Ekert. Quantum cryptography and Bell's theorem. In *Quantum Measurements in Optics*, pages 413–418. Springer, 1992.

[235] Juan Ignacio Cirac, Peter Zoller, H Jeff Kimble, and Hideo Mabuchi. Quantum state transfer and entanglement distribution among distant nodes in a quantum network. *Physical Review Letters*, 78(16):3221, 1997.

[236] Danilo Boschi, Salvatore Branca, Francesco De Martini, Lucien Hardy, and Sandu Popescu. Experimental realization of teleporting an unknown pure quantum state via dual classical and Einstein-Podolsky-Rosen channels. *Physical Review Letters*, 80(6):1121, 1998.

[237] Dik Bouwmeester, Jian-Wei Pan, Klaus Mattle, Manfred Eibl, Harald Weinfurter, and Anton Zeilinger. Experimental quantum teleportation. *Nature*, 390(6660):575–579, 1997.

[238] Rupert Ursin, F Tiefenbacher, T Schmitt-Manderbach, H Weier, Thomas Scheidl, M Lindenthal, B Blauensteiner, T Jennewein, J Perdigues, P Trojek, et al. Entanglement-based quantum communication over 144 km. *Nature Physics*, 3(7):481–486, 2007.

[239] Peter C Humphreys, Norbert Kalb, Jaco PJ Morits, Raymond N Schouten, Raymond FL Vermeulen, Daniel J Twitchen, Matthew Markham, and Ronald Hanson. Deterministic delivery of remote entanglement on a quantum network. *Nature*, 558(7709):268–273, 2018.

[240] Sören Wengerowsky, Siddarth Koduru Joshi, Fabian Steinlechner, Hannes Hübel, and Rupert Ursin. An entanglement-based wavelength-multiplexed quantum communication network. *Nature*, 564(7735):225–228, 2018.

[241] Toby S Cubitt, Frank Verstraete, W Dür, and J Ignacio Cirac. Separable states can be used to distribute entanglement. *Physical Review Letters*, 91(3):037902, 2003.

[242] L. Mišta Jr. and N. Korolkova. Distribution of continuous-variable entanglement by separable Gaussian states. *Physical Review A*, 77:050302(R), 2008.

[243] TK Chuan, J Maillard, Kavan Modi, Tomasz Paterek, Mauro Paternostro, and Marco Piani. Quantum discord bounds the amount of distributed entanglement. *Physical Review Letters*, 109(7):070501, 2012.

[244] Harold Ollivier and Wojciech H Zurek. Quantum discord: a measure of the quantumness of correlations. *Phys. Rev. Lett.*, 88(1):017901, 2001.

[245] Charles H Bennett, David P DiVincenzo, John A Smolin, and William K Wootters. Mixed-state entanglement and quantum error correction. *Physical Review A*, 54(5):3824, 1996.

[246] Animesh Datta and Guifre Vidal. Role of entanglement and correlations in mixed-state quantum computation. *Physical Review A*, 75(4):042310, 2007.

[247] Nan Li and Shunlong Luo. Classical states versus separable states. *Physical Review A*, 78(2):024303, 2008.

[248] Vlatko Vedral and Martin B Plenio. Entanglement measures and purification procedures. *Physical Review A*, 57(3):1619, 1998.

[249] Michał Horodecki, Paweł Horodecki, Ryszard Horodecki, Jonathan Oppenheim, Aditi Sen, Ujjwal Sen, Barbara Synak-Radtke, et al. Local versus nonlocal information in quantum-information theory: formalism and phenomena. *Physical Review A*, 71(6):062307, 2005.

[250] K Modi, T Paterek, W Son, V Vedral, and M Williamson. Unified view of quantum and classical correlations. *Physical Review Letters*, 104:080501, 2010.

[251] A. Streltsov, H. Kampermann, and D. Bruß. Quantum cost for sending entanglement. *Physical Review Letters*, 108:250501, 2012.

[252] Frank Verstraete, Markus Popp, and J Ignacio Cirac. Entanglement versus correlations in spin systems. *Physical review letters*, 92(2):027901, 2004.

[253] T. Werlang, S. Souza, F. F. Fanchini, and C. J. Villas Boas. Robustness of quantum discord to sudden death. *Physical Review A*, 80:024103, 2009.

[254] A. Ferraro, L. Aolita, D. Cavalcanti, F. M. Cucchietti, and A. Acín. Almost all quantum states have nonclassical correlations. *Physical Review A*, 81:052318, 2010.

[255] B. Wang, Z. Y. Xu, Z. Q. Chen, and M. Feng. Non-Markovian effect on the quantum discord. *Physical Review A*, 81:014101, 2010.

[256] F. F. Fanchini, T. Werlang, C. A. Brasil, L. G. E. Arruda, and A. O. Caldeira. Non-Markovian dynamics of quantum discord. *Physical Review A*, 81:052107, 2010.

[257] L. Mazzola, J. Piilo, and S. Maniscalco. Sudden transition between classical and quantum decoherence. *Physical Review Letters*, 104:200401, 2010.

[258] A. Kay. Using separable Bell-diagonal states to distribute entanglement. *Physical Review Letters*, 109:080503, 2012.

[259] L. Mišta Jr. and N. Korolkova. Improving continuous-variable entanglement distribution by separable states. *Physical Review A*, 80:032310, 2009.

[260] L. Mišta Jr. Entanglement sharing with separable states. *Physical Review A*, 87:062326, 2013.

[261] Alessandro Fedrizzi, Margherita Zuppardo, GG Gillett, MA Broome, MP Almeida, Mauro Paternostro, AG White, and Tomasz Paterek. Experimental distribution of entanglement with separable carriers. *Physical Review Letters*, 111(23):230504, 2013.

[262] C. E. Vollmer, D. Schulze, T. Eberle, V. Händchen, J. Fiurášek, and R. Schnabel. Experimental entanglement distribution by separable states. *Physical Review Letters*, 111:230505, 2013.

[263] C. Peuntinger, V. Chille, L. Mišta Jr., N. Korolkova, M. Förtsch, J. Korger, C. Marquardt, and G. Leuchs. Distributing entanglement with separable states. *Physical Review Letters*, 111:230506, 2013.

[264] M Horodecki, P Horodecki, R Horodecki, J Oppenheim, A Sen(De), U Sen, and B Synak-Radtke. Local versus nonlocal information in quantum-information theory: Formalism and phenomena. *Physical Review A*, 71:062307, 2005.

[265] Vahid Karimipour, Laleh Memarzadeh, and Najmeh Tabe Bordbar. Systematics of entanglement distribution by separable states. *Physical Review A*, 92(3):032325, 2015.

[266] M Horodecki, P Horodecki, and R Horodecki. Separability of mixed states: necessary and sufficient conditions. *Physics Letters A*, 223:1, 1996.

[267] N. K. Langford, T. J. Weinhold, R. Prevedel, K. J. Resch, A. Gilchrist, J. L. O'Brien, G. J. Pryde, and A. G. White. Demonstration of a simple entangling optical gate and its use in Bell-state analysis. *Physical Review Letters*, 95:210504, Nov 2005.

[268] Alex E. Jones, Adrian J. Menssen, Helen M. Chrzanowski, Tom A. W. Wolterink, Valery S. Shchesnovich, and Ian A. Walmsley. Multiparticle interference of pairwise distinguishable photons. *Physical Review Letters*, 125:123603, Sep 2020.

[269] G. Murta, F. Grasselli, H. Kampermann, and D. Bruß. Quantum conference key agreement: a review. *Advanced Quantum Technologies*, 3:2000025, 2020.

[270] S.-K. Liao, W.-Q. Cai, J. Handsteiner, B. Liu, J. Yin, L. Zhang, D. Rauch, M. Fink, J.-G. Ren, W.-Y. Liu, Y. Li, Q. Shen, Y. Cao, F.-Z. Li, J.-F. Wang, Y.-M. Huang, L. Deng, T. Xi, L. Ma, T. Hu, L. Li, N.-L. Liu, F. Koidl, P. Wang, Y.-A. Chen, X.-B. Wang, M. Steindorfer, G. Kirchner, C.-Y. Lu, R. Shu, R. Ursin, T. Scheidl, C.-Z. Peng, J.-Y. Wang, A. Zeilinger, and J.-W. Pan. Satellite-relayed intercontinental quantum network. *Physical Review Letters*, 120:030501, 2018.

[271] J. F. Dynes, A. Wonfor, W. W.-S. Tam, A. W. Sharpe, R. Takahashi, M. Lucamarini, A. Plews, Z. L. Yuan, A. R. Dixon, J. Cho, Y. Tanizawa, J.-P. Elbers, H. Greißer, I. H. White, R. V. Penty, and A. J. Shields. Cambridge quantum network. *npj Quantum Information*, 5:101, 2019.

[272] A. Aguago, V. López, D. López, M. Peev, A. Poppe, A. Pastor, J. Folgueira, and V. Martín. The engineering of software-defined quantum key distribution networks. *IEEE Communication Magazine*, 57:20, 2019.

[273] G. Carrara, H. Kampermann, D. Bruß, and G. Murta. Genuine multipartite entanglement is not a precondition for secure conference key agreement. *Physical Review Research*, 3:013264, 2021.

[274] F. Grasselli, H. Kampermann, and D. Bruß. Finite-key effects in multipartite quantum key distribution protocols. *New Journal of Physics*, 20:113014, 2018.

[275] Daniel M Greenberger, Michael A Horne, and Anton Zeilinger. Going beyond bell's theorem. In *Bell's theorem, quantum theory and conceptions of the universe*, pages 69–72. Springer, 1989.

General acknowledgements

Needless to say, I would not have made it alone. And not only because actually performing three or four experiments on my own would have been at least impractical, but, above all, because most of the time I did not have any idea of what and how and why, but someone was always there to show me the way. One of my worst flaws, I believe, consists of the fact that I am a taker rather than a giver, and a hungry one. As a consequence, I have many to thank.

I am deeply grateful to Prof. Mataloni: these four years together, from my master thesis to the end of my PhD, have been a wonderful journey. The morning I entered his office looking for a thesis proposal, I noticed something different. I was not even sure I wanted to do experiments, but the feeling he was able to transmit to me, it was just something else. That choice, I think I will never regret. He gave me freedom and trust, he scolded me when I needed to be (let me say, not a few times), he was kind and understanding and, notwithstanding his very busy schedule, he was always there when I needed. I wish I had the attitude to ask more. He taught me far more than how to be a good scientist; I have already thanked him for that and I will again.

I have to thank Andrea so much: most of the things I know now, I know thanks to him. He turned me from a clumsy lazy brooding chap into a true lab animal (still a bit lazy though). Jokes apart, I have found in him a great companion through these years and, I have to admit, I have felt a bit lost without him. But I have managed to carry on with my own strength, and I definitely owe it to him. I have found in him a fun, competent, hardworking partner, the best I could ask for. I have found in him a friend.

I have also to thank and apologize to the unfortunate people who worked with me during their master thesis: dear Federico, Frenkli, Nicola, I have not thanked you enough for your help, I only hope I have been able to teach you something.

I also want to thank Prof. Trotta for welcoming in his laboratory during my last months of PhD and showing me his trust. I hope we will keep working together for long. I thank Michele, Francesco and Giuseppe for making me feel at home in the blink of an eye.

I wish to thank prof. Sciarrino for his helpfulness and support, both as a "neighbouring scientist" and as the Coordinator of the PhD course. I am thankful to the whole G21, that is now partly scattered around the globe: indeed, it was easier to work with you around, surrounded by your playful and constant warmth.

My thanks also go to Prof. Paternostro: working with him was an extraordinary experience, I enjoyed every bit of it, mainly due to his great generosity and brightness. I thank him for giving me the chance to live as a theorist, at least once in my life. I thank all the people from Queen's University of Belfast that I crossed my path with: you made my staying nicer than I would have ever thought. I have left a piece of my heart in Northern Ireland, and this is also your doing, for

sure.
Attending a PhD course is a very intense experience, that permeates the mind and soul of a man (my back cries "and the body too!"). It is not like you can get at home and just stop thinking about "THE RESEARCH". Thus, PhD life and personal life inevitably cross and tangle; and there is little chance of successfully separating them. Sometimes, this does not turn out well, but for me it was the other way around.
Arianna, thank you and thank you a thousand times: you have been there next to me through it all, notwithstanding my crippling anxiety, my complains, my laziness, my constant distraction, my gluttonous need of attention, and my literally intolerable personality. You make me happy, you make me better and wishful to be better. You are the best person I know and I am so very lucky to have you in my life.
To my family, I also give my thanks: I know I have not been the most loving and caring son, but take these words as a token of my gratitude for your support and your patience. I know you care and I am grateful.
I apologize if I forgot to thank anyone; in conclusion, most of what I have accomplished, one way or the other, I owe it to someone or something that occurred in my life.
If it ever meant anything, I would have to thank Luck, that has never abandoned me through the years. I do not know if this is part of some imposter syndrome, but I am aware of the amount of good things and people that my life have been endowed with, without any recognizable reason.
I feel blessed, and I am on my way to try to deserve it.